# SEARCH FOR DARK MATTER AND SUPERSYMMETRY VIA VECTOR BOSON FUSION AT THE LARGE HADRON COLLIDER

By

Andrés G. Delannoy

Dissertation

Submitted to the Faculty of the

Graduate School of Vanderbilt University

in partial fulfillment of the requirements

for the degree of

DOCTOR OF PHILOSOPHY

in

Physics

May, 2016

Nashville, Tennessee

Approved:

Professor Will E. Johns, Ph.D.

Professor Andreas Berlind, Ph.D.

Professor Thomas Kephart, Ph.D.

Professor Paul Sheldon, Ph.D.

Professor Julia Velkovska, Ph.D.

TABLE OF CONTENTS

LIST OF TABLES

LIST OF FIGURES

# Chapter 1

# Introduction

Cosmological measurements indicate that dark matter (DM) constitutes 85% of all matter in the universe [2]. The identity of DM is one of the most fundamental open questions in both particle physics and cosmology. Many extensions of the standard model (SM) predict a DM candidate in the form of a weakly interacting massive particle at the electroweak symmetry breaking scale. The lightest supersymmetric particle (LSP) in R-parity conserving supersymmetry (SUSY) [3] is potentially one such candidate [4].

Previous searches for SUSY at the CERN LHC have relied on signatures of large missing transverse momentum, energetic leptons, photons, and/or hadronic jets from the decay of heavier supersymmetric particles. Such searches have limited sensitivity in scenarios where the LSP is almost mass degenerate with the parent particle, resulting in visible particles with too little energy to be detected efficiently. For example, in very *compressed mass spectrum* scenarios with promptly decaying charginos, ATLAS and CMS searches do not extend the LSP mass bounds from LEP [5, 6, 7].

This document describes a general search for new physics that gives rise to events with large missing transverse momentum and two jets consistent with a vector boson fusion (VBF) topology. Such a topology arises when a parton from each proton radiates a vector boson, and that pair of vector bosons couples to a particle [8, 9] or a pair of particles. The recoiling partons yield jets in opposite hemispheres, with large rapidity separation and large dijet invariant mass [10, 11]. The two jets boost the decay products of the new particles, which aids event selection and analysis. The technique is similar to requiring a jet from initial state radiation [12, 13, 14] but with enhanced rejection of multijet background. Missing transverse momentum arises when some or all of the decay products of the new particles escape undetected. The dijet mass spectrum is analyzed to search for new physics

in events with missing transverse momentum and two jets consistent with a VBF topology.

As examples of new physics yielding the above signature, generic DM production through VBF [15] is considered, i.e. pure electroweak production, and strong production of supersymmetric bottom quark (bottom squark) pairs in a compressed mass spectrum scenario (see Fig. 1.1). We assume the DM particle to be a Dirac fermion and its interaction with the electroweak gauge bosons to be mediated by a heavy particle. We use an effective field theory approach with a contact interaction of scale $\Lambda = \mathscr{M} / g_{\text{eff}} = \mathscr{M} / \sqrt{g_\chi g_{\text{V}}}$, where $\mathscr{M}$ is the mass of the heavy mediator, $g_\chi$ is its coupling to the DM particle, and $g_{\text{V}}$ is its coupling to vector bosons V=$\gamma$, Z, or W. Only Higgs portal operators of dimension 5 are considered [15]. In the case of bottom squark pair production the bottom squark and LSP are assumed to be nearly mass degenerate, and the bottom plus LSP decay to be the only open channel. For very small mass differences, the bottom squark lifetime increases. The analysis is sensitive as long as the bottom squark decays before reaching the calorimeter or muon detectors. As the mass difference increases, the bottom quark jets carry larger momentum, and events start to elude our selection.

Figure 1.1: Feynman diagrams of bottom squark pair production (left) and DM pair production (right).

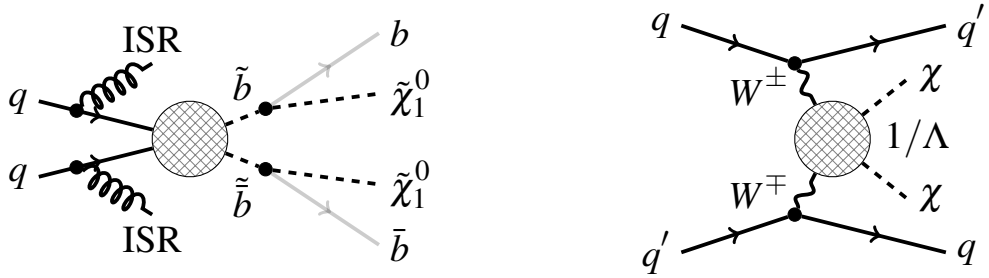


The analysis is performed using data collected with CMS at the LHC in proton-proton (pp) collisions at a center-of-mass energy of 8 TeV. The data sample corresponds to an integrated luminosity of 18.5 $\text{fb}^{-1}$.

# Chapter 2

# Physics Background

## 2.1 The Standard Model

The Standard Model of particle physics is presently the best description of the fundamental constituents of matter and their interactions. In the context of this model, which is rooted in quantum field theory, the observable universe consists of a collection of quantized fields which permeate the entirety of space. A discrete local excitation of such a field, i.e. its quanta, corresponds to an individual particle. This set of quantized fields, and their corresponding quanta, can be classified into two categories: *fermions* and *bosons*. Excitations in the fermionic fields make up what we consider "conventional" matter, while the quanta corresponding to bosonic fields, known as gauge bosons, mediate or communicate the interactions between fermions.

## 2.2 Statistics

Fermions satisfy *Fermi-Dirac* statistics and bosons satisfy *Bose-Einstein* statistics. Any system is fully described by its single wave-function, $|\psi\rangle$. If we consider a system made up of identical particles, it is impossible to tell which particle is in which position. Thus, the physical state ($|\psi|^2$) has to be invariant to the exchange in position of two identical particles. The wave-function of a system obeying Bose-Einstein statistics is symmetric under the exchange of two particles. The *Spin-statistics theorem* [16, 17] implies that bosons always carry integer spin. Similarly, the wave-function of a system obeying Fermi-Dirac statistics is anti-symmetric under the exchange of two particles. Thus, fermions carry half-integer spin. A consequence of this is the *Pauli Exclusion Principle*:

- Bosons tend to congregate in the same single-particle state, whereas two fermions

cannot occupy the same single-particle state [18].

This is easily seen if we let $\phi_1(x_1)$ and $\phi_2(x_2)$ be the wave-functions for identical, individual particles at positions $x_1$ and $x_2$, respectively. Then, we can write the system's wave-function as

$$\psi(x_1,x_2) = \phi_1(x_1)\phi_2(x_2) \pm \phi_1(x_2)\phi_2(x_1), \tag{2.1}$$

where the $+$ sign corresponds to Bose statistics and the $-$ sign to Fermi statistics. Given the exchange in the position of each particle,

$$\begin{aligned} \psi_{\text{Bose}}(x_2,x_1) &= \phi_1(x_2)\phi_2(x_1) + \phi_1(x_1)\phi_2(x_2) \\ \psi_{\text{Fermi}}(x_2,x_1) &= \phi_1(x_2)\phi_2(x_1) - \phi_1(x_1)\phi_2(x_2), \end{aligned} \tag{2.2}$$

it is readily seen that the wave function of the system obeying Fermi statistics would be zero if the particles were in the same position (i.e. $\psi_{\text{Fermi}}(x_1,x_1) = 0$).

## 2.3 Fundamental Particles and their Interactions

All fundamental fermions are spin-1/2 particles (in units of $\hbar$) and we can classify them into *quarks* and *leptons*. Leptons are classified into 6 flavors: the *electron* ($e$), *muon* ($\mu$), *tau* ($\tau$), and their associated *neutrinos* ($\nu_e$, $\nu_\mu$, $\nu_\tau$). Likewise, quarks are classified into 6 flavors: *up* ($u$), *down* ($d$), *charmed* ($c$), *strange* ($s$), *top* ($t$), and *bottom* ($b$) as shown in Figure 2.1. In addition, each fermion has a corresponding *anitiparticle* with the same mass but opposite charge.

All the phenomena that we observe can be described by four types of interactions between fermions. These interactions are the *electromagnetic*, *weak*, *strong*, and *gravitational* forces. To each corresponds a gauge boson that mediates the interaction (see Figure 2.1): the *photon* ($\gamma$), the *gluon* ($g$), *weak bosons* ($W^{\pm}, Z^0$), and the hypothetical *graviton* ($G$), respectively. Leptons only interact electromagnetically and weakly, whereas quarks interact electromagnetically, weakly, and strongly.

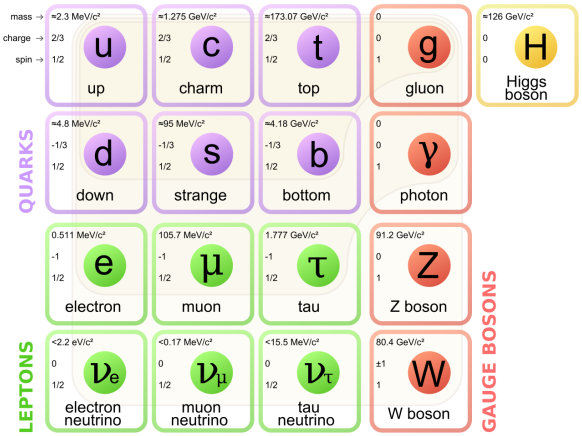


Figure 2.1: Elementary Particles of the Standard Model

Although the range of gravity is infinite, it is the weakest of all the interactions. The reason gravity dominates at cosmological scales is because it is generated by a single kind of "charge" which is always attractive (i.e. gravity cannot be shielded or neutralized like other forces). The Standard Model does not include a description of gravity.

By the late 1800's, it was realized that a changing electric field produces a magnetic field and that a changing magnetic field generates an electric field [19]. Thus, they are regarded as two aspects of the electromagnetic interaction. Moreover, the electromagnetic interaction is responsible for practically all observed macroscopic phenomena (e.g. light, friction, tension, etc.) ignoring gravitational phenomena.

The weak interaction was first introduced to describe radioactive decay. In particular, $\beta$ decay ($n \rightarrow p + e^{-} + \bar{\nu}_e$), illustrated in Figure 2.2, was particulary puzzling because its observed product—electrons—were observed to have a continuous, rather than discrete, energy spectrum. This implied that the decay violated energy and momentum conservation. Pauli famously suggested a solution to this problem in a letter in 1930 with the prediction of a new particle with no charge and extremely small mass [20]. The neutrino, as we know it today, was experimentally observed in 1956, 26 years after it was first postulated [21].

All fermions are influenced by the weak interaction. It is the only interaction capable of changing the flavor of quarks. *Lepton number*, i.e. the number of leptons minus the

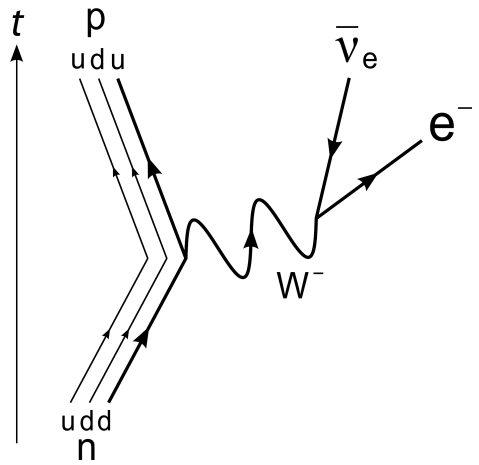


Figure 2.2: Beta Decay

number of anti-leptons, is "accidentally" conserved under all interactions observed so far. All particles are assigned a quantum number which is conserved under weak processes called *weak isospin*. It reflects the manner in which the weak interaction discriminates between left- and right-handed fermions [22].

The strong interaction is responsible for binding inside the nucleus. Any particle affected by the strong interaction is said to be a *hadron*. It was suspected that nucleons were made up of three elementary quarks and it was deduced that some bound states combine identical fermions in a completely symmetric ground-state (e.g. $\Delta^{++}$). This type of configuration violates Pauli exclusion, since quarks are spin-1/2 fermions. Thus, a new fundamental charge called *color* was introduced to accommodate distinct quantum states for each quark [23]. The color charge can adopt three values: red ($R$), blue ($B$), or green ($G$).

Moreover, it was postulated that only a "colorless" combination of quarks can create a bound state (e.g. proton = $u_{\mathrm{R}}u_{\mathrm{G}}d_{\mathrm{B}}$). This is consistent with the observation that quarks are never detected in isolation, a property known as *color confinement* [24]. Thus, a large amount of energy supplied to a single hadron results in multiple hadrons spontaneously appearing instead of isolated quarks; analogous to a bar magnet breaking into two bar magnets instead of splitting into two monopoles. This process is called *hadronization* and

leads to the production of narrow cones of hadrons called *jets* [25].

As remarked, quarks will always form colorless composite particles called hadrons which are commonly sub-classified as *baryons* or *mesons*. Baryons are fermions made up of three quarks (e.g. proton, neutron). Mesons are unstable bosons composed of a quark and an anti-quark (e.g. pion). *Baryon number*, i.e. the number of baryons minus the number of anti-baryons, is "accidentally" conserved under all interactions observed so far.

The residual strong force outside colorless hadrons binds them into atomic nuclei, in spite of electromagnetic repulsion. The positively charged nuclei and negatively charged leptons (electrons) are bound into atoms by the electromagnetic interaction. The residual electromagnetic force outside electrically neutral atoms binds them into molecules, and their electromagnetic interaction with other molecules and atoms given rise to all macroscopic phenomena, except for gravity [26].

## 2.4 Symmetry

In physics, we say that there is a symmetry when a system undergoes some change or transformation yet some observable or intrinsic quantity remains unchanged. The Principle of Relativity is an example of such a symmetry. *Noether's theorem* states that to each continuous symmetry in a physical system described by a Lagrangian there corresponds a conserved quantity [27]. For instance, a system that exhibits invariance under translation in space will, correspondingly, exhibit conservation of linear momentum. Time translation symmetry yields conservation of energy; rotation symmetry leads to conservation of angular momentum, etc. [24].

## 2.5 Relativity

Any physical theory must be consistent with special relativity, which postulates:

- The Principle of Relativity — The mathematical formulation of all physical theories

is covariant under all interial reference frames.

- The Invariance of $c$ — The measured speed of light in vacuum in all inertial reference frames is the same, i.e. 299792458 m/s.

The general idea is that physical phenomena cannot depend on how a human observer chooses to describe them (i.e. there should be no preferred or absolute reference frame). Coordinates are a human contrivance and should play no role in the formulation of physical theories.

We can define a *Lorentz transformation* as a change of space-time coordinates which will keep the speed of light invariant. A scalar quantity which remains invariant under this kind of a transformation (e.g. the space-time interval, $\Delta s^2 = g_{mn}\Delta x^m \Delta x^n = c^2\Delta t^2 - \Delta r^2$) is said to be *Lorentz invariant* [28]. A way to guarantee that the physical phenomena are independent of coordinate choice is to write all physical theories as tensor equations. Tensors are geometrical entities which, by construction, are independent of any chosen coordinate system. They are defined by their transformation laws with respect to the conversion from one system of coordinates to another [28, 29]. Thus, any equation that holds in a given inertial frame and can be written down in terms of Lorentz covariant terms will hold in *all* inertial frames.

## 2.6 Quantum Mechanics

The Standard Model is deeply rooted in quantum mechanics. Its formal mathematical basis was developed in the mid 1920's to describe the behavior of matter at very small scales. It postulates that there corresponds a quantum operator (e.g. $\hat{A}$) to every observable quantity, such that a measurement of this observable yields an *eigenvalue* (e.g. $a$) of the operator:

$$\hat{A}\psi_a = a\psi_a. \qquad \text{(eigenvalue equation)} \tag{2.3}$$

The measurement of $\hat{A}$ forces the system to assume the eigenstate $\psi_a$ [30]. The wave-function $\psi$ contains all information regarding the state of the system. In order to extract information from the wave function, we calculate the *expectation value* of an operator,

$$< \hat{C} >= \int \psi^* \hat{C} \psi d^3 r. \tag{2.4}$$

The expectation value can be interpreted as the average value obtained after making a very large number of observations from an ensemble of identical systems in the same state.

The time evolution of the state of the system is given by:

$$i\hbar \frac{\partial}{\partial t} \psi(\mathbf{x},t) = \hat{H} \psi(\mathbf{x},t). \qquad \text{(time-dependent Schrödinger Equation)} \tag{2.5}$$

By defining,

$$\rho \equiv |\psi|^2, \qquad \text{(probability density)} \tag{2.6}$$

$$\mathbf{J} \equiv -\frac{i\hbar}{2m} \left( \psi^* \nabla \psi - \psi \nabla \psi^* \right), \qquad \text{(current density)} \tag{2.7}$$

and adding Schrödinger's Equation (2.5) to its complex conjugate, we obtain the continuity equation expressing the conservation of matter [30]:

$$\nabla \cdot \mathbf{J} + \frac{\partial \rho}{\partial t} = 0. \qquad \text{(continuity equation)} \tag{2.8}$$

## 2.7 Electromagnetism

Another crucial ingredient to the Standard Model is electromagnetism. By the early 1900's electricity and magnetism were unified in a mathematical formalism know as Maxwell's

equations:

$$\nabla \cdot \mathbf{E} = \frac{\rho}{\varepsilon_0} \qquad \text{(Gauss's law for electricity)}, \tag{2.9}$$

$$\nabla \cdot \mathbf{B} = 0 \qquad \text{(Gauss's law for magnetism)}, \tag{2.10}$$

$$\nabla \times \mathbf{E} = -\frac{\partial \mathbf{B}}{\partial t} \qquad \text{(Faraday's law of induction)}, \tag{2.11}$$

$$\nabla \times \mathbf{B} = \mu_0 \mathbf{J} + \mu_0 \varepsilon_0 \frac{\partial \mathbf{E}}{\partial t}. \qquad \text{(Ampere's law with Maxwell's correction)} \tag{2.12}$$

We can formulate Maxwell's equations in a manifestly covariant way and thus consistent with the postulates of relativity. Using Maxwell's equations we can write the electric and magnetic fields in terms of their potentials [26]

$$\mathbf{E} = -\nabla \phi - \frac{1}{c}\frac{\partial \mathbf{A}}{\partial t}, \tag{2.13}$$

$$\mathbf{B} = \nabla \times \mathbf{A}. \tag{2.14}$$

We introduce the *four-potential*, a covariant four-vector containing the electric potential and the magnetic vector potential

$$A^{\mu} = (\phi, \boldsymbol{A}) \ . \tag{2.15}$$

Recalling that $\partial^{\mu} \equiv \dfrac{\partial}{\partial x_{\mu}} = \left(\dfrac{\partial}{c\partial t}, -\nabla\right) = \left(\partial^0, -\partial^1, -\partial^2, -\partial^3\right)$, we can write:

$$E^i = -\partial^i A^0 - \partial^0 A^i, \tag{2.16}$$

$$B_k = \varepsilon_{mnk} \partial^m A^n, \tag{2.17}$$

$$\varepsilon^{ijk} B_k = (\delta^i_m \delta^j_n - \delta^i_n \delta^j_m) \partial^m A^n = \partial^i A^j - \partial^j A^i. \tag{2.18}$$

This suggests the introduction of the *electromagnetic tensor*:

$$F^{\mu\nu} = \partial^{\mu} A^{\nu} - \partial^{\nu} A^{\mu}. \qquad \text{(electromagnetic tensor)} \tag{2.19}$$

It allows us to write the conventional electromagnetic Lagrangian density (where $\rho$ is the charge density and $\mathbf{J}$ the current density),

$$\mathscr{L} = \frac{1}{2}(\varepsilon_0 E^2 - \frac{1}{\mu_0} B^2) - \rho\phi + \mathbf{J} \cdot \mathbf{A}, \tag{2.20}$$

in a covariant way:

$$\mathscr{L} = -\frac{1}{4} F_{\mu\nu} F^{\mu\nu} - \frac{1}{c} J_{\mu} A^{\mu}, \tag{2.21}$$

where $J_{\mu} \equiv (c\rho, -\mathbf{J})$ is the current four-vector. Given this Lagrangian, the Euler-Lagrange equations yield Maxwell's equations [26].

## 2.8 Quantum Field Theory

The combination of quantum theory and relativity leads to the introduction of quantized fields. A quantum field is the quantized version of a classical field, and consists of operators attached to each point of space-time. In the context of perturbation theory, a quantized field is associated with a particle with well-defined properties (e.g. the electron is the quanta of the electron-positron field) [31]. The interaction between these "matter particles" is mediated via other quantized fields (e.g. the photon is the quanta of the electromagnetic field and mediates said interaction between charged particles).

### 2.8.1 Electromagnetic Field Quantization

We can quantize the electromagnetic field by expressing the radiation inside a box as a Fourier series:

$$\mathbf{A}(\mathbf{x},t) = \sum_{k,r} N^{1/2} \varepsilon_r(\mathbf{k}) \left[ a_r(\mathbf{k},t) e^{i(\mathbf{k}\cdot\mathbf{x}+\omega_\mathbf{k} t)} + a_r^*(\mathbf{k},t) e^{-i(\mathbf{k}\cdot\mathbf{x}+\omega_\mathbf{k} t)} \right], \tag{2.22}$$

where $N \equiv \left( \dfrac{\hbar c^2}{2L^3 \omega_\mathbf{k}} \right)$, $\varepsilon_r(\mathbf{k})$ are orthogonal unit vectors, $\mathbf{k} = \dfrac{2\pi}{L}(n_1, n_2, n_3)$, $L$ =dimension of box, $n_1, n_2, n_3 = 0, \pm 1, \pm 2, \cdots$ and $\omega_\mathbf{k} = c|\mathbf{k}|$. We introduce commutation relations similar to the quantum mechanical harmonic oscillator,

$$\begin{aligned} \left[ a_r(\mathbf{k}), a_s^\dagger(\mathbf{k}') \right] &= \delta_{rs} \delta_{\mathbf{k}\mathbf{k}'} \\ \left[ a_r(\mathbf{k}), a_s(\mathbf{k}') \right] = \left[ a_r^\dagger(\mathbf{k}), a_s^\dagger(\mathbf{k}') \right] &= 0, \end{aligned} \tag{2.23}$$

and write the Hamiltonian as

$$H = \sum_{k,r} \hbar \omega_\mathbf{k} \left[ a_r^\dagger(\mathbf{k}) a_r(\mathbf{k}) + \frac{1}{2} \right]. \tag{2.24}$$

The *number operators*, $N_r(\mathbf{k}) \equiv a_r^\dagger(\mathbf{k}) a_r(\mathbf{k})$, have eigenvalues $n_r(\mathbf{k}) = 0, 1, 2, \cdots$ and eigenfunctions

$$|n_r(\mathbf{k})\rangle = \frac{\left[ a_r^\dagger(\mathbf{k}) \right]^{n_r(\mathbf{k})}}{\sqrt{n_r(\mathbf{k})!}} |0\rangle. \tag{2.25}$$

Here $a_r(\mathbf{k})$ and $a_r^\dagger(\mathbf{k})$ are the field operators, which operate on the vacuum, $|0\rangle$, to create or annihilate photons of a given energy ($\omega_\mathbf{k}$), momentum ($\hbar\mathbf{k}$), and linear polarization ($\varepsilon_r(\mathbf{k})$).

### 2.8.2 Number Representation for Bosons

In order to quantize a bosonic field in a similar way as the electromagnetic field, we consider a particle of rest mass $m$. Its energy and momentum are related by

$$E^2 = m^2c^4 + \mathbf{p}^2c^2. \tag{2.26}$$

Implementing the non-relativistic quantum mechanics operator representation for energy and momentum,

$$\begin{aligned} \hat{H} &\to i\hbar\frac{\partial}{\partial t} \\ \hat{p} &\to \frac{\hbar}{i}\nabla, \end{aligned} \tag{2.27}$$

leads to the Klein-Gordon equation:

$$(\Box^2 + \mu^2)\phi(\mathbf{x},t) = 0, \qquad \text{(Klein-Gordon equation)} \tag{2.28}$$

where $\Box \equiv \frac{1}{c^2}\frac{\partial^2}{\partial t^2} - \nabla^2$ and $\mu \equiv mc/\hbar$. We note that this result, as it stands, introduces negative energy solutions and makes a probability density interpretation impossible [32]. Adding the Klein-Gordon equation (2.28) to its complex conjugate leads to

$$\partial_\mu j^\mu \equiv \partial_\mu(\phi\partial^\mu\phi^* - \phi^*\partial^\mu\phi) = 0. \tag{2.29}$$

The time component of this conserved current, $j^0 = \phi^*(\partial\phi/\partial t) - (\partial\phi^*/\partial t)\phi$, is not positive-definite, and therefore cannot be a probability density.

Following our treatment of the electromagnetic field, if we expand the real field $\phi$ in a Fourier series (given $k_\mu \equiv (\omega_\mathbf{k}, \mathbf{k})$),

$$\phi(\mathbf{x},t) = \sum_{k,r} N^{1/2}\left[a_r(\mathbf{k})e^{-ik_\mu x^\mu} + a_r^\dagger(\mathbf{k})e^{ik_\mu x^\mu}\right], \tag{2.30}$$

we obtain the same set of commutation relations (2.23) [31]. Again, the eigenvalues of number operator, $N_r(\mathbf{k}) \equiv a_r^\dagger(\mathbf{k})a_r(\mathbf{k})$, will be the occupation numbers, $n_r(\mathbf{k}) = 0, 1, 2, \cdots$. The interpretation of the field operator changes to the creation and annihilation of bosons of energy ($\hbar\omega_{\mathbf{k}}$) and momentum ($\hbar\mathbf{k}$).

### 2.8.3 Number Representation for Fermions

To treat fermions in the same way, we must introduce the *anti-commutator*:

$$[\hat{A}, \hat{B}]_+ \equiv \hat{A}\hat{B} + \hat{B}\hat{A}. \tag{2.31}$$

By assuming that the field operators obey anti-commutation relations,

$$\begin{aligned} \left[a_r(\mathbf{k}), a_s^\dagger(\mathbf{k}')\right]_+ &= \delta_{rs}\delta_{\mathbf{k}\mathbf{k}'} \\ \left[a_r(\mathbf{k}), a_s(\mathbf{k}')\right]_+ = \left[a_r^\dagger(\mathbf{k}), a_s^\dagger(\mathbf{k}')\right]_+ &= 0, \end{aligned} \tag{2.32}$$

we limit the possible occupation numbers which are eigenvalues of the number operator:

$$\begin{aligned} N_r^2 = (a_r^\dagger a_r)(a_r^\dagger a_r) = a_r^\dagger(1 - a_r^\dagger a_r)a_r = N_r \\ N_r^2 - N_r = 0 \end{aligned} \tag{2.33}$$

i.e. the eigenvalues of $N_r$ are limited to $n_r = 0$ or $n_r = 1$, thereby satisfying Fermi-Dirac statistics.

## 2.9 The Dirac Equation

Relativistic quantum mechanics requires time and space to be treated on an equal footing. An equation linear in the time derivative is required to guarantee conservation of

probability [26]. P.A.M. Dirac developed such an equation in 1928,

$$(i\hbar\gamma^\mu\partial_\mu - mc)\psi = 0. \qquad \text{(Dirac equation)} \tag{2.34}$$

Here the *Dirac matrices*, $\gamma^\mu$, satisfy the anticommutation relations $[\gamma^\mu,\gamma^\nu]_+ = 2g^{\mu\nu}$ and the Hermicity conditions $\gamma^{\mu\dagger} = \gamma^0\gamma^\mu\gamma^0$. They are most frequently represented by

$$\begin{aligned} \gamma^0 &= \begin{bmatrix} \mathbb{I}_2 & 0 \\ 0 & -\mathbb{I}_2 \end{bmatrix}, \ \gamma^1 = \begin{bmatrix} 0 & \sigma_x \\ -\sigma_x & 0 \end{bmatrix}, \\ \gamma^2 &= \begin{bmatrix} 0 & \sigma_y \\ -\sigma_y & 0 \end{bmatrix}, \ \gamma^3 = \begin{bmatrix} 0 & \sigma_z \\ -\sigma_z & 0 \end{bmatrix}, \end{aligned} \tag{2.35}$$

where $\sigma_i$ are the *Pauli matrices*:

$$\sigma_1 = \begin{bmatrix} 0 & 1 \\ 1 & 0 \end{bmatrix}, \ \sigma_2 = \begin{bmatrix} 0 & -i \\ i & 0 \end{bmatrix}, \ \sigma_3 = \begin{bmatrix} 1 & 0 \\ 0 & -1 \end{bmatrix}. \qquad \text{(Pauli matrices)} \tag{2.36}$$

Defining $\bar{\phi} \equiv \phi^\dagger\gamma^0$, we can write the Hermitian conjugate of Dirac's equation (2.34) as

$$i\hbar(\partial_\mu\bar{\psi})\gamma^\mu + mc\bar{\psi}, \tag{2.37}$$

which, added to Dirac's equation (2.34), can be written as $\partial_\mu(\bar{\psi}\gamma^\mu\psi) = 0$. This defines a *conserved electric current*,

$$j^\mu = -e\bar{\psi}\gamma^\mu\psi. \qquad \text{(conserved electric current)} \tag{2.38}$$

If we solve Dirac's equation (2.34) for a free particle at rest we find two plane-wave solutions corresponding to positive energy ($\psi^1,\psi^2$), and two corresponding to negative

energy($\psi^3, \psi^4$):

$$\psi^r = \omega^r e^{-\varepsilon^r \frac{i}{\hbar}(mc^2)t}, \qquad (r = 1,2,3,4) \tag{2.39}$$

where

$$\varepsilon^r = \begin{cases} +1, & r = 1,2 \\ -1, & r = 3,4 \end{cases}, \tag{2.40}$$

$$\omega^1 = \begin{bmatrix} 1 \\ 0 \\ 0 \\ 0 \end{bmatrix}, \ \omega^2 = \begin{bmatrix} 0 \\ 1 \\ 0 \\ 0 \end{bmatrix}, \ \omega^3 = \begin{bmatrix} 0 \\ 0 \\ 1 \\ 0 \end{bmatrix}, \ \omega^4 = \begin{bmatrix} 0 \\ 0 \\ 0 \\ 1 \end{bmatrix}. \tag{2.41}$$

The first two solutions ($\psi^1, \psi^2$) describe the two spin-degrees of freedom of an electron. The negative-energy solutions ($\psi^3, \psi^4$) correspond to the two spin-degrees of freedom of an anti-electron, called *positron*. It shares the same properties as the electron, but its charge is opposite. The positron was observed experimentally in 1932 [33].

### 2.9.1 Klein-Gordon probability current

If we redefine the Klein-Gordon probability current (2.29) by inserting the charge of the particle $e$,

$$j^\mu \equiv -ie(\phi^* \partial^\mu \phi - \phi \partial^\mu \phi^*), \tag{2.42}$$

it can be interpreted as a charge-current density and the fact that it can be negative is no longer objectionable [23]. Feynman and Stückelberg proposed a prescription for handling

negative-energy solutions. The idea is that these negative-energy solutions describe a particle which propagates backwards in time or, equivalently, a positive energy anti-particle propagating forward in time [23].

## 2.10 Gauge Theories

The theories which describe the particles and their interactions are known as gauge theories, i.e. quantum theories where there is an invariance principle which necessarily implies the existence of interactions mediated by gauge bosons [26].

### 2.10.1 Gauge Invariance in Classical Electromagnetic

Suppose we transform the classic electromagnetic fields as follows,

$$\begin{aligned} \mathbf{A} &\rightarrow \mathbf{A}' = \mathbf{A} + \nabla\chi \\ \phi &\rightarrow \phi' = \phi + \frac{\partial}{c\partial t}\chi, \end{aligned} \tag{2.43}$$

$$\text{i.e.} A^{\mu} \rightarrow A'^{\mu} = A^{\mu} + \partial^{\mu}\chi. \qquad \text{(electromagnetic gauge transformation)} \tag{2.44}$$

This is called a *gauge tranformation*. The electromagnetic Lagrangian (2.21) is invariant under this transformation [26]. This invariance emerges from the fact all observable quantities related to electromagnetism can be expressed in terms of **E** and **B**. Gauge invariance is a fundamental requirement of any theory expressed in terms of potentials, i.e. that predictions for observable quantities be unaffected under such gauge transformations [31].

### 2.10.2 Gauge Invariance in Quantum Theory

Since observables only depend on $|\psi|^2$, we can demand that the theory be invariant under the transformation

$$\psi(\mathbf{x},t) \to \psi'(\mathbf{x},t) = e^{-i\alpha}\psi(\mathbf{x},t), \qquad \text{(global gauge transformation)} \tag{2.45}$$

where $\alpha$ is a constant. This is known as a *global gauge transformation*, since $\psi(\mathbf{x},t)$ transforms the same way at all points of space-time. In other words, we are free to choose the phase of the wave function at all points of space-time without having any effect on the observables.

A more strict condition is to demand that the theory be invariant to selecting a different phase at different points of space-time:

$$\psi(\mathbf{x},t) \to \psi'(\mathbf{x},t) = e^{-i\chi(\mathbf{x},t)}\psi(\mathbf{x},t), \qquad \text{(local gauge transformation)} \tag{2.46}$$

where $\chi(\mathbf{x},t)$ is an arbitrary function of space-time. This is known as a *local gauge transformation*. Schödinger's equation (2.5) must be modified to satisfy local gauge invariance:

$$\frac{\hbar^2}{2m}\left(-i\nabla + e\mathbf{A}\right)^2 \psi(\mathbf{x},t) = \left(i\hbar\frac{\partial}{\partial t} + e\phi\right)\psi(\mathbf{x},t). \tag{2.47}$$

Then, the form of equation (2.47) is invariant under the simultaneous transformations (2.44) and (2.46). We interpret this result by concluding that local gauge invariance requires the presence of a field $A^\mu = (\phi, \mathbf{A})$.

Since this field can be Fourier expanded in terms of creation and annihilation field operators, as in (2.22), there will be an associated particle. Since the field is a four-vector, the associated particle will be a spin-one vector particle [26]. We recognize this vector particle as the photon. Thus, local gauge invariance implies the existance of a gauge boson. If a given particle carries any kind of charge and the theory is invariant under certain gauge

transformations, then associated fields (called gauge fields) and their associated quanta, i.e. particles with spin-one (called gauge bosons), must exist. Another way to express this result is that we cannot distinguish between the effects of a local gauge invariance and the effects of a new vector field.

We can express (2.47) in a covariant form to satisfy the postulates of relativity. Defining the *covariant derivative*,

$$\begin{aligned} \mathscr{D} &\equiv -\nabla - ie\mathbf{A} \\ \mathscr{D}^0 &\equiv \frac{\partial}{c\partial t} - ie\phi, \end{aligned} \tag{2.48}$$

$$\text{i.e.} \mathscr{D}^\mu \equiv \partial^\mu - ieA^\mu, \qquad \text{(covariant derivative)} \tag{2.49}$$

(2.47) then becomes

$$\frac{\hbar}{2m}(i\mathscr{D})^2\psi(\mathbf{x},t) = i\mathscr{D}^0\psi(\mathbf{x},t). \tag{2.50}$$

It is simple to show that $\mathscr{D}^\mu\psi$ transforms as a wave function if $\psi$ does, and that any equation written in terms of the covariant derivative (2.49) satisfies gauge invariance.

## 2.11 Non-Abelian Gauge Theories

### 2.11.1 Group Theory

In order to describe the known particles and their interactions, three internal symmetries are needed. These are representations of group spaces. A *group G* is defined as a set of elements ($a_i = a_1, a_2, ...$) and a composition rule, $\cdot$, such that:

(a) $a_i \cdot a_j = a_k$

(b) $\exists\, \mathbb{I}\ \varepsilon\ G$ such that $a_i \cdot \mathbb{I} = \mathbb{I} \cdot a_i = a_i$

(c) $\exists\, a_i^{-\mathbb{I}}\ \varepsilon\ G$ such that $a_i^{-\mathbb{I}} \cdot a_i = a_i \cdot a_i^{-\mathbb{I}} = \mathbb{I}$

(d) $a_i \cdot (a_j \cdot a_k) = (a_i \cdot a_j) \cdot a_k$

In an *Abelian* group, the order of operations commutes, whereas in a *non-Abelian group* they do not commute. The function $f(\theta) \equiv e^{i\theta}$ is an example of a one-dimensional unitary group, called $U(1)$. The rotations in an $n$-dimensional Euclidean space form a group, called $O(n)$. If it is represented by a $n \times n$ unitary, orthogonal matrix with determinant 1, it is called $SU(n)$ [26].

### 2.11.2 Non-Abelian Gauge Theories for Quarks and Leptons

Our previous treatment of gauge invariance in quantum theory was an example of phase invariance under a $U(1)$ space, meaning that the theory is invariant to rotations in $U(1)$ space. Quarks and leptons can be placed in spinors in analogy to spin states $\begin{bmatrix} \uparrow \\ \downarrow \end{bmatrix}$, known as an *SU(2) doublet*. This motivates us to expand the gauge invariant treatment to $SU(2)$ and $SU(3)$ spaces. In SU(2) space, a phase transformation takes the form

$$\begin{bmatrix} a_1' \\ a_2' \end{bmatrix} = e^{\frac{i}{2}\boldsymbol{\epsilon}(\mathbf{x},t)\cdot\boldsymbol{\sigma}} \begin{bmatrix} a_1 \\ a_2 \end{bmatrix}. \tag{2.51}$$

Here $\boldsymbol{\sigma}$ are the Pauli matrices and $\boldsymbol{\epsilon}(\mathbf{x},t)$ are three paramaters analogous to $\chi(\mathbf{x},t)$ in the $U(1)$ space. Similary, in SU(3) space, a phase transformation takes the form

$$\begin{bmatrix} a_1' \\ a_2' \\ a_3' \end{bmatrix} = e^{\frac{i}{2}\alpha_i(\mathbf{x},t)\cdot\lambda_i} \begin{bmatrix} a_1 \\ a_2 \\ a_3 \end{bmatrix}. \tag{2.52}$$

Here $\lambda_i$ $(i = 1,2,\cdots,8)$ are analogous to the Pauli matrices and obey the commutation relation $[\lambda_a, \lambda_b] = 2if_{abc}\lambda_c$, where $f_{abc}$ are anti-symmetric half-integers known as *structure constants* [31]. The $\alpha_i(\mathbf{x},t)$ are eight rotation parameters, similar to $\chi(\mathbf{x},t)$ in $U(1)$ space.

In analogy to the $U(1)$ transformations, we then demand invariance under these kinds of local transformations (2.51), (2.52). This kind of theory with local non-Abelian phase invariance is called a *Yang-Mills gauge theory* [26]. We define the covariant derivative for $SU(2)$ as

$$\mathscr{D}^{\mu} = \partial^{\mu} - \frac{ig_2}{2}\boldsymbol{\sigma} \cdot W^{\mu}, \tag{2.53}$$

where the coupling $g_2$ is an arbitrary constant which will determine interaction strengths. Note that $W^{\mu}$ is analogous to $A^{\mu}$ and should correspond to spin-one particles, like the photon. However, $W^{\mu}$ must be a $2 \times 2$ matrix, since it is multiplied by the Pauli matrices [26].

We can generalize and write a full covariant derivative as such

$$\mathscr{D}^{\mu} = \partial^{\mu} - \frac{ig_1}{2}Y \cdot B^{\mu} - \frac{ig_2}{2}\sigma_i \cdot W_i^{\mu} - \frac{ig_3}{2}\lambda_a \cdot G_a^{\mu}. \tag{2.54}$$

Here $i = 1,2,3$ and $a = 1,2,\cdots,8$. $B^{\mu}$ is the spin-one field needed to maintain gauge invariance. $Y$ is the generator of $U(1)$ transformations; a constant, but perhaps different for different fermions. Analogous remarks describe the last two terms: $W_i^{\mu}$ corresponds to the three spin-one fields needed to maintain gauge invariance and $\sigma_i$ are the Dirac matrices, generators of $SU(2)$ transformations. $G_a^{\mu}$ corresponds to eight such spin-one fields, one for each generator of the transformations, and $\lambda_a$ correspond to a the Gell-Mann matrices, generators of $SU(3)$ transformations. The first two terms are singlets in $SU(2)$ and $SU(3)$ spaces. The third term is a $2 \times 2$ matrix in $SU(2)$ and a singlet in all other spaces. Similarly, the last term is a $3 \times 3$ matrix in $SU(3)$ and a singlet in all other spaces.

## 2.12 Standard Model Lagrangian

We can obtain our full Standard Model Lagrangian by replacing the ordinary derivative by the full covariant derivative (2.54) in the free particle Lagrangian. We place particles

with spin-zero in singlets, spin-1/2 particles are put in doublets, $\begin{bmatrix} \uparrow \\ \downarrow \end{bmatrix}$, and spin-one particles form triplets, $J_z = \begin{bmatrix} +1 \\ 0 \\ -1 \end{bmatrix}$.

Every fermion is separated into left-handed and right-handed spin states since they each transform differently under electro-weak processes. Right-handed neutrinos are not observed, thus right-handed electrons are electro-weak singlets ($e_R^- = SU(2)$ singlet), but left-handed electrons form a doublet with the electron neutrino $\left( \begin{bmatrix} \nu_e \\ e^- \end{bmatrix}_L = SU(2) \text{ doublet} \right)$. The $W$ bosons generate rotations in electro-weak $SU(2)$ space which turn $\nu_{e_L} \leftrightarrow e_L^-$, just as rotations in spin space turn spin-up into spin-down. Since $e_R^-$ is a $SU(2)$ singlet it is not connected to any other state by electro-weak transitions, just as a state of spin zero has only one spin state.

All leptons are color singlets and all quarks are color triplets. Gluons can generate transitions from one quark color to another because they carry the color-charge. In contrast to the electric-charge, quarks and gluons can change both their momentum and color charge by emitting or absorbing a gluon. Since gluons can connect any of the color charges $r$, $g$, or $b$ to any other, there appears to be nine gluons required. But, since the combination $r\bar{r} + g\bar{g} + b\bar{b}$ is invariant under rotations in the color space (i.e. it is "colorless"), there are eight independent color-charge states for gluons; normally it is said that there are eight gluons [26]. In analogy to leptons, we place right-handed quarks in electro-weak singlets ($u_{R\alpha}, d_{R\alpha} = SU(2)$ singlet) and left-handed quarks in electro-weak doublets $\left( \begin{bmatrix} u_\alpha \\ d_\alpha \end{bmatrix}_L = SU(2) \text{ doublet} \right)$, where $\alpha = r, g, b$.

### 2.12.1 Quark and Lepton Lagrangian

Here we consider only the first generation of quarks and leptons, the theory simply replicates itself for the other two families. For fermions, we replace $\partial_\mu$ in the kinetic-energy term of the Dirac Lagrangian with the covariant derivative $\mathscr{D}_\mu$ (2.54),

$$\bar{\psi}\gamma^\mu\partial_\mu\psi \to \bar{\psi}\gamma^\mu\mathscr{D}_\mu\psi \tag{2.55}$$

for each fermion. If we define

$$f \equiv \left( \begin{bmatrix} \nu_e \\ e^- \end{bmatrix}_L, e_R^-, \begin{bmatrix} u_\alpha \\ d_\alpha \end{bmatrix}_L, u_R, d_R \right) \tag{2.56}$$

and adopt a convention where a term in $\mathscr{D}_\mu$ acting on a state of different matrix form is zero, by definition, we can write out the full Lagrangian for fermions as

$$\mathscr{L}_{fermions} = i\sum_f \bar{f}\gamma^\mu\mathscr{D}_\mu f. \tag{2.57}$$

## 2.13 Electro-Weak Theory

We write down the $U(1)$ Lagrangian terms for the first family of leptons using (2.54) and (2.57),

$$\mathscr{L}_{U(1),\text{leptons}} = \frac{g_1}{2}[Y_L(\bar{\nu}_L\gamma^\mu\nu_L + \bar{e}_L\gamma^\mu e_L) + Y_R\bar{e}_R\gamma^\mu e_R]B_\mu. \tag{2.58}$$

By defining

$$\begin{aligned} W^+ &\equiv \frac{1}{\sqrt{2}}(-W^1 + iW^2), \\ W^- &\equiv \frac{1}{\sqrt{2}}(-W^1 - iW^2), \\ W^0 &\equiv W^3 \end{aligned} \tag{2.59}$$

we can write the same equation for $SU(2)$ using (2.54), (2.57), and (2.59)

$$\begin{aligned}\mathscr{L}_{SU(2),\text{leptons}} = \frac{g_2}{2}[&\bar{\nu}_L\gamma^\mu\nu_L W_\mu^0 - \sqrt{2}\bar{\nu}_L\gamma^\mu e_L W_\mu^+ \\ &- \sqrt{2}\bar{e}_L\gamma^\mu\nu_L W_\mu^- - \bar{e}_L\gamma^\mu e_L W_\mu^0].\end{aligned} \tag{2.60}$$

### 2.13.1 Neutral Currents

We realize that the neutrino terms in (2.58) and (2.60), $\left(\frac{g_1}{2}Y_L B_\mu + \frac{g_2}{2}W_\mu^0\right)\bar{\nu}_L\gamma^\mu\nu_L$, should not interact electromagnetically. We define this coefficient as $Z_\mu$ and assume that the electromagnetic field $A_\mu$ is a combination of $B_\mu$ and $W_\mu^0$, orthogonal to said neutrino terms:

$$Z_\mu \equiv \frac{g_1 Y_L B_\mu + g_2 W_\mu^0}{\sqrt{g_2^2 + g_1^2 Y_L^2}} \tag{2.61}$$

$$A_\mu \equiv \frac{g_2 B_\mu + g_1 Y_L W_\mu^0}{\sqrt{g_2^2 + g_1^2 Y_L^2}} \tag{2.62}$$

By solving these equations for $B_\mu$ and $W_\mu^0$ and substituting into the electron terms in (2.58) and (2.60), $\bar{e}_L\gamma^\mu e_L\left(-\frac{g_1}{2}Y_L B_\mu + \frac{g_2}{2}W_\mu^0\right) + \bar{e}_R\gamma^\mu e_R\left(-\frac{g_1}{2}Y_R B_\mu\right)$, we can identify electromagnetic charge terms, which simplify to

$$e = \frac{g_1 g_2}{\sqrt{g_1^2 + g_2^2}}. \tag{2.63}$$

where $Y_L = -1$ is set for convenience. We can then introduce the electroweak mixing angle, $\theta_w$:

$$sin\theta_w \equiv \frac{g_1}{\sqrt{g_1^2 + g_2^2}} = e/g_2 \tag{2.64}$$

$$cos\theta_w \equiv \frac{g_2}{\sqrt{g_1^2 + g_2^2}} = e/g_1. \tag{2.65}$$

With these definitions, the neutrino terms from (2.58) and (2.60) become

$$\left(\frac{g_1}{2}Y_L B_\mu + \frac{g_2}{2}W_\mu^0\right)\bar{\nu}_L\gamma^\mu\nu_L = -\frac{g_2}{2cos\theta_w}Z_\mu\bar{\nu}_L\gamma^\mu\nu_L. \tag{2.66}$$

We interpret the coefficient $\frac{g_2}{2cos\theta_w}$ for this $\nu_L - Z$ vertex as the strength factor of the interaction. Similarly, the electron terms in (2.58) and (2.60) become

$$\bar{e}_L\gamma^\mu e_L\left(-\frac{g_1}{2}Y_L B_\mu + \frac{g_2}{2}W_\mu^0\right) = \frac{e}{cos\theta_w sin\theta_w}\left(\frac{-1}{2} + sin^2\theta_w\right)\bar{e}_L\gamma^\mu e_L, \tag{2.67}$$

$$\bar{e}_R\gamma^\mu e_R\left(-\frac{g_1}{2}Y_R B_\mu\right) = \frac{e}{cos\theta_w sin\theta_w}\left(-sin^2\theta_w\right)\bar{e}_R\gamma^\mu e_R. \tag{2.68}$$

This motivates the definition

$$\frac{e}{cos\theta_w sin\theta_w}\left(T_3^f - Q_f sin^2\theta_w\right). \tag{2.69}$$

We identify $T_3^f$ with weak isospin and $Q_f$ with the electric charge. If $f$ is a singlet (e.g. $e_R, u_R, d_R$) then $T_3^f = 0$ and if it is a member of a doublet it takes values $T_3^f = \pm 1/2$. The electroweak theory can thus be interpreted as containing the ordinary electomagnetic interaction, plus an additional photon-like particle called the Z-boson. This new boson interacts with any fermion having electric charge, due to the $Q_f$ term in (2.69), or weak isospin different than zero, due to the $T_3^f$ term in (2.69) [26].

### 2.13.2 Charged Current

There are also off-diagonal terms in (2.60) which lead to transitions $\nu_L \leftrightarrow e_L$ via $W^+$ or $W^-$ $\left(\text{i.e.}\frac{g_2}{\sqrt{2}}\bar{\nu}_L\gamma^\mu e_L W_\mu^+ + \bar{e}_L\gamma^\mu\nu_L W_\mu^-\right)$. Note that $e_R$ does not participate in these transitions, resulting in parity violation of the weak interactions. Neutron beta-decay, $d \to uW^- \to u(e^-\bar{\nu}_e)$, is the best known charged current interaction.

### 2.13.3 Quark Terms

The $SU(2)$ terms for quarks look the same as for leptons, hence they couple to the same gauge bosons ($\gamma, W^{\pm}, Z^0$). As previously remarked, a charged current process can change the flavor of a left-handed quark $u_L \xleftrightarrow{W^{\pm}} d_L$. The $SU(3)$ contribution to the Lagrangian is due only to the color charge,

$$\frac{g_3}{2}\bar{q_\alpha}\gamma^\mu\lambda^a_{\alpha\beta}G^a_\mu q_\beta \quad (\alpha,\beta = r,g,b), \tag{2.70}$$

where $G^a_\mu$ are the eight electrically neutral gluons, which can change the color of a quark.

This allows us to write down our Lagrangian for all Standard Model particles in the first family:

$$\begin{aligned}\mathscr{L} = &\sum_f eQ_f(\bar{f}\gamma^\mu f)A_\mu \\ &+ \frac{g_2}{cos\theta_w}\sum_f[\bar{f}_L\gamma^\mu f_L(T_3^f - Q_f sin^2\theta_w) + \bar{f}_R\gamma^\mu f_R(Q_f sin^2\theta_w)]Z_\mu \\ &+ \frac{g_2}{2}[(\bar{u}_L\gamma^\mu d_L + \bar{\nu}_{eL}\gamma^\mu e_L)W^+_\mu + (\bar{d}_L\gamma^\mu u_L + \bar{e}_L\gamma^\mu \nu_{eL})W^-_\mu] \\ &+ \frac{g_3}{2}\bar{q_\alpha}\gamma^\mu\lambda^a_{\alpha\beta}G^a_\mu q_\beta \quad (\alpha,\beta = r,g,b).\end{aligned} \tag{2.71}$$

## 2.14 Higgs Mechanism

The Brout-Englert-Higgs mechanism provides the means by which gauge vector bosons can acquire nonzero masses in the process of spontaneous symmetry breaking. The mechanism was developed in the context of the empirical observation of the very short range of the weak force. This implied that the weak interaction must be mediated by massive vector bosons, unlike the massless photon. However, adding mass terms explicitly to the Lagrangian ruins gauge invariance [26].

Spontaneous symmetry breaking occurs when the ground state of a system does not

display the full symmetry of the underlying theory. We introduce the Higgs potential,

$$V_H = \left(\frac{1}{2}\mu^2\phi^2 + \frac{1}{4}\lambda\phi^4\right), \tag{2.72}$$

interpreted as a field with its associated quanta, the Higgs boson, which all massive particles interact with. Note that it is symmetric under $\phi \to -\phi$. We are interested in the case $\mu^2 < 0$, in which case the minimum of the potential becomes $\phi_{min} = \pm\sqrt{\frac{-\mu^2}{\lambda}} \equiv \pm\upsilon$. We expand about a region near the minimum $\phi(x) \to \upsilon + \eta(x)$,

$$V_H \to (\lambda\upsilon^2\eta^2 + \lambda\upsilon\eta^3 + 1/4\lambda\eta^4) + \text{constants}. \tag{2.73}$$

The $\eta^2$ term can then be interpreted as a mass term, $m_\eta^2 = 2\lambda\upsilon^2 = -2\mu^2$. Note that the $\phi \to -\phi$ symmetry is broken when we choose a specific value of the vaccum ($\phi = \upsilon$ instead of $\phi = -\upsilon$).

A massless particle (like the photon) travels at the speed of light. There is no "rest frame" in which a massless particle is at rest. On the other hand, a massive particle travels at less than the speed of light. It is always possible to change to a different reference frame such that the helicity or handedness of the massive particle is reversed (by moving faster than a massive particle). However, the chirality of a particle is fixed all reference frames. Since the Standard Model is a chiral theory, left-chiral particles are treated differently from right-chiral ones. Thus, a propagating electron will interact with the Higgs field and exhibit quantum mixing. The $e_L^-$ is "swapped" by a $\bar{e}_R^-$ once it interacts with the Higgs vacuum expectation value in such a way that the charge and chirality remain constant. In other words, the "physical" electron in the mass basis is a mixture of the $e_L^-$ (which interacts with the $W$ boson, since it carries a weak charge) and the $\bar{e}_R^-$ (which doesn't interact with the $W$ boson, since it carries no weak charge). The Higgs carries weak charge. Thus, when it obtains a vacuum expectation value, it "breaks" the conservation of weak charge and allows the electron to mix with the anti-positron, even though they have different weak

charges.

## 2.15 Beyond the Standard Model

Generally speaking, "Beyond the Standard Model" (BSM) refers to any possible extension of the Standard Model, typically expressed as in terms of coupling constants for new interactions, new charges or other quantum numbers, and parameters describing possible new degrees of freedom or new symmetries.

Despite being the most successful theory of particle physics to date, the Standard Model is deficient on a number of issues. These include its failure to incorporate gravitational interactions, the inability to describe dark matter and dark energy, inconsistencies when incorporating the empirical observation of neutrino masses [34], the asymmetry in matter-antimatter abundance in the universe [35], etc.

### 2.15.1 Dark Matter

Dark matter is a placeholder term used to describe matter that can be inferred to exist from its gravitational effects, but does not interact electromagnetically in a measurable way. Based on observations of the temperature and polarization anisotropies of the cosmic background radiation (CMB), dark matter is estimated to account for nearly 85% of the total amount of matter in the universe [2]. There is a wealth of indirect evidence of additional gravitational interaction and influence that cannot be accounted for by the observable baryonic content of the universe. The total amount of baryonic matter in the universe can be inferred from Big Bang nucleosynthesis and observations of the CMB, and it is estimated to be much smaller than the total amount of dark matter [36].

Some of the earliest evidence of an excess of gravitational influence proceeded from motion of galaxies and galaxy clusters. The amount of visible mass in galaxy clusters can be inferred from the luminous matter. It can then be compared to the gravitational mass estimated from doppler shift observations — the Virial theorem can be utilized to relate

the kinetic energy of the system, based on doppler shifts, to the potential energy of the system, which yields its gravitational mass. The motion of individual galaxies suggests the presence and influence of additional matter by means of their galaxy rotation curves. From standard Newtonian dynamics, we expect the velocity of stars to fall as you move from the near the center of mass of a galaxy to its outer edges. However, numerous Doppler-shift-based observations of the rotation curves of head-on spiral galaxies indicate that the velocity of stars remained approximately constant, regardless of how far they were from the galactic center [37].

Gravitational lensing also provides a measure of the amount of matter in a massive object, such as a cluster of galaxies, located in front of a more distant light source. Again, the amount of mass deduced from the gravitational interaction is greater than the amount estimated from luminous matter. The most direct observational evidence for dark matter comes from the Bullet Cluster, shown in Figure 2.3. The Bullet Cluster reveals the aftermath of a collision between two galaxy clusters, as evidenced by the electromagnetic emissions which have caused the gas to slow down and concentrate near the point of impact. On the other hand, the dark matter accompanying each cluster passed through each other since it experienced no electromagnetic interactions. This was determined by estimating the mass distribution of the dark matter via gravitaional lensing observations [38].

**Dark Matter Detection**

Dark matter detection is one of the most active research areas in contemporary physics. The goal of such research is to clarify the composition of DM. Since DM does not appear to be baryonic in nature, many BSM candidate particles have been proposed. Among them, weakly interacting massive particles (WIMPs) have gained traction, in part, due to their connection to cosmological thermal relic density: WIMPs are postulated to exist in thermal equilibrium and in abundance in the early Universe, when the temperature of the Universe exceeds the mass $m_\chi$ of the particle. The equilibrium abundance is maintained by

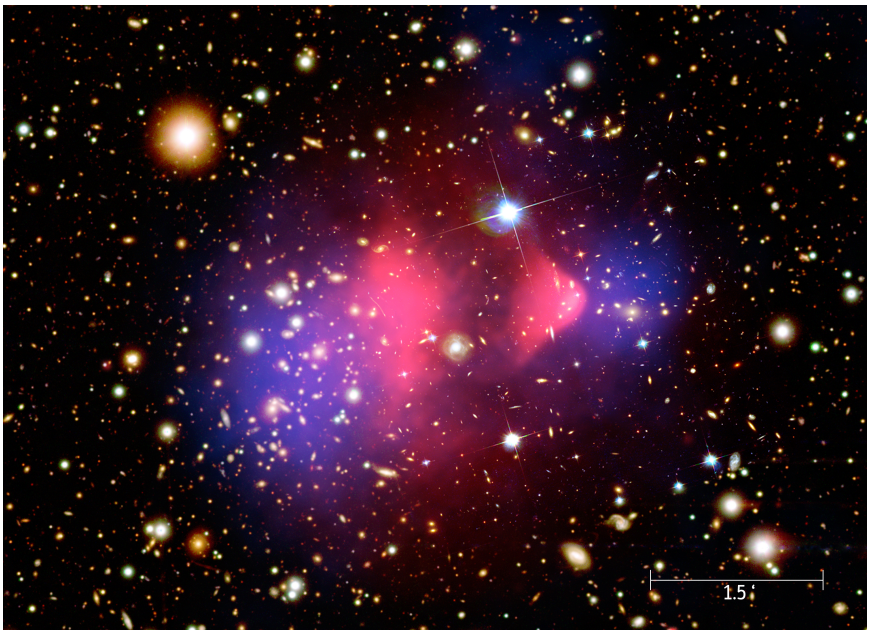


Figure 2.3: The Bullet Cluster as photographed by the Hubble Space Telescope. The mass distribution deduced from gravitational lensing is highlighted by the blue onverlay, while the red overlay highlights X-ray emission as observed by the Chandra telescope

annihilation of the particle with its antiparticle $\bar{\chi}$ into lighter particles, ($\chi\bar{\chi} \rightarrow \ell\bar{\ell}$) and vice versa ($\ell\bar{\ell} \rightarrow \chi\bar{\chi}$). As the Universe cools to a temperature less than the mass of the particle, the equilibrium abundance drops exponentially until the rate for the annihilation reaction ($\chi\bar{\chi} \rightarrow \ell\bar{\ell}$) falls below the expansion rate $H$, at which point the interactions which maintain thermal equilibrium "freeze out", and a relic cosmological abundance freezes in [39]. Obtaining the correct abundance of dark matter today via thermal production requires a self-annihilation cross section of $\langle\sigma\upsilon\rangle \simeq 10^{-26}\text{cm}^3\text{s}^{-1}$, which is roughly what is expected for a new particle in the 100 GeV mass range that interacts via the electroweak force [39].

Indirect detection experiments generally search for the products of DM co-annihilaiton. Asumming the DM is made up of Majorana particles (their own antiparticle), then they could annihilate after a collision to produce $\gamma$-rays or SM particle-antiparticle pairs. This excess radiation could potentially be observed over background *gamma*-ray sources.

Direct detection experiments rely on the assumption that dark matter particles might

particpate in the weak interaction, and thus mainly focus on WIMP searches. Typically, cryogenic- or noble-liquid-based detectors are operated underground, to reduce interference from cosmic rays, and detect heat or scintillation produced by the collision of an incoming particle. These experiments distinguish background particles, which scatter off electrons, from dark matter particles, which scatter of nuclei. Searches for WIMP dark matter at the LHC are also classified as direct detection experiments, but instead of relying on an external source of DM particles, the LHC collisions concentrate enough energy to potentially produce and identify WIMPs.

A generic WIMP is among the best motivated DM candidates since it can be thermally produced in the early Universe in the right amount to account for the observed DM density [39].

### 2.15.2 The Hierarchy Problem

In addition to the open observational issues above, the Higgs mechanism, responsible for spontaneous symmetry breaking of the electroweak interaction, introduces fine-tuning that some consider "unnatural". To illustrate, consider the electron self-energy. From electrostatics, we expect the energy of a uniformly-charged spherical shell with charge $q$ and radius $R$ to be

$$E = \frac{1}{2}\frac{1}{4\pi\varepsilon_0}\frac{q^2}{R}, \tag{2.74}$$

where $\varepsilon_0$ is the vacuum permittivity [40]. If we then apply this description to an electron of size $r_e$ (to avoid a divergent expression), we obtain an expression for the electron's "self-energy". This self-energy must then be part of the observed electron's rest energy. Therefore, the "bare" mass of the electron receives an additional contribution due to this Coulomb self-energy:

$$(m_e c^2)_{\text{observed}} = (m_e c^2)_{\text{bare}} + \frac{1}{2}\frac{1}{4\pi\varepsilon_0}\frac{q^2}{R}. \tag{2.75}$$

The "size" of the electron has been experimentally constrained to $r_e \lesssim 10^{-19} m$ [41]. Thus, we can estimate the value of the bare mass of the electron:

$$0.511\,\text{MeV} = (m_e c^2)_{\text{bare}} + 7200\,\text{Mev}. \tag{2.76}$$

Under this model — even after setting aside the problem with an electron with negative mass — we can conclude that the bare mass of the electron has to be fine-tuned to several orders of magnitude in order to cancel the contribution from the Coulomb self-energy.

However, with the introduction of the positron into the picture, we can consider vacuum fluctuations where electron-positron pairs are created spontaneously and linger, as allowed by the uncertainty principle, before annihilating. This new phenomenon modifies the physics occurring at scales smaller than $d \sim c\Delta t \sim \hbar c/\Delta E \sim \hbar c/(2m_e c^2) \sim 2 \cdot 10^{-13}$ m. After taking the vacuum fluctuation process into consideration, expression for the electron rest energy in the $r_e \to 0$ limit becomes [42]

$$(m_e c^2)_{\text{observed}} = (m_e c^2)_{\text{bare}}[1 + \frac{3\alpha}{4\pi} log \frac{\hbar}{m_e c r_e}], \tag{2.77}$$

which is proportional to the bare mass of the electron and contains a logarithmic leading correction term, thereby greatly reducing the amount of fine-tuning required. We can conclude that fine-tuning in a physical model's prediction might suggest that the range of applicability of said model is near its limit and a new model is required to describe the phenomena beyond this scale.

In the case of electroweak symmetry breaking, quantum corrections to the Higgs mass suffer from the same kind of fine-tuning. The Higgs mass is around 125 GeV (not too far from W and Z masses), but quantum vacuum energy tends to make its mass much larger through interactions with virtual particles. This is largely driven by the immense difference between the Higgs mass and the Plank mass, $m_p = \sqrt{\hbar c/G}$. This line of reasoning is often used to argue the case for BSM physics, such as supersymmetry and extra dimensions.

### 2.15.3 Supersymmetry

The main idea behind supersymmetry (SUSY) is that there is an additional physical symmetry between fermions and bosons. The formalism offers an extension of the familiar symmetries of quantum fields theory by defining an operator which can change only the spin of a given particle by an amount of $1/2$. This implies that every Standard Model particle has a superpartner which is identical but obeys the opposite spin statistics, as pictured in Figure 2.4. Evidently, supersymmetry is a spontaneously broken symmetry since none of the, presumably very massive, superpartners have been observed.

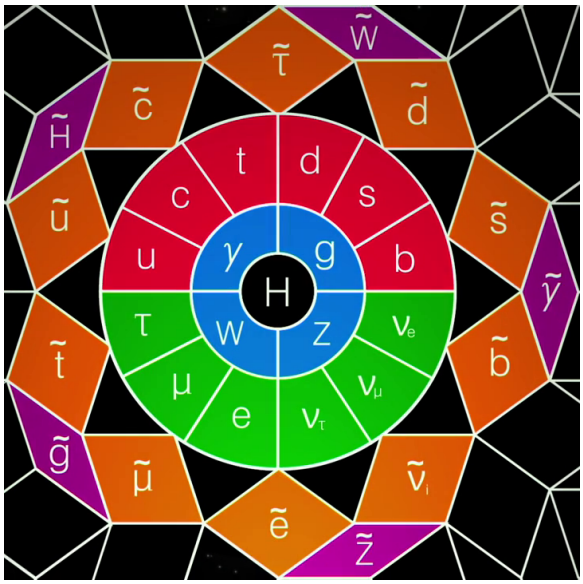


Figure 2.4: Depiction of the Standard Model Particles, located around the inner circle, and their supersymmetric partners positioned around the outer circle

The naming convention for superpartners of fermions is to add the prefix *s-* to the fermion name to identify its bosonic superpartner (e.g. squark, slepton, selectron, sbottom, etc.). Conversely, fermionic superpartners of bosons are labeled by adding the suffix *-ino* to the boson name (e.g. photino, Zino, Wino, Higgsino, Gluino).

According to most versions of supersymmetry, including the simplest realization of spontaneously-broken supersymmetry called the Minimal Supersymmetric Model (MSSM), superparticles or sparticles can only be created or destroyed in pairs. This is a consequence

of $R$-parity conservation: $P_R = (-1)^{3(B-L+2s)}$, where $s$ is spin, $B$ is baryon number, and $L$ is lepton number. Hence, in $R$-parity conserving models, the decay of a sparticle must yield at least one sparticle in the final state. The lightest such particle, known as the lightest neutralino $\tilde{\chi}_1^0$ (mixture of the Photino, Higgsino and Zino), must be stable [4]. This lightest supersymmetric particle (LSP) is a cold dark matter WIMP candidate since it is stable and only interacts weakly and gravitationally. The Higgs mechanism is more complicated in MSSM and requires three neutral and two charged Higgs bosons with their corresponding Higgsinos.

If supersymmetry exists close to the TeV energy scale, it allows for a solution of the hierarchy problem. Fine-tuning is avoided in supersymmetric models by automatic cancellations between the contributions of particles and their superpartners, provided that their masses are not too different [4]. This would make the observation of superpartners accessible with current particle accelerators. When supersymmetry is promoted to a local gauge symmetry, then the theory automatically incorporates general relativity [43]. Theories with local supersymmetry are called super-gravity (SUGRA) theories.

Contrary to popular shorthand jargon, supersymmetry (SUSY) is not a BSM model: it is a symmetry principle characterizing a BSM framework with an infinite number of models. The SUSY framework plays an important role in BSM physics partly because it includes examples of models that are 'complete' in the same sense as the Standard Model, i.e. in principle, the model predicts consequences for any observable, from cosmology, to $b$ physics, to precision, electroweak data, to LHC collisions.

# Chapter 3

# Experimental High-Energy Physics

The goal of experimental High-Energy Physics is to investigate fundamental physical processes at ever smaller distances. This drive to build the most powerful "microscopes" possible has steadily pushed the energy frontier in collider physics. The kinetic energy of incoming particles is concentrated in a collision and converted into new forms of matter, whose interaction with "conventional" matter can reveal new physical phenomena. The surviving remnants of these collisions are then detected, identified, and/or tracked by exploiting the fact that they will ionize the detector material as they traverse it.

## 3.1 The Large Hadron Collider

The Large Hadron Collider (LHC) [44] is currently the largest and most powerful particle accelerator complex in the world, designed to collide proton beams at a center-of-mass energy of $\sqrt{s} = 14$ TeV and a nominal instantaneous luminosity of $\mathscr{L} = 10^{34}$ cm$^{-2}$s$^{-1}$. The LHC tunnel is 26.659 km in circumference and lies 50–175 m beneath the French-Swiss border near Geneva, Switzerland. Four detectors are installed in the experimental caverns around the collision points: two general purpose experiments, ATLAS [45, 46] and CMS [47, 48], the LHCb [49] experiment dedicated to $B$ Physics, and the ALICE [50] experiment which investigates the physics of heavy ion collisions.

A schematic view of the LHC accelerator with the injection chain is shown in Figure 3.1. Each machine in the chain injects the beam into the next one, successively increasing the beam energy. Initially, hydrogen atoms are taken from an ordinary hydrogen bottle and stripped of their electrons by a duoplasmatron, thus providing protons (i.e. $H^+$ ion plasma) for the beam [51]. Protons are injected at an energy of 50 MeV from Linac2 into the PS Booster (PSB). The Booster delivers a 1.4 GeV beam to the Proton Synchrotron

(PS) which, in turn, accelerates it to 25 GeV. The protons are sent to the Super Proton Synchrotron (SPS) and exit with an energy of 450 GeV [52].

Finally, the beam is transferred to the LHC, where it is accelerated for 20 minutes to its nominal energy. Under nominal operation, a total of 2808 bunches of protons in each LHC beam pipe are circulated in opposite directions, with $\sim 10^{11}$ particles per bunch. Thus, the LHC beam may collectively store up to 700 MJ of energy at 14 TeV, comparable to the energy in a typical lightning bolt. The beam line is maintained at a vacuum pressure of $10^{-13}$ atm. Superconducting dipole magnets provide a magnetic field of 8 T when a 12 kA current flows across their niobium-titanium (NbTi) wires. In total, 1232 dipole magnets are required to keep the protons in orbit around the LHC tunnel, and each is cooled using liquid helium at a temperature of 1.9 K. In addition, 392 quadrupole magnets are used to focus the beam and minimize its transverse width at the collision points. A total of eight superconducting radio-frequency (SRF) cavities per beam deliver an accelerating field of 5 MV/m and operate at 400 MHz and 4.5 K, and help keep protons tightly bunched [44].

At the interaction point, the proton beams are squeezed to an RMS radius of $\sim 16\,\mu$m [53] and collisions happen every 25 ns. The total inelastic proton-proton cross section at $\sqrt{s} = 14$ TeV is expected to be on the order of $\sigma_{\text{p-p}}^{inelastic} \sim 100$ mb. Therefore, approximately $N = \mathscr{L} \cdot \sigma_{\text{p-p}}^{inelastic} \sim 10^9$ inelastic events per second will be observed in the multi-purpose experiments at design luminosity [54]. This enormous event rate leads to many simultaneous collisions in each bunch crossing, referred to as "pile-up", which imposes a challenge on the online event selection process, called the "trigger", and the detector read-out systems.

During its first run, from March 30th 2010 to February 13th 2013, the LHC was operated at a collision rate of 20 MHz and collided two opposing particle beams at a center-of-mass energy of $\sqrt{s} = 3.5$ TeV per beam and incrementing to $\sqrt{s} = 4$ TeV per beam from 2012, almost 4 times more than any previous collider. The first operational run also included a period of lead ion collisions at a center-of-mass energy of $\sqrt{s} = 2.76$ TeV per

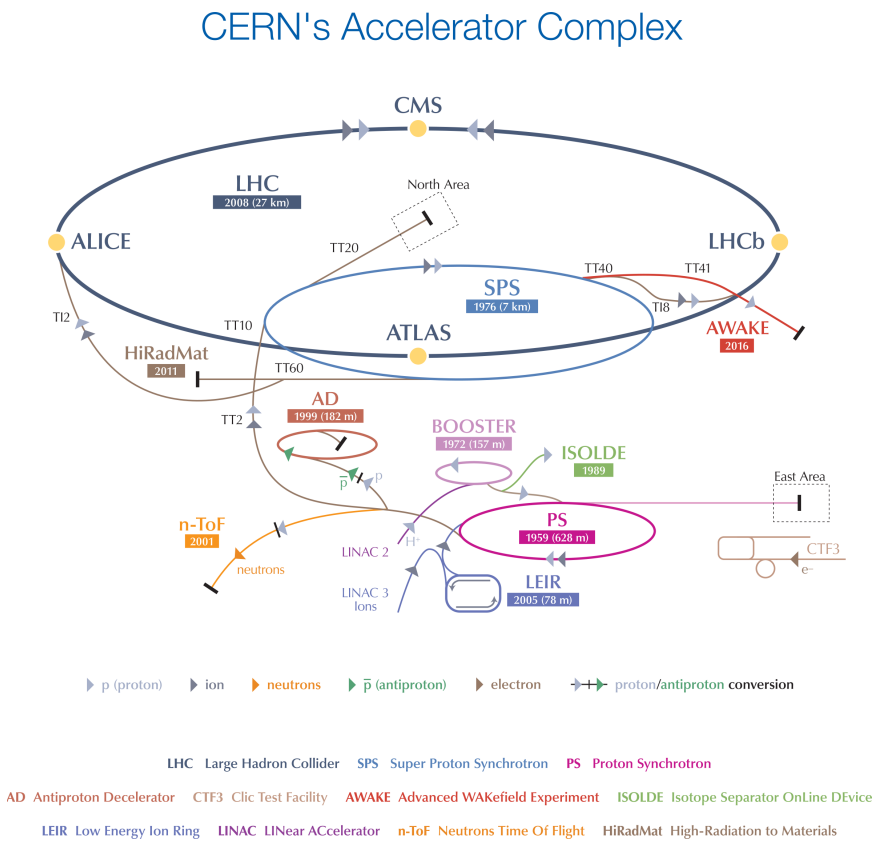


Figure 3.1: Overview of the LHC acceletator complex

nucleon. From June 3rd 2015, the collision rate was increased to 40 MHz and the center-of-mass energy raised to $\sqrt{s} = 6.5$ TeV per beam.

## 3.2 The Compact Muon Solenoid Experiment

The Compact Muon Solenoid (CMS) detector is a general purpose detector installed at the LHC interaction point 5 (P5) near the village of Cessy in France. It consists of multiple layers of materials which exploit the properties of fundamental particles in order to determine their energy and momentum. The CMS detector is divided into a silicon tracking system, an electromagnetic and a hadron calorimeter, and a muon system. A magnetic field of 3.8 T is provided by a superconducting solenoid magnet. The CMS detector is 22 m long, has a diameter of 15 m, and an overall weight of $14 \cdot 10^6$ kg. This makes it almost

twice as heavy as the Eiffel Tower in Paris, yet 400 times less voluminous. It was designed in a modular fashion, with fifteen separate sections or "slices", which permitted partial assembly on the ground before lowering each section into the cavern, and made the sub-detectors more easily accessible for easier and faster maintenance. Figure 3.2 presents an exploded view of the CMS detector.

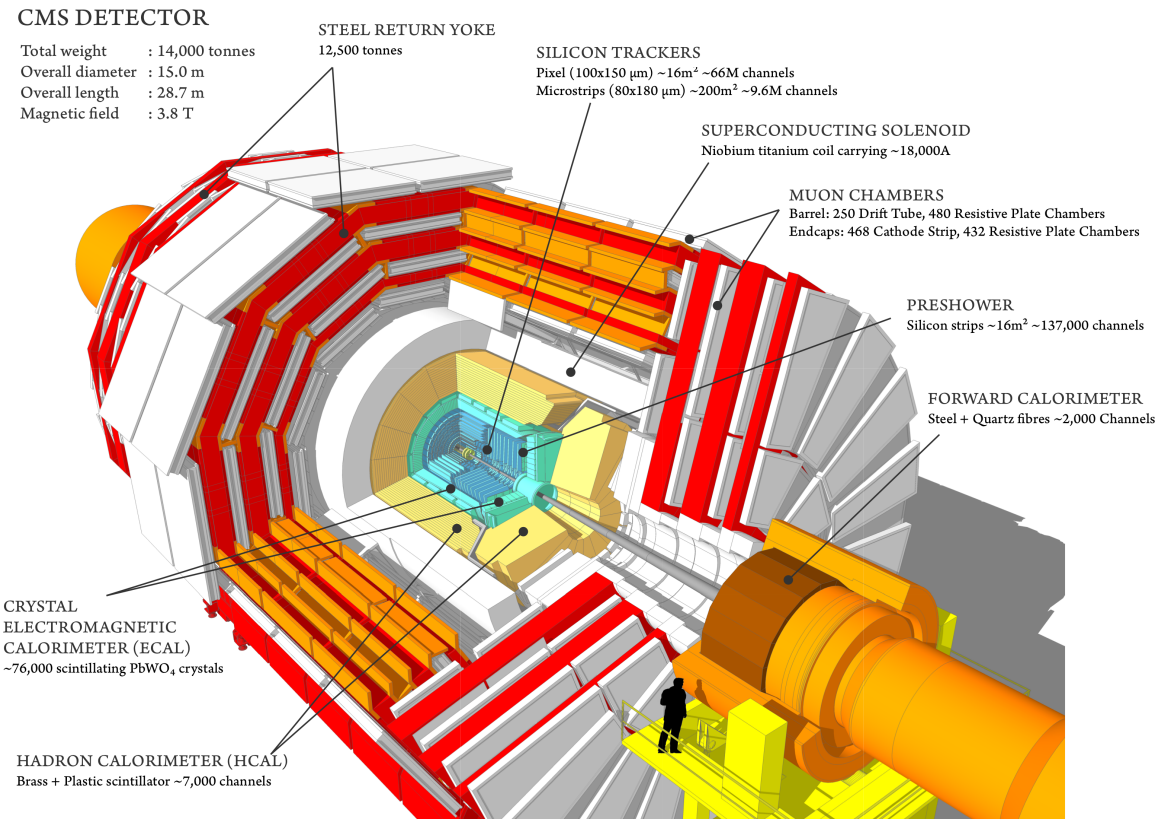


Figure 3.2: Overview of the Compact Muon Solenoid detector

A particle emerging from a collision will first encounter the tracking system, composed of silicon pixels and silicon strip detectors. These accurately measure the position of charged particles as they transverse the tracking system, allowing the reconstruction of their trajectories or "tracks". The trajectories of these charged particles become curved under the strong magnetic field, which enables the calculation of their momenta. The first calorimeter layer, called the electromagnetic calorimeter (ECAL), is designed to measure the energies of electrons and photons with great precision. Particles which participate in strong interac-

tions, called hadrons, deposit most of their energy in the next layer, the hadron calorimeter (HCAL). The CMS detector is designed to quasi-hermetically capture most of the particles produced following a collision within the solenoid volume, with the exception of the muon and the neutrino. Muons are heavier and unstable versions of the electron, thus they don't accelerate as abruptly under electromagnetic fields causing them to easily penetrate matter. Finally, layers of dedicated muon chambers are employed to determine, in combination with the tracking sub-detector, the trajectory of escaping muons. Neutrinos will entirely escape detection since they barely interact with matter, and more elaborate analysis techniques are required to infer their passage through the detector. Figure 3.3 illustrates the way in which various elementary particles interact with the layers of sub-detectors in the CMS experiment.

### 3.2.1 Coordinate Convention

The coordinate system adopted by CMS has the origin centered at the nominal collision point inside the experiment, the y-axis pointing vertically upward, and the x-axis pointing radially inward toward the center of the LHC ring. The z-axis points along the beam direction in a counter-clockwise direction, as seen from above. A cylindrical coordinate system is commonly used, with the azimuthal angle $\phi$ measured from the $x$-axis in the $x$-$y$ plane and the radial coordinate in this plane denoted by $r$. The polar angle $\theta$ is measured from the $z$-axis in the $r$-$z$ plane, and the pseudorapidity is defined as $\eta \equiv -\ln tan(\theta/2)$. Thus, the momentum transverse to the beam direction, denoted by $p_{\mathrm{T}}$, is computed from the $x$ and $y$ components. A more detailed description of the CMS detector, together with a definition of the coordinate system used and the relevant kinematic variables, can be found in Ref. [54].

### 3.2.2 Superconducting Solenoid

The central feature of the CMS apparatus is a superconducting solenoid of 6 m internal diameter (see Figure 3.4), providing a magnetic field of 3.8 T when operating under 20 kA

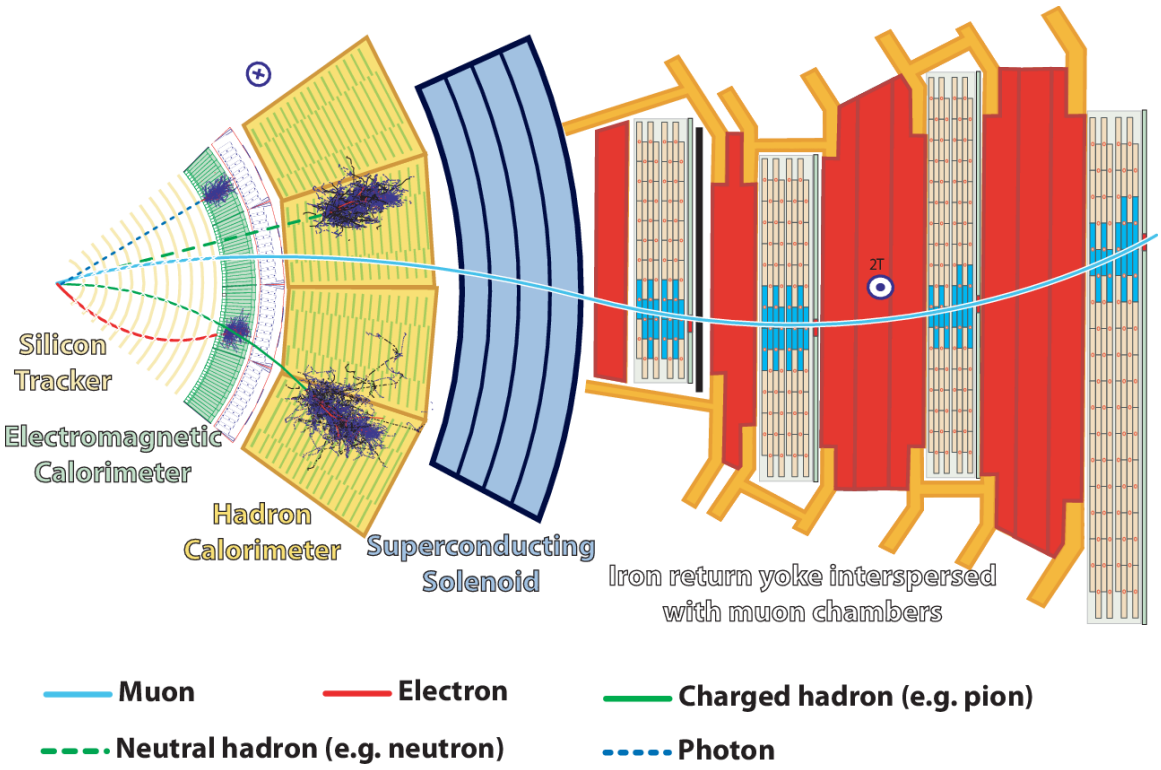


Figure 3.3: Transverse view of a slice of the CMS detector. A muon, represented by a blue line, leaves hits in the tracking sub-detector and curves through the magnetic field. It also produces hits in the muon chambers and curves in opposite direction before escaping the detector. An electron, illustrated by a red line, bends under the solenoid's magnetic field, leaves hits in the inner tracker layers, and is stopped after depositing its energy within the ECAL volume. The dashed blue line represents a photon, which deposits most of its energy in the ECAL sub-detector. Hadrons (shown as green lines) deposit most of their energy in the HCAL volume and leave curved tracks if they are charged (e.g. $\pi^+$).

of current at a temperature of 4.5 K [55]. A higher momentum charged particle will have a higher resistance to deflection by a magnetic field, thus tracing its trajectory yields a measure of its momentum. In particular, a particle of mass $m$ and charge $q$ moving with velocity $v$ under a perpendicular magnetic field $B$ will follow a circular path with a bending radius of $\rho = p/qB$, where $p = mv$.

The CMS solenoid was designed to provide the strongest possible magnetic field in order to determine the momentum of high-energy particles within a relatively small amount of volume. The tracker and calorimeter sub-detectors (ECAL and HCAL) are accommo-

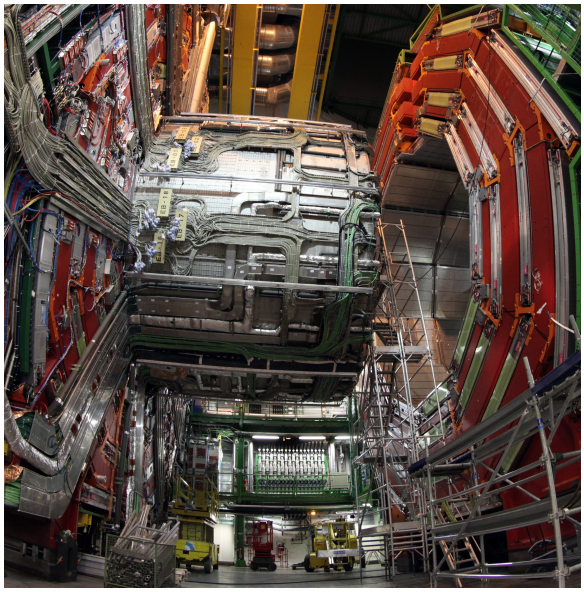

Figure 3.4: CMS Solenoid Magnet during Long Shutdown 1 (LS1). Photograph by M.Hoch, 2013.

dated inside the magnet coil while the muon detectors are interleaved with a 12-sided iron structure that surrounds the magnet coils to contain and guide the field. Made up of three layers, this "return yoke" extends to 14 m in diameter and also seals the detector practically hermetically, allowing through only muons and weakly-interacting particles, such as neutrinos. The solenoid, being the largest superconducting magnet ever built, also provides most of the experiment's structural support and was designed to be strong enough to withstand the forces of its own magnetic field. It has the capacity to store an energy of 2.6 GJ at full current [55], enough to melt 18 tonnes of gold.

### 3.2.3 Tracking Detectors

The CMS tracker records the paths taken by charged particles by finding their positions as they traverse its sensors. It allows the reconstruction of the trajectories of high-energy electrons, muons, hadrons, and products of b-quark decay. Tracking sub-detectors are generally designed to be thin and lightweight to minimize material interactions, which can

interfere with the trajectory of the particles, but also thick enough to provide sufficient signal. Charged particles ionize the silicon as they travel through the sensors, liberating electrons which are guided by an electric field and collected by a read-out chip under the sensitive material. The final design consists of a tracker with planar modules arranged in cylinders and discs and made entirely of silicon sensors: the pixel sub-detector located closest to the interaction region, and the silicon microstrip sub-detector that surrounds it. The tracking system provides an acceptance up to a pseudorapidity of $|\eta| < 2.5$ [56]. With about 200 $m^2$ of active silicon area the CMS tracker is the largest silicon tracker ever built [56]. The radiation environment close to the interaction region will cause damage to the pixel sensors and hence limit their lifetime. This effect can be substantially mitigated by maintaing the operating temperature of the silicon sensors around $-20^\circ$ C [56].

**Pixel Sub-detector**

The CMS pixel detector consists of a central barrel and pairs of forward disks, as shown in Figure 3.5. The barrel pixel (BPIX) comprises three 53 cm long barrel layers, located at mean radii of 4.3 cm, 7.2 cm, and 11.0 cm, and is composed of 768 detector modules arranged into half-ladders of 4 identical modules each. In the first barrel layer, the hit rate density is expected to be as large as $4 \cdot 10^7$ $cm^{-2}s^{-1}$ at the full LHC design luminosity. The forward pixel (FPIX) disks are placed 34.5 cm and 46.5 cm from the center of BPIX, and are composed of 672 detector modules of 7 different sizes arranged into blades [56].

The basic building blocks of the pixel detector are silicon sensors which are highly segmented into $100 \times 150$ $\mu m^2$ pixels and bump-bonded to PSI46V2 read-out chips (ROCs) [57]. This pixel size was selected in order to help maintain the occupancy per channel below 1%, which corresponds to $\sim 10^{-4}$ hits per pixel per bunch crossing [56]. In total, the pixel detector comprises around 16000 ROCs, each consisting of 4160 read-out pixels arranged in a matrix of 52 columns $\times$80 rows and organized into double-column read-out [57].

The FPIX sensors are tilted at $20^\circ$ in a fan-like geometry in order to induce charge

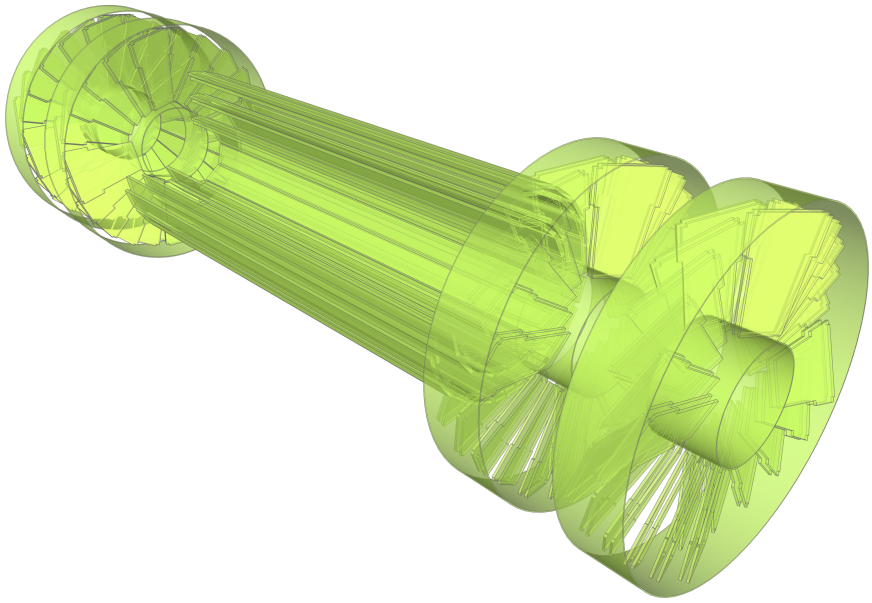

Figure 3.5: Three-dimensional model of the CMS pixel detector.

sharing between pixels. This guarantees that the drift direction of the charge carriers is not parallel to the magnetic field. A position resolution of 10 µm in the $r$-$\phi$ direction and 17 µm in the $z$-direction can be achieved with charge sharing between neighboring pixels [56, 58].

The control and read-out systems for the pixel detector are handled by two types of VME modules, the front-end driver (FED) and the front-end controller (FEC). The FED is a read-out module which digitizes the analog input signals, builds event fragments, and sends them to the data acquisition (DAQ) system. The FEC is responsible for sending the clock, trigger, and other signals to the front-ends. The connection between the front-ends and the FEC/FED is provided by optical links; analog for the read-out modules and digital for the control modules [59].

### Silicon Strip Tracker

The CMS silicon strip tracker consists of ten barrel layers extending outwards to a radius of 1.1 m and nine end-cap disks, as shown in Figure 3.6. It is composed of three different subsystems: The Tracker Inner Barrel and Disks (TIB/TID) extend in radius to

55 cm and are composed of four barrel layers, supplemented by three disks at each end-cap. The Tracker Outer Barrel (TOB) encompasses the TIB with an outer radius of 116 cm and consists of six barrel layers of micro-strip sensors. The Tracker EndCaps (TEC+ and TEC-, where the sign indicates the location along the z axis) each consist of nine disks. Each TEC disk is made up of wedge-shaped carbon fiber support plates called "petals". The CMS silicon strip tracker has a total of 9.3 million strips and 198 $m^2$ of active silicon area [56].

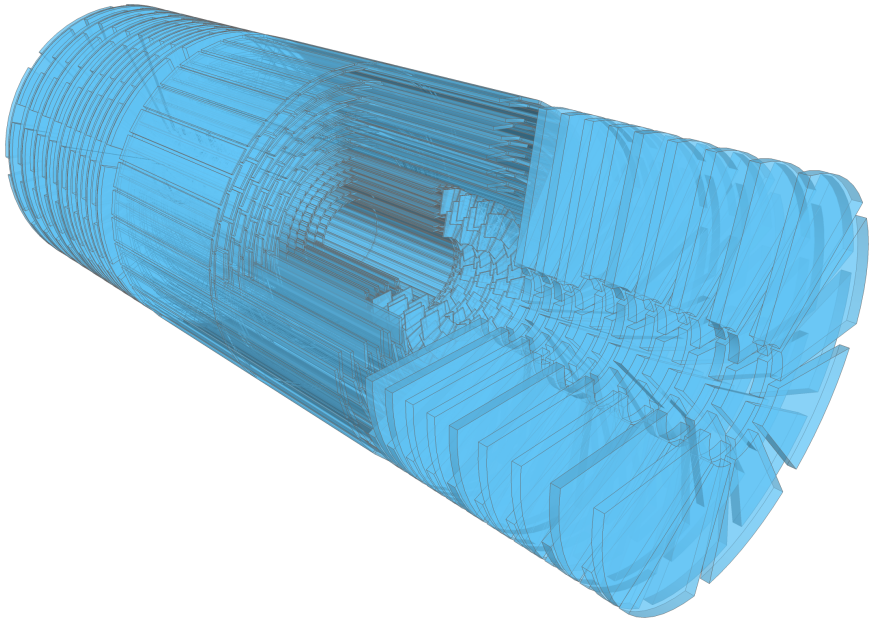

Figure 3.6: Three-dimensional model of the CMS silicon strip tracker.

The basic building block of the Silicon Strip Tracker is called a module, which consists of a support frame, a strip that delivers the bias voltage to the sensor, front-end electronics, and one or two micro-strip sensors. The front-end electronics in each module include several APV25 128-channel radiation hard read-out chips [60]. The strip tracker Front End Driver (FED) is a 9U VME module which receives data from 96 optical fibers, each corresponding to 2 APV25 or 256 detector channels. Its output is a list of clusters with address information and signal height (8-bit resolution) for each strip in the cluster, thus passing to the central DAQ only those objects which are relevant for track reconstruction

and physics analysis [56]. Clock, trigger, and control data are transmitted to the tracker by Front End Controller (FEC) cards.

### 3.2.4 Calorimeter Subdetectors

The CMS detector employs two layers of scintillating calorimeters, which envelop the tracking volume, to measure the energy that a particle loses as it passes through. They are designed to stop entirely or "absorb" most of the particles coming from a collision, forcing them to deposit all of their energy within the bulk of the calorimeter. The calorimeters generally consist of layers of "passive" or "absorbing" high-density material interleaved with layers of an "active" scintillating medium. After incident ionizing radiation excites its atoms, a scintillating material produces energy in the form of photons as the atoms return to a relaxed state. The amount of light produced is proportional to the energy deposited in the sensitive material by the incoming particle. The electromagnetic calorimeter measures the energy of electrons and photons as they interact with the electrically charged particles in matter — producing a shower of electrons, positrons, and photons in the process — and the hadron calorimeter samples the energy of hadrons (particles containing quarks, such as protons and neutrons) as they interact with atomic nuclei, typically characterized by a shower of secondary particles.

#### Electromagnetic Calorimeter

The CMS electromagnetic calorimeter (ECAL) is a homogeneous calorimeter made of 61200 lead tungstate ($PbWO_4$) crystals mounted in the central barrel section covering a pseudorapidity range of $|\eta| < 1.48$, sealed by 7324 crystals in each of the two end-caps which extend the coverage up to $|\eta| = 3.0$, as seen in Figure 3.7. The ECAL provides a measurement of the energies of incident electrons and photons. The use of high density $PbWO_4$ crystals facilitates a fast, high granularity, and radiation resistant calorimeter.

Lead tungstate crystals are made primarily of metal and are heavier than stainless steel,

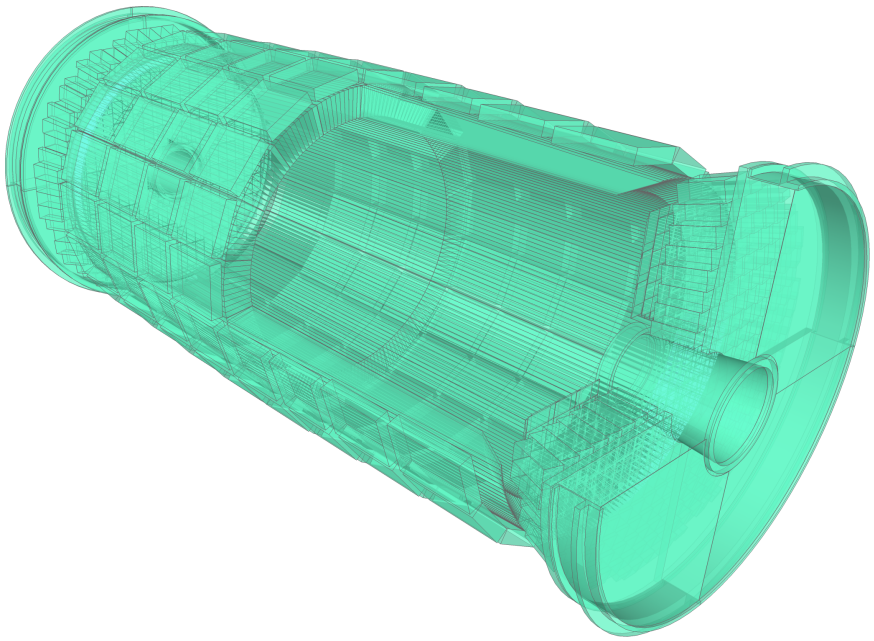

Figure 3.7: Three-dimensional model of the CMS electromagnetic calorimeter.

but oxygen doping makes the crystals highly transparent. Each crystal was grown, in a process taking two or three days, around a "seed" — an existing piece of the crystal with the required properties — from a 1165° C melt of tungsten oxide, lead oxide, and "doping" materials, i.e. small amounts of other materials that refine the crystals' properties. Crucially, $PbWO_4$ crystals "scintillate" when electrons and photons travel through them, i.e. an amount of light proportion to the particle's energy and of a characteristic spectrum is emitted by the crystals following the absorption of ionizing radiation. The crystals emit blue-green scintillation light with a broad maximum at 420–430 nm with a scintillation decay time of the same order of magnitude as the LHC bunch crossing time: about 80% of the light is emitted in 25 ns [61].

Photodetectors especially designed to work within the high magnetic field are glued onto the back of each of the crystals to collect the scintillation light and convert it to an electrical signal that is amplified and sent to the DAQ system. Avalanche photodiodes (APDs) are used as photodetectors in the barrel and vacuum phototriodes (VPTs) in the

endcaps [61].

The number of scintillation photons emitted by the crystals and the amplification of the APD are both temperature dependent. Therefore, the nominal operating temperature of the system, $18^{\circ}$ C, has to be maintained constant to high precision, requiring a cooling system capable of extracting the heat dissipated by the read-out electronics and of keeping the temperature of crystals and photodetectors stable within $\pm 0.1^{\circ}$ C to preserve energy resolution [53]. The energy resolution for electrons is better than 2% in the central region of the ECAL barrel and 2-5% elsewhere. The derived energy resolution for photons varies across the barrel from 1.1%-2.6% and from 2.2%-5% in the endcaps [62]. The $PbWO_4$ crystals suffer limited radiation damage which manifests as a wavelength-dependent loss of light transmission without changes to the scintillation mechanism. The amount of damage can be tracked and corrected for by monitoring the optical transparency of the crystals by means of injected laser light [61].

The ECAL read-out has to acquire the small signals of the photo-detectors with high speed and precision. Digital sums representing the energy deposit in a trigger tower are generated and sent to the trigger system for each bunch crossing. Ref [61] details the full read-out and trigger architecture.

**Preshower Sub-detector**

The principal aim of the CMS preshower detector is to identify neutral pions in the end-caps within a fiducial region $1.65 < |\eta| < 2.61$. It also helps the identification of electrons against minimum ionizing particles, and improves the position determination of electrons and photons with high granularity [61].

The preshower is a sampling calorimeter with two layers: a layer of lead provokes electromagnetic showers from incoming photons or electrons, while silicon strip sensors placed after each plane of lead measure the deposited energy and the transverse shower profiles. It has a much finer granularity than the ECAL with detector strips 2 mm wide,

compared to the 30 mm-wide ECAL crystals. The total thickness of the preshower is 20 cm, which introduces a considerable design challenge since the thin preshower must be kept at temperatures below $-10^{\circ}$ C without compromising the sensitive operating temperature of the ECAL.

### Hadron Calorimeter

The hadron calorimeter (HCAL) is a sampling calorimeter enabling the determination of an incoming particle's position, energy, and arrival time using alternating layers of absorber and fluorescent scintillator materials. The active elements of the central hadron calorimeter are 4 mm-thick plastic scintillator tiles which are read out using wavelength-shifting (WLS) plastic fibers [63]. The HCAL is organised into inner and outer barrel (HB and HO), endcap (HE), and forward (HF) sections. There are 36 barrel "wedges", each weighing 26 tonnes. These form the last layer of detector inside the magnet coil, while the outer barrel (HO) sits outside the coil ensuring no energetic particles leak out of the HB undetected. Similarly, 36 end-cap wedges assembled into disks measure particle energies as they emerge through the ends of the solenoid magnet. The geometry of the HCAL sub-detector is illustrated by Figure 3.8. Lastly, the two hadronic forward calorimeters (HF) are placed at 11.2 m from the interaction point and extend the pseudorapidity coverage down to $|\eta| = 5.2$ using a Cherenkov-based, radiation-hard technology.

When an energetic hadron hits a plate of absorber, in this case brass and steel, it typically interacts copiously with the absorber material producing numerous secondary particles. Interestingly, the brass used as absorber in the HCAL end-caps was provided by re-purposed Russian Navy artillery shells dating from WWII, since they were designed to endure high internal stress as required for the structural integrity of the detector [64]. As these secondary particles flow through successive layers of absorber they too can interact and a cascade or "shower" of particles results. As this shower develops, the particles pass through the alternating layers of active scintillation material causing them to emit blue-

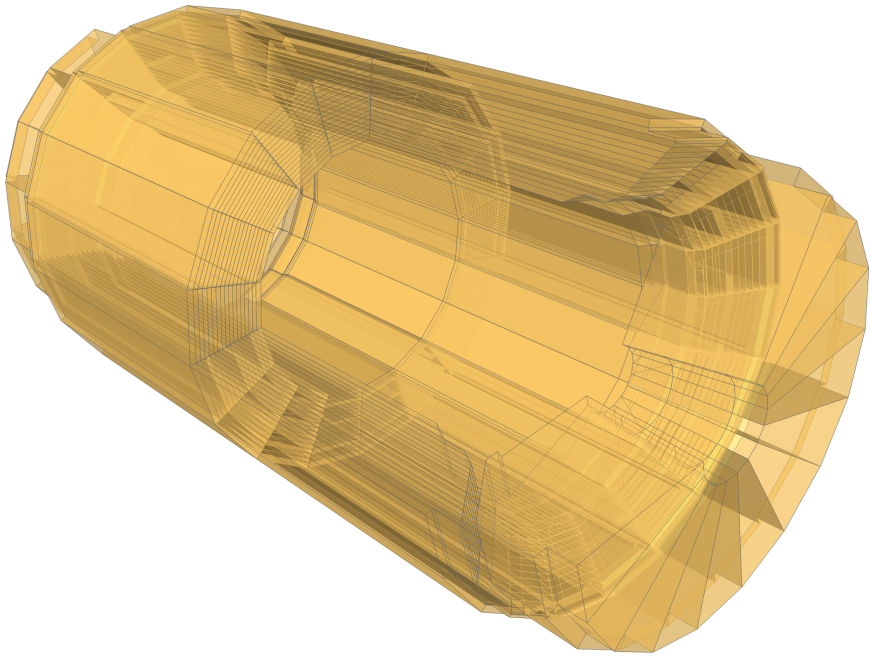

Figure 3.8: Three-dimensional model of the CMS hadron calorimeter.

violet light. Within each scintillator tile, optical wavelength-shifting fibers, with a diameter of less than 1 mm, absorb this light. The fiber shifts the blue-violet light into the green region of the spectrum, and clear optic cables then carry the green light away to read-out boxes located at strategic locations within the HCAL volume [63]. The light produced is collected, converted to an electrical signal, and amplified by Hybrid Photodiodes (HPDs) — photodetectors especially configured for CMS that can operate in a high magnetic field and yield an amplified response, in proportion to the original signal, for a large range of particle energies.

The HCAL read-out consists of an optical-to-electrical converter followed by a fast charge-integrating Analog-to-Digital Converter (ADC). The digital output of the ADC is transmitted for every bunch over a digital optical fiber to the service cavern, housing the off-detector electronics where it is formatted and sent to the trigger and DAQ systems. An overview of the full HCAL read-out chain is laid out in detail in Ref. [63].

### 3.2.5 Muon Detectors

CMS uses three types of gaseous particle detectors for muon identification. In the barrel region, four layers of drift tube (DT) chambers with rectangular drift cells are used. In the end-cap regions of CMS, where there is large occupancy and the magnetic field is large and non-uniform, the muon system uses cathode strip chambers (CSC) which provide fast response times, fine segmentation, and radiation resistance for an acceptance between $0.9 < |\eta| < 2.4$. A crucial characteristic of the DT and CSC subsystems is that they can each select events of interest based on the $p_{\mathrm{T}}$ of muons with good efficiency and high background rejection, independent of the rest of the detector. A complementary muon triggering system consisting of resistive plate chambers (RPCs) is included in both the barrel and end-cap regions. They produce a fast response, with good time resolution but coarser position resolution than the DTs or CSCs. They also help to resolve ambiguities in attempting to reconstruct tracks from multiple hits in a chamber. In total there are 1400 muon chambers: 250 DTs and 540 CSCs track the particles' trajectories and provide a muon trigger, while 610 RPCs constitute an additional muon trigger system. An overview of the muon system is shown in Figure 3.9.

**Drift Tube system**

The drift tube (DT) system measures muon positions as they travel through the barrel section of the detector. Each 4-cm-wide tube contains a 50-μm-diameter gold-plated stainless-steel wire stretched within an Ar-$CO_2$ gas volume [65]. When a charged particle passes through the volume it rips electrons off the atoms of the gas. These move along the applied electric field ending up at the positively-charged wire.

Each drift cell attains a maximum drift time of approximately 400 ns and exhibits a linear relationship between time and drift path [65]. The four layers are staggered by half a cell, making it possible to use the correlation of the drift times in the different planes to compute the coordinate and the angle of the crossing tracks without any external time

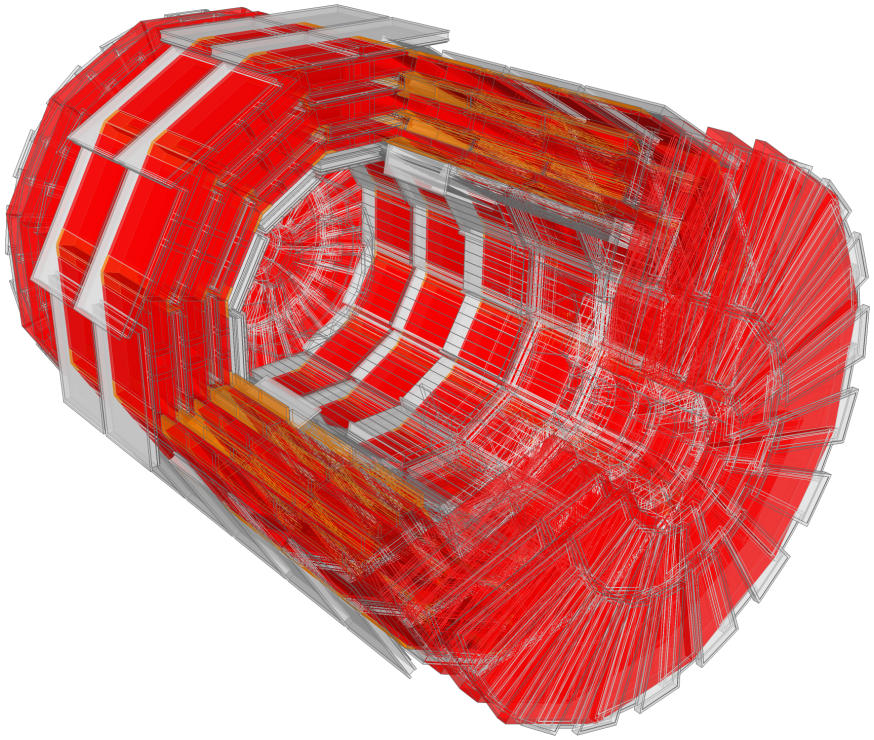

Figure 3.9: Three-dimensional model of the CMS muon detectors.

tag [65] This fast response reduces the total number of wires required to less than $2 \cdot 10^5$, while still keeping the occupancy negligible. The DT electronics is a complex, heavily integrated system, which includes trigger logic, read-out data handling, and service electronics, such as the LV and HV systems. A description of the DT electronic system layout together with the functions associated to each sub-task is detailed in Ref. [65].

### Cathode Strip Chamber system

Each endcap region of CMS has four cathode strip chamber (CSC) muon stations. These chambers have trapezoidal shape and are arranged in a series of concentric rings centered on the beam line. The CSCs are multiwire proportional chambers comprised of 6 anode wire planes interleaved among 7 cathode panels.

Anode wires run azimuthally at approximately constant spacing and define a track's radial coordinate. Strips are milled on cathode panels and run lengthwise at constant $\Delta\phi$

width. An incident muon will ionize the gas mixture — 40% Ar, 50% $CO_2$, 10% $CF_4$ — and liberate electrons which move towards the anode wires and induce charges on the cathode strips. The muon coordinate along the wires ($\phi$ in the CMS coordinate system) is obtained by interpolating charges induced on strips (see Figure 3.10).

The overall area covered by the sensitive planes of all cathode strip chambers is about 5000 $m^2$, the gas volume is $> 50$ $m^3$, and the number of wires amounts to about 2 million in total. There are about 9000 high-voltage channels in the system, around 220000 cathode strip read-out channels with 12-bit signal digitisation, and about 180000 anode wire read-out channels. A more detailed description of CSC read-out and electronic system can be found in Ref. [65].

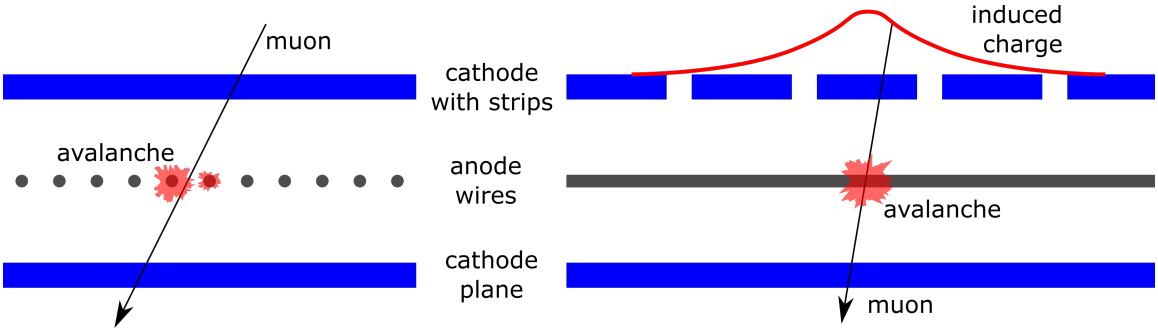


Figure 3.10: Illustration of cathode strip chamber operation. Side view (left), radial view (right). By interpolating charges induced on cathode strips by avalanche positive ions near a wire, a precise localisation of an avalanche along the wire direction can be obtained.

**Resisitive Plate Chamber system**

The resistive plate chamber (RPC) system comprises gaseous parallel-plate detectors that combine adequate spatial resolution with a time resolution comparable to that of scintillators. RPCs consist of two parallel plates, a positively-charged anode and a negatively-charged cathode, both made from very high resistivity plastic material (bakelite) and separated by a gas volume mixture of 96.2% R134a ($C_2H_2F_4$), 3.5% $iC_4H_{10}$, and 0.3% $SF_6$. The inner bakelite surfaces of the RPC are coated with linseed oil for good noise perfor-

mance [53]. Six layers of RPCs, totalling 480 rectangular chambers, are embedded in the barrel iron yoke. In the endcap region, four layers of RPCs cover the region up to $\eta = 1.6$ [66].

An RPC is capable of tagging the time of an ionising event in a much shorter time than the 25 ns between two consecutive LHC bunch crossings [65]. Therefore, a fast dedicated muon trigger device based on RPCs can identify the relevant bunch crossing to which a muon track is associated.

The read-out strips are connected to Front-End Boards (FEB). After having been amplified and discriminated, signals are sent unsynchronized to Link Boards (LB) placed around the detector. The LBs synchronize the signals with the 40-MHz LHC clock and transmit them to the trigger logic located in the CMS counting room over a 90 m optical link at 1.6 GHz [65].

The RPC power systems operate in a hostile environment due to the high magnetic field and high radiation flux. Large portions of the especially designed power systems are near the detectors on the balcony racks placed around the barrel wheels and the endcap disks.

RPC operation is sensitive to both temperature and atmospheric pressure. Therefore, the chambers are constantly monitored to compensate in real time for the detector operating point (high voltage value). More details on the RPC system can be found in ref. [65].

### 3.2.6 Trigger

The trigger organizes the physics event selection process. The irreversible decision to retain an event for further consideration is based on the event's suitability for inclusion in one of the various data sets to be used for analysis. The LHC bunch crossing rate of 40 MHz leads to $\sim 10^9$ interactions per second at design luminosity. Data from only about $10^2$ crossings per second can be written to archival media; hence, the trigger system has to achieve a rejection factor of nearly $10^6$ [53]. The rate is reduced in two steps called Level-1 (L1) trigger and High-Level Trigger (HLT). The L1 trigger consists of custom-

designed, largely programmable electronics and performs an extremely fast and wholly automatic process that looks for simple signs of interesting physics. The HLT is a more sophisticated, software-based filter system implemented in a farm of about one thousand commercial processors.

Prior to the CMS design, L1 triggers would typically count objects, e.g. the number of electrons/muons over a certain threshold. The CMS L1 trigger is able to retain characteristics of objects, including their energy and co-ordinates, which requires sorting of the objects so that only the prime candidates would be selected. Thus, the CMS L1 trigger is able to perform more comprehensive calculations, whereas previous systems would have traditionally carried out such tasks in the second stage of the trigger.

**Level-1 Trigger**

The Level-1 trigger evaluates coarsely segmented data from the calorimeters and the muon system, while holding the high-resolution data in pipelined memories in the front-end electronics. The size of the LHC detectors and the underground caverns imposes a minimum transit time for signals from the front-end electronics to reach the services cavern housing the L1 trigger logic and return back to the detector front-end electronics. The total time allocated for the transit and for reaching a decision to keep or discard data from a particular beam crossing is 3.2 μs — equivalent to $128 \times 25$ ns beam crossings [53]. During this time, the detector data must be held in buffers, while trigger data is collected from the front-end electronics and decisions reached that discard a large fraction of events. Of the total latency, the time allocated to L1 trigger calculations is less than 1 μs [67].

The L1 triggers involve the calorimetry and muon systems, as well as some correlation of information between these systems. The L1 decision is based on the presence of "trigger primitive" objects such as photons, electrons, muons, and jets above set energy or momentum thresholds. It also employs global sums of $p_{\mathrm{T}}$ and $p_{\mathrm{T}}^{\mathrm{miss}}$. The design output rate limit of the L1 trigger is set at 100 kHz due to the average time required to transfer full detector

information through the read-out system. [67].

The L1 trigger comprises local, regional and global components. Local triggers are based on energy deposits in the calorimeter trigger towers and track segments or hit patterns in the muon chambers. Regional triggers combine this information and use pattern logic to determine ranked and sorted trigger objects such as electron or muon candidates in limited spatial regions. The rank is determined as a function of energy or momentum and quality. The Global Calorimeter Trigger (GCT) and Global Muon Trigger (GMT) determine the highest-rank calorimeter and muon objects across the entire experiment and transfer them to the Global Trigger, the top entity of the L1 hierarchy. The Global Trigger takes the decision to reject an event or to accept it for further evaluation by the HLT [54]. The decision is based on algorithm calculations and on the readiness of the sub-detectors and the DAQ. The Level-1 Accept (L1A) decision is communicated to the sub-detectors through the Timing, Trigger and Control (TTC) system [54].

**High-Level Trigger**

The High Level Trigger (HLT) provides further event rate reduction by analyzing full-granularity detector data, using software reconstruction and filtering algorithms running on a large computing cluster consisting of commercial processors called the Event Filter Farm [68]. The HLT must reduce the accepted event rate to a final output rate of O(100 Hz), consistent with an archival storage capability of O(100 MB/s). Upon receipt of a Level-1 Accept (L1A) signal, the data from the pipelines is transferred to front-end read-out buffers. The event building "switch" flags data from a given event to transferred to a processor [53].

The assembling of the event fragments coming from each detector front-end module takes place in two stages. First, the front end data are assembled into larger fragments (super-fragments) which are then delivered to Readout Units (RUs) in eight different and independent sets (DAQ slices), such that all super-fragments of an event are delivered to the same DAQ slice. In each DAQ slice, the super-fragments are managed by the Event

Builder through a complex of switched networks (Gigabit Ethernet) and passed to event buffers (Builder Units, BUs) where they are finally assembled into complete events.

From the BUs, the events are handed to the Filter Units (FUs), the applications which run the actual High-Level Trigger reconstruction and selection. Events accepted by the HLT are forwarded to the Storage Managers (SMs) — two for each DAQ slice — which stream event data on disk and eventually transfer raw data files to the CMS Tier-0 computing center at CERN for permanent storage and offline processing [68].

### 3.2.7 Luminosity Monitors

The rate of events observed by the CMS detector is proportional to a quantity called the instantaneous luminosity — a measure of the rate of useful interactions occurring in the detector. Luminosity is a quantity that measures the ability of a particle accelerator to produce the required number of interactions. It is the proportionality factor between the rate of interactions per second ($dR/dt$) and the cross-section of a given process ($\sigma_p$): $dR/dt = \mathscr{L} \cdot \sigma_p$ [69]. An accelerator operating at high luminosity offers the opportunity to produce very interesting and rare events more often. Moreover, even for more frequently-occurring processes, higher luminosity provides a larger sample size and better statistical accuracy, which allows for more precise measurements.

The CMS luminosity measurement is used to monitor the LHC's performance on a bunch-by-bunch basis in real time and to provide an overall normalization for physics analyses. The design goal for the real-time measurement is to determine the average luminosity with a 1% statistical accuracy with an update rate of 1 Hz. Since the luminosity is directly proportional to the rate of interactions, luminosity measurement techniques usually involve fast counting devices which provide such a signal [69]. This relative signal must be calibrated to deliver the absolute luminosity, which takes into account factors which cause deviations from ideal head-on collisions.

**HF luminosity monitor**

The forward hadron calorimeter, or HF, covers the pseudorapidity range between $3 < |\eta| < 5$ and is composed of quartz fibers embedded in a steel matrix. The signal from the HF originates from Cerenkov light emitted in the quartz fibers, which is then channeled by the fibers to photomultipliers. Each HF endcap is divided into 36 segments in azimuth and 12 segments in $\eta$ — i.e. each physical tower subtends an angular region of $\Delta\eta \times \Delta\phi \sim 0.175 \times 0.175$ [53]. In addition, crude longitudinal segmentation is achieved through the use of long fibers that run from the front face of the HF to the phototube read-out at the back end and short fibers that cover only the rear part of the modules. The HF-based luminosity measurement is based solely on the long fibers.

Two methods for extracting a real-time relative instantaneous luminosity measurenent from the HF have been developed. The 'zero counting' method uses the average fraction of empty towers to infer the mean number of interactions per bunch crossing. The number of interactions, $n$, in a given bunch crossing is distributed according to Poisson statistics: $p(n|\mu) = \mu^n \cdot e^{-\mu}/n!$, where $\mu$ is the mean number of interactions per bunch crossing [53]. At very low luminosities $\mu$ is small and thus approximately equal to the fraction of bunch crossings that contain interactions. Determining this fraction is relatively straightforward using the HF, since nearly all interactions produce summed $E_{\mathrm{T}}$ signals well above the noise. Since a single interaction cannot be reliably distinguished from a bunch crossing with multiple interactions, it is not possible to count interactions in a straightforward way. However, in a large fraction of cases, bunch crossings with zero interactions can be distinguished from those with one or more interactions [53]. The mean number of interactions can thus be determined by: $\mu = -\ln p(0)$, which is known as "zero counting".

The second method exploits the linear relationship between the the total $E_{\mathrm{T}}$ deposited in the HF and the number of interactions, and thus the luminosity. Since the HF is very far forward, the maximum $E_{\mathrm{T}}$ is kinematically limited to a few hundred GeV. This suppresses the large statistical fluctuations that can accompany unbounded power-law distributions [53].

### Pixel Luminosity Telescope

The Pixel Luminosity Telescope (PLT) is a dedicated luminometer at CMS. It employs silicon pixel sensors (sharing the same sensors and read-out chips as the pixel detector) arranged into "telescopes" of three planes mounted along the beam direction. The PLT can be read out in a "fast-or" mode at the full bunch crossing rate of 40 MHz, which provides a signal showing if any pixels in the sensor were hit, thus providing online per-bunch luminosity with excellent statistical precision. The full pixel hit data, which is used to measure corrections and systematic uncertainties for the online measurement, can be read out at a lower trigger rate.

The PLT itself consists of 48 sensors, arranged into 16 telescopes (see Figure 3.11). Each telescope contains three sensors, each mounted in the $x$-$y$ plane. The PLT is installed just outside of the FPIX disks.

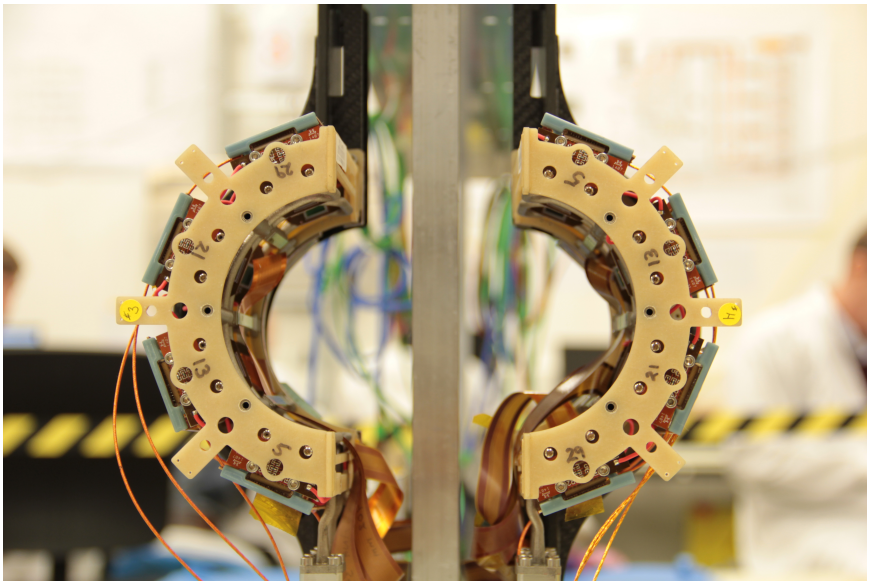

Figure 3.11: Front view of the Pixel Luminosity Telescope.

The luminosity measurement is obtained from the fast-or rate using the "zero-counting" technique. Specifically, if the fraction of scopes with no triple coincidences is given by $f_0$ , then the mean number of tracks per collision is given by $\mu = -\ln f_0$. The luminosity should

then be proportional to $\mu$, with the calibration constant to be determined using the Van der Meer scan method. The calculation of $\mu$ is done on a per-telescope, per-bunch crossing basis. The final luminosity value corresponds to the sum of $\mu$ over all bunch crossings, averaged over all telescopes, and muliplied by the calibration constant.

Chapter 4

# Strategy and Methodology

## 4.1 Vector Boson Fusion

Vector Boson Fusion (VBF), also called weak-boson fusion (WBF) or vector-boson scattering (VBS), is an electroweak process which can be exploited to observe electroweak phenomena with small signal rates. It yields a distinct signature, characteristic for the whole class of weak-boson fusion processes, which consists of two energetic jets produced after two colliding protons radiate $W$ or $Z$ bosons which subsequently interact or "fuse". Figure 4.1 describes one way to interpret VBF processes.

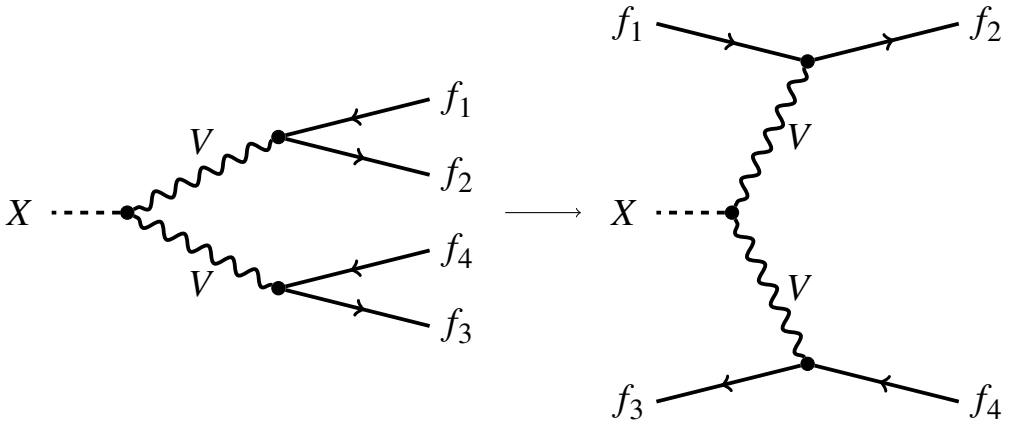


Figure 4.1: Vector boson fusion processes can be understood in analogy to the decay of a heavy resonance $X$ into two vector bosons $V$, which themselves decay into two fermions each ($f$, $f'$), as illustrated on the left. If this process is time-reversed and one of the fermions, $f$, moved to the initial state, we obtain a vector boson fusion process where two fermions (quarks, in the case of the LHC) radiate two vector bosons that subsequently interact to produce a heavy resonance, as shown on the right.

Given that the process occurs through a $t$-channel and both the incoming and outgoing particles are very energetic, the transferred momentum is small (i.e. $Q^2 \sim 0$). Thus, the polar angle with respect to the beamline of the scattered jets in the final state, $\theta$, is expected

to be small:

$$Q^2 = (p_f^2 - p_i^2) = E_q^2 \cdot (1-x) \cdot \theta, \tag{4.1}$$

where $p_i$ and $p_f$ are the initial and final momenta of a quark of initial energy $E_q$, and $x$ is the fraction of the energy carried away the vector boson [70]. The outgoing energetic jets experience limited scattering away from the beamline and are detected in the endcap, or forward, regions of the detector.

These two forward jets are commonly referred to as *tagging jets*. They offer very efficient discriminating power against QCD backgrounds. Due to their back-to-back geometry and very large longitudinal momentum, the invariant mass of the two jet system, $m_{jj}$, may easily exceed a TeV at the LHC's full design center-of-mass energy [71]. This will not be the case for any kind of QCD background.

Being a pure electroweak (EWK) process, color exchanges between the tagging jets are suppressed, i.e. very little hadronic activity is expected in the central region of the detector. This type of process can also be considered analogous to a two-sided deep-inelastic scattering (DIS) process, where the electron side of the DIS process is replaced by the other quark in each case [71]. Thus, the dijet system is characterized by a large gap in pseudo-rapidity ($\Delta\eta$). Figure 4.2 illustrates a candidate VBF event in the ATLAS detector.

**Vector Boson Fusion in the Standard Model**

The process class of vector boson fusion has first been studied in the context of Higgs searches (see Figure 4.3), where the two tagging jets serve as an trigger and allow for a reduction of background processes. Later on, the focus has been extended to VBF production of single gauge bosons (W, Z, $\gamma$) and finally to diboson production.

In order to to elucidate the nature of electroweak symmetry breaking in the Standard Model, it is crucial to measure the way the Higgs boson couples to gauge bosons and fermions. VBF plays a fundamental role in the measurement of the Higgs boson couplings to gauge bosons and fermions because it allows for independent observation in different

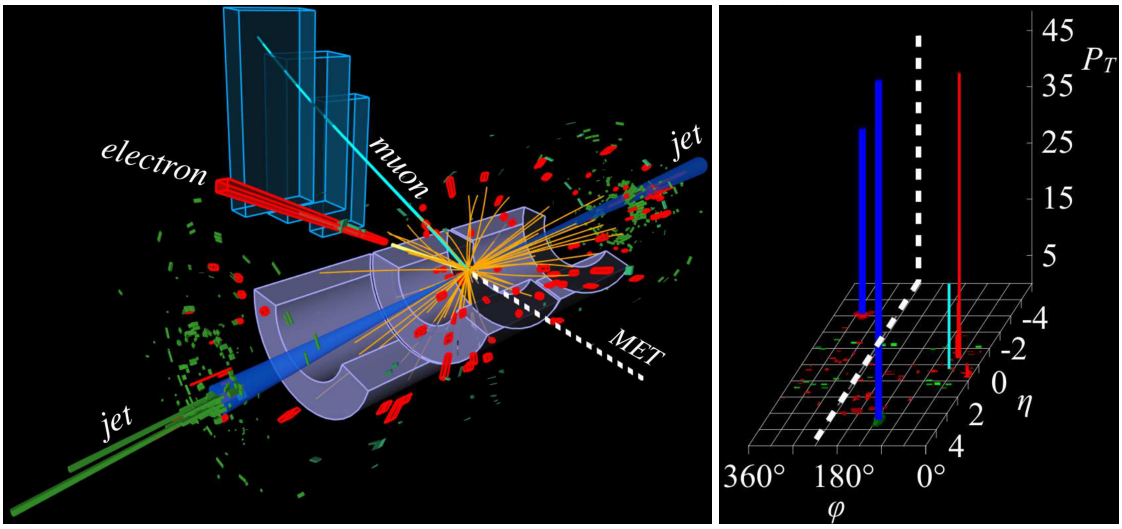


Figure 4.2: Event display for a $H \to WW \to e\nu\mu\nu$ candidate event at the ATLAS detector. (a) Longitudinal view and (b) projected $\eta$-$\phi$ view. Note the large separation in $\eta$ for the two jets (blue spikes) in the event and the central leptonic activity at smaller $\eta$ [1].

channels: $H \to \tau\tau$, $H \to WW$, $H \to \gamma\gamma$, and $H \to \nu\nu$.

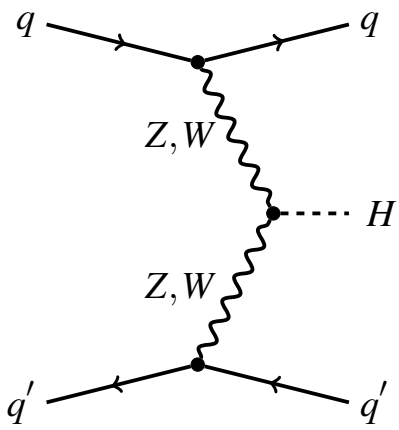


Figure 4.3: Higgs production via Vector boson fusion: two incoming quarks each radiate a $W$ or $Z$ boson which merge and form a Higgs.

The production of gauge bosons via VBF is a background for many collider searches and measurements, both within the Standard Model and beyond. They are important both for the discovered light Higgs state with a mass of around 125 GeV and for searches for heavy Higgs bosons. The study of VBF production of the $Z$ boson is an important benchmark in establishing the presence of VBF processes in general and to cross-check measure-

ments of Higgs VBF processes. Electroweak $Zjj$ production in the leptonic decay channel is defined to include contributions to $\ell^+\ell^- jj$ production for which there is a $t$-channel exchange of an electroweak gauge boson. These contributions include $Z$-boson production via vector boson fusion, $Z$-boson bremsstrahlung, and non-resonant production, as shown in Figure 4.4. Detailed calculations reveal the presence of a large negative interference between the pure VBF process and the two other categories.

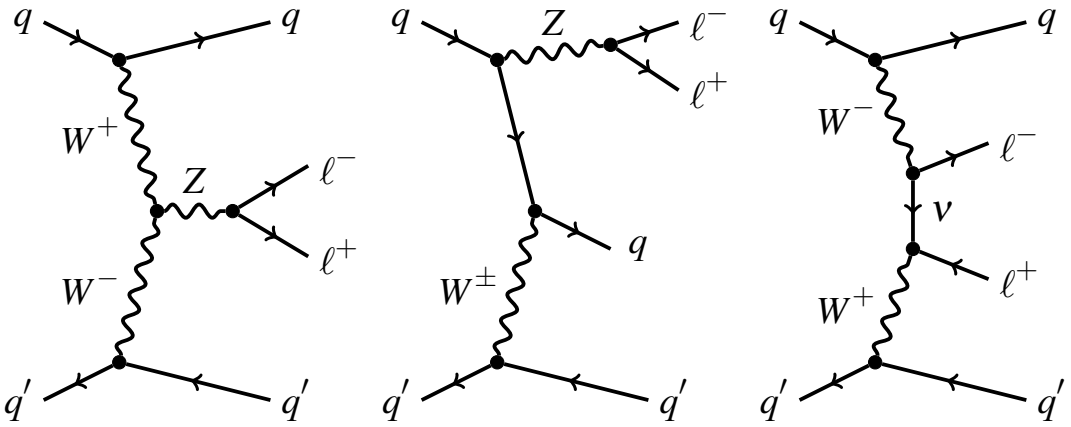


Figure 4.4: Representative leading-order Feynman diagrams for electroweak $Zjj$ production at the LHC: (a) vector boson fusion (b) $Z$-boson bremsstrahlung and (c) non-resonant $\ell^+\ell^- jj$ production.

**Vector Boson Fusion Beyond the Standard Model**

Vector boson fusion has recently gained interest as a tool for exploring phenomena beyond the Standard Model. One advantage of the VBF signature in this context is the potential for probing model-independent phenomena. For instance, Figure 4.1 (right) depicts a VBF process which results in a heavy resonance, which may correspond to any new phenomena that couples to the vector boson. In other words, the VBF topology allows the reduction of large backgrounds and provides a direct window to new phenomena while being agnostic to the underlaying structure of the new model.

To illustrate, we can consider a search for supersymmetry through vector boson fusion production. The VBF topology provides a way to probe the parameter space of various

SUSY models, such as the SUSY electroweak sector and compressed mass spectra sectors, where conventional searches are limited by the thresholds of lepton or jet trigger paths. Since VBF can be used as a tool to observe small electroweak signal rates in a region of phase space with limited QCD activity, the VBF signature may help to discover sleptons and weakinos at LHC [72]. These particles can be extremely difficult to observe in direct production channels due to small rates and very large backgrounds, and their appearance in squark and gluino cascade decays can depend on the SUSY breaking scenario.

The VBF topology can be especially versatile for compressed mass spectra supersymmetric model searches. Given a final state with two VBF-tagged jets and large $p_{\mathrm{T}}^{\mathrm{miss}}$ (VBF+invisible), which is the signature detailed in this document, several sectors of the SUSY parameter space can be explored.

The compressed electroweak SUSY sector may be explored by considering two similar processes. The VBF+invisible signature can be used to investigate direct pair production of the LSP via VBF processes, shown in Figure 4.5. However, this kind of direct electroweak SUSY production suffers from small prodution cross sections at the current LHC luminosity.

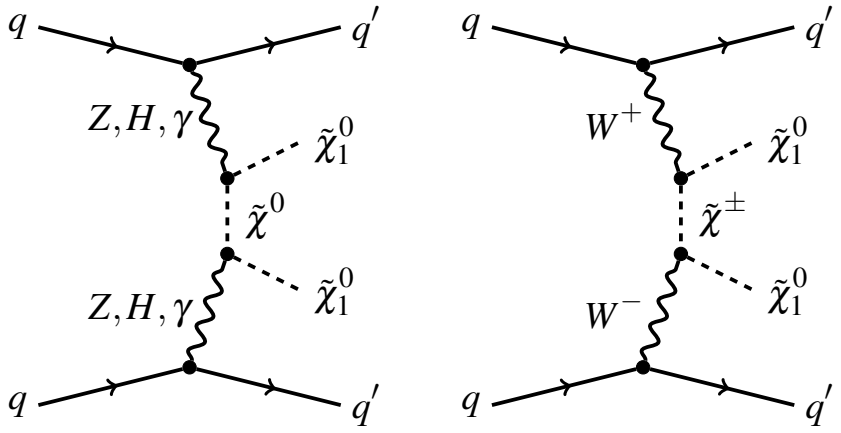


Figure 4.5: Direct LSP pair production via vector boson fusion.

The production of heavier charginos — which is expected to have a more favorable coupling to the vector bosons [73] — may also be studied with the same VBF+invisible

final state. Given a compressed mass spectrum, where the mass of the parent chargino is nearly degenerate with the neutralino mass ($m_{\tilde{\chi}^{\pm}} \sim m_{\tilde{\chi}^0}$), the intermediate slepton is expected to decay into a very soft lepton in addition to the stable LSP (see Figure 4.6). In this scenario, the final-state lepton would not be energetic enough to be identified. Therefore, this process would share the same VBF+invisible final state.

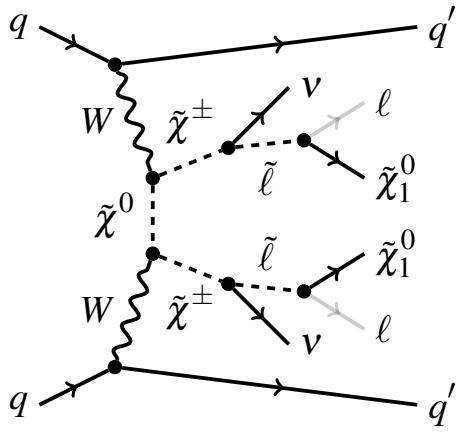


Figure 4.6: Feynman diagram for electroweak chargino-chargino pair production through vector-boson fusion followed by their decays to leptons and LSP, $\tilde{\chi}_1^0$.

Likewise, the compressed colored SUSY sector may be accessible by considering the very same VBF+invisible topology. For instance, compressed $\tilde{t}$ production ($m_{\tilde{t}} - \sim m_{\tilde{\chi}^0}$) and compressed $\tilde{b}$ production ($m_{\tilde{b}} - \sim m_{\tilde{\chi}^0}$) will yield the VBF+invisible final state when produced in association with two initial state radiation (ISR) jets meeting the VBF tagging criteria (see Figure 4.7). Again, due to the near mass degeneracy, the final-state colored products are likely to be too soft to be identified. Such an ISR system will act much like the VBF jets and the LSP will escape undetected leading to large $p_{\mathrm{T}}^{\mathrm{miss}}$.

## 4.2 Dark Matter Searches at the LHC

Dark matter particles may be produced at collider experiments given that they participate in the weak interaction. This kind of dark matter particle candidate is generally referred to as a weakly interacting massive particle (WIMP). Much like neutrinos produced

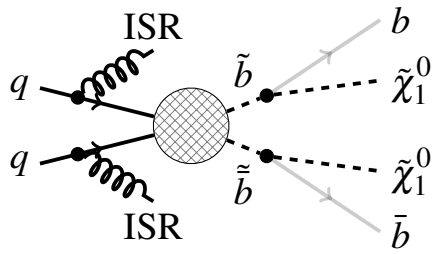


Figure 4.7: Feynman diagram for colored $\tilde{b}$ pair production in association with ISR jets followed by their decays to bottom quarks and LSP, $\tilde{\chi}_1^0$.

in particle colliders, WIMPs would escape the detector without leaving any tracks or energy deposits. The crucial strategy to identify this kind of particle production is to carefully measure the transverse momenta of all particles produced in an interaction and check for any momentum imbalance, $p_{\mathrm{T}}^{\mathrm{miss}}$.

This approach follows from simple energy conservation: Before the collision, the momenta of the particles in the beam is completely longitudinal; their transverse momentum is negligible. Thus, after the collision, the vector sum of the transverse momenta of the collision products must again be negligible, $\sum_\alpha \vec{p}_{\mathrm{T}}{}^{\alpha} = 0$. The accuracy of this calculation hinges on the resolution and geometry of the sub-detectors. The $p_{\mathrm{T}}$ measurement of each visible particle has a finite resolution, which will be propagated to the sum of $p_{\mathrm{T}}$'s. Invisible or escaping particles are more likely to have been produced when the reconstructed $p_{\mathrm{T}}^{\mathrm{miss}}$ is significantly larger than the propagated resolution [74].

WIMPs may be produced as back-to-back pairs at collider experiments thereby balancing the $p_{\mathrm{T}}$ and spoiling the $p_{\mathrm{T}}^{\mathrm{miss}}$ signature. A very common strategy for dealing with this possibility is with DM searches involving "boosted" invisible particles, where an energetic object — such as a jet, a photon, or a vector boson — provides momentum imbalance [75]. Figure 4.8 shows a so-called monojet event observed in the CMS detector.

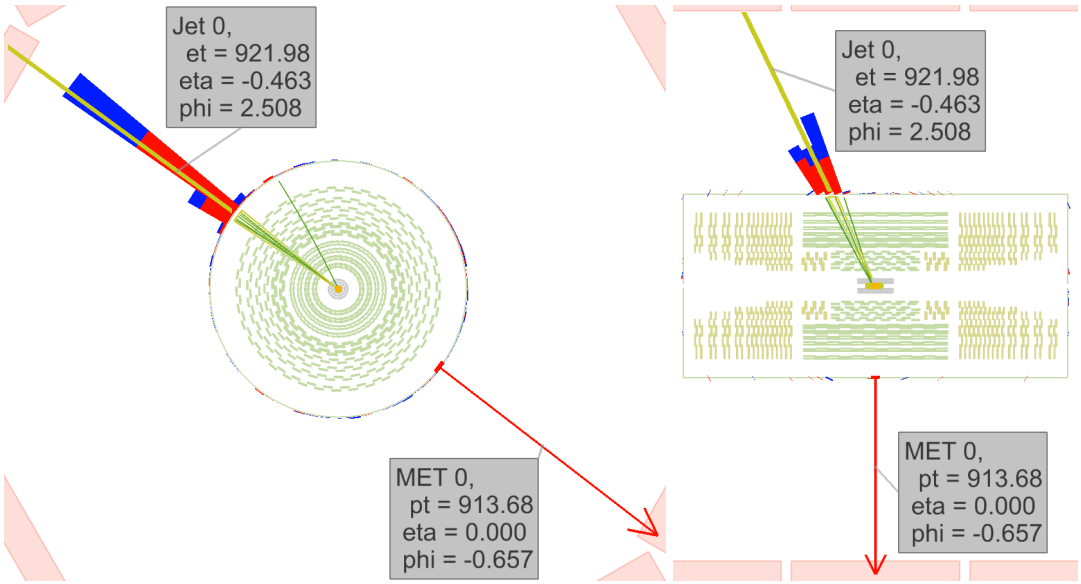


Figure 4.8: Front and side views of a monojet event at the CMS detector. Note that the $p_{\mathrm{T}}^{jet}$ vector is back-to-back with respect to the $p_{\mathrm{T}}^{\mathrm{miss}}$ vector and both have a magnitude of $\sim 900\,\mathrm{GeV}$.

## 4.3 Analysis Strategy

The VBF topology provides a similar mechanism as the monojet process as a window for exploring new physics with $p_{\mathrm{T}}^{\mathrm{miss}}$ signatures. The following section summarizes the analysis strategy for a final state signature of two VBF-tagged jets and large-$p_{\mathrm{T}}^{\mathrm{miss}}$.

As in the more traditional cascade decay SUSY searches, VBF tagging exploits high-$p_{\mathrm{T}}$ jets ($p_{\mathrm{T}} > 50$ GeV) to reduce the background rates. Although the signal production cross-sections are relatively small, the distinctive forward-backward character of the jets makes the signal stand out and reduces the SM backgrounds to manageable levels. Therefore, apart from the *lepton* and *b-jet vetoes* (which will be referred to as *central selections*), our search strategy consists of applying the *VBF selections*: requiring one pair of high-$p_{\mathrm{T}}$ jets with large separation in pseudorapidity ($\Delta\eta$), in opposite hemispheres ($\eta_1 \times \eta_2 < 0$), and with large invariant mass ($m_{jj}$). Figure 4.9 illustrates the VBF topology. In addition to the VBF requirements, a relatively strict $p_{\mathrm{T}}^{\mathrm{miss}}$ requirement is imposed due to the presence of the LSP, which escapes detection.

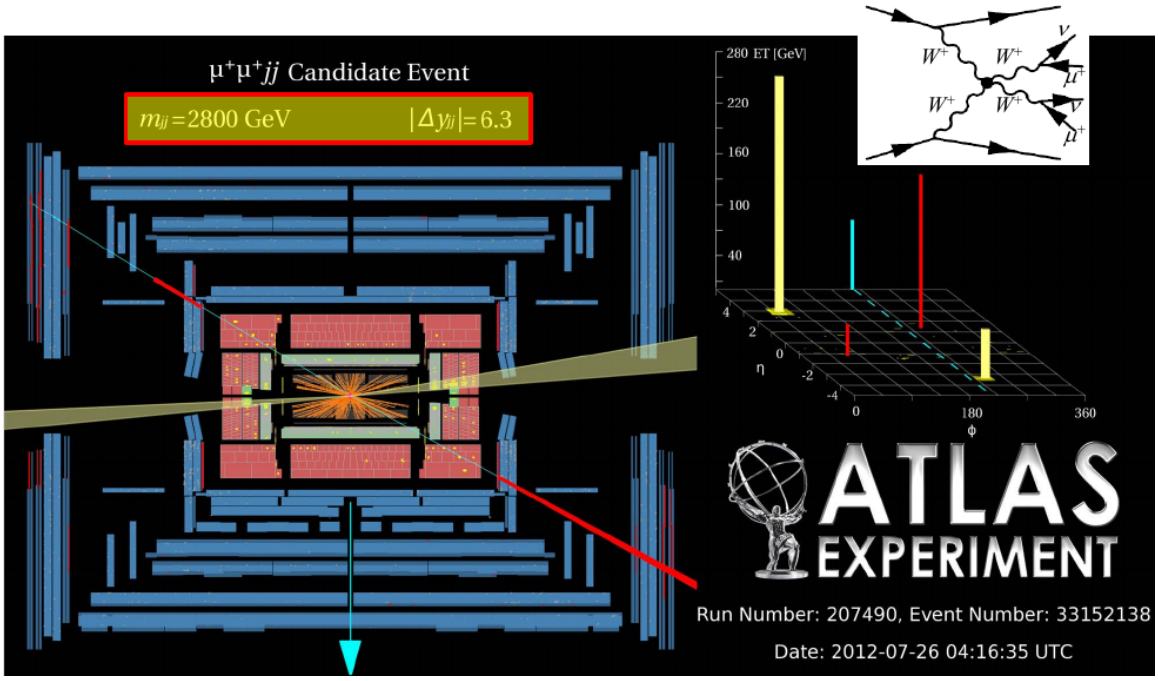


Figure 4.9: Vector boson fusion event observed in the ATLAS detector. Note the large separation in pseudorapidity between the jets (highlighted in yellow) and the large value of the dijet invariant mass, $m_{jj} = 2800$ GeV.

The general methodology used for the estimation of background contributions in the signal region (SR) is based on both simulation and data. Since the dominant backgrounds in this analysis contain "real" $p_{\mathrm{T}}^{\mathrm{miss}}$ from neutrinos, which is well-understood and modeled by MC in various other studies utilizing high-$p_{\mathrm{T}}^{\mathrm{miss}}$ events, the BG estimation methodology hinges on control samples used to validate good modeling of the $p_{\mathrm{T}}^{\mathrm{miss}}$ by the simulation. Understanding the efficiency of the VBF topological selections is the "*uncharted*" territory. Mismodeling of the MC background rates in the SR may be due to the VBF selections. Therefore, the estimate of the background contribution is determined by obtaining background enriched control regions (CR), which contain negligible signal contamination to (i) validate the correct modeling of the central selections and/or determine a correction factor for the efficiency of the central selections, and (ii) measure and/or validate the VBF efficiency (i.e. fraction of events passing the VBF selections) from data. In general, the

following equation is used to estimate the background contributions:

$$N_{\mathrm{SR}}^{\mathrm{BG}} = N_{\mathrm{central}}^{\mathrm{BG}} \cdot SF_{\mathrm{central}}^{\mathrm{BG}} \cdot \varepsilon_{\mathrm{VBF}} \tag{4.2}$$

where $N_{\mathrm{SR}}^{\mathrm{BG}}$ is the predicted background rate in the signal region, $N_{\mathrm{central}}^{\mathrm{BG}}$ the predicted rate in simulation without the VBF selections, $SF_{\mathrm{central}}^{\mathrm{BG}}$ the data-to-simulation correction factor for the central selections as determined from the background enriched control sample, and $\varepsilon_{\mathrm{VBF}}$ the efficiency of the VBF selections, which is determined directly from data in the background enriched control sample. It is important to note that, in general, the data-to-simulation correction factor for the central selections, $SF_{\mathrm{central}}^{\mathrm{BG}}$, contains the corrections for everything: object identification and isolation, misidentification rates, efficiency of topological cuts (not including VBF), etc. The BG estimation method described above relies on one key aspect: the VBF efficiency, $\varepsilon_{\mathrm{VBF}}$, remains unbiased by the definition of the CR. The MC samples are used to check the closure of this method by ensuring that the VBF shapes are similar between the CR and SR. Various samples are utilized to validate the correct determination of the scale factors and VBF efficiencies with the data itself.

# Chapter 5

# Physics Object Reconstruction

## 5.1 Physics Object Reconstruction

This section details the object reconstruction and identification selections. These selections correspond to a set of criteria which determine whether a collecion of tracks and energy deposits will be considered an electron, or a muon, or a jet, etc.

The particle-flow event reconstruction algorithm aims at reconstructing all stable particles in the event by combining information from all CMS sub-detectors. The algorithm optimizes the determination of particle types, directions and their energies. The resulting list of particles are then used to reconstruct higher level objects such as jets, taus, missing transverse energy, to compute charged lepton and photon isolation, etc. The basic elements of the particle-flow event reconstruction are the charged particle tracks reconstructed in the central tracker and the energy clusters reconstructed in electromagnetic and hadronic calorimeters.

The energy clustering is performed in each sub-detector of the calorimeters separately using a specific clustering algorithm, developed for particle-flow event reconstruction, which aims for a high detection efficiency even for low energy particles and separation of close energy deposits. These basic elements are then connected to each other using a link algorithm to fully reconstruct each single particle, while removing any possible double counting from different detectors. The algorithm produces blocks of elements linked directly or indirectly. The particle-flow algorithm is then used to reconstruct and identify a set of particles from each block of elements.

Charged hadrons are reconstructed from the tracks in the central tracker. Photons and neutral hadrons are reconstructed from energy clusters in calorimeters. Clusters separated from the extrapolated position of tracks in the calorimeters constitute a clear signature

of these neutral particles. A neutral particle overlapping with charged particles in the calorimeters can be detected as a calorimeter energy excess with respect to the sum of the associated track momenta. The resulting list of reconstructed particles constitute a global description of each event, available for subsequent physics analysis [76].

### 5.1.1 Jet Reconstruction

This analysis employs Particle Flow jets (PFJets). PFJets use complimentary information from all subdetectors to produce a mutually exclusive collection of reconstructed particles (namely muons, electrons, photons, charged hadrons and neutral hadrons) that are used as inputs to the jet clustering algorithms. The anti-$k_{\mathrm{T}}$ clustering algorithm [77] with a reconstruction cone of R = 0.5 is adopted (where $R = \sqrt{\Delta\eta^2 + \Delta\phi^2}$). The PFJets used are corrected using L1 FastJet, L2 Relative, and L3 Absolute corrections: The L1 FastJet corrections use the event-by-event UE/PU (UE: Underlying Event, PU: Pile Up) densities to remove the additional contributions to the measured jet energies due to underlying event and pile-up particles. The L2 and L3 corrections use jet balancing and $\gamma$+Jet events to improve and provide a better energy response as a function of $p_{\mathrm{T}}$ and $\eta$ [78, 76].

The "loose" Jet-Id working point selection criteria was chosen for this analysis since the jet recoonstrucion/identification efficiency in simulation is $> 98\%$ for the entire range of $\eta$ and $p_{\mathrm{T}}$ (see Figure 5.1). Table 5.1 summarizes the selection criteria used for the "loose" working point. The "loose" Jet-Id working point has been validated in other studies [79].

#### b-Jet Tagging

Since a top quark nearly always decays into a b–quark, b-tagged jets are used to reduce $t\bar{t}$ background in the signal region and to obtain $t\bar{t}$ enriched control samples used to estimate the signal rate. This analysis uses the "loose" working point of the combined secondary vertex algorithm. The details of the algorithm can be found in [80]. The EPS13 prescription is used for the b-tagging and mis-tagging scale factors and efficiencies. They are applied

Table 5.1: Loose Jet-ID Selections.

| Selection | Cut |
|---|---|
| Neutral Hadron Fraction | $< 0.99$ |
| Neutral EM Fraction | $< 0.99$ |
| Number of Constituents | $> 1$ |
| And for $\eta < 2.4$ , $\eta > -2.4$ in addition apply | |
| Charged Hadron Fraction | $> 0$ |
| Charged Multiplicity | $> 0$ |
| Charged EM Fraction | $< 0.99$ |

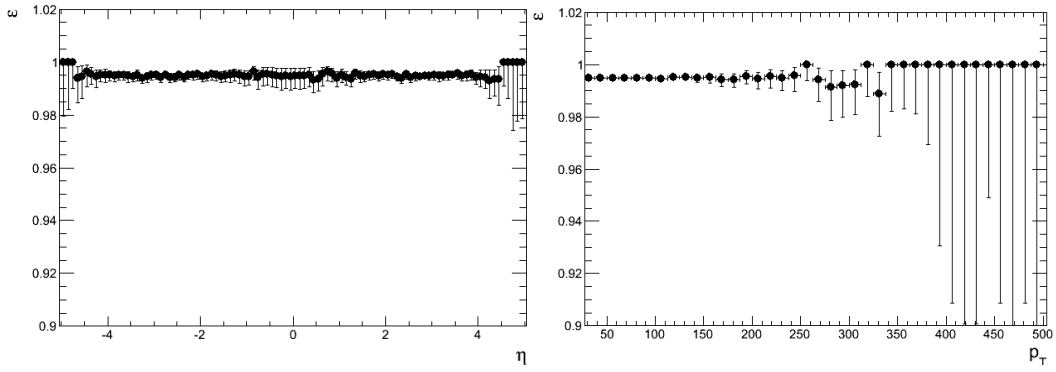


Figure 5.1: Jet reco/ID efficiency as a function of (a) $\eta$ and (b) $p_{\mathrm{T}}$.

using the method called "Event reweighting using scale factors only" [81].

### 5.1.2 Electron Reconstruction and Identification

Electrons are reconstructed using information from the Tracker and Electromagnetic Calorimeter (ECAL) sub-detectors. As electrons pass through the silicon tracker material, they lose energy due to Bremsstrahlung radiation [82]. The energy of the radiated photons is scattered over several crystals of the ECAL detector along the electron trajectory, mostly in the $\phi$ direction (since the magnetic field points in the z-direction). Two algorithms based on energy clustering, "Hybrid" for the barrel and "Island" for the endcaps, are used to measure the energy of electrons and photons [83].

Electron tracks are reconstructed by matching trajectories in the silicon strip tracker to seed hits in the Pixel detector. A pixel seed is composed of two pixel hits compatible with

the beam spot. A Gaussian Sum Filter (GSF) is used for the reconstruction of trajectories in the silicon strips. In order to minimize the many possible trajectories due to different combinations of hits, the track that best matches an energy supercluster in the ECAL is chosen to be the reconstructed track.

The preselection of primary electron candidates requires good geometrical matching and good agreement between the momentum of the track and the energy of the ECAL supercluster. Two quantities used to estimate the geometrical matching are $\Delta\eta_{in} = \eta_{sc} - \eta_{vertex}^{Track}$ and $\Delta\phi_{in} = \phi_{sc} - \phi_{vertex}^{Track}$. The $\eta_{sc}$ and $\phi_{sc}$ coordinates correspond to the ECAL supercluster position and are measured using an energy-weighted algorithm. The $\eta_{vertex}^{Track}$ and $\phi_{vertex}^{Track}$ coordinates are defined as a perfect-helix extrapolation of the track from the interaction vertex to the ECAL detector. The good energy-momentum matching is measured by taking the ratio between the corrected energy $E_{corr}$ in the ECAL supercluster and the momentum of the track $P_{in}$ measured in the inner layers of the tracker.

Electron selections have two main components, electron identification (eID) and electron isolation. The main eID selections are driven by the selections imposed at the trigger level. In addition, electrons which arise from photon conversions are removed by requiring that the track associated with the electron has hits in the inner layers of the pixel detector. The electron trigger/identification efficiencies and scale factors used to correct the MC expectations in these analyses have been taken from [84].

### 5.1.3 Muon Reconstruction and Identification

Muon reconstruction is a multi-step process that begins with the information gathered from the Muon subdetectors. Initially, standalone muons are reconstructed from hits in the individual Drift Tubes (DT) and Cathode Strip Chambers (CSC). Hits from the innermost muon stations are combined with hits in the other muon segments using a Kalman fitting technique. The standalone muon trajectory is reconstructed by extrapolating from the innermost muon station to the outer tracker surface. This standalone trajectory is then used

to find a matching track reconstructed in the silicon tracker. Finally, standalone muons and matching silicon tracks are used to perform a global fit resulting in a "global" muon. Muon reconstruction is described in more detail in [85].

Global muons are reconstructed by combining tracker muons from the silicon tracker and standalone muons from the muon chambers. Once a muon is required to have matching tracks in the inner and outer detectors, the main source of background consists of charged hadrons (e.g. charged pions) that leave a signature in the silicon tracker while also penetrating through the hadronic calorimeter and creating hits in the muon chambers. Charged hadrons that penetrate the hadronic calorimeter and leave hits in the muon system will also deposit significant energy in the calorimeters. Therefore, a calorimeter-compatibility algorithm can be used to significantly reduce the number of mis-tagged charged pions. However, calorimeter-compatibility is not used in this analysis due to our uncertainty of the performance of such algorithms in the presence of high PU. The presence of punch-throughs often occur due to pions from the fragmentation of quarks and gluons. These punch-throughs can often be discriminated against using isolation requirements. Similarly, non-prompt muons, originating from heavy-flavor decays and in-flight decays, are expected to be enveloped within jets and can be discriminated against by imposing an isolation requirement. Muon identification is described in more detail in [85] and [86].

Isolated muons are required to have minimal energy from PF neutral and charged candidates in a cone of $\Delta R = 0.4$ around the lepton trajectory. PF charged candidates considered in the isolation calculation are required to be near the primary vertex. Isolation for muons is defined as:

$$I = \frac{\sum_i p_T^i}{p_T^\mu} \tag{5.1}$$

where the index $i$ runs over PF neutral and charged candidates. Table 5.2 shows the complete list of muon identification criteria. The muon trigger/identification efficiencies and scale factors used to correct the MC expectations in this analysis have been taken

from [87].

Table 5.2: $\mu$ Identification

| Cut |
|---|
| "Global" $\mu$ |
| Tracker hits $\geq 10$ |
| Pixel hits $\geq 1$ |
| $\geq 2$ chambers with matching segments |
| Global fit $\chi^2/NDOF < 10$ |
| $\geq 1$ hit in muon system |
| impact parameter $\lvert d_0 \rvert < 0.2$ cm |
| $(\Sigma^{\Delta R<0.4}_{photons,hadrons} E_T)/(p^{\mu}_T) < 0.2$ |

### 5.1.4 Tau Reconstruction and Identification

Identifying hadronically-decaying taus at the LHC is quite challenging since they must be discriminated against generic quark and gluon QCD jets, which are produced with a cross–section several orders of magnitude larger. CMS has developed several algorithms to reconstruct and identify hadronically-decaying taus based on Particle Flow (PF) objects [88]. For this analysis, the CMS Tau POG recommends the Hadron Plus Strips algorithm (HPS). HPS makes use of PFJets as inputs to an algorithm that uses strips of clustered electromagnetic particles to reconstruct neutral pions. The electromagnetic strips ("neutral pions") are combined with the charged hadrons within the PFJets to attempt to reconstruct the main tau decay modes outlined in Table 5.3.

Table 5.3: Reconstructed Tau Decay Modes

| HPS Tau Decay Modes |
|---|
| Single Hadron + Zero Strip |
| Single Hadron + One Strip |
| Single Hadron + Two Strips |
| Three Hadrons |

The "single hadron plus zero strips" decay mode attempts to reconstruct $\tau \to \nu\pi^{\pm}$, or $\tau \to \nu\pi^{\pm}\pi^0$ decays where the neutral pion has very low energy. The "single hadron plus

one electromagnetic strip" decay mode attempts to reconstruct tau decays which produce neutral pions, where the resulting neutral pions decay into collinear photons. Similarly, the "single hadron plus two strips" mode attempts to reconstruct taus that decay via e.g., $\tau \to \nu\pi^{\pm}\pi^{0}$ where the neutral pion produces well-separated photons as it decays, resulting in two electromagnetic strips. The "three hadrons decay" mode attempts to reconstruct 3-prong tau decays from a common vertex. In all cases, electromagnetic strips are required to have $E_T > 1$ GeV. Additionally, the PF charged hadrons are required to be compatible with a common vertex and have a net charge of $|q| = 1$.

In order to enforce the isolation requirements on the reconstructed tau, a region of size R = 0.5 around the tau decay mode direction is defined. The remaining PF candidates not involved in tau decay mode reconstruction, nor in electromagnetic strips and charged hadron reconstruction will be used to calculate isolation. The "Tight" or "Medium" MVA (MultiVariate Analysis) isolation (with lifetime) working points are used [89].

In order to discriminate against muons, HPS taus are required to pass the lepton rejection discriminator which requires the lead track of the tau to not be associated with a global muon signature. In order to distinguish from electrons, HPS taus are required to pass an MVA discriminator which evaluates the amount of HCAL energy associated to the tau in contrast to the measured momentum of the track (H/p). Additionally, the MVA electron discriminator considers the amount of electromagnetic energy in a narrow strip around the leading track with respect to the total electromagnetic energy of the tau. Finally, HPS taus must not reside in the ECAL cracks (i.e. gaps between ECAL modules).

### 5.1.5 $p_{\mathrm{T}}^{\mathrm{miss}}$

The measurement of a large transverse momentum imbalance ($p_{\mathrm{T}}^{\mathrm{miss}}$) at CMS could be strong evidence of new physics, such as SUSY, due to the presence of heavy and stable weakly interacting particles, such as the LSP. The transverse momentum imbalance is reconstructed as the negative of the vector sum of the transverse momenta of all final-state

particles reconstructed in the detector. For the analysis outlined, we make use of PFMET. PFMET employs more complex Particle Flow algorithms to reconstruct the momenta of individual particles:

$$\vec{p}_{\mathrm{T}}^{\,\mathrm{miss}} = -\sum_{i} \vec{p}_{\mathrm{T}}^{\,i} \tag{5.2}$$

where the index $i$ runs over all particle flow candidates. $p_{\mathrm{T}}^{\mathrm{miss}}$ is the magnitude of $\vec{p}_{\mathrm{T}}^{\,\mathrm{miss}}$. A three-step correction is devised to remove the bias in the $p_{\mathrm{T}}^{\mathrm{miss}}$ scale due to the non-linearity of the response of the calorimeter for neutral and charged hadrons, caused by event pile-up, large bending of low $p_{\mathrm{T}}$ tracks due to strong magnetic field in CMS, etc. The correction procedure relies on the fact that $p_{\mathrm{T}}^{\mathrm{miss}}$ can be factorized into contributions from jets, isolated high $p_{\mathrm{T}}$ photons, electrons, muons, and unclustered energies. The Type-I correction is a propagation of the jet energy corrections (JEC) to MET. It replaces the vector sum of transverse momenta of particles, which can be clustered as jets, with the vector sum of the transverse momenta of the jets to which JEC is applied. The Type-II correction corrects the $\vec{p}_{\mathrm{T}}^{\,\mathrm{miss}}$ of unlustered particles by uniformly scaling it by a constant scale factor. The Type-0 correction is a mitigation for the degradation of the MET reconstruction due to the pile-up interactions. For each pile-up vertex the expected missing neutral momentum is calculated using an improved PF candidate to vertex association technique and added vectorially to PF $p_{\mathrm{T}}^{\mathrm{miss}}$ [76]. Pile-up interactions have little true MET because they produce few invisible particles, e.g., neutrinos from Kaon decays. Therefore, if we were able to measure all visible particles precisely and accurately, pile-up interactions would not much degrade the MET reconstruction. However, in practice, because our measurement of visible particles is not perfect, the MET reconstruction degrades as the number of the pile-up interactions increases. The PFMET version used in this analysis contains type-0 and type-I corrections.

### 5.1.6 Pile-Up Corrections

The additional energy attributed to jets which comes from pp interactions other than the hard-scatter event at the primary vertex (PV) is called pile-up. Quantities such as jet energy, $p_{\mathrm{T}}^{\mathrm{miss}}$, and isolation, where energy depositions are summed up over some range of the detector, can suffer large inefficiencies or systematic effects due to particles from pile-up interactions.

There are three major classifications of pileup based upon the time at which the additional energy enters the calorimeter system. In-time (IT) pileup refers to energy from pp collisions in the current bunch-crossing (BX) other than that at the hard scatter PV. This is the largest source of pileup energy. In addition, there is early out-of-time (EOOT) pileup, which refers to energy left in the calorimeters from previous bunch crossings, and late out-of-time (LOOT) pileup, which refers to energy from later bunch crossings that is integrated with the current event's energy.

A simple and robust method must be employed to subtract off the contribution from secondary interactions. In the case of $p_{\mathrm{T}}^{\mathrm{miss}}$, this is done by using FastJet corrections to determine the density of PU on an event-by-event basis. For taus, pile-up corrections are defined as:

$$I = \sum_i p_{\mathrm{T}}^{i,charged} + max(E_{\mathrm{T}}^{i,gamma} + E_{\mathrm{T}}^{i,neutral} - 0.5 \times E_{\mathrm{T}}^{PU}, 0.0) \tag{5.3}$$

where $E_{\mathrm{T}}^{PU}$ is the $p_{\mathrm{T}}$ sum of charged particle originating from PU vertices. The pile-up corrections use the fact that the contribution to isolation from neutral particle deposits can be determined by using the percentage of PF charged hadrons considered for isolation that arise from PU.

# Chapter 6

# Trigger Performance

## 6.1 Triggers

CMS has developed several triggers for VBF jet signatures. Since the 2012B data taking period, CMS has opted to trigger on events with jet properties conforming to VBF processes. Reconstruction of these events was performed in a different time scale from that of normal primary datasets and is referred to as parked data. The VBF triggered data samples are useful for searches such as the one outlined in this document which focuses on SUSY particles in compressed scenarios. In this analysis we utilize the following triggers in an 'OR' configuration:

- **DiJet35_MJJ700_AllJets_DEta3p5_VBF_v***
- **HLT_DiPFJet40_PFMETnoMu65_MJJ600VBF_LeadingJets_v***
- **HLT_DiPFJet40_PFMETnoMu65_MJJ800VBF_AllJets_v***

In the remainder of this section, we provide a detailed account of the trigger performance for each of the aforementioned VBF triggers, as well as the combined trigger efficiency. The CALO-based trigger (**DiJet35_MJJ700_AllJets_DEta3p5_VBF_v***) requires two calorimeter jets with a transverse momentum of 35 GeV, $|\Delta\eta| > 3.5$ between these jets, and an invariant dijet mass of 700 GeV. This trigger is seeded by both Level-1 $p_{\mathrm{T}}^{\mathrm{miss}}$ and Level-1 $H_{\mathrm{T}}$ (where $H_{\mathrm{T}} = \sum_{jets} p_{\mathrm{T}}$) set up as **L1_ETM40 OR L1_HTT150 OR L1_HTT175 OR L1_HTT200**. The PF-based triggers (**HLT_DiPFJet40_PFMETnoMu65_MJJ600VBF_LeadingJets_v*** and **HLT_DiPFJet40_PFMETnoMu65_MJJ800VBF_AllJets_v***) require two PFJets with $p_{\mathrm{T}} > 40\,\mathrm{GeV}$, PF $p_{\mathrm{T}}^{\mathrm{miss}} > 65\,\mathrm{GeV}$, and an invariant dijet mass of 600 GeV and 800 GeV, respectively. The PF-based triggers are seeded by L1

$p_{\mathrm{T}}^{\mathrm{miss}}$ (**L1_ETM40**). In addition, the Z+Jets and W+Jets background estimates employ the **HLT_IsoMu24_eta2p1_v*** SingleMu trigger which selects events at least one muon with $p_{\mathrm{T}} > 25\,\mathrm{GeV}$ and $|\eta| < 2.1$.

The trigger efficiency is studied as a function of a given kinematic variable by relaxing any requirement on that variable while enforcing all other selections. The dijet mass and $p_{\mathrm{T}}^{\mathrm{miss}}$ are expected to be the most important trigger requirements, so the trigger efficiency is estimated as a function of these parameters. The selection criteria for studying the trigger efficiency are as follows:

- 2 jets with $p_{\mathrm{T}} > 50\,\mathrm{GeV}$ and $|\eta| < 5.0$
- $|\Delta\eta| \geq 4.2$
- b-jet and lepton vetoes
- $p_{\mathrm{T}}^{\mathrm{miss}} > 50, 100, 150, 200\,\mathrm{GeV}$ and study the trigger effciency vs $m_{jj}$
- $M(j_1, j_2) > 750, 1000, 1250, 1500\,\mathrm{GeV}$ and study the trigger effciency vs $p_{\mathrm{T}}^{\mathrm{miss}}$

### 6.1.1 VBF Trigger Performance with Monte Carlo Samples

The trigger study focused on $\mathrm{Z}(\rightarrow \nu\bar{\nu})$ + jets and $\widetilde{\chi}_1^0\widetilde{\chi}_1^0 jj$ MC signal samples for LSP mass points of $0, 25, 50, 75, 100\,\mathrm{GeV}$.

Appendix A.2 details the performance of each individual trigger.

Figures 6.1 and 6.2 show the trigger efficiency for **DiJet35_MJJ700_AllJets_DEta3p5_VBF_v*** $\vee$ **HLT_DiPFJet40_PFMETnoMu65_MJJ600VBF_LeadingJets_v*** $\vee$ **HLT_DiPFJet40_PFMETnoMu65_MJJ800VBF_AllJets_v*** triggers in an "OR" configuration as a function of $m_{jj}$ for various $p_{\mathrm{T}}^{\mathrm{miss}}$ cuts. In this "OR" configuration, the trigger becomes efficient after about 750 GeV. Figures 6.3 and 6.4 show the trigger efficiency for the same triggers in an "OR" configuration as a function of $p_{\mathrm{T}}^{\mathrm{miss}}$ for various $m_{jj}$ cuts. As visible in the $p_{\mathrm{T}}^{\mathrm{miss}}$ distribution, the trigger efficiency plateaus after 75 GeV.

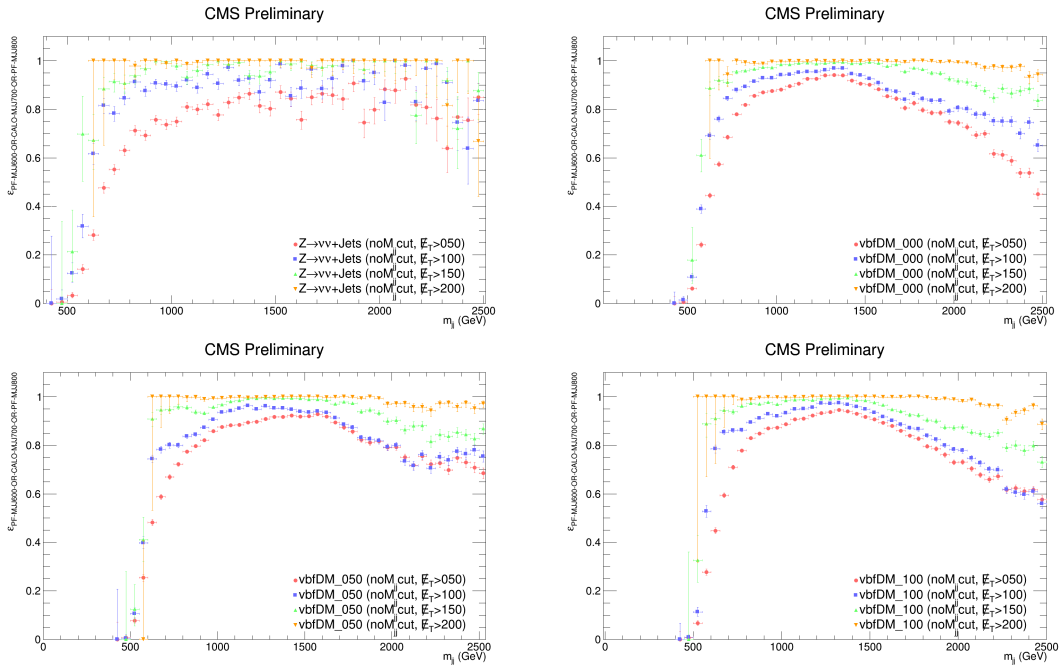


Figure 6.1: $\varepsilon_{\text{VBF\_triggers\_"OR"\_config}}$ vs. $m_{jj}$ given various $p_{\text{T}}^{\text{miss}}$ selections for (a) $\text{Z}(\rightarrow \nu\bar{\nu})$ + jets and $\widetilde{\chi}_1^0\widetilde{\chi}_1^0 jj$ with LSP mass of (b) 0 GeV, (c) 50 GeV, and (d) 100 GeV.

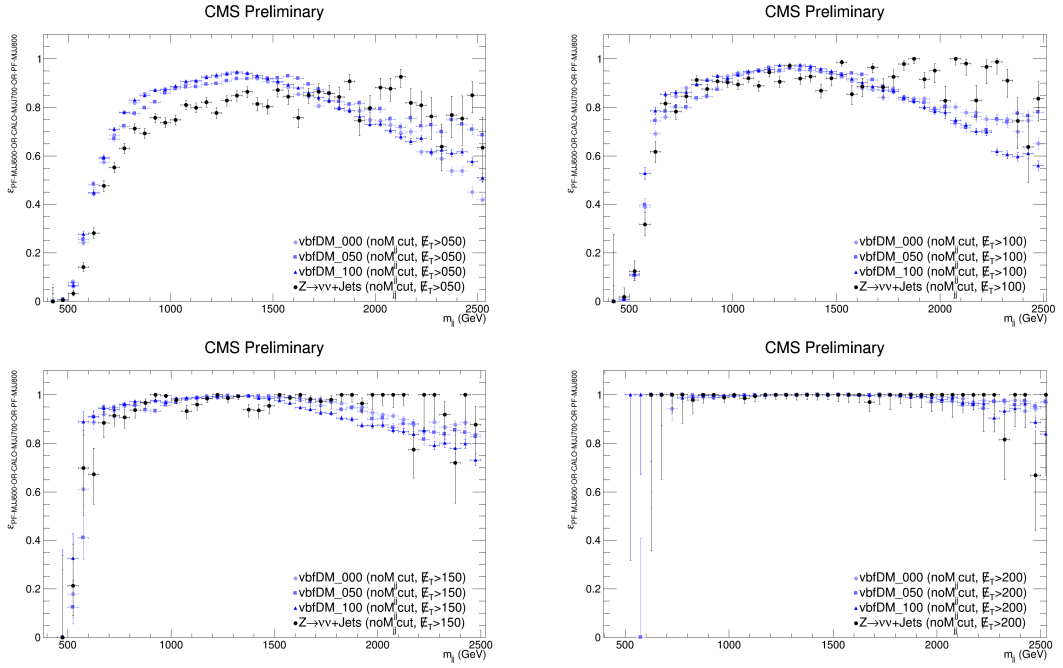


Figure 6.2: $\varepsilon_{\text{VBF\_triggers\_"OR"\_config}}$ vs. $m_{jj}$ given various $p_{\text{T}}^{\text{miss}}$ selections for (a) $\text{Z}(\rightarrow \nu\bar{\nu})$ + jets and $\widetilde{\chi}_1^0\widetilde{\chi}_1^0 jj$ with LSP mass of (b) 0 GeV, (c) 50 GeV, and (d) 100 GeV.

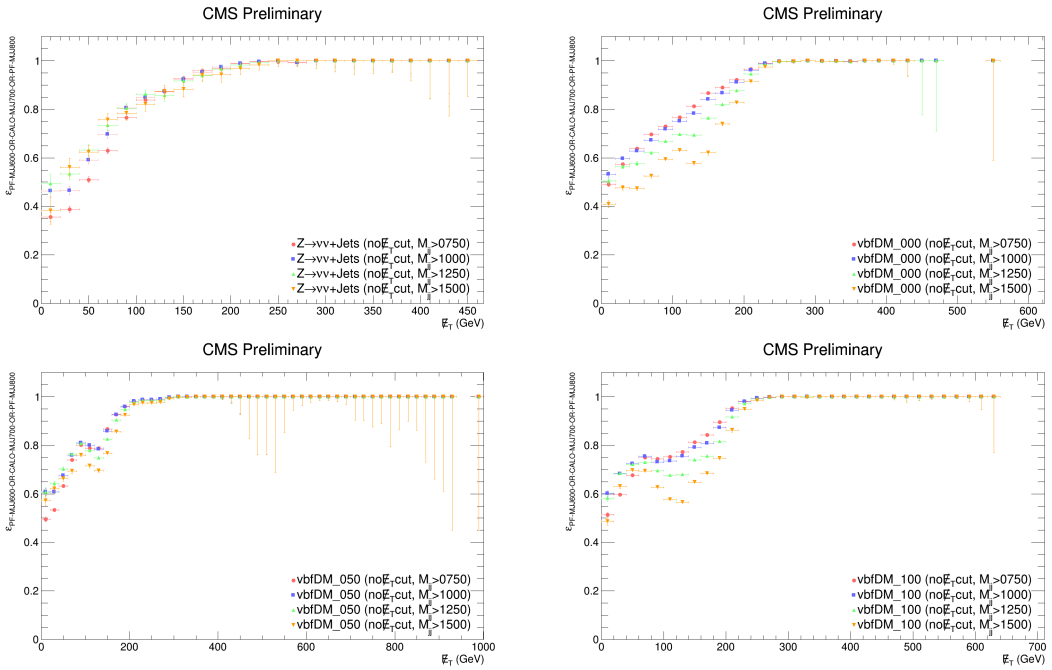


Figure 6.3: $\varepsilon_{\text{VBF\_triggers\_"OR"\_config}}$ vs. $p_{\text{T}}^{\text{miss}}$ given various $m_{jj}$ selections for (a) $\text{Z}(\rightarrow \nu\bar{\nu})$ + jets and $\widetilde{\chi}_1^0\widetilde{\chi}_1^0 jj$ with LSP mass of (b) 0 GeV, (c) 50 GeV, and (d) 100 GeV.

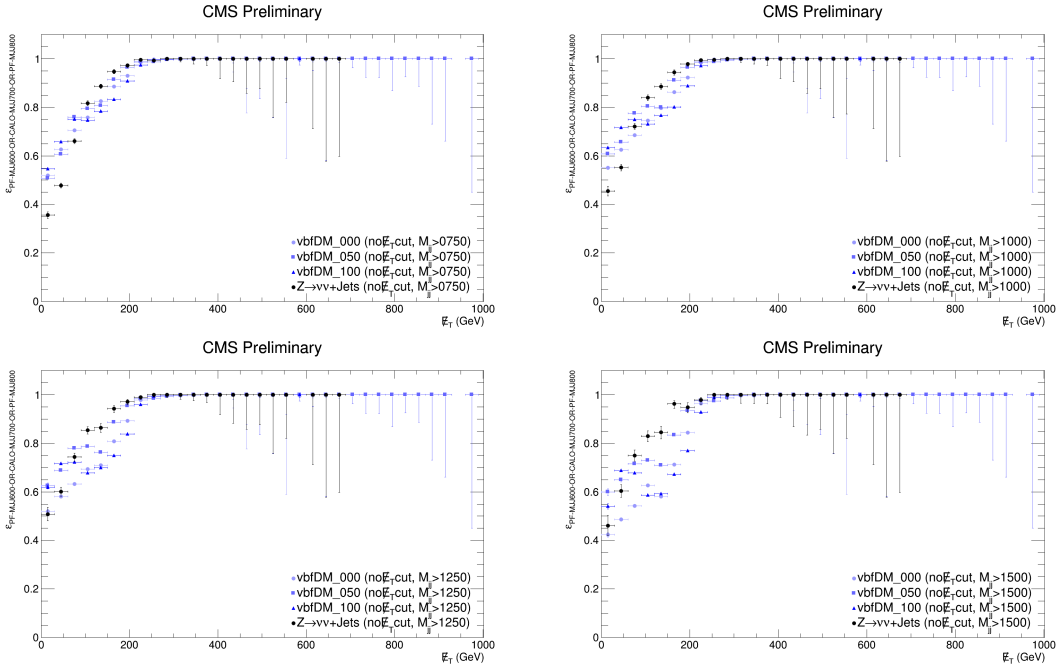


Figure 6.4: $\varepsilon_{\text{VBF\_triggers\_"OR"\_config}}$ vs. $p_{\text{T}}^{\text{miss}}$ given various $m_{jj}$ selections for (a) $\text{Z}(\rightarrow \nu\bar{\nu})$ + jets and $\widetilde{\chi}_1^0\widetilde{\chi}_1^0 jj$ with LSP mass of (b) 0 GeV, (c) 50 GeV, and (d) 100 GeV.

Figure 6.5 shows the trigger efficiency for each individual trigger in addition to the "OR" trigger configuration as a function of $m_{jj}$ given various $p_{\mathrm{T}}^{\mathrm{miss}}$ cuts for the $\widetilde{\chi}_1^0\widetilde{\chi}_1^0 jj$ signal MC sample with LSP mass $= 0\,\mathrm{GeV}$. These plots make it easier to compare the trigger turn-on curve for the trigger under considerarion. The $m_{jj}$ distribution shows that the PF-based trigger has a faster turn-on curve. Figure 6.6 shows the trigger efficiency for each individual trigger and the "OR" trigger configuration as a function of $p_{\mathrm{T}}^{\mathrm{miss}}$ given various $m_{jj}$ cuts for the $\widetilde{\chi}_1^0\widetilde{\chi}_1^0 jj$ signal MC sample with LSP mass $= 0\,\mathrm{GeV}$. The $p_{\mathrm{T}}^{\mathrm{miss}}$ distributions illustrate how the CALO-based trigger achieves a faster turn-on efficiency curve than the PF-based triggers.

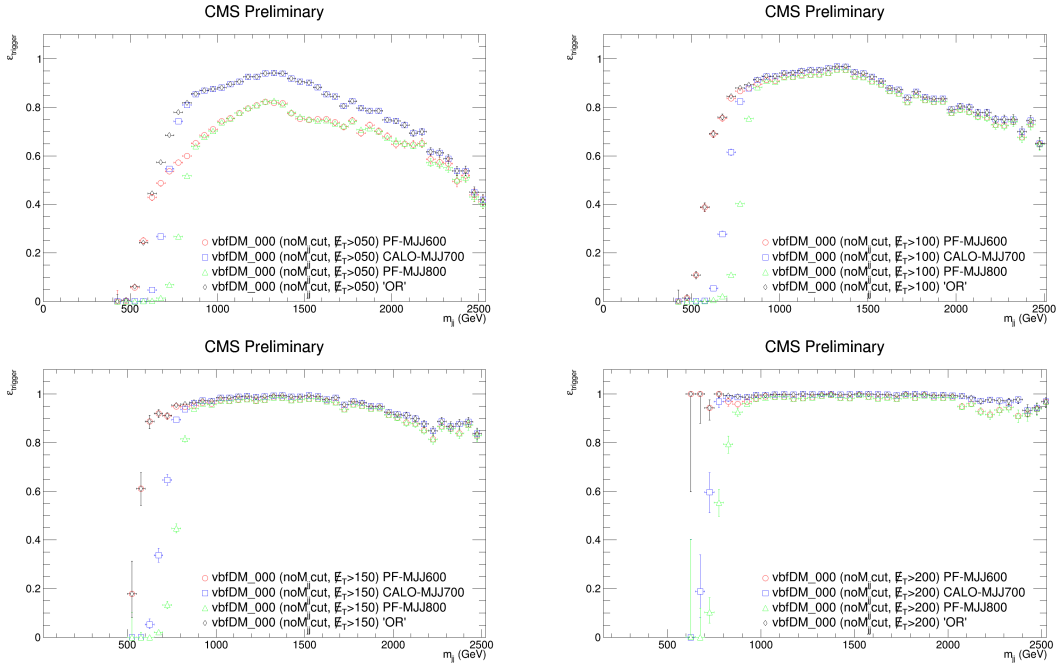


Figure 6.5: $\varepsilon_{\mathrm{VBF\_trigger}}$ vs. $m_{jj}$ for $\widetilde{\chi}_1^0\widetilde{\chi}_1^0 jj$ with LSP mass of 0 GeV given (a) $p_{\mathrm{T}}^{\mathrm{miss}} > 50$ GeV, (b) $p_{\mathrm{T}}^{\mathrm{miss}} > 100$ GeV, (c) $p_{\mathrm{T}}^{\mathrm{miss}} > 150$ GeV, and (d) $p_{\mathrm{T}}^{\mathrm{miss}} > 200$ GeV.

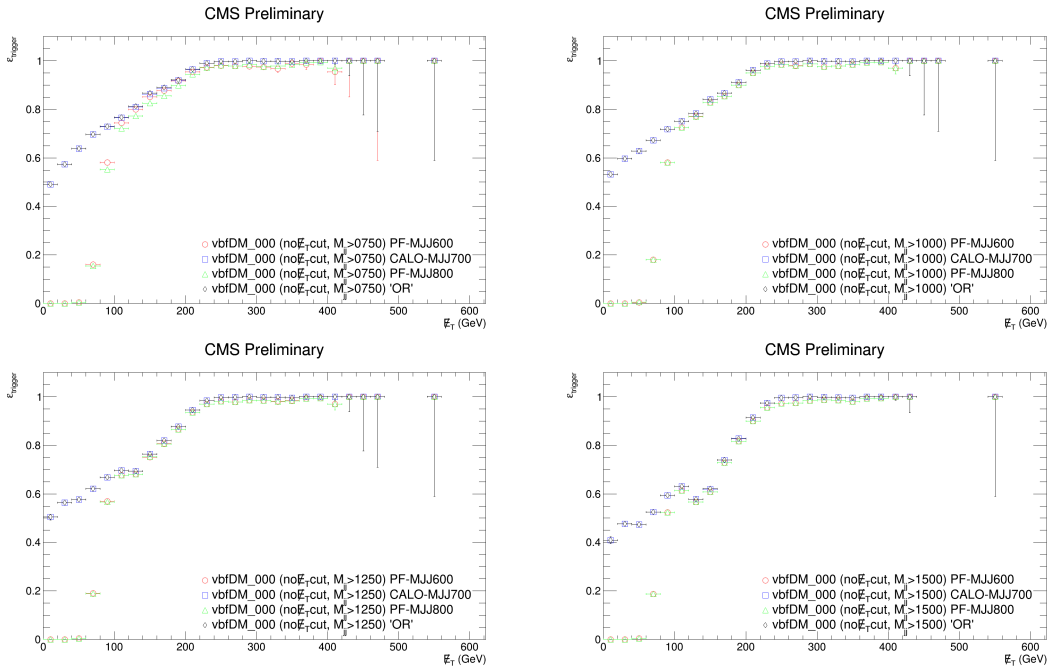


Figure 6.6: $\varepsilon_{\text{VBF\_trigger}}$ vs. $p_{\text{T}}^{\text{miss}}$ for $\widetilde{\chi}_1^0\widetilde{\chi}_1^0 jj$ with LSP mass of 0 GeV given (a) $m_{jj} > 750$ GeV, (b) $m_{jj} > 1000$ GeV, (c) $m_{jj} > 1250$ GeV, and (d) $m_{jj} > 1500$ GeV.

Figure 6.7 shows the trigger efficiency for each individual trigger in addition to the "OR" trigger configuration as a function of $m_{jj}$ given various $p_{\mathrm{T}}^{\mathrm{miss}}$ cuts for the $\widetilde{\chi}_1^0\widetilde{\chi}_1^0 jj$ signal MC sample with LSP mass $= 50\,\mathrm{GeV}$. For the second mass point, the PF-based trigger again performs better in the $m_{jj}$ distribution. Figure 6.8 shows the trigger efficiency for each individual trigger and the "OR" trigger configuration as a function of $p_{\mathrm{T}}^{\mathrm{miss}}$ given various $m_{jj}$ cuts for the $\widetilde{\chi}_1^0\widetilde{\chi}_1^0 jj$ signal MC sample with LSP mass $= 50\,\mathrm{GeV}$. Likewise, the CALO-based trigger achieves a faster turn-on curve than the PF-based triggers on the $p_{\mathrm{T}}^{\mathrm{miss}}$ distribution.

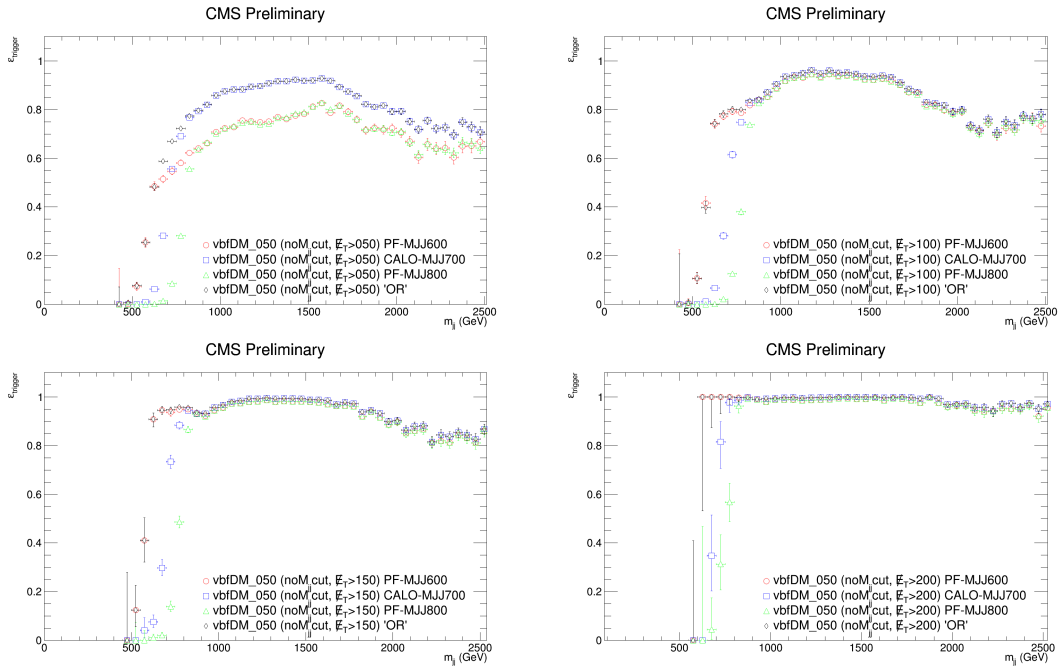


Figure 6.7: $\varepsilon_{\mathrm{VBF\_trigger}}$ vs. $m_{jj}$ for $\widetilde{\chi}_1^0\widetilde{\chi}_1^0 jj$ with LSP mass of 50 GeV given (a) $p_{\mathrm{T}}^{\mathrm{miss}} > 50$ GeV, (b) $p_{\mathrm{T}}^{\mathrm{miss}} > 100$ GeV, (c) $p_{\mathrm{T}}^{\mathrm{miss}} > 150$ GeV, and (d) $p_{\mathrm{T}}^{\mathrm{miss}} > 200$ GeV.

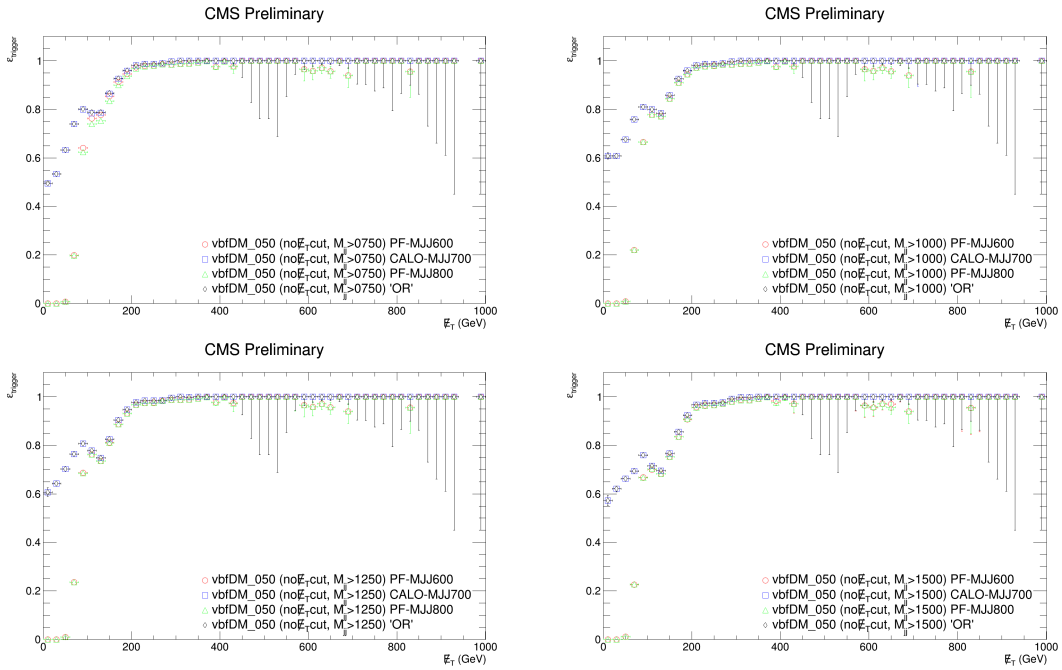


Figure 6.8: $\varepsilon_{\text{VBF\_trigger}}$ vs. $p_{\text{T}}^{\text{miss}}$ for $\widetilde{\chi}_1^0\widetilde{\chi}_1^0 jj$ with LSP mass of 50 GeV given (a) $m_{jj} > 750$ GeV, (b) $m_{jj} > 1000$ GeV, (c) $m_{jj} > 1250$ GeV, and (d) $m_{jj} > 1500$ GeV.

Figure 6.9 shows the trigger efficiency for each individual trigger and the "OR" trigger configuration as a function of $m_{jj}$ given various $p_{\mathrm{T}}^{\mathrm{miss}}$ cuts for the $\widetilde{\chi}_1^0\widetilde{\chi}_1^0 jj$ signal MC sample with LSP mass $= 100\,\mathrm{GeV}$. The PF-based trigger displays a faster increase in efficicency for the $m_{jj}$ distribution. Figure 6.10 shows the trigger efficiency for each individual trigger and the "OR" trigger configuration as a function of $p_{\mathrm{T}}^{\mathrm{miss}}$ given various $m_{jj}$ cuts for the $\widetilde{\chi}_1^0\widetilde{\chi}_1^0 jj$ signal MC sample with LSP mass $= 100\,\mathrm{GeV}$. The CALO-based trigger shows an improvement over the PF-based trigger for the efficiency turn-on in the $p_{\mathrm{T}}^{\mathrm{miss}}$ distribution.

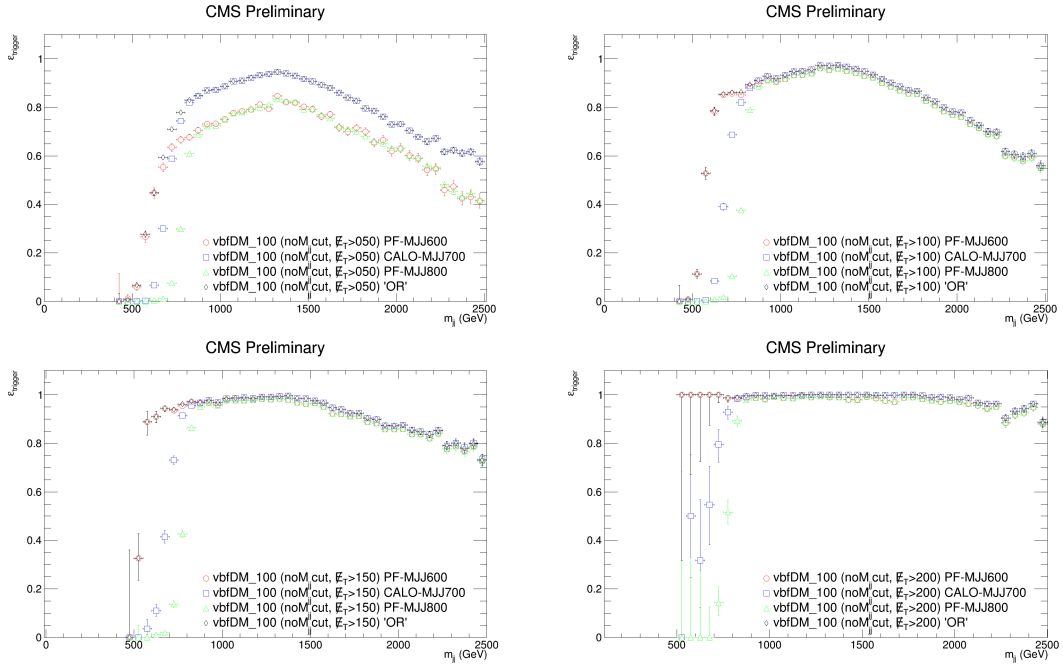


Figure 6.9: $\varepsilon_{\mathrm{VBF\_trigger}}$ vs. $m_{jj}$ for $\widetilde{\chi}_1^0\widetilde{\chi}_1^0 jj$ with LSP mass of 100 GeV given (a) $p_{\mathrm{T}}^{\mathrm{miss}} > 50$ GeV, (b) $p_{\mathrm{T}}^{\mathrm{miss}} > 100$ GeV, (c) $p_{\mathrm{T}}^{\mathrm{miss}} > 150$ GeV, and (d) $p_{\mathrm{T}}^{\mathrm{miss}} > 200$ GeV.

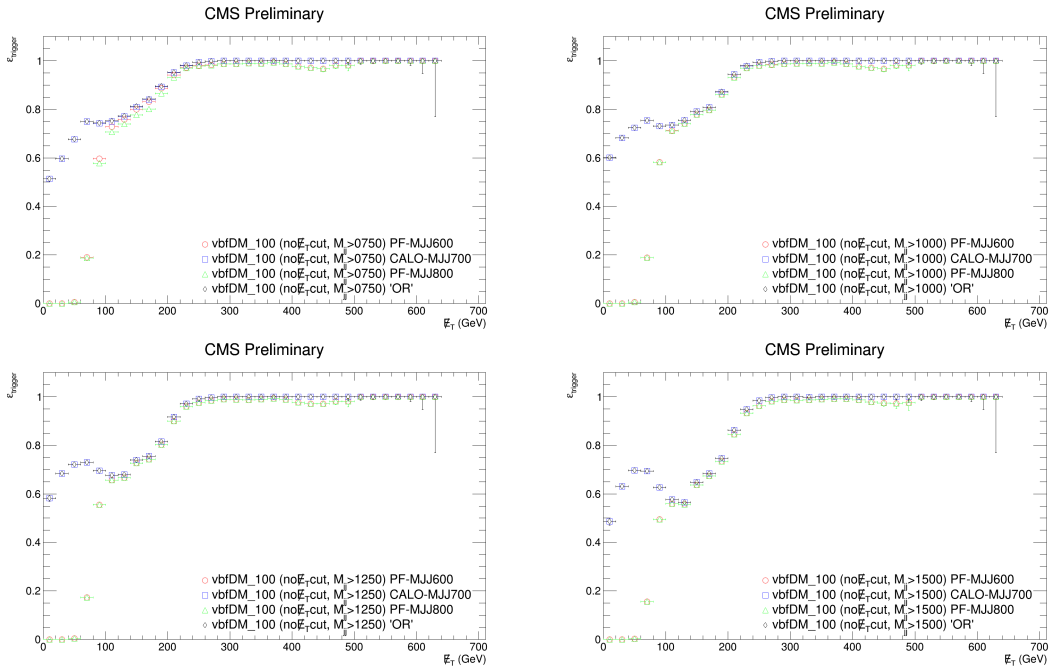


Figure 6.10: $\varepsilon_{\text{VBF\_trigger}}$ vs. $p_{\text{T}}^{\text{miss}}$ for $\tilde{\chi}_1^0\tilde{\chi}_1^0 jj$ with LSP mass of 100 GeV given (a) $m_{jj} >$ 750 GeV, (b) $m_{jj} > 1000$ GeV, (c) $m_{jj} > 1250$ GeV, and (d) $m_{jj} > 1500$ GeV.

Figure 6.11 shows the trigger efficiency for each individual trigger in addition to the "OR" trigger configuration as a function of $m_{jj}$ given various $p_{\mathrm{T}}^{\mathrm{miss}}$ cuts for the $\mathrm{Z}(\rightarrow \nu\bar{\nu})$ + jets MC sample. When $\mathrm{Z}(\rightarrow \nu\bar{\nu})$ + jets are considered, the PF-based trigger again shows a faster $m_{jj}$ trigger efficiency turn-on curve. Figure 6.12 shows the trigger efficiency for each individual trigger and the "OR" trigger configuration as a function of $p_{\mathrm{T}}^{\mathrm{miss}}$ given various $m_{jj}$ cuts for the $\mathrm{Z}(\rightarrow \nu\bar{\nu})$ + jets MC sample. As before, the CALO-based trigger performs better in the $p_{\mathrm{T}}^{\mathrm{miss}}$ distribution, showing a faster turn-on curve.

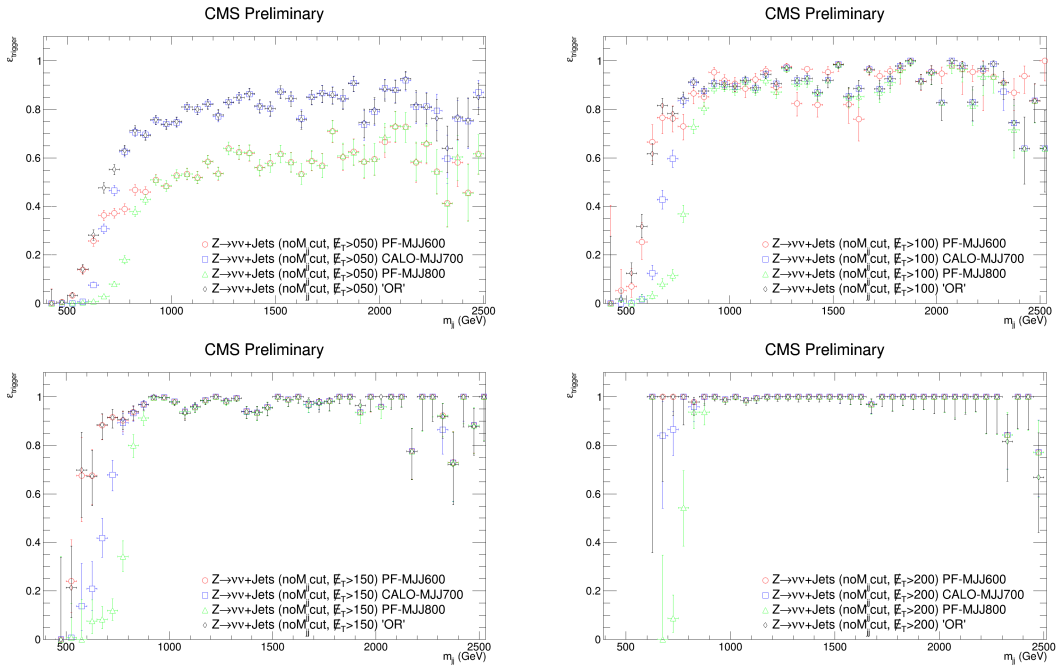


Figure 6.11: $\varepsilon_{\mathrm{VBF\_trigger}}$ vs. $m_{jj}$ for $\mathrm{Z}(\rightarrow \nu\bar{\nu})$ + jets MC sample given (a) $p_{\mathrm{T}}^{\mathrm{miss}} > 50$ GeV, (b) $p_{\mathrm{T}}^{\mathrm{miss}} > 100$ GeV, (c) $p_{\mathrm{T}}^{\mathrm{miss}} > 150$ GeV, and (d) $p_{\mathrm{T}}^{\mathrm{miss}} > 200$ GeV.

A consistent trend is seen in the performance of the PF-based and CALO-based triggers. The PF-based trigger yields a faster turn-on curve for the $m_{jj}$ distribution. On the other hand, the CALO-based triggers performs better – as evidenced by the faster turn-on curve – for the $p_{\mathrm{T}}^{\mathrm{miss}}$ distribution. This complementary behaviour in the performance of both kinds of triggers suggests the use of all three VBF triggers in an "OR" configuration.

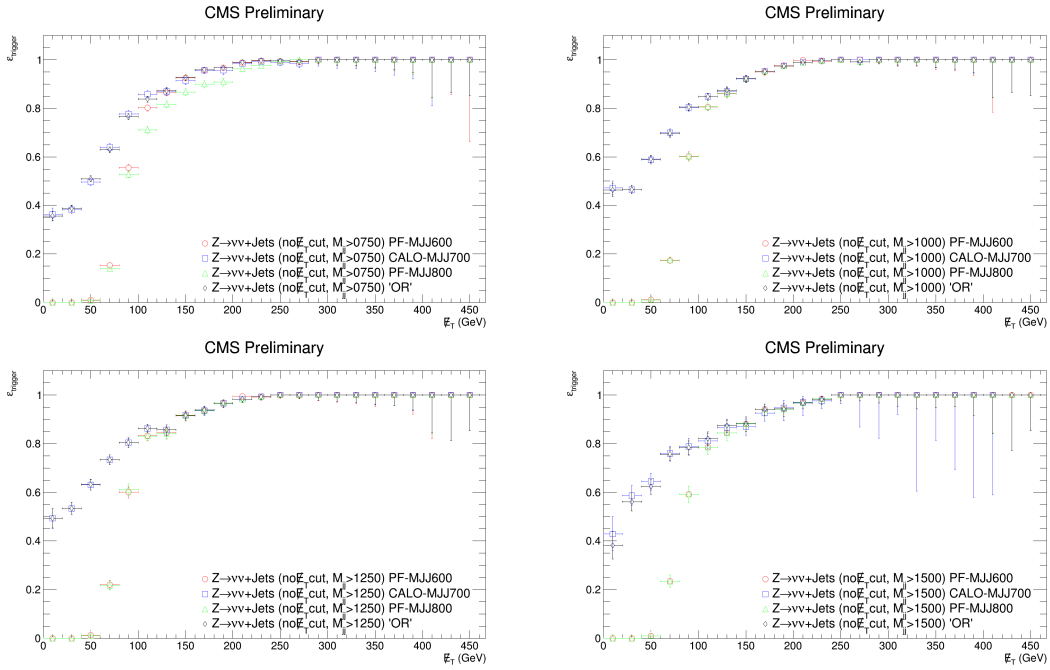


Figure 6.12: $\varepsilon_{\text{VBF\_trigger}}$ vs. $p_{\text{T}}^{\text{miss}}$ for $\text{Z}(\rightarrow \nu\bar{\nu})$ + jets MC sample given (a) $m_{jj} > 750$ GeV, (b) $m_{jj} > 1000$ GeV, (c) $m_{jj} > 1250$ GeV, and (d) $m_{jj} > 1500$ GeV.

### 6.1.2 VBF Trigger Performance in Data Events

Figures 6.2 and 6.4 show consistency between the trigger efficiency curves for $\text{Z}(\rightarrow \nu\bar{\nu})$ + jets and $\widetilde{\chi}_1^0\widetilde{\chi}_1^0 jj$ MC samples. This similarity motivates using a $Z \rightarrow \mu\mu$+Jets control region to estimate the performace of the trigger under data events. The same selection criteria used to study the trigger efficiency with MC samples is imposed, except a muon pair is required instead of a muon veto. Further, the $p_T$ of the muon pair is included in the $p_{\text{T}}^{\text{miss}}$ computation (i.e. the muons are treated as neutrinos). The trigger efficiency is estimated by taking the ratio of events surviving the **HLT_IsoMu24_eta2p1_v*** SingleMu trigger and VBF triggers in "OR" divided by the number of events surviving only the SingleMu trigger.

Figures 6.13 show the trigger efficiency as a function of $m_{jj}$ given various $p_{\text{T}}^{\text{miss}}$ cuts for both $\text{Z}(\rightarrow \nu\bar{\nu})$ + jets MC and data events. Figures 6.14 show the trigger efficiency as a function of $p_{\text{T}}^{\text{miss}}$ given various $m_{jj}$ cuts for both $\text{Z}(\rightarrow \nu\bar{\nu})$ + jets MC and data events. These plots demonstrate resonable agreement from modelling the trigger performance of

data events with a $Z \to \mu\mu$+Jets control sample, where the muons are treated as neutrinos. In addition to guiding the the final event selection, the level of agreement between the trigger curves for data and simulation may be used to assign a systematic uncertainty on the trigger efficiency.

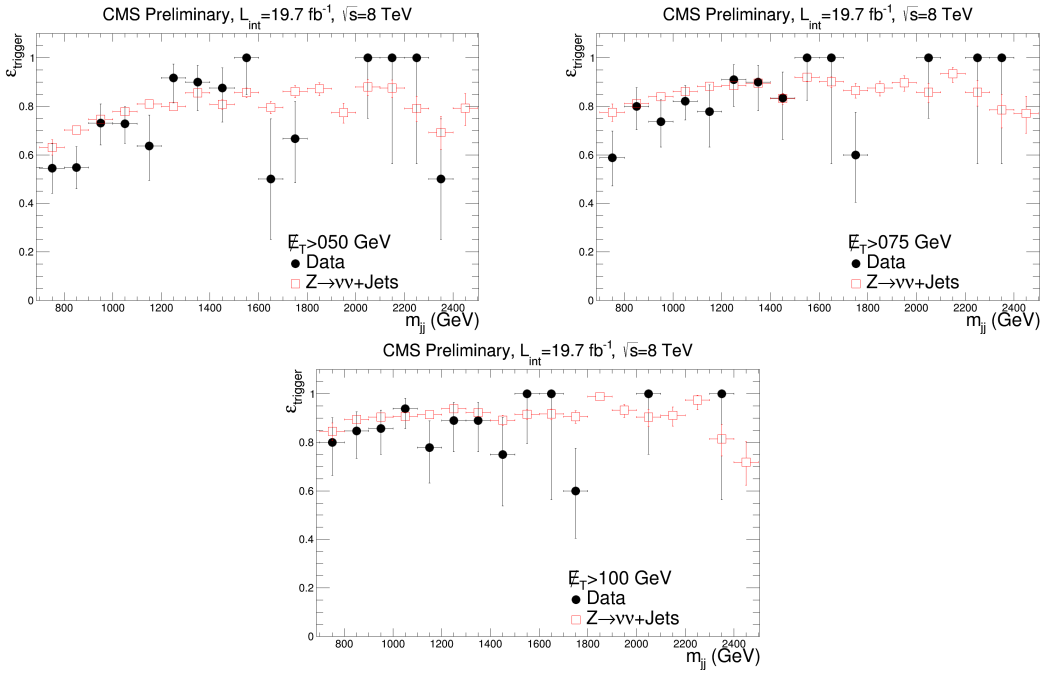


Figure 6.13: $\varepsilon_{\text{VBF\_trigger}}$ vs. $m_{jj}$ for $\text{Z}(\to \nu\bar{\nu})$ + jets MC and data events given (a) $p_{\text{T}}^{\text{miss}} > 50$ GeV, (b) $p_{\text{T}}^{\text{miss}} > 75$ GeV, and (c) $p_{\text{T}}^{\text{miss}} > 100$ GeV.

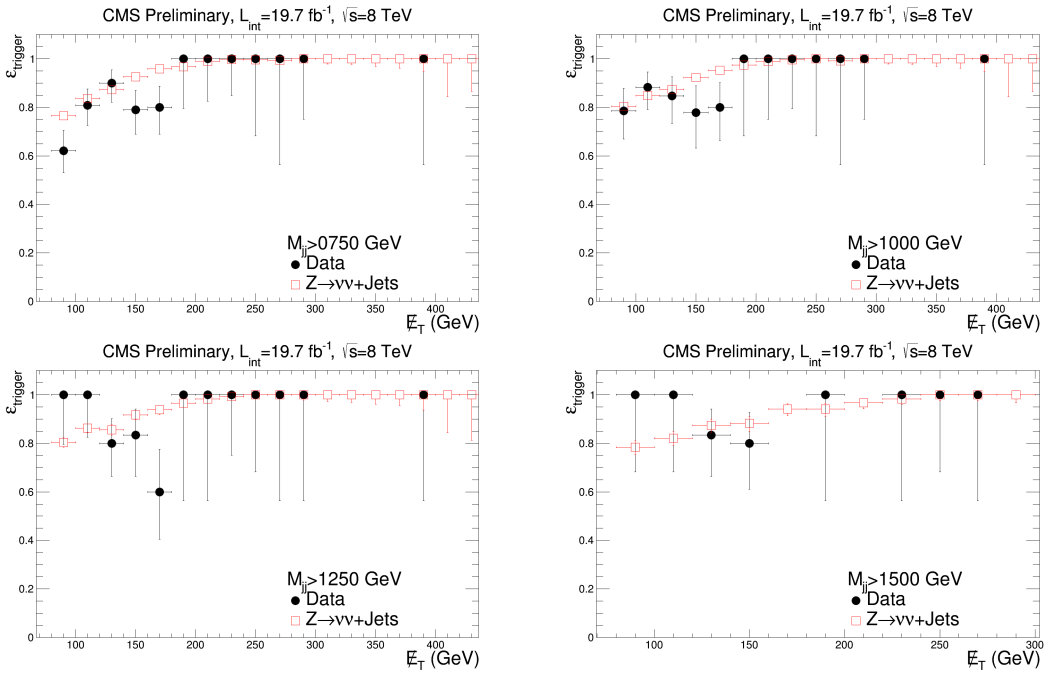


Figure 6.14: $\varepsilon_{\text{VBF\_trigger}}$ vs. $p_{\text{T}}^{\text{miss}}$ for $\text{Z}(\rightarrow \nu\bar{\nu})$ + jets MC and data events given (a) $m_{jj} >$ 750 GeV, (b) $m_{jj} > 1000$ GeV, (c) $m_{jj} > 1250$ GeV, and (d) $m_{jj} > 1500$ GeV.

# Chapter 7

# Event Selection

The main sources of background are $Z(\rightarrow \nu\bar{\nu})$ + jets, $W(\rightarrow l\nu)$ + jets, and a significantly smaller contribution from QCD multijet, $t\bar{t}$, and diboson production. The $Z(\rightarrow \nu\bar{\nu})$ + jets background has the same topology as the signal, and is mostly irreducible. Leptons in $W(\rightarrow l\nu)$ + jets events that fail the veto identification criteria contribute to the $p_T^{miss}$ in the event, making this process an important background in the search.

## 7.1 Event Selection

As mentioned in section 1, the VBF topology is characterized by the presence of two energetic jets in the forward direction, in opposite hemispheres, and with large dijet invariant mass. Candidate signal events are recorded with dedicated trigger conditions that require events to satisfy $p_T^{miss} > 65$ GeV and contain two jets with $p_T > 35$ GeV in the VBF topology. Events firing the **DiJet35_MJJ700_AllJets_DEta3p5_VBF_v***, or **HLT_DiPFJet40_PFMETnoMu65_MJJ600VBF_LeadingJets_v***, or **HLT_DiPFJet40_PFMETnoMu65_MJJ800VBF_AllJets_v*** triggers are pre-selected for final analysis.

These events must satisfy a light lepton veto by requiring exactly zero isolated "global" muon candidates, and zero electrons candidates, with $p_T > 10$ GeV and $|\eta| < 2.5$ passing the "Veto" working point. We require the sum of the $p_T$ of all PF charged and neutral candidates (excluding the lepton $p_T$) within $\Delta R = 0.3$ of the lepton track, divided by the lepton $p_T$ to be less than 20%. In order to suppress backgrounds from $W \rightarrow \tau\nu$, events are required to have exactly zero reconstructed HPS taus passing the decay mode finding criteria, passing the "VLoose" isolation working point, and having $p_T > 15$ GeV and $|\eta| < 2.5$.

The "Loose" pileup jet ID is used to enforce exactly two jets with $p_T > 50$ GeV and

$|\eta| < 5$, and veto events with additional jets with $p_{\mathrm{T}} > 30$ GeV. This additional jet rejection will be referred to as additional jet veto (AJV). In order to further suppress QCD light quark and gluon multijet backgrounds, the absolute value of the azimuthal separation between the sub-leading jet and the $\vec{E}_{\mathrm{T}}^{\mathrm{miss}}$ vector in events is required to satisfy $|\Delta\phi(p_{\mathrm{T}}^{\mathrm{miss}}, j_2)| > 0.5$. In order to reduce top-quark contamination, we require the event to have zero jets identified as a b-quark jet by the b-tagging algorithms using the combined secondary vertex loose (CSVL) working point. Only jets with $p_{\mathrm{T}}$ greater than 20 GeV are examined for b-tags.

Finally, the *VBF selections* are imposed by requiring the two jets to be in opposite halves of the detector ($\eta_1 \cdot \eta_2 < 0$), well separated in pseudorapidity ($|\Delta\eta| > 4.2$), and with $m_{jj} > 750$ GeV. The jet $p_{\mathrm{T}}$, $\Delta\eta$, and $m_{jj}$ requirements defining the search region are chosen to achieve a trigger efficiency greater than 98% in order to avoid systematic errors due to trigger inefficiency.

Figures 7.1-7.2 show the VBF related distributions for $\mathrm{Z}(\rightarrow \nu\bar{\nu})$ + jets and $\widetilde{\chi}\widetilde{\chi}jj$ (for $m(\widetilde{\chi}_1^0) = 100$ GeV) simulated samples. As expected, the jets in $\mathrm{Z}(\rightarrow \nu\bar{\nu})$ simulated events are mostly central and have small dijet invariant masses. On the other hand, the simulated signal events are characterized by high-$p_{\mathrm{T}}$ forward jets with large dijet invariant masses. The plots illustrate the remarkable discriminting power of the VBF topology. It is easy to estimate by eye which selections or cuts would reject a vast number of background events while maintaining a good acceptance of signal events. Thus, the VBF selections are expected to provide a drastic reduction in the contribution from background events.

### 7.1.1 Optimization

The requirement of $m_{jj} > 750$ GeV is driven by the performance of the VBF trigger. Instead of optimizing the VBF dijet mass cut and considering a larger threshold, the strategy was to carry out a shape-based analysis by fitting the data to the predicted VBF dijet mass spectrum. The invariant mass of the dijet spectrum is used to look for a potential disagreement between data and simulation and, in this manner, determine the sensitivity

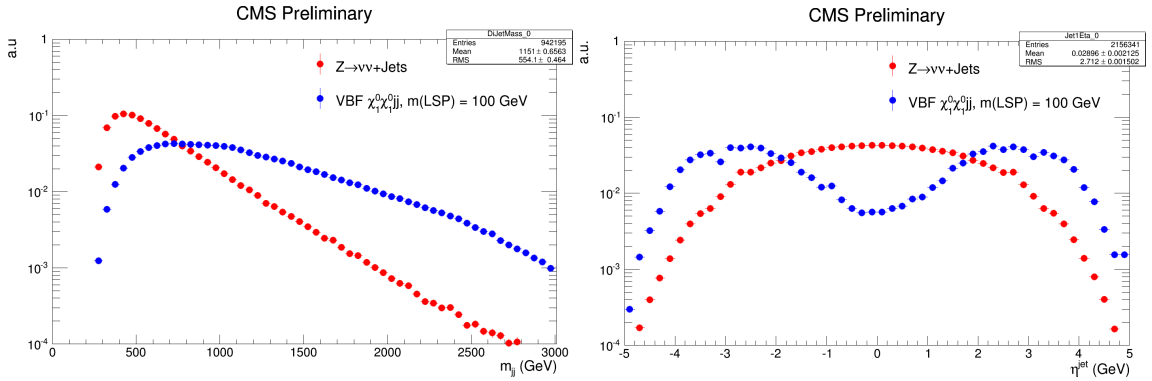


Figure 7.1: (a) $m_{jj}$, and (b) $\eta^{jet}$ distributions for $Z(\rightarrow \nu\bar{\nu})$ + jets and $\tilde{\chi}\tilde{\chi}jj$ surviving the selections detailed in section 6.1.

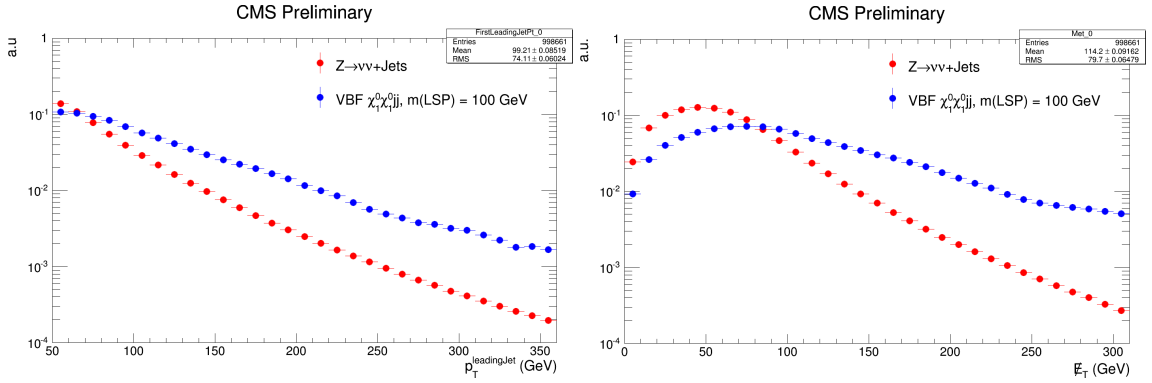


Figure 7.2: (a) leading jet $p_{\mathrm{T}}$, and (b) $p_{\mathrm{T}}^{\mathrm{miss}}$ distributions for $Z(\rightarrow \nu\bar{\nu})$ + jets and $\tilde{\chi}\tilde{\chi}jj$ surviving the selections detailed in section 6.1.

of the analysis. Since the jet $p_{\mathrm{T}}$ and $\Delta\eta$ requirements are strongly correlated with $m_{jj}$, $m_{jj} \sim \sqrt{2p_T^{j_1}p_T^{j_2}}e^{\frac{1}{2}\Delta\eta}$, the optimization of the VBF selections are encompassed by the fit of the dijet mass spectrum. Therefore, in this section we only discuss the optimization of the $p_{\mathrm{T}}^{\mathrm{miss}}$ selection.

The studies were performed by considering the $\tilde{b}_1\tilde{b}_1jj$ signal samples and choosing the $p_{\mathrm{T}}^{\mathrm{miss}}$ cut that produced the best 95% C.L. upper limit on the mass of the lightest bottom squark, $m(\tilde{b}_1)$. Figure 7.3(a) shows the expected upper limit on the cross-section (using the $m_{jj}$ shape) as a function of $m(\tilde{b}_1)$ for the baseline selections outlined in the previous section. It indicates the potential to exclude $\tilde{b}_1$ masses up to $\sim$ 300 GeV, and thus suggests

optimizing the $p_{\mathrm{T}}^{\mathrm{miss}}$ cut at $m(\tilde{b}_1) = 300$ GeV.

A range of missing transverse momentum requirements between 75 and 400 GeV were studied. Starting with the baseline selections outlined in section 7, the dijet mass distribution yields in the SR are calculated for $\tilde{b}_1\tilde{b}_1 jj$, Z($\rightarrow \nu\bar{\nu}$) + jets, and W+jets. These yields were then scaled down by a "$p_{\mathrm{T}}^{\mathrm{miss}}$ cut efficiency" factor, defined as:

$$\varepsilon_{p_{\mathrm{T}}^{\mathrm{miss}}} = \frac{\text{events } (p_{\mathrm{T}}^{\mathrm{miss}} > X)}{\text{events } (p_{\mathrm{T}}^{\mathrm{miss}} > 75)} \tag{7.1}$$

where the numerator, events $(p_{\mathrm{T}}^{\mathrm{miss}} > X)$, corresponds the number of events surviving a $p_{\mathrm{T}}^{\mathrm{miss}} > X$ GeV cut, and the denominator, events $(p_{\mathrm{T}}^{\mathrm{miss}} > 75)$, corresponds to the number of events surviving the baseline cut of $p_{\mathrm{T}}^{\mathrm{miss}} > 75$ GeV.

Figure 7.3(b) plots the "$p_{\mathrm{T}}^{\mathrm{miss}}$ cut efficiency" factor as a function of the respective $p_{\mathrm{T}}^{\mathrm{miss}}$ cut for the main backgrounds and two benchmark signal samples. As the $p_{\mathrm{T}}^{\mathrm{miss}}$ cut increases, $\varepsilon_{p_{\mathrm{T}}^{\mathrm{miss}}}$ for signal is consistently larger compared to the corresponding scale factor for the main backgrounds ($S/B$ increases for larger $p_{\mathrm{T}}^{\mathrm{miss}}$ cuts). Although an improved Signal-to-Background ratio doesn't necessarily result in an improved upper limit, Figure 7.3 suggests the optimal $p_{\mathrm{T}}^{\mathrm{miss}}$ cut to be more stringent than the baseline criteria of $p_{\mathrm{T}}^{\mathrm{miss}} > 75$ GeV. Figures 7.4 and 7.5 illustrate the reduction in the $m_{jj}$ yield due to the application of the "$p_{\mathrm{T}}^{\mathrm{miss}}$ cut efficiency" scale factor for several $p_{\mathrm{T}}^{\mathrm{miss}}$ cuts.

The *Higgs Limit Tool* was employed to determine the optimal $p_{\mathrm{T}}^{\mathrm{miss}}$ cut (detailed information on the Higgs Limit Tool is available in Ref. [90]). The $m_{jj}$ distribution yields were divided into 100 GeV bins to create "limit cards" (one data card per bin). Such "limit cards" contain the event yield for each process being considered in addition to the main sources of assigned systematics. The cards were then merged into a single card (one card per signal mass point) and processed by the Higgs Limit Tool using the Asymptotic likelihood method [91]. The Higgs limit tool propagates the systematic uncertainties for each process and calculates the 95% C.L. upper limit on the signal cross section. Figure 7.6

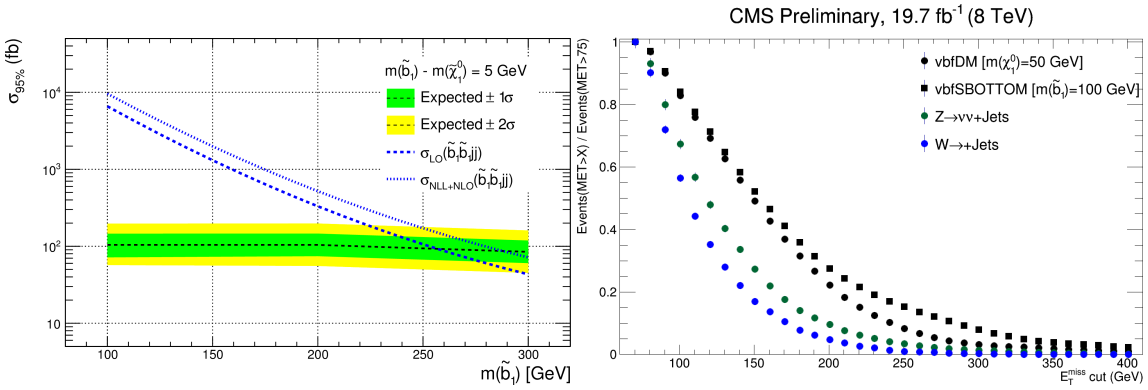


Figure 7.3: (a) $\sigma$ (fb) vs. $m(\tilde{b}_1)$ for $p_{\mathrm{T}}^{\mathrm{miss}} > 75$ GeV. (b) "$p_{\mathrm{T}}^{\mathrm{miss}}$ cut efficiency" scaling factor vs $p_{\mathrm{T}}^{\mathrm{miss}}$ cut

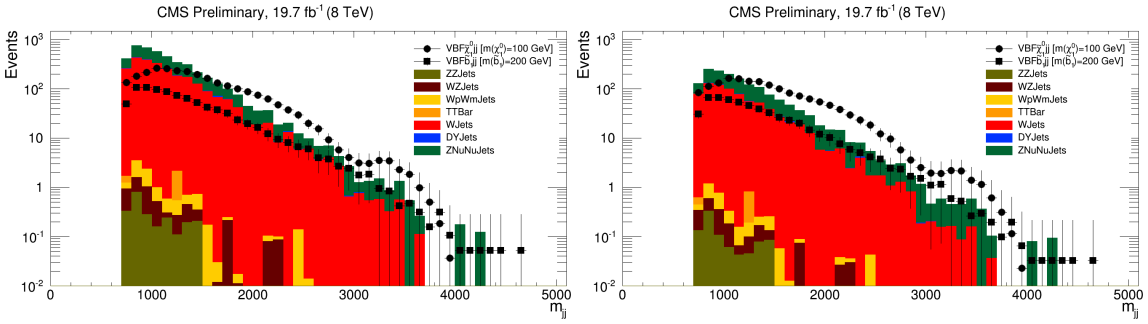


Figure 7.4: (a) $p_{\mathrm{T}}^{\mathrm{miss}} > 100$ GeV, and (b) $p_{\mathrm{T}}^{\mathrm{miss}} > 150$ GeV. Note how the simulated background events are rejected by larger amounts than the simulated signal events as the $p_{\mathrm{T}}^{\mathrm{miss}}$ cut is increased.

shows the 95% C.L. upper limit on the signal cross-section as a function of the corresponding $p_{\mathrm{T}}^{\mathrm{miss}}$ cut for $m(\tilde{b}_1) = 300$, and $\Delta M = m(\tilde{b}_1) - m(\tilde{\chi}^0) = 5$ GeV signal sample. Given that an optimal $p_{\mathrm{T}}^{\mathrm{miss}}$ cut will minimize the upper limit on the cross-section, we conclude that a $p_{\mathrm{T}}^{\mathrm{miss}} > 250$ GeV will optimize the signal significance for the compressed sbottom scenario.

### 7.1.2 Signal Selections

Finally, the signal region is defined by the following selections, applied in succession:

- Trigger pre-selection ('OR'):

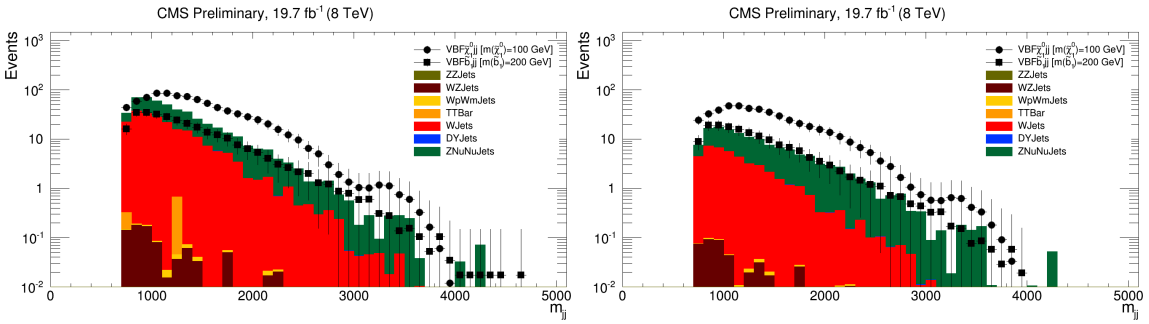


Figure 7.5: (a) $p_{\mathrm{T}}^{\mathrm{miss}} > 200$ GeV, and (b) $p_{\mathrm{T}}^{\mathrm{miss}} > 250$ GeV. Note how the simulated background events are rejected by larger amounts than the simulated signal events as the $p_{\mathrm{T}}^{\mathrm{miss}}$ cut is increased.

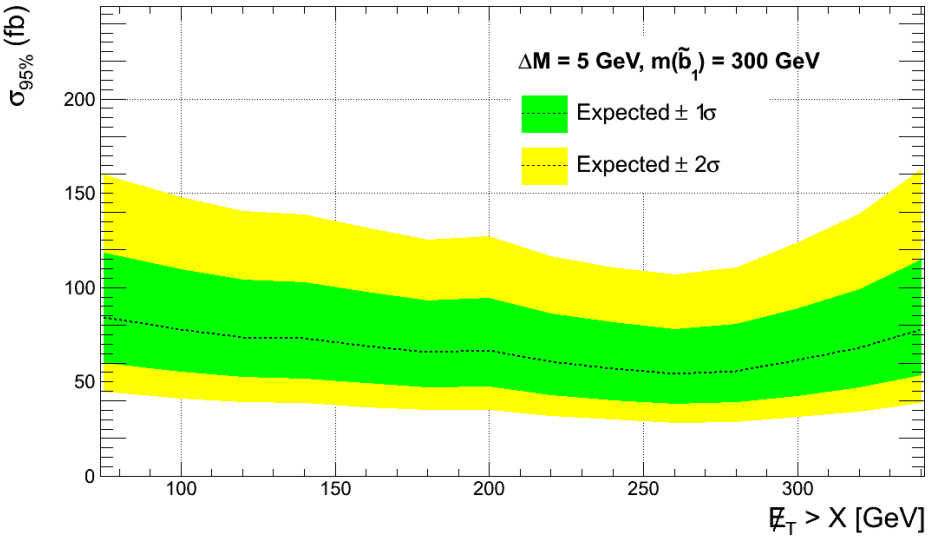


Figure 7.6: $\sigma_{95\%}$ (fb) vs. $p_{\mathrm{T}}^{\mathrm{miss}}$ cut for $m(\tilde{b}_1) = 300$ GeV.

- DiJet35_MJJ700_AllJets_DEta3p5_VBF_v*
- HLT_DiPFJet40_PFMETnoMu65_MJJ600VBF_LeadingJets_v*
- HLT_DiPFJet40_PFMETnoMu65_MJJ800VBF_AllJets_v*

• *L*Vetos:

- Veto electrons with $p_T^e > 10$ GeV, $|\eta_e| < 2.5$, and passing the "Veto" working point
- Veto isolated "Loose" muons with $p_T^\mu > 10$ GeV and $|\eta_\mu| < 2.5$

- Veto HPS taus with $p_T^{\tau} > 15$ GeV passing decay mode finding and MVA-based VLoose isolation

- *L*Vetos+2j:
  - e/$\mu$/$\tau$ vetoes
  - 2 jets with $p_T^j > 50$ GeV and $|\eta_j| < 5.0$
  - Veto events with additional jets with $p_T^j > 30$ GeV (loose pileup jet ID is used)
    - This requirement will be referred to as the additional jet veto (AJV).

- $L/b$Vetos+2j:
  - e/$\mu$/$\tau$ vetoes
  - 2 jet requirement
  - Veto events with a b-tagged jet of $p_T^j > 20$ GeV and $|\eta_j| < 2.4$ using CSVL

- $E_T^{miss}$:
  - e/$\mu$/$\tau$/b-jet vetoes
  - 2 jet requirement
  - $E_T^{miss} > 250$ GeV

- VBFcuts:
  - e/$\mu$/$\tau$/b-jet vetoes
  - $E_T^{miss} > 250$ GeV
  - 2 *VBF-tagged* jets with $p_T^j > 50$ GeV, $|\eta_j| < 5.0$, veto events with additional jets with $p_T^j > 30$ GeV, $m_{jj} > 750$ GeV, $|\Delta\eta_{jj}| > 4.2$, $\eta_{j1} \cdot \eta_{j2} < 0$

- DeltaPhi:
  - $|\Delta\phi(p_{\mathrm{T}}^{\mathrm{miss}}, j_2)| > 0.5$

# Chapter 8

# Background Estimates

## 8.1 $Z(\rightarrow \nu\bar{\nu})$ + jets Background Estimate

$Z(\rightarrow \nu\bar{\nu})$ + jets processes are one of the main sources of background to the analysis since they exhibit the same final state as the signal of interest. Note that this background can have contributions from both Z+VBF jets events or Z+ISR jets events, but these two sub-processes are not distinguished when carrying out this estimate. The contribution from this background is determined by applying similar selection criteria to those used in the final analysis to obtain a sample of $Z(\rightarrow \mu^+\mu^-)$ + jets events with two clean muons. We define several "Z control regions" in order to carry out the background estimate, with similar kinematic requirements as the signal region.

The overall strategy for the background estimate proceeds as follows: Starting from the signal region selections, we replace the muon veto with a $Z(\rightarrow \mu^+\mu^-)$ requirement (two high-quality oppositely-charged muons with $p_{\mathrm{T}} > 30$ GeV and with $60 < m(\mu^+\mu^-) < 120$ GeV), maintain the veto on the additional leptons, and recompute the $p_{\mathrm{T}}^{\mathrm{miss}}$ after subtracting the $p_T(Z_{\mu^+\mu^-})$ in order to treat the muon pair as neutrinos and properly model the large $p_{\mathrm{T}}^{\mathrm{miss}}$ values associated with $Z(\rightarrow \nu\bar{\nu})$ + jets events. It is easier to obtain a clean sample of $Z(\rightarrow \mu^+\mu^-)$ + jets events due to the low probability for jets to fake muons. Once a clean control sample of $Z(\rightarrow \mu^+\mu^-)$ + jets events is obtained, the VBF efficiencies for $Z(\rightarrow \nu\bar{\nu})$ + jets can be measured and the level of agreement between data and MC for non-VBF related distributions is used to validate good modeling of the central selections (for all cuts except the VBF selections).

Three control regions are defined for various stages of the cut flow in order to factorize scale factors and gauge the level of agreement between data and MC for the lepton selections (including the vetos), validate the modeling of $p_{\mathrm{T}}^{\mathrm{miss}}$, and perform a measurement of

the VBF efficiency.

The first control region (Z_CR1) is obtained by replacing the muon veto with a requirement of exactly two muons while maintaining the veto for additional leptons and b-jets. The $p_{\mathrm{T}}^{\mathrm{miss}}$ and VBF-tag requirements are dropped in this control region. Such a control region allows us to validate our expectation that the MC does indeed correctly model the acceptance and shapes for this background after the central selections. Figure 8.1 shows non-VBF-related distributions obtained for events passing the above selections. One can see that both the shapes and event rates for the central selections/variables between data and MC are consistent. Table 8.1 lists the predicted and observed rates in Z_CR1. The measured data-to-MC scale factor is SF(Z_CR1)$= 0.98 \pm 0.01$.

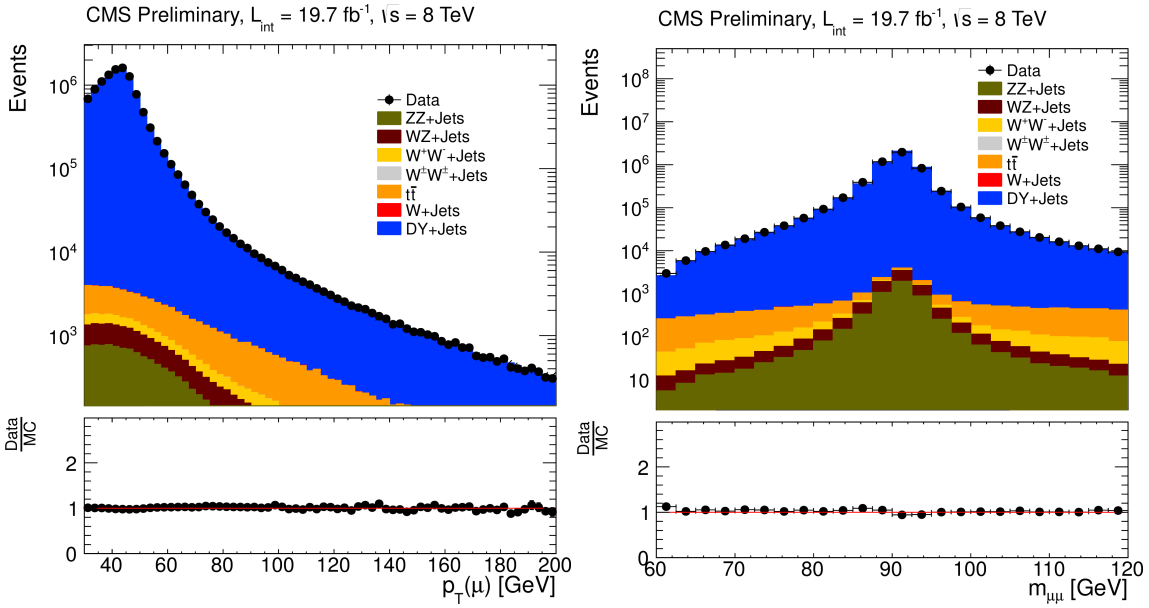


Figure 8.1: (a) Muon $p_{\mathrm{T}}$ distribution, (b) Reconstructable $m_{\mu^+\mu^-}$ distribution in Z_CR1. Note that both the shapes and event rates between data and MC are consistent, indicating good modelling of the central selections/variables.

Further confidence in this conclusion is achieved by defining a second control region (Z_CR2) with the same selections as Z_CR1, but recomputing the $p_{\mathrm{T}}^{\mathrm{miss}}$ after subtracting the $p_T(Z_{\mu^+\mu^-})$ (thereby treating the muons as neutrinos) and requiring $p_{\mathrm{T}}^{\mathrm{miss}} > 250$ GeV. Figure 8.2 shows distributions obtained for events in Z_CR2. Similar to Z_CR1, there is relatively

good agreement between data and MC. The measured scale factor is SF(Z_CR2)$= 0.95 \pm$ 0.06. The level of agreement between the MC and data yields and shapes indicates that treating muons as neutrinos adequately models the $p_{\mathrm{T}}^{\mathrm{miss}}$ spectrum.

Figure 8.3 shows the $p_{\mathrm{T}}^{\mathrm{miss}}$ and $m_{jj}$ distributions obtained for events in Z_CR2. We observe that the VBF shapes/efficiencies are well modeled by simulation for backgrounds with real $p_{\mathrm{T}}^{\mathrm{miss}}$. Backgrounds with fake $p_{\mathrm{T}}^{\mathrm{miss}}$ are driven by jet mis-measurements, typically not well modeled by MC, and thus indirectly show up in the mis-modeling of the VBF efficiencies and shapes. This is not the case here, and thus, the VBF efficiencies and shapes are expected to be fairly well-modeled. However, we choose to directly use the VBF efficiency from data since this approach results in lower systematic uncertainties (no need to propagate the uncertainty on MC).

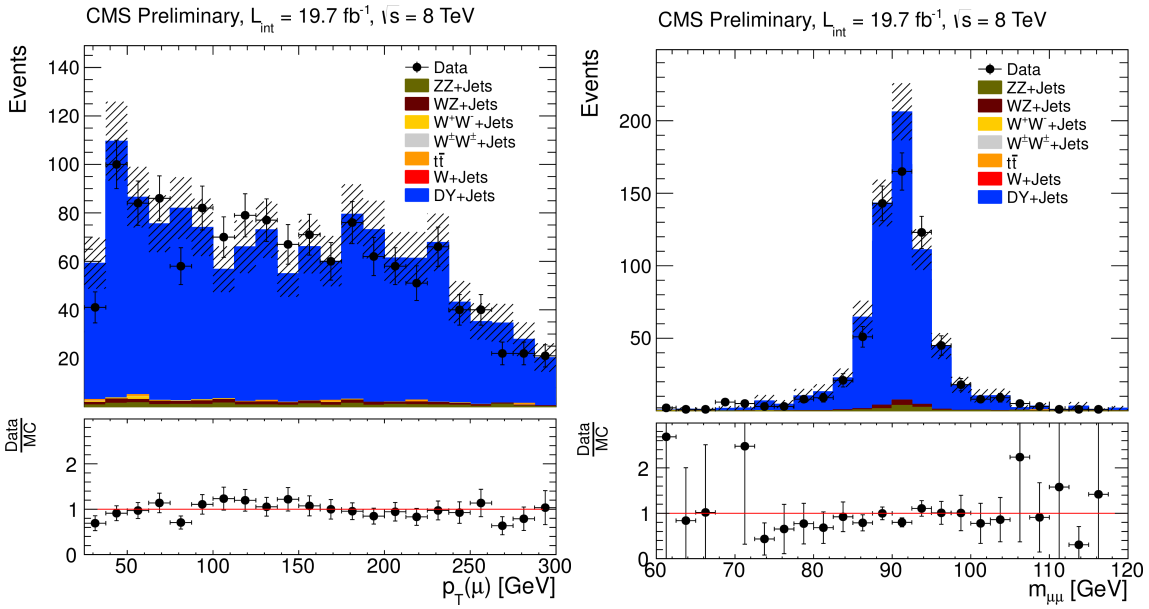


Figure 8.2: (a) Muon $p_{\mathrm{T}}$ distribution, (b) Reconstructable $m_{\mu^+\mu^-}$ distribution in Z_CR2. The resonable consistency between data and MC shapes and event rates indicates good modelling of the $p_{\mathrm{T}}^{\mathrm{miss}}$ by treating muons as neutrinos.

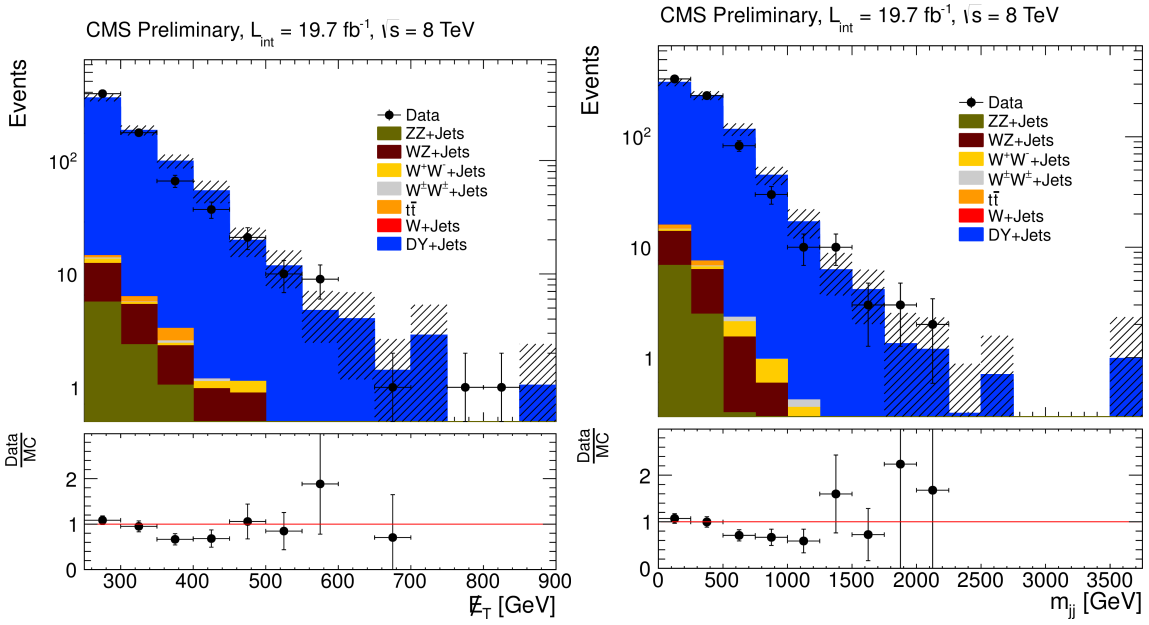


Figure 8.3: (a) $p_{\mathrm{T}}^{\mathrm{miss}}$ distribution, (b) $m_{jj}$ distribution in Z_CR2.

Finally, a third $Z(\to \nu\bar{\nu})$ + jets control region (Z_CR3) is defined by the same selections as Z_CR2, but adding the VBF requirements (2 *VBF-tagged* jets with $p_T^j > 50$ GeV and $|\eta_j| < 5.0$, veto events with additional jets with $p_T^j > 30$ GeV, $m_{jj} > 750$ GeV, $|\Delta\eta_{jj}| > 4.2$, and $\eta_{j1} \cdot \eta_{j2} < 0$). Figure 8.4 shows an adequate level of agreement between data and MC yields in this control region, despite very low statistics, thus validating that the VBF efficiency and correlation with other selections is modeled well by the simulation.

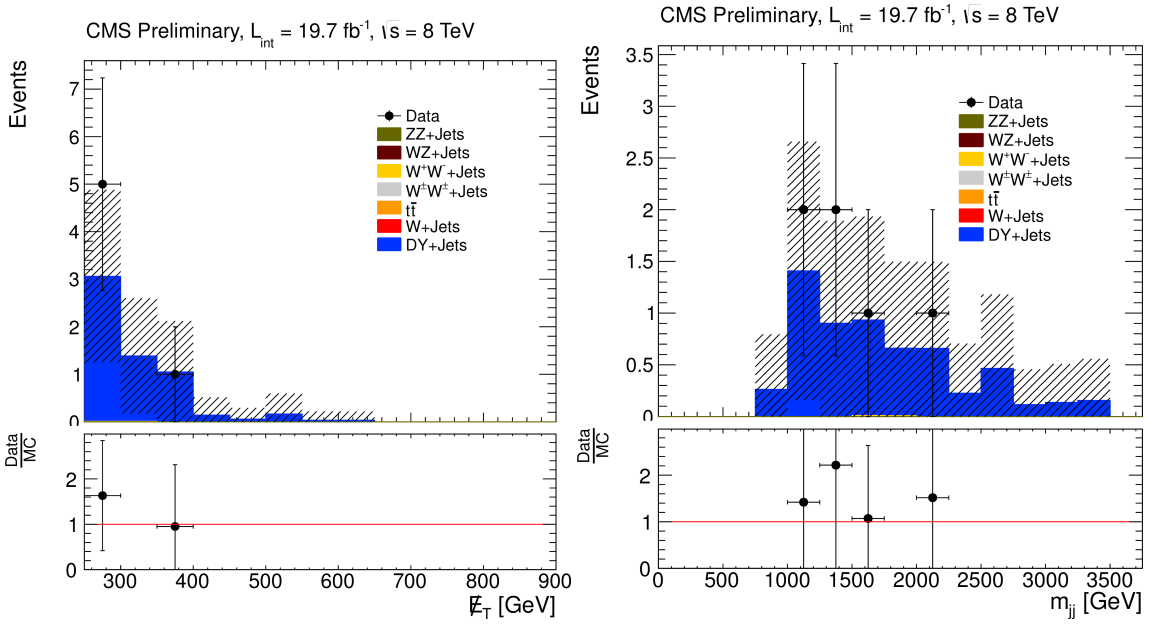


Figure 8.4: (a) $p_{\mathrm{T}}^{\mathrm{miss}}$ distribution, (b) $m_{jj}$ distribution in Z_CR3. Despite very low statistics, there is reasonable agreement in the normalization of the distributions.

The following equation is used to estimate the $Z(\to \nu\bar{\nu})$ + jets background contribution to the signal region:

$$N^{\mathrm{SR}}_{\mathrm{Z}(\to \nu\bar{\nu})\,+\,\mathrm{jets}} = N^{\mathrm{MC}}_{\mathrm{Z}(\to \nu\bar{\nu})\,+\,\mathrm{jets}}(\mathrm{noVBF}) \cdot SF^{\mathrm{Z\_CR2}}_{\mathrm{noVBF}} \cdot \varepsilon^{\mathrm{Z\_CR3}}_{\mathrm{VBF}} \tag{8.1}$$

where $N^{\mathrm{SR}}_{\mathrm{Z}(\to \nu\bar{\nu})\,+\,\mathrm{jets}}$ is the predicted $Z(\to \nu\bar{\nu})$ + jets background rate in the Signal Region, $N^{\mathrm{MC}}_{\mathrm{Z}(\to \nu\bar{\nu})\,+\,\mathrm{jets}}$ (noVBF) the predicted MC $Z(\to \nu\bar{\nu})$ + jets rate without VBF selections, $SF^{\mathrm{Z\_CR2}}_{\mathrm{noVBF}}$ the correction factor for the central selections determined from the Z_CR2, and $\varepsilon^{\mathrm{Z\_CR3}}_{\mathrm{VBF}}$ the efficiency of VBF selections determined from the Z_CR3.

These terms are calculated from each control sample as follows: $SF_{\text{noVBF}}^{\text{Z\_CR2}}$ is calculated by subtracting the total non-Z MC-based background rate from the observed yield in Data for Z_CR2 and dividing by the Z($\rightarrow \mu^+\mu^-$) + jets yield inside Z_CR2:

$$(N_{\text{Data}}^{\text{Z\_CR2}} - \Sigma N_{\text{non-Z}}^{\text{Z\_CR2}})/N_{\text{Z+Jets}}^{\text{Z\_CR2}}. \tag{8.2}$$

Finally, $\varepsilon_{\text{VBF}}^{\text{Z\_CR3}}$ is measured by taking the ratio of the number of events in data inside Z_CR3 and Z_CR2:

$$N_{\text{Data}}^{\text{Z\_CR3}}/N_{\text{Data}}^{\text{Z\_CR2}}. \tag{8.3}$$

The contamination from non-Z backgrounds in the control regions is used to assign a systematic uncertainty on the measured *SF* and VBF efficiency.

Table 8.1 lists the number of observed events in data as well as the expected MC contributions in the control regions. The uncertainties are based on the statistics of the MC samples. The measured data-to-MC scale factor is $0.95 \pm 0.06$. The uncertainty on the correction factor is purely statistical. The level of contamination ($\sim 3\%$) from other background sources is treated as a systematic uncertainty on the correction factor.

Table 8.1: Predicted and observed rates for the Z + jets Control Regions. The yields are used to calculate correction factors for the central selections and measure the VBF selection efficiencies.

| Sample | Z_CR1 | Z_CR2 | Z_CR3 |
|---|---|---|---|
| DY+Jets | $5.1 \cdot 10^6 \pm 4.6 \cdot 10^3$ | $675.3 \pm 35.2$ | $5.6 \pm 2.4$ |
| W+Jets | $99.5 \pm 20.9$ | $0.0^{+2.4}_{-0.0}$ | $0.0^{+2.4}_{-0.0}$ |
| $t\bar{t}$ | $1.7 \cdot 10^4 \pm 158$ | $1.6 \pm 1.4$ | $0.0^{+0.7}_{-0.0}$ |
| VV | $1.3 \cdot 10^4 \pm 115$ | $24.0 \pm 4.9$ | $0.02^{+0.25}_{-0.02}$ |
| Z($\rightarrow \nu\bar{\nu}$) + jets | - | - | - |
| $\Sigma_{MC}$ | $5.16 \cdot 10^6 \pm 4632$ | $700.9 \pm 35.6$ | $5.6 \pm 2.4$ |
| Data | $5.07 \cdot 10^6$ | 666 | 6 |
| Purity | $0.994 \pm 0.001$ | $0.964 \pm 0.0701$ | $0.997 \pm 0.602$ |
| SF | $0.983 \pm 0.001$ | $0.949 \pm 0.0629$ | $1.079 \pm 0.639$ |

## 8.2 $W \to l\nu$ + jets Background Estimate

The $W \to l\nu$ + jets process results in a background in the signal region when the lepton from the decay of the $W$ boson is not reconstructed or identified, either because it falls outside of the geometric acceptance of the detector or it fails the identification criteria and thus survives the lepton veto.

To estimate the W+jets rate in the signal region from unidentified $W$-bosons, we define three control regions with well-identified $W$'s together with jets having similar kinematic properties as the signal region. Specifically, the first W+jets control region (W_CR1) is obtained by replacing the muon veto with a requirement of exactly one muon, and maintaining the veto for additional leptons and b-jets. The $p_{\mathrm{T}}^{\mathrm{miss}}$ and VBF-tag requirements are dropped in this control region. Such a control region allows us to validate our expectation that the MC does indeed correctly model the acceptance and shapes for this background after central selections. Figure 8.5 shows non-VBF-related distributions obtained for events passing the above selections. One can see that both the shapes and event rates for the central selections/variables between data and MC are consistent. Table 8.2 lists the predicted and observed rates in W_CR1. The measured data-to-MC scale factor is nearly consistent with unity, SF(W_CR1)$= 0.97 \pm 0.01$.

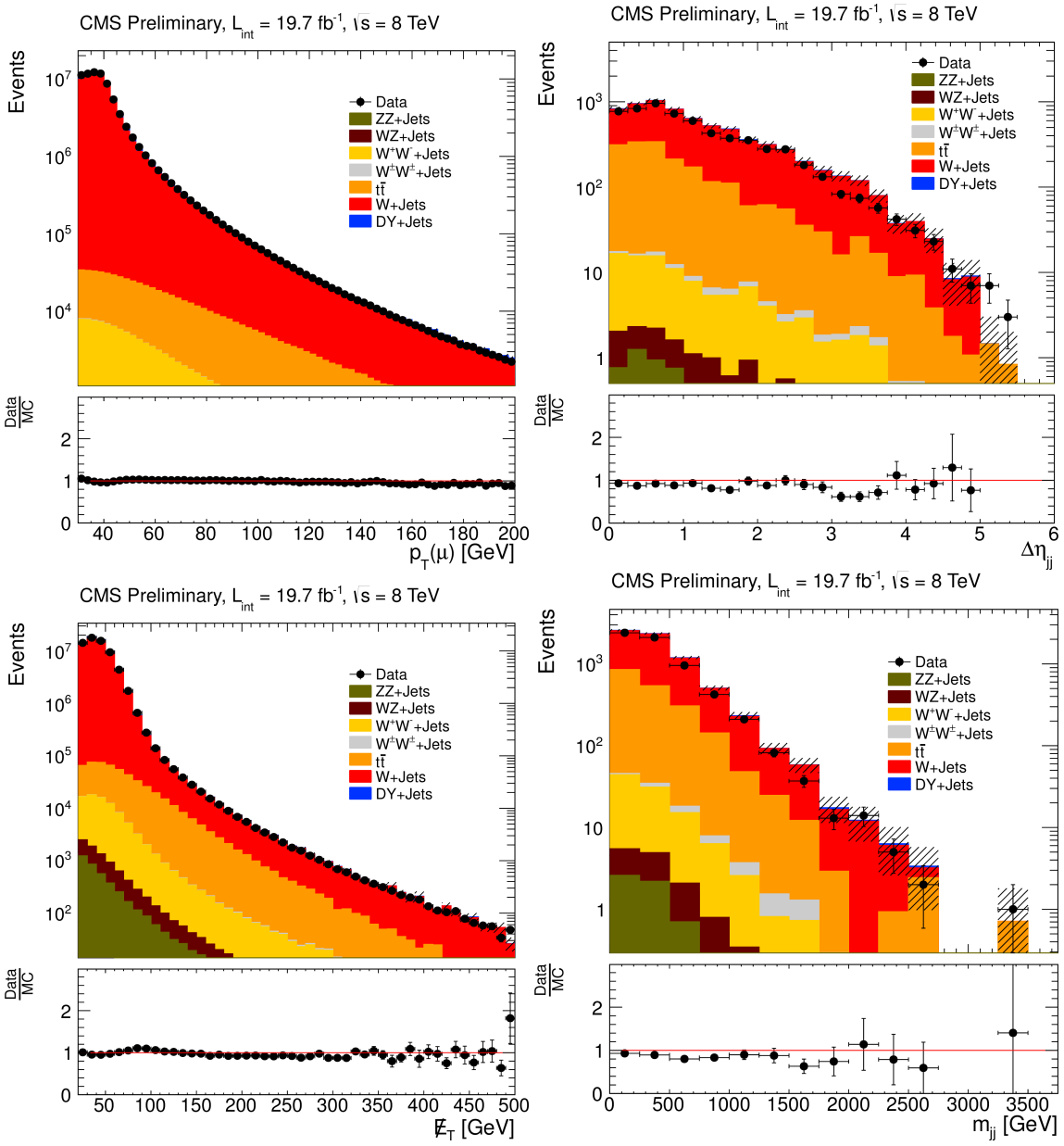


Figure 8.5: (a) Muon $p_{\mathrm{T}}$ distribution, (b) $\Delta\eta_{jj}$ distribution, (c) $p_{\mathrm{T}}^{\mathrm{miss}}$ distribution, and (d) $m_{jj}$ distribution for W+Jets in W_CR1 (require one muon, veto other leptons, invert VBF selections, no $p_{\mathrm{T}}^{\mathrm{miss}}$ requirement). Note that both the shapes and event rates between data and MC are consistent, indicating good modelling of the central selections/variables.

Further confidence in this conclusion is achieved by defining a second control region (W_CR2) with the same selections as W_CR1, but additionally requiring $p_{\mathrm{T}}^{\mathrm{miss}} > 250$ GeV, and also recomputing the $p_{\mathrm{T}}^{\mathrm{miss}}$ after subtracting the $p_T(W_\mu)$ (thereby treating the muon as a neutrino). Figures 8.6(a)-(d) show distributions obtained for events in W_CR2. Similar to W_CR1, the shapes and event rates for the central selections/variables between data and MC are consistent, and the measured data-to-MC scale factor is found to be SF(W_CR2)= $0.80 \pm 0.042$. The level of agreement between the MC and data yields and shapes indicates that treating muons as neutrinos adequately models the $p_{\mathrm{T}}^{\mathrm{miss}}$ spectrum.

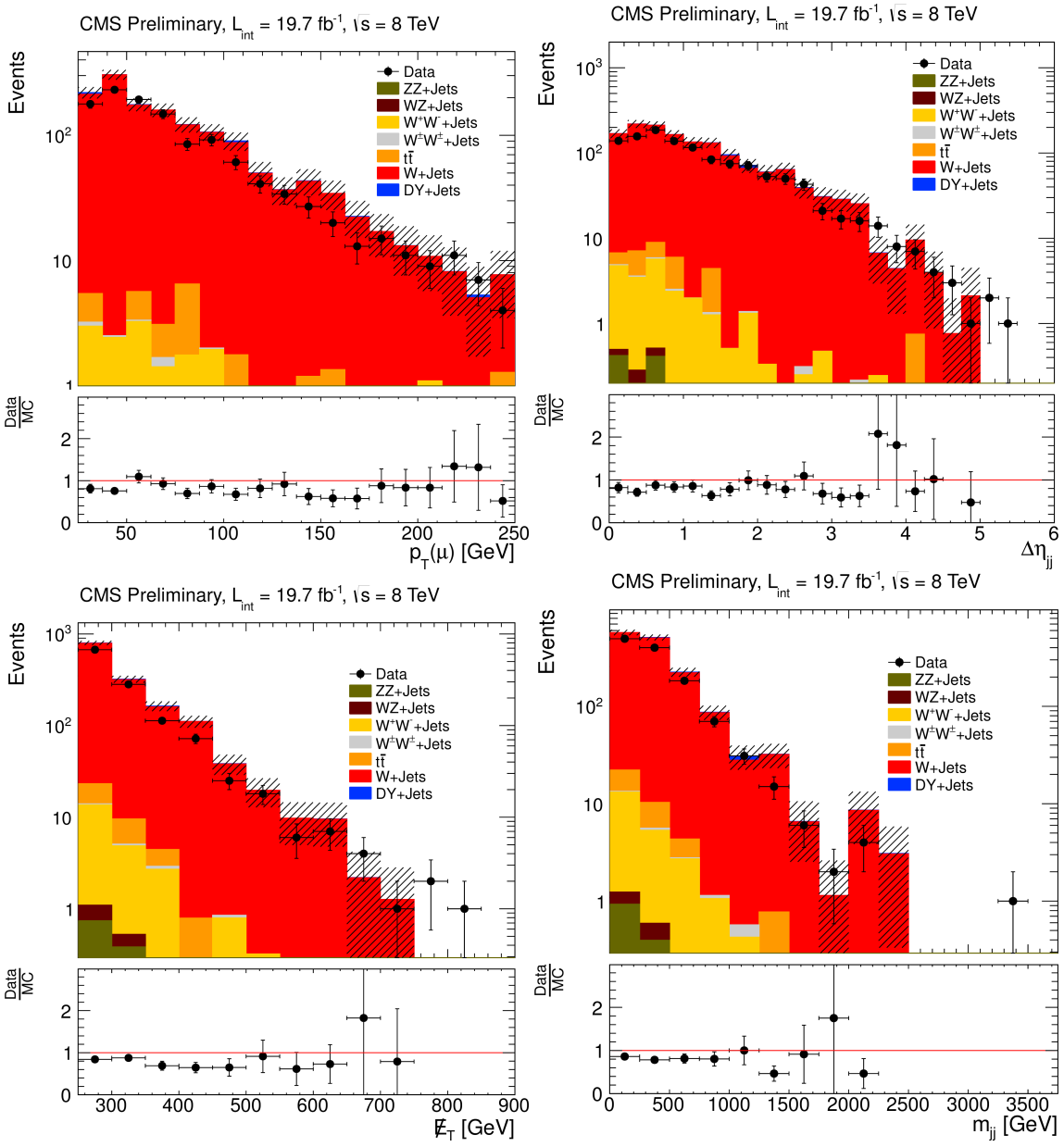


Figure 8.6: (a) Muon $p_{\mathrm{T}}$ distribution, (b) $\Delta\eta_{jj}$ distribution, (c) $p_{\mathrm{T}}^{\mathrm{miss}}$ distribution, and (d) $m_{jj}$ distribution for W+Jets in W_CR2 (require one muon, veto other leptons, invert VBF selections, $p_{\mathrm{T}}^{\mathrm{miss}}$ computed from muons). The resonable consistency between data and MC shapes and event rates indicates good modelling of the $p_{\mathrm{T}}^{\mathrm{miss}}$ by treating muons as neutrinos.

Finally, a third W+jets control region (W_CR3) is defined by the same selections as W_CR2, but adding the VBF requirements (2 *VBF-tagged* jets with $p_T^j > 50$ GeV and $|\eta_j| < 5.0$, veto events with additional jets with $p_T^j > 30$ GeV, $m_{jj} > 750$ GeV, $|\Delta\eta_{jj}| > 4.2$, and $\eta_{j1} \cdot \eta_{j2} < 0$). Figure 8.7 shows an adequate level of agreement between data and MC yields in this control region, despite very low statistics, thus validating that the VBF efficiency and correlation with other selections is modeled well by the simulation.

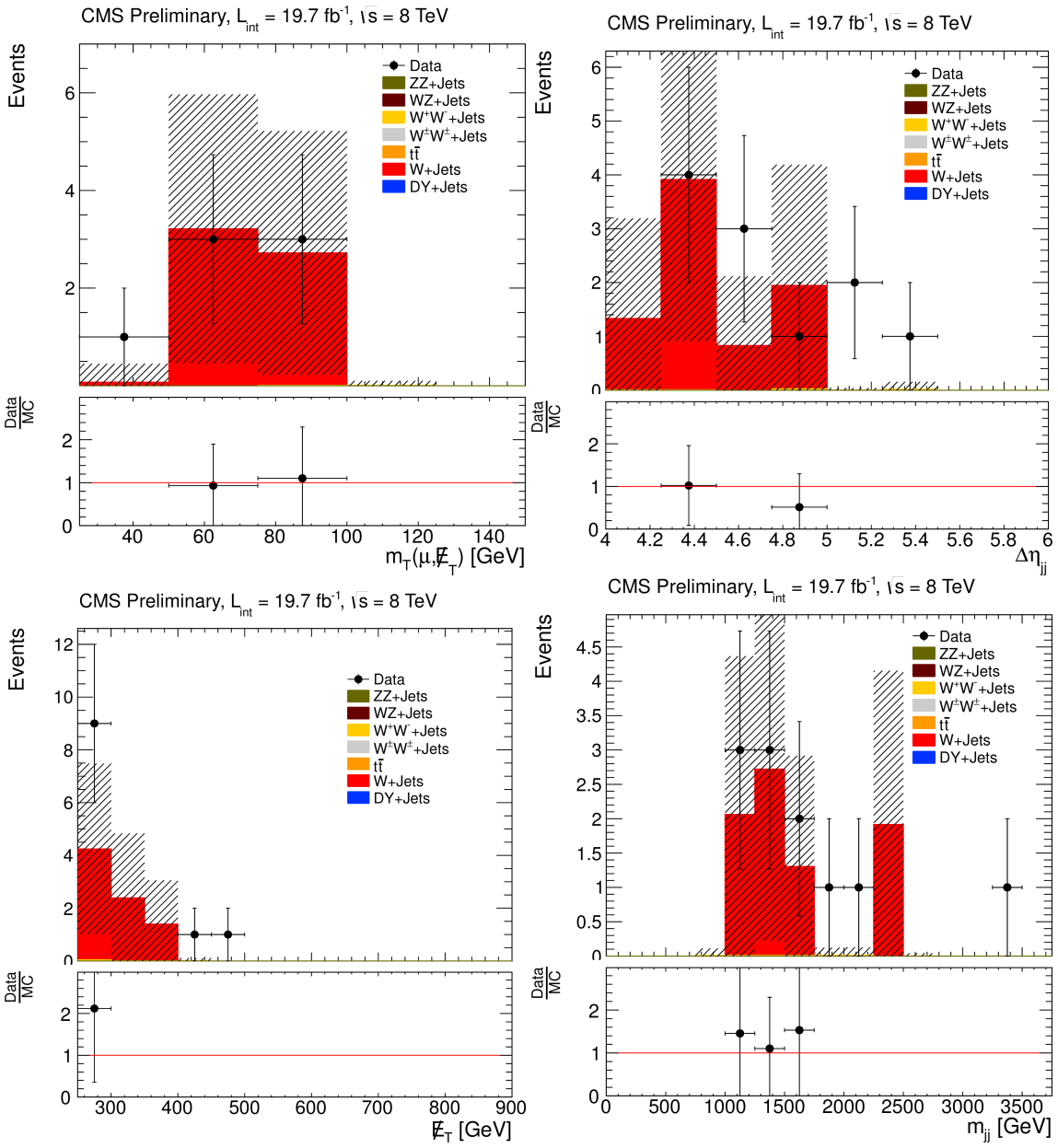


Figure 8.7: (a) Transverse mass distribution of the muon and $p_{\mathrm{T}}^{\mathrm{miss}}$, (b) $\Delta\eta_{jj}$ distribution, (c) $p_{\mathrm{T}}^{\mathrm{miss}}$ distribution, and (d) $m_{jj}$ distribution for W+Jets in W_CR3 (require one muon, veto other leptons, apply VBF selections). Despite very low statistics, there is reasonable agreement in the normalization of the distributions.

The following equation is used to estimate the W+jets background contributions:

$$N^{\mathrm{SR}}_{\mathrm{W+Jets}} = N^{\mathrm{MC}}_{\mathrm{W+Jets}}(\mathrm{noVBF}) \cdot SF^{\mathrm{W\_CR2}}_{\mathrm{noVBF}} \cdot \varepsilon^{\mathrm{W\_CR3}}_{\mathrm{VBF}} \tag{8.4}$$

where $N^{\mathrm{SR}}_{\mathrm{W+Jets}}$ is the predicted W+Jets background rate in the Signal Region, $N^{\mathrm{MC}}_{\mathrm{W+Jets}}$ (noVBF) is the predicted MC W+Jets rate without VBF selections, $SF^{\mathrm{W\_CR2}}_{\mathrm{noVBF}}$ the correction factor for the central selections determined from the W_CR2, and $\varepsilon^{\mathrm{W\_CR3}}_{\mathrm{VBF}}$ is the efficiency of VBF selections determined from the W_CR3.

These terms are calculated from each control region as follows: $SF^{\mathrm{W\_CR2}}_{\mathrm{noVBF}}$ is calculated by subtracting the total non-Z MC based background rate from the observed yield in Data for W_CR2 and dividing by the W+Jets yield inside W_CR2:

$$(N^{\mathrm{W\_CR2}}_{\mathrm{Data}} - \Sigma N^{\mathrm{W\_CR2}}_{\mathrm{non\text{-}W}})/N^{\mathrm{W\_CR2}}_{\mathrm{W+Jets}}. \tag{8.5}$$

Finally, $\varepsilon^{\mathrm{W\_CR3}}_{\mathrm{VBF}}$ is measured by taking the ratio of the number of events in data inside W_CR3 and W_CR2:

$$N^{\mathrm{W\_CR3}}_{\mathrm{Data}}/N^{\mathrm{W\_CR2}}_{\mathrm{Data}}. \tag{8.6}$$

The contamination from non-W backgrounds in the control regions is used to assign a systematic uncertainty on the measured *SF* and VBF efficiency.

Table 8.2 lists the number of observed events in data as well as the expected MC contributions in the W+Jets control regions. The uncertainties are based on the statistics of the MC samples. The measured data-to-MC scale factor is $0.80 \pm 0.04$. The uncertainty on the correction factor is purely statistical. The level of contamination ($\sim 3.5\%$) from other background sources is treated as a systematic uncertainty on the correction factor.

Table 8.2: Predicted and observed rates for the W Control Regions. The yields are used to calculate correction factors for the central selections and VBF selection efficiencies.

| Sample | W_CR1 | W_CR2 | W_CR3 |
|---|---|---|---|
| DY+Jets | $6.0 \cdot 10^6 \pm 4.0 \cdot 10^3$ | $12.4 \pm 4.4$ | $0.0^{+1.9}_{-0.0}$ |
| W+Jets | $6.7 \cdot 10^7 \pm 4.4 \cdot 10^4$ | $1.3 \cdot 10^3 \pm 55$ | $8.0 \pm 4.4$ |
| $t\bar{t}$ | $4.1 \cdot 10^5 \pm 747$ | $13.4 \pm 4.4$ | $0.0^{+0.7}_{-0.0}$ |
| VV | $1.0 \cdot 10^5 \pm 331$ | $22.3 \pm 5.0$ | $0.07^{+0.34}_{-0.07}$ |
| $\Sigma_{MC}$ | $7.3 \cdot 10^7 \pm 4.5 \cdot 10^4$ | $1.4 \cdot 10^3 \pm 56$ | $8.0 \pm 4.4$ |
| Data | $7.1 \cdot 10^7$ | 1112 | 9 |
| Purity | $0.912 \pm 0.001$ | $0.965 \pm 0.056$ | $0.992 \pm 0.766$ |
| SF | $0.967 \pm 0.001$ | $0.796 \pm 0.042$ | $1.141 \pm 0.732$ |

## 8.3 QCD Background Estimate

QCD multijet background cannot be estimated appropriately due to low statistics in the Monte-Carlo samples. Thus, a data-driven QCD background estimation is performed by employing two control samples with inverted $p_{\mathrm{T}}^{\mathrm{miss}}$ and jet veto selections. The QCD multijet contribution in the signal region is then calculated using the following formulation:

$$N_{\mathrm{QCD}}^{\mathrm{SR}} = N_{\mathrm{QCD}}^{\mathrm{CR1}} \cdot \varepsilon_{\frac{NJet=2}{NJet\geq 3}}^{CR2} \cdot \varepsilon_{|\Delta\phi(jet_2, E_T^{miss})|>0.5}. \tag{8.7}$$

The first control region (QCD_CR1) is obtained by requiring similar selections as the signal region (including VBF and $p_{\mathrm{T}}^{\mathrm{miss}}$ selections), except for inverted NJet $\geq 3$ and $|\Delta\phi(jet_2, E_T^{miss})| < 0.5$) requirements. An upper bound to the QCD contribution in this first control region is determined by subtracting the simulated non-QCD events from the number of data events, $N_{\mathrm{QCD}}^{\mathrm{CR1}} = N_{\mathrm{data}}^{\mathrm{CR1}} - N_{\text{non-QCD}}^{\mathrm{CR1}}$. The QCD contribution in this first control region is estimated as $78.69 \pm 15.18$ events.

The requirement of small $|\Delta\phi(jet_2, E_T^{miss})|$ is motivated by the expectation that most of the QCD contribution arises from mismeasured jets. Figure 8.8 (a) supports this presumption: additional data events in the low $|\Delta\phi(jet_2, E_T^{miss})|$ region not accounted for by the non-QCD background prediction, are apparent given a back-to-back di-jet system, i.e. where one jet will is anti-parallel to the other (i.e. $\hat{p_{\mathrm{T}}}^{A} = -\hat{p_{\mathrm{T}}}^{B}$). If one of the jets is mismeasured (e.g. $p_{\mathrm{T}}^{A} > p_{\mathrm{T}}^{B}$), then the $p_{\mathrm{T}}^{\mathrm{miss}}$ vector will point in the direction of the less energetic jet. This may be seen by writing the sum of transverse momentum before and after the collision, $0 = \vec{p}_{\mathrm{T}}^{A} + \vec{p}_{\mathrm{T}}^{B} + \vec{E}_{\mathrm{T}}^{\mathrm{miss}}$. Then $\vec{E}_{\mathrm{T}}^{\mathrm{miss}} = -(p_{\mathrm{T}}^{A} \cdot \hat{p_{\mathrm{T}}}^{A} + p_{\mathrm{T}}^{B} \cdot \hat{p_{\mathrm{T}}}^{B}) = \hat{p_{\mathrm{T}}}^{B}(p_{\mathrm{T}}^{A} - p_{\mathrm{T}}^{B})$ and therefore the $p_{\mathrm{T}}^{\mathrm{miss}}$ will be colinear to the less energetic jetB, $\hat{E_{\mathrm{T}}^{\mathrm{miss}}} \parallel \hat{p_{\mathrm{T}}}^{B}$.

More concretely, $jet_2$ in the cut definition *always* represents the sub-leading jet (i.e. less energetic jet). With this definition, $|\Delta\phi(jet_2, E_T^{miss})|$ is always $\sim 0$ for QCD dijet, regardless of whether a jet loses or gains energy from the mismeasurement. Suppose both jets had true energy of 400 GeV: jetA = 400 GeV and jetB = 400 GeV. If jetB is mismeasured as 150

GeV and loses energy, then $jet_2$ will be jetB. The $p_{\mathrm{T}}^{\mathrm{miss}}$ will point in the direction of jetB with magnitude 250 GeV in order to balance jetA. In this scenario, $|\Delta\phi(jet_2, E_T^{miss})| \sim 0$. If instead jetB is mismeasured as 650 GeV and gains energy, then $jet_2$ will be jetA. The $p_{\mathrm{T}}^{\mathrm{miss}}$ will point in the direction of jetA with magnitude 250 GeV in order to balance jetB. In this scenario $|\Delta\phi(jet_2, E_T^{miss})|$ is still $\sim 0$.

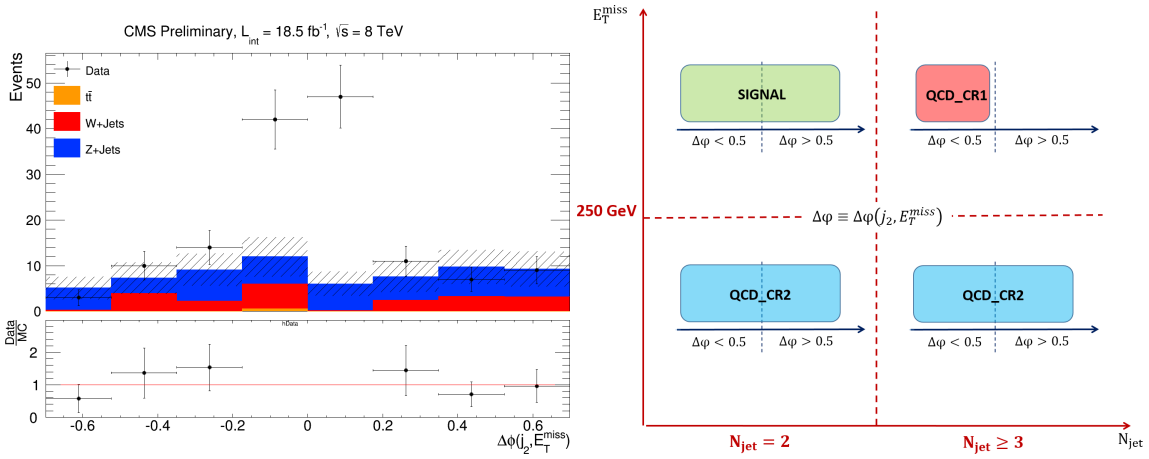


Figure 8.8: (a) $|\Delta\phi(jet_2, E_T^{miss})|$ distribution in the QCD_CR1 control region. (b) QCD background estimate strategy.

The second QCD control region (QCD_CR2) is defined by similar selections as the signal region (including VBF selections), except for a NJet $\geq 2$ and an inverted $p_{\mathrm{T}}^{\mathrm{miss}} < 250$ GeV requirement. This control region is employed to measure the jet veto correction factor:

$$\varepsilon^{CR2}_{\frac{NJet=2}{NJet\geq 3}} \equiv \frac{(N_{\mathrm{data}} - N_{\text{non-QCD}})^{CR2}_{NJet=2}}{(N_{\mathrm{data}} - N_{\text{non-QCD}})^{CR2}_{NJet\geq 3}}. \tag{8.8}$$

This factor is defined as the ratio of QCD events surviving a NJet $= 2$ requirement divided by the number of QCD events surviving a NJet $\geq 3$ requirement. The QCD contribution for each NJet requirement is again an upper bound determined by subtracting the simulated non-QCD events from the number of data events. The computation of this ratio yields $0.301 \pm 0.001$.

Table 8.3 lists the yields obtained in the two QCD control regions for the main back-

grounds, as well as data. A summary of each QCD control region definition is shown in Figure 8.8 (b). The corresponding QCD contribution in the signal region amounts to $N_{\text{QCD}}^{\text{SR}} = (78.69 \pm 15.18) \cdot (0.301 \pm 0.001) = 23.65 \pm 4.56$ events.

Table 8.3: Predicted and observed rates for the QCD Control Regions.

| Sample | CR1 | CR2($N_{jet} = 2$) | CR2($N_{jet} \geq 3$) |
|---|---|---|---|
| W+Jets | $20.8 \pm 6.7$ | $1.00 \cdot 10^5 \pm 1.1 \cdot 10^3$ | $2.16 \cdot 10^5 \pm 1.3 \cdot 10^3$ |
| $Z_{\nu\nu}$+Jets | $39.9 \pm 6.7$ | $3.5 \cdot 10^4 \pm 253$ | $6.0 \cdot 10^4 \pm 294$ |
| $t\bar{t}$ | $0.6^{+1.0}_{-0.6}$ | $443 \pm 27$ | $7.4 \cdot 10^4 \pm 348$ |
| $\Sigma_{\text{non-QCD MC}}$ | $61.3 \pm 9.5$ | $1.4 \cdot 10^5 \pm 1.1 \cdot 10^3$ | $3.5 \cdot 10^5 \pm 1.3 \cdot 10^3$ |
| data | 140 | $5.9 \cdot 10^6$ | $1.9 \cdot 10^7$ |

Finally, the $|\Delta\phi(jet_2, E_T^{miss})| > 0.5$ cut efficiency is estimated using a $Z(\rightarrow \mu^+\mu^-)$ + jets sample, since it is dominated by fake $p_{\text{T}}^{\text{miss}}$ events (just as QCD events). The figures 8.9 show the $|\Delta\phi(jet_2, E_T^{miss})|$ and di-muon mass distributions for said sample. A $p_{\text{T}}^{\text{miss}}$ sideband of $p_{\text{T}}^{\text{miss}} > 75$ GeV is employed in order to improve the sample statistics. The $|\Delta\phi(jet_2, E_T^{miss})|$ distribution of data events gets more narrow (i.e. data events accumulate closer to $|\Delta\phi(jet_2, E_T^{miss})| = 0$) as the $p_{\text{T}}^{\text{miss}}$ increases, but there's not enough statistics at $p_{\text{T}}^{\text{miss}} > 250$ GeV. The looser/inverted $p_{\text{T}}^{\text{miss}}$ requirement in CR2 leads to a broader $|\Delta\phi(jet_2, E_T^{miss})|$ distribution, which affects the $|\Delta\phi(jet_2, E_T^{miss})|$ cut efficiency, and ultimately yields a more conservative overestimate of QCD events in the signal region.

This $|\Delta\phi(jet_2, E_T^{miss})|$ cut efficiency is determined as:

$$\varepsilon_{|\Delta\phi(jet_2, E_T^{miss})|>0.5} = \frac{(N_{\text{data}} - N_{\text{non-QCD}})@\text{large}\Delta\phi}{(N_{\text{data}} - N_{\text{non-QCD}})@\text{all}\Delta\phi}, \tag{8.9}$$

where the numerator corresponds to data events with $|\Delta\phi(jet_2, E_T^{miss})| > 0.5$ after subtracting non-QCD simulated events, and the denominator corresponds to the total number of data events after subtracting simulated events fro non-QCD backgrounds. Note that the poisson uncertainty on the data and the systematics on the non-QCD samples are propagated thoroughout. This method yields a cut efficiency of $\varepsilon_{|\Delta\phi(jet_2, E_T^{miss})|>0.5} = 0.1 \pm 0.5$. Also note that in the large $|\Delta\phi(jet_2, E_T^{miss})|$ region, the QCD purity is not very good. The

large amount of MC background presence at small $|\Delta\phi(jet_2, E_T^{miss})|$ leads to the large uncertainty in the $|\Delta\phi(jet_2, E_T^{miss})|$ cut efficiency (500%). Another advantage of having a relatively strict $p_{\mathrm{T}}^{\mathrm{miss}}$ cut is that it suppresses the QCD contribution and reduces the importance of this purity issue. Thus, QCD events are estimated to contribute $N_{\mathrm{QCD}}^{\mathrm{SR}} = N_{\mathrm{QCD}}^{\mathrm{CR1}} \cdot \varepsilon_{\frac{NJet=2}{NJet\geq 3}}^{CR2} \cdot \varepsilon_{|\Delta\phi(jet_2, E_T^{miss})|>0.5} = 2.36 \pm 11.81$ to the signal region.

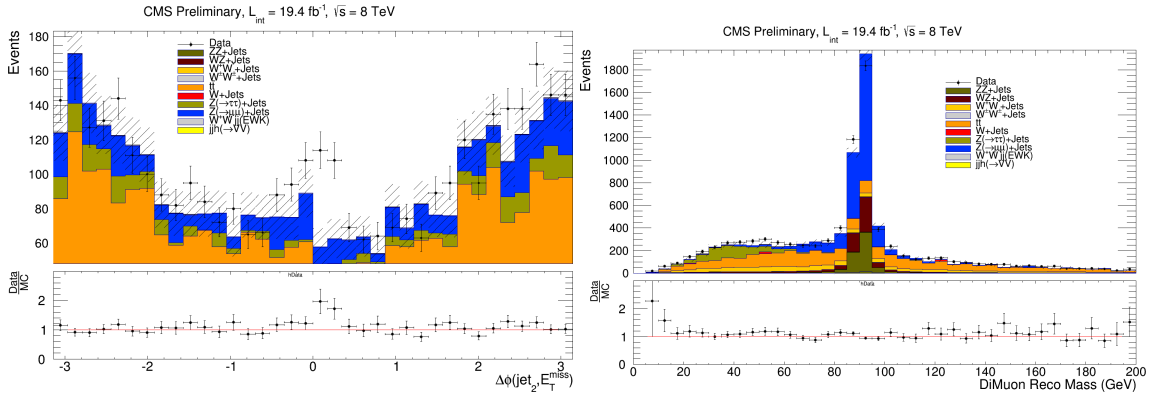


Figure 8.9: (a) $|\Delta\phi(jet_2, E_T^{miss})|$ distribution and (b) Di-muon reco mass distribution for the $Z(\rightarrow \mu^+\mu^-)$ + jets sample. Note that there is only discrepancy in the number of events between these distributions because the $\Delta\phi(jet_2, E_T^{miss})$ histogram is only filled by events with $\geq 2$ jets, whereas the $M_{\mu\mu}$ distribution is filled by all events and is used to validate good data/MC modeling.

To summarize, the small contribution to the SR from the QCD multijet background is estimated using the fractions of events passing the $p_{\mathrm{T}}^{\mathrm{miss}}$ and additional jet veto (AJV) requirements. Four QCD multijet dominated CRs are defined with similar selections to the SR, but with the following modifications: (A) failing the $p_{\mathrm{T}}^{\mathrm{miss}}$, AJV, and $|\Delta\phi(p_{\mathrm{T}}^{\mathrm{miss}}, j_2)|$ requirements; (B) passing the $p_{\mathrm{T}}^{\mathrm{miss}}$ requirement, failing the AJV requirement, and failing the $|\Delta\phi(p_{\mathrm{T}}^{\mathrm{miss}}, j_2)|$ requirement; (C) failing the $p_{\mathrm{T}}^{\mathrm{miss}}$ requirement, passing the AJV requirement, and failing the $|\Delta\phi(p_{\mathrm{T}}^{\mathrm{miss}}, j_2)|$ requirement; (D) passing the $p_{\mathrm{T}}^{\mathrm{miss}}$ requirement, passing the AJV requirement, and failing the $|\Delta\phi(p_{\mathrm{T}}^{\mathrm{miss}}, j_2)|$ requirement. These requirements are illustrated by Figure 8.10. The QCD multijet background yields in control regions A, B, and C are estimated from data after subtracting the non-QCD background yields using estimations from simulation. The QCD multijet component in region D is then determined

as $N^{\mathrm{D}}_{\mathrm{QCD}} = N^{\mathrm{B}}_{\mathrm{QCD}} \cdot N^{\mathrm{C}}_{\mathrm{QCD}} / N^{\mathrm{A}}_{\mathrm{QCD}}$ , yielding a prediction of 23.7 $\pm$ 4.6 events. Since region D is defined with an inverted $|\Delta\phi(p_{\mathrm{T}}^{\mathrm{miss}}, j_2)|$ requirement, the QCD contribution to the SR is obtained by correcting the prediction in region D by the efficiency of the $|\Delta\phi(p_{\mathrm{T}}^{\mathrm{miss}}, j_2)|$ cut, $N^{|\Delta\phi(p_{\mathrm{T}}^{\mathrm{miss}}, j_2)|>0.5}_{\mathrm{QCD}} / N^{|\Delta\phi(p_{\mathrm{T}}^{\mathrm{miss}}, j_2)|<0.5}_{\mathrm{QCD}}$, which is measured from a Z($\rightarrow \mu^+\mu^-$) + jets control sample with $p_{\mathrm{T}}^{\mathrm{miss}} > 75$ GeV.

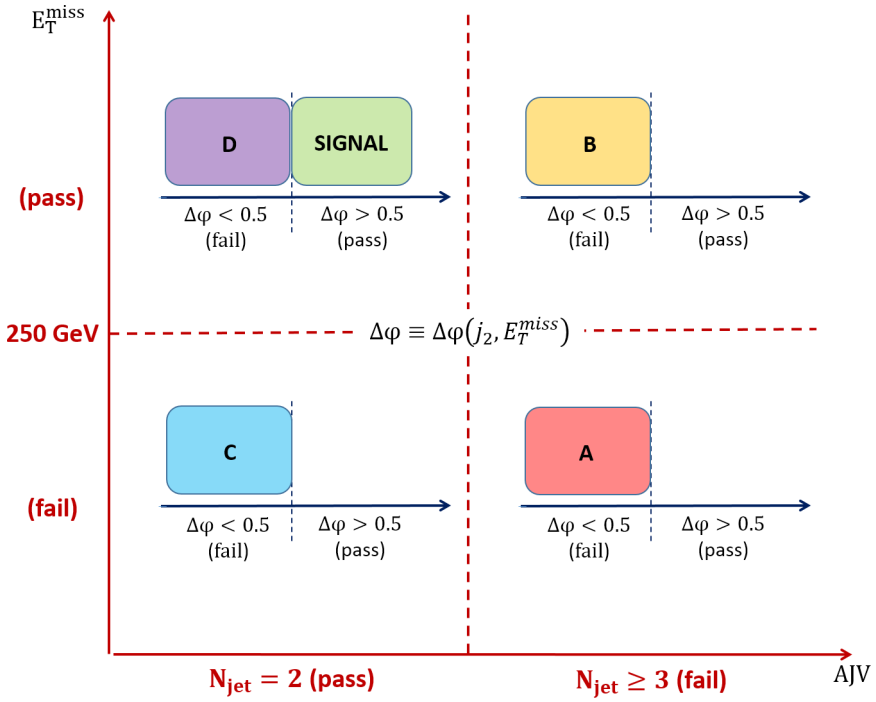


Figure 8.10: Summary of QCD background estimate strategy. The QCD multijet component in region D is determined as $N^{\mathrm{D}}_{\mathrm{QCD}} = N^{\mathrm{B}}_{\mathrm{QCD}} \cdot N^{\mathrm{C}}_{\mathrm{QCD}} / N^{\mathrm{A}}_{\mathrm{QCD}}$, yielding a prediction of 23.7 $\pm$ 4.6 events. The QCD contribution to the SR is obtained by correcting the prediction in region D by the efficiency of the $|\Delta\phi(p_{\mathrm{T}}^{\mathrm{miss}}, j_2)|$ cut.

## 8.4 VBF Higgs Background Estimate

The strict $p_{\mathrm{T}}^{\mathrm{miss}}$ requirement drastically reduces contributions from VBF Higgs processes. In addition, VBF Higgs corresponds to s-channel weak boson fusion, whereas VBF SUSY proceeds through t-channel (because there are two SUSY particles compared to one Higgs). Therefore the VBF jets are harder in SUSY, so the VBF cuts help reduce the number of surviving VBF Higgs events. This is illustrated in Figure 8.11, which shows the

leading jet $p_{\mathrm{T}}$ distributions for VBF Higgs and VBF SUSY simulated samples. Table 8.4 lists the predicted rates for all relevant VBF Higgs decay modes in the signal region and shows that their contribution is negligible. Therefore, their expected rates in the signal region are taken directly from MC after accounting for proper systematic uncertainties due to Parton Distribution Functions (PDFs), ISR/FSR, jet energy scale (JES), etc.

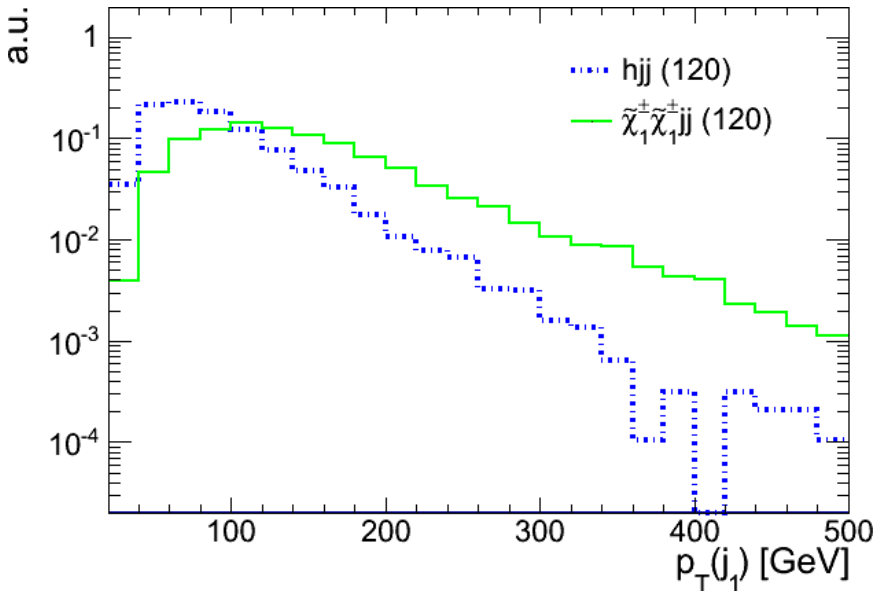


Figure 8.11: Leading jet $p_{\mathrm{T}}$ distributions for simulated VBF Higgs and VBF SUSY simulated samples. Note that the VBF jets are more energetic in the SUSY sample, so the more stringent VBF cuts reduce the number of surviving VBF Higgs events.

Table 8.4: Predicted rates for after various stages of the cut flow for VBF Higgs processes.

| Sample | $l/b$Vetos + 2j | $E_T^{miss}$ | VBF | SR |
|---|---|---|---|---|
| $\Sigma\text{Higgs}_{\text{VBF}}$ | $45.2 \pm 6.8$ | $0.4^{+0.6}_{-0.4}$ | $0.1^{+0.4}_{-0.1}$ | $0.1^{+0.4}_{-0.1}$ |
| $\text{Higgs}_{\text{VBF}} \to ZZ \to 4\nu$ | $4.5 \pm 0.4$ | $0.21 \pm 0.01$ | $0.07 \pm 0.01$ | $0.07 \pm 0.01$ |
| $\text{Higgs}_{\text{VBF}} \to ZZ \to 2l2\nu$ | $0.7 \pm 0.2$ | $0.006 \pm 0.001$ | $0.003 \pm 0.001$ | $0.002 \pm 0.001$ |
| $\text{Higgs}_{\text{VBF}} \to WW \to 2\tau 2\nu$ | $12.0 \pm 0.8$ | $0.10 \pm 0.02$ | $0.03 \pm 0.01$ | $0.03 \pm 0.01$ |
| $\text{Higgs}_{\text{VBF}} \to 2\tau$ | $26.6 \pm 2.1$ | $0.08 \pm 0.01$ | $0.03 \pm 0.01$ | $0.03 \pm 0.01$ |
| $\text{Higgs}_{\text{VBF}} \to ZZ \to 4l$ | $0.03^{+0.07}_{-0.03}$ | $0.00^{+0.01}_{-0.00}$ | $0.00^{+0.01}_{-0.00}$ | $0.00^{+0.01}_{-0.00}$ |
| $\text{Higgs}_{\text{VBF}} \to ZZ \to 2l2Q$ | $1.4 \pm 0.7$ | $0.00^{+0.01}_{-0.00}$ | $0.00^{+0.01}_{-0.00}$ | $0.00^{+0.01}_{-0.00}$ |
| $\tilde{b}\tilde{b}$jj $[m(\tilde{b}_1) = 300\text{GeV}]$ | $434.7 \pm 25.5$ | $41.3 \pm 7.9$ | $38.6 \pm 7.6$ | $38.6 \pm 7.6$ |

## 8.5 Other Backgrounds

As can be seen from Figures 7.4 and 7.5, the $t\bar{t}$ and di-boson backgrounds present a very small contribution to the signal region. The topology of $\gamma$+jet events is similar to QCD di-jet events, yet its production cross-section much smaller. Thus, the $\gamma$+jet events contribution to the signal region is expected to be negligible. Therefore, the expected rates for these processes in the signal region are taken directly from MC after accounting for proper systematic uncertainties due to PDFs, ISR/FSR, jet energy scale (JES), etc.

# Chapter 9

# Systematics

## 9.1 Closure and Validation Tests

The background estimates hinge on the correct and unbiased measurements of the VBF selection efficiencies and $m_{jj}$ shapes from the background enriched control regions. Figure 9.1 shows a comparison between the $m_{jj}$ and $p_{\mathrm{T}}^{\mathrm{miss}}$ distributions for $\mathrm{Z}(\rightarrow \nu\bar{\nu})$ + Jets in the signal region and $Z_{\mu^+\mu^-\rightarrow\nu\bar{\nu}}$+Jets in the Z control region. It shows consistency between the distributions in the control and signal regions, validating the extrapolation from Z_CR to SR. Similarly, Figure 9.2 shows a similar comparison between the $m_{jj}$ and $p_{\mathrm{T}}^{\mathrm{miss}}$ distributions for W+Jets in the signal region and $W_{\mu\rightarrow\nu}$+Jets in the W control region. The consistency between the distributions in the W_CR and distributions in the SR validate the background estimation methodology utilized in this analysis. The level of agreement between the distributions is used to assign a systematic uncertainty on the background predictions due to closure.

The effect of the large uncertainty in the QCD prediction on the quoted limits was studied, and found to be negligible. This study was done by obtaining a template shape from QCD MC events and normalizing it to the upper-bound of the statistical uncertainty (12 events). Since QCD MC statistics are so low, the central lepton vetos were relaxed to obtain the mjj shape from QCD MC. The removal of the central lepton vetos is not expected to cause any significant bias in the mjj distribution.

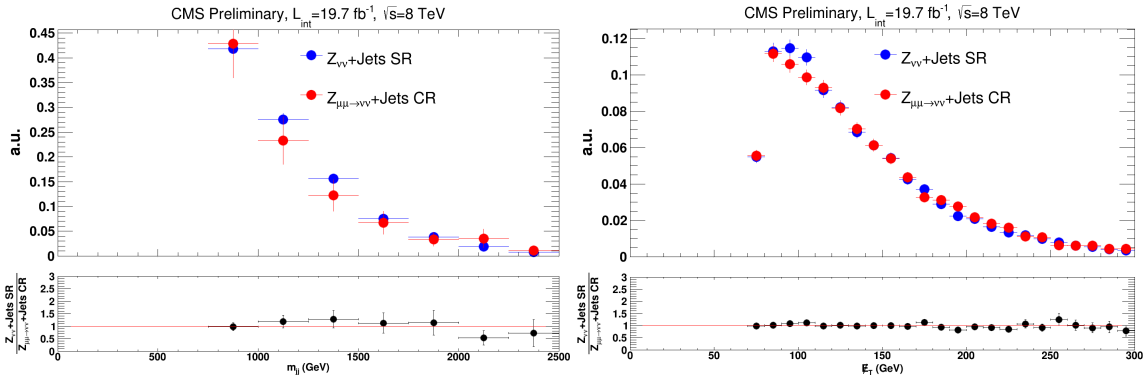


Figure 9.1: (a) $m_{jj}$ distribution (b) $p_{\mathrm{T}}^{\mathrm{miss}}$ distribution in Z_CR and Signal Region.

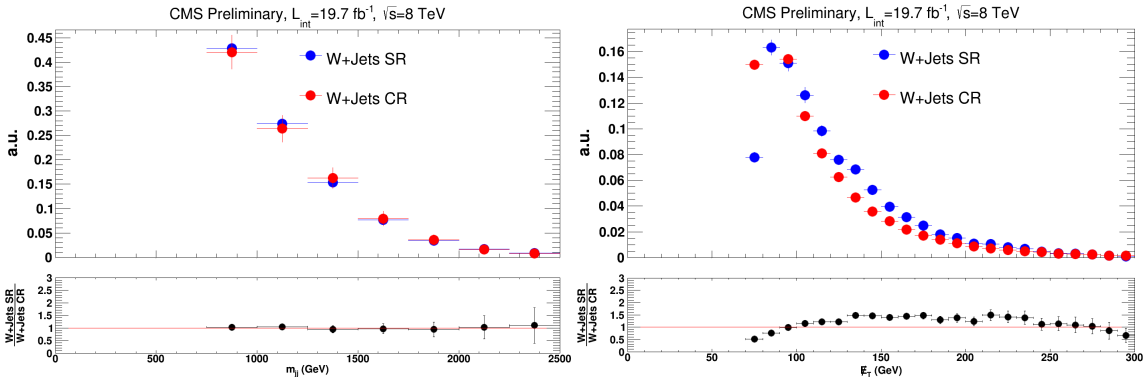


Figure 9.2: (a) $m_{jj}$ distribution (b) $p_{\mathrm{T}}^{\mathrm{miss}}$ distribution in W_CR and Signal Region.

### 9.1.1 Validation of mjj Shape Systematics

Very few events survive after the $p_{\mathrm{T}}^{\mathrm{miss}} > 250$ GeV cut is applied. Too few events remain to validate that the $m_{jj}$ shapes are correctly modeled by the MC (i.e. the shape of the VBF efficiency is limited by statistics). The normalization can be extracted from data but a smooth shape can't be extracted from the data itself. The best/only strategy at hand is to inspect the low-$p_{\mathrm{T}}^{\mathrm{miss}}$ side-band with the VBF selections applied and see how the shape agrees.

The $m_{jj}$ shape is taken directly from MC, normalized to the data-driven rate. Validation shows that MC correctly models the $m_{jj}$ distribution in the low-$p_{\mathrm{T}}^{\mathrm{miss}}$ sidebands. However,

does this correct modeling of $m_{jj}$ shape extrapolate to the large-$p_{\mathrm{T}}^{\mathrm{miss}}$ region? How can this be verified without looking inside the signal region or getting crippled by low statistics? The real $m_{jj}$ shape is expected to be mis-modeled by events with fake $p_{\mathrm{T}}^{\mathrm{miss}}$. However, events in the large-$p_{\mathrm{T}}^{\mathrm{miss}}$ signal region will be dominated by real $p_{\mathrm{T}}^{\mathrm{miss}}$, and are thus expected to be well modeled.

A study was carried out to validate the MC modeling of the $m_{jj}$ shape in bins of $p_{\mathrm{T}}^{\mathrm{miss}}$. Insead of simply inspecting a single low-$p_{\mathrm{T}}^{\mathrm{miss}}$ sideband, various low-$p_{\mathrm{T}}^{\mathrm{miss}}$ sidebands were investigated to see how the level of data/MC agreement in the $m_{jj}$ shape "evolves" as the $p_{\mathrm{T}}^{\mathrm{miss}}$ cut is tightened. It can then be determined whether the level of agreement in the low-$p_{\mathrm{T}}^{\mathrm{miss}}$ sidebands is consistent with the shape systematics. Otherwise, additional shape systematics would need to be implemented.

Figures 9.3(a) and 9.3(b) show the $m_{jj}$ distributions given $p_{\mathrm{T}}^{\mathrm{miss}} > 50$ GeV and $p_{\mathrm{T}}^{\mathrm{miss}} > 200$ GeV, respectively. These figures demonstrate that, although the data/MC agreement in the $m_{jj}$ shape suffers due to reduced statistics as the $p_{\mathrm{T}}^{\mathrm{miss}}$ cut increases, the agreement is still consistent with the level of assigned systematics. This can be seen in more detail by inspecting Figures 9.4(a-d). These figures show how the level of data/MC agreement in the $m_{jj}$ shape changes as the $p_{\mathrm{T}}^{\mathrm{miss}}$ cut is increased in steps of 50 GeV (50-200 GeV). The shaded regions correspond to the $m_{jj}$ shape systematics, defined as the level of data/MC agreement in the $m_{jj}$ shapes and their associated uncertainties as observed in the inverted-$p_{\mathrm{T}}^{\mathrm{miss}}$ sideband in the Z and W control regions. Since the level of agreement in the $p_{\mathrm{T}}^{\mathrm{miss}}$ sidebands is seen to be consistent with the assigned shape systematics, no further shape systematics need to be implemented.

As a further check, the level of agreement is studied inside a $75 < p_{\mathrm{T}}^{\mathrm{miss}} < 250$ GeV sideband. Again, the level of agreement in the data/MC $m_{jj}$ shape is observed (see Figure 9.5) to be consistent with the assigned shape systematics.

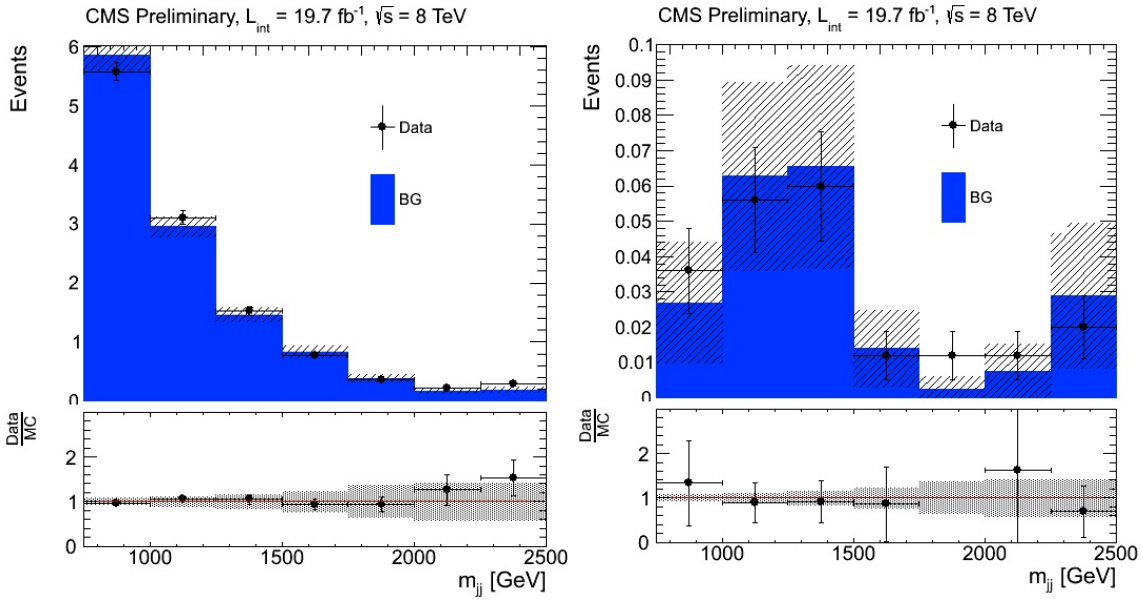


Figure 9.3: (a) $m_{jj}$ distribution with $p_{\mathrm{T}}^{\mathrm{miss}} > 50$ GeV and (b) $p_{\mathrm{T}}^{\mathrm{miss}} > 200$ GeV.

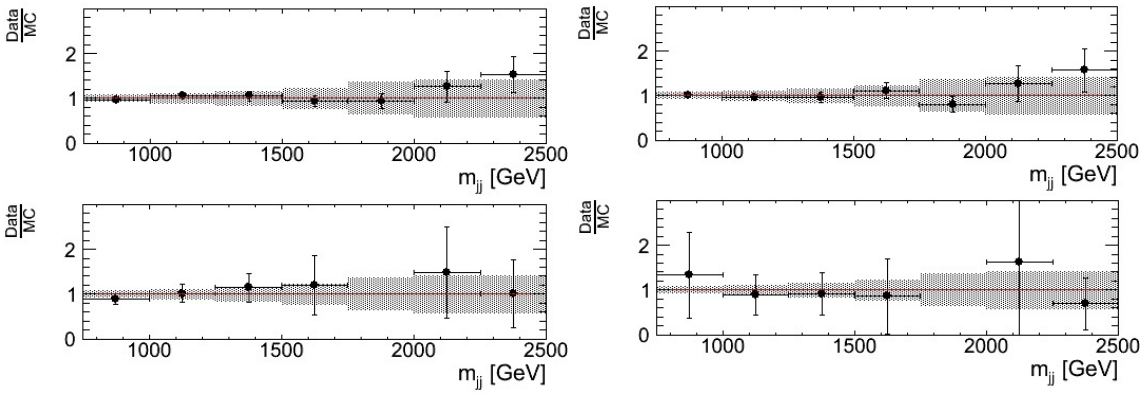


Figure 9.4: (a) $m_{jj}$ distribution of the ratio of data/MC events with $p_{\mathrm{T}}^{\mathrm{miss}} > 50$ GeV, (b) $p_{\mathrm{T}}^{\mathrm{miss}} > 100$ GeV, (c) $p_{\mathrm{T}}^{\mathrm{miss}} > 150$ GeV, and (d) $p_{\mathrm{T}}^{\mathrm{miss}} > 200$ GeV

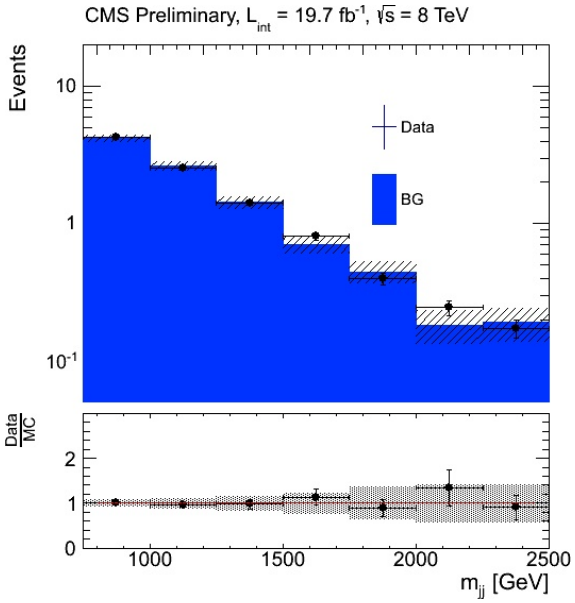


Figure 9.5: (a) $m_{jj}$ distribution with $75 < p_{\mathrm{T}}^{\mathrm{miss}} < 250$ GeV.

### 9.1.2 Validation of QCD Background Estimate Correction Factors

Recall that the contribution of QCD di-jet events to the signal region is estimated using several correction factors. One of these factors, $\varepsilon^{CR2}_{\frac{NJet=2}{NJet\geq 3}} = N^{\mathrm{C}}_{\mathrm{QCD}}/N^{\mathrm{A}}_{\mathrm{QCD}} = N_{\mathrm{QCD}}(p_{\mathrm{T}}^{\mathrm{miss}} < 250, NJet = 2)/N_{\mathrm{QCD}}(p_{\mathrm{T}}^{\mathrm{miss}} < 250, NJet \geq 3)$, is calculated in an inverted-$p_{\mathrm{T}}^{\mathrm{miss}}$ and inverted-$|\Delta\phi(p_{\mathrm{T}}^{\mathrm{miss}}, j_2)|$ sideband. In order to verify that this correction factor can be extrapolated to the (large-$p_{\mathrm{T}}^{\mathrm{miss}}$, large-$|\Delta\phi(p_{\mathrm{T}}^{\mathrm{miss}}, j_2)|$) signal region, a $\mathrm{Z}(\rightarrow \mu^+\mu^-)$ + jets control sample with nominal (i.e. large) $p_{\mathrm{T}}^{\mathrm{miss}}$ and $|\Delta\phi(p_{\mathrm{T}}^{\mathrm{miss}}, j_2)|$ cuts is employed. As discussed in section 8.3, this sample is expected to accurately model QCD di-jet events since both processes are dominated by fake $p_{\mathrm{T}}^{\mathrm{miss}}$ events. Figure 9.6 shows good closure in the NJets distribution between the inverted-$p_{\mathrm{T}}^{\mathrm{miss}}$, inverted-$|\Delta\phi(p_{\mathrm{T}}^{\mathrm{miss}}, j_2)|$ QCD control sample and the large-$p_{\mathrm{T}}^{\mathrm{miss}}$, large-$|\Delta\phi(p_{\mathrm{T}}^{\mathrm{miss}}, j_2)|$ $\mathrm{Z}(\rightarrow \mu^+\mu^-)$ + jets control sample.

### 9.1.3 Validation of Polarization in W+Jets Background Estimate

A validation study was performed in order to check whether the polarization in W+Jets events biases their kinematics. The MC prediction for W+Jets processes was separated into

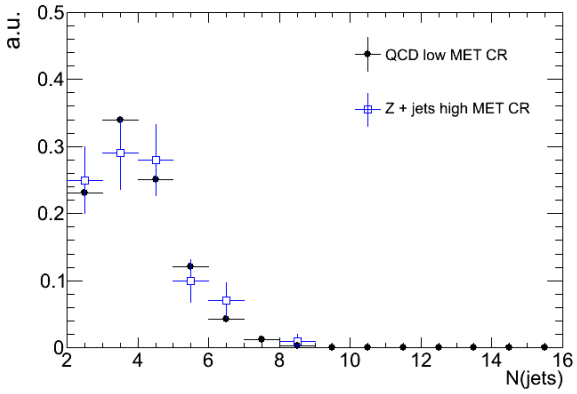


Figure 9.6: Number of jets distribution for inverted-$p_{\mathrm{T}}^{\mathrm{miss}}$, inverted-$|\Delta\phi(p_{\mathrm{T}}^{\mathrm{miss}}, j_2)|$ QCD control sample and large-$p_{\mathrm{T}}^{\mathrm{miss}}$, large-$|\Delta\phi(p_{\mathrm{T}}^{\mathrm{miss}}, j_2)|$ Z$\rightarrow \mu\mu$+Jets control sample.

its $W^+$ and $W^-$ components and studied in the W_CR2. Figure 9.7 show relevant kinematic distributions for the $W^+$ and $W^-$ contributions to the W_CR2. No significant deviation is observed due to polarizarion of W-boson decays, and assigned systematics cover any small effects.

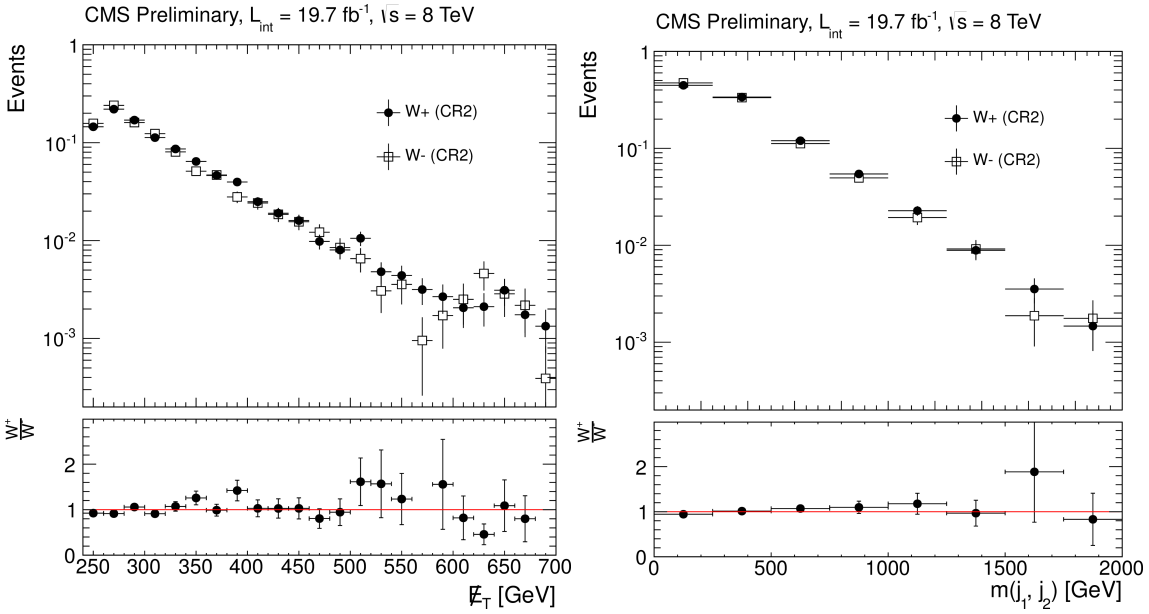


Figure 9.7: Comparison of $W^+$ and $W^-$ components of W+Jets events in W_CR2 for (a) $p_{\mathrm{T}}^{\mathrm{miss}}$ distribution and (b) Leading Jets Mass ($m_{j_1,j_2}$) distribution.

## 9.2 Systematic Uncertainties

Since the estimation of the background contributions in the signal region is partly based on simulation, both the signal and background are affected by similar sources of systematic uncertainties. The dominant source of systematic uncertainties on the background predictions are due to uncertainties in the correction factors.

The $p_{\mathrm{T}}^{\mathrm{miss}}$ scale uncertainties contribute via the jet energy scale (2-5% depending on $\eta$ and $p_{\mathrm{T}}$) and unclustered energy scale (10%), where unclustered energy is defined as the energy not associated with the reconstructed leptons and jets with $p_{\mathrm{T}} > 10$ GeV. The unclustered energy scale uncertainty has a negligible systematic effect on the signal acceptance.

The systematic uncertainty on the background predictions is also dominated by the statistical uncertainty of the data used in the control regions, which determines the uncertainty on the VBF efficiency. These uncertainties are on the order of 25%. The contamination from other backgrounds in these control regions contributes around 2% to the systematic uncertainty. The efficiencies for electron/muon reconstruction and identification are measured with the "tag-and-probe" method [92, 93], resulting in a a negligible effect on the signal acceptance. The uncertainty on the probability for a light quark or gluon jet to be misidentified as a b-quark jet (30%) has a negligible effect on the signal acceptance.

The uncertainty on signal acceptance due to the Parton Distribution Function (PDF) set included in the simulated samples is evaluated by comparing CTEQ6.6L, MRST2006, and NNPDF10 PDF sets [94, 95, 96]. The systematic effect due to imprecise modeling of initial- and final-state radiation is determined by reweighting events to account for effects such as missing $\alpha$ terms in the soft-collinear approach [97] and missing NLO terms in the parton shower approach [98]. Finally, the uncertainty in the luminosity measurement is 2.6% [99].

Table 9.2 lists the uncertainties applied in the shape-based analysis of the $m_{jj}$ distribution for the different $m_{jj}$ bins. Uncertainties in the two columns are propagated as if they

Table 9.1: Summary of systematic uncertainties.

| Source | Signal | $W+Jets$ | $Z+Jets$ |
|---|---|---|---|
| MC stat ($SF_{\text{central}}$) | 0.1% | 4.1% | 5.1% |
| MC stat ($\varepsilon_{\text{VBF}}$) | 0.3% | $--$ | $--$ |
| Data stat ($SF_{\text{central}}$) | $--$ | 2.9% | 3.8% |
| Data stat ($\varepsilon_{\text{VBF}}$) | $--$ | 24.3% | 24.3% |
| Contamination | $--$ | 2.0% | 2.0% |
| PDF | 5% | 3.5% | 3.5% |
| ISR/FSR | 2.0% | 1.0% | 1.0% |
| Luminosity | 2.6% | 2.6% | 2.6% |
| Trigger | 5.0% | 5.0% | 5.0% |
| Lepton mis-tag rate | $<<1\%$ | $<<1\%$ | $<<1\%$ |
| b-jet mis-tag rate | $<<1\%$ | $<<1\%$ | $<<1\%$ |
| Jet Energy Scale (JES) | 2.5% | 2.5% | 2.5% |
| $p_{\text{T}}^{\text{miss}}$ uncertainty | $<<1\%$ | $<<1\%$ | $<<1\%$ |

are uncorrelated. The table does not include the global 25% systematic uncertainty from $\varepsilon_{VBF}$ measurement in data.

Table 9.2: A statistical uncertainty ($\sqrt{n}$) which varies bin-by-bin is assigned to the mjj shape systematics. The level of disagreement is less than one $\sigma$ in the tails.

| $m_{jj}$ | $\sigma$(Data/MC) in CR | Fit of Data/MC in CR |
|---|---|---|
| $[700-800]$ | 0.22 | 0.16 |
| $[800-900]$ | 0.23 | 0.16 |
| $[900-1000]$ | 0.33 | 0.16 |
| $[1000-1100]$ | 0.38 | 0.16 |
| $[1100-1200]$ | 0.43 | 0.16 |
| $[1200-1300]$ | 0.48 | 0.16 |
| $[1300-1400]$ | 0.46 | 0.16 |
| $[1400-1500]$ | 0.60 | 0.16 |
| $[1500-1600]$ | 0.83 | 0.16 |
| $[1600-1700]$ | 0.84 | 0.16 |
| $[1700-2000]$ | 0.72 | 0.16 |
| $[2000-2500]$ | 0.59 | 0.16 |
| $[2500-5000]$ | 1.28 | 0.16 |

# Chapter 10

# Results and Interpretation

## 10.1 Results and Conclusions

The number of surviving events after each consecutive cut is listed in Table 10.1 for both the expected MC background contributions and observed data events. Figure 10.1 shows the expected and observed signal rate in bins of VBF dijet mass. The observed yields in the SR are compatible with the background expectations.

Table 10.1: Predicted and observed rates for the control regions and signal region. The yields are used to calculate correction factors for the *central selections* and VBF selection efficiencies. Statistical uncertainties are cited for the predicted yields.

| Sample | $\ell/b$Vetos + 2j | $E_T^{miss}$ | VBF | SR |
|---|---|---|---|---|
| W+Jets | $1.9 \cdot 10^6 \pm 3.8 \cdot 10^3$ | $4.0 \cdot 10^3 \pm 99$ | $43.6 \pm 10.3$ | $43.6 \pm 10.3$ |
| $Z_{\nu\bar{\nu}}$+Jets | $5.6 \cdot 10^5 \pm 1.0 \cdot 10^3$ | $8.4 \cdot 10^3 \pm 99$ | $96.1 \pm 10.7$ | $88.2 \pm 9.8$ |
| $\text{Higgs}_{\text{VBF}}$ | $45.2 \pm 6.7$ | $0.4^{+0.6}_{-0.4}$ | $0.1^{+0.4}_{-0.1}$ | $0.1^{+0.4}_{-0.1}$ |
| $Z_{\ell\bar{\ell}}$+Jets | $7.9 \cdot 10^5 \pm 2.2 \cdot 10^3$ | $19.2 \pm 5.4$ | $0.03^{+0.18}_{-0.03}$ | $0.03^{+0.17}_{-0.03}$ |
| WW | $3.0 \cdot 10^4 \pm 187$ | $42.2 \pm 7.0$ | $0.1^{+0.3}_{-0.1}$ | $0.1^{+0.3}_{-0.1}$ |
| WZ | $4.3 \cdot 10^3 \pm 68$ | $132.3 \pm 12.0$ | $0.4^{+0.6}_{-0.4}$ | $0.4^{+0.6}_{-0.4}$ |
| ZZ | $3.9 \cdot 10^3 \pm 66$ | $120.1 \pm 11.6$ | $0.0^{+0.2}_{-0.0}$ | $0.0^{+0.2}_{-0.0}$ |
| $t\bar{t}$ | $4.6 \cdot 10^3 \pm 88$ | $38.3 \pm 8.0$ | $0.0^{+0.7}_{-0.0}$ | $0.0^{+0.7}_{-0.0}$ |
| $\Sigma_{\text{MC}}$ | $3.4 \cdot 10^6 \pm 4.5 \cdot 10^3$ | $1.3 \cdot 10^4 \pm 142$ | $140.3 \pm 14.8$ | $132.4 \pm 14.2$ |
| Data | $4.1 \cdot 10^6$ | 307 | 120 | 118 |

The results are used to constrain the production of new phenomena in the context of two signal models: $\chi\chi jj$ and $\tilde{b}\tilde{b}jj$. The interaction between the DM particle, $\chi$, and the electroweak gauge bosons of the SM is assumed to be mediated by a heavy particle such that it can be treated as a contact interaction characterized by a scale $\Lambda = \mathscr{M}/g_{eff} = \mathscr{M}/\sqrt{g_\chi g_V}$, where $\mathscr{M}$ is the mass of the mediator, $g_\chi$ its coupling to $\chi$, and $g_V$ its coupling to V=$\gamma$/Z/W [100]. The DM particle $\chi$ is assumed to be a Dirac fermion. In this paper, only the Higgs portal operators of scaling dimension $d = 5$ are considered. For these operators only the 4-point $\chi\chi$VV contact interactions are allowed. In the case of the $\tilde{b}\tilde{b}jj$ signal

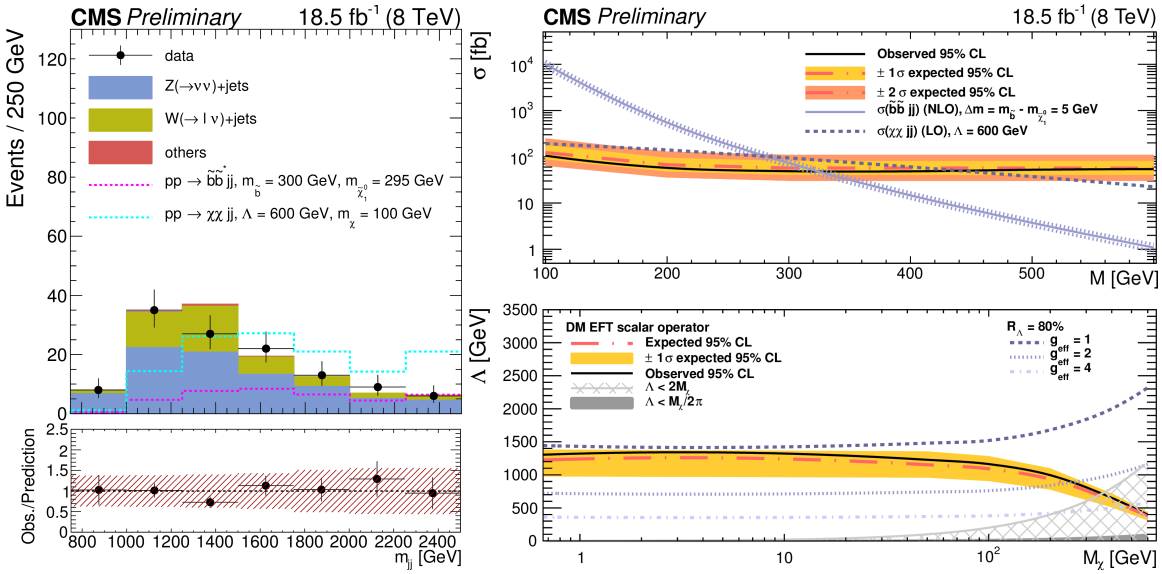


Figure 10.1: (top) $m_{jj}$ distribution after all signal region selections, where the shaded band in the ratio plot includes the systematic and statistical uncertainties in the background prediction. (upper right) Upper limit at the 95% CL on the cross-section as a function of mass $M = m_\chi = m_{\tilde{b}}$. (lower right) The 95% CL on the contact interaction scale, $\Lambda$, as a function of the DM mass, $M_\chi$, for the scalar effective field theory DM model. The validity of the effective field theory is quantified by $R_\Lambda = 80\%$ contours, corresponding to different values of the effective coupling $g_{eff}$.

model, the results are interpreted by assuming $Br(\tilde{b} \to b\tilde{\chi}_1^0) = 1$. The mass difference between $\tilde{b}$ and $\tilde{\chi}_1^0$ is 5 GeV, and thus the $\tilde{b}$ decays into a soft b-quark which is typically not identified. The signal samples were generated for masses of $100 - 600$ GeV, in step sizes of 50 GeV. The signal acceptance for these samples is on the order of 3-6%, depending on the mass.

The calculation of the exclusion limit is obtained by computing the 95% confidence level (CL) upper limit on the signal cross-section using the $CL_s$ method [101, 102]. Systematic uncertainties are represented by nuisance parameters, which are removed by marginalization, assuming a gamma or log-normal prior for normalization parameters, and Gaussian priors for mass-spectrum shape uncertainties.

Figure 10.1 (upper right) shows the expected and observed upper limits, as well as the theoretical cross-sections, as functions of mass $M = m_\chi = m_{\tilde{b}}$. DM masses below 420 GeV

are excluded for a contact interaction scale $\Lambda = 600$ GeV. Since the $\chi\chi jj$ cross-sections are proportional to $1/\Lambda^2$ for contact operators of dimension $d = 5$, results for $\Lambda \neq 600$ GeV can be obtained by appropriately scaling the theoretical cross-section. The validity of the DM signal model using an effective field theory (EFT) approach is quantified by the fraction of signal events, $R_\Lambda$, satisfying the condition that the center of mass energy of DM-DM system is less than $\Lambda$ times $g_{eff}$ of the model. Figure 10.1 (lower right) shows curves corresponding to $R_\Lambda$ = 80% with $g_{eff}$ = 1,2,4. For a nearly mass-degenerate bottom squark and LSP ($m_{\tilde{b}} - m_{\tilde{\chi}_1^0} = 5$ GeV) this analysis sets the most stringent limits reported to date, excluding scalar bottom quarks up to masses of 315 GeV at 95% confidence limit.

# Appendix A

# Appendix

## A.1 Simulated Samples

Table A.1: MC Samples

| Process | Official CMS Datasets |
|---|---|
| $Z \to \tau\tau$ | */DYToTauTau_M-20_CT10_TuneZ2star_v2_8TeV-powheg-tauola-pythia6/Summer12_DR53X-PU_S10_START53_V7A-v2* |
| $Z \to \mu\mu$ | */DYToMuMu_M-20_CT10_TuneZ2star_v2_8TeV-powheg-pythia6/Summer12_DR53X-PU_S10_START53_V7A-v1* |
| $Z \to ee$ | */DYToEE_M-20_CT10_TuneZ2star_v2_8TeV-powheg-pythia6/Summer12_DR53X-PU_S10_START53_V7A-v1* |
| $Z \to ll(10 < m_{ll} < 50)$ | */DYJetsToLL_M-10To50_TuneZ2Star_8TeV-madgraph/Summer12_DR53X-PU_S10_START53_V7A-v1/AODSIM* |
| $Z \to ll(m_{ll} > 50)$ | */DYJetsToLL_M-50_TuneZ2Star_8TeV-madgraph-tarball/Summer12_DR53X-PU_S10_START53_V7A-v1/AODSIM* |
| $Z \to ll + 1\,jets$ | */DY1JetsToLL_M-50_TuneZ2Star_8TeV-madgraph/Summer12_DR53X-PU_S10_START53_V7A-v1/AODSIM* |
| $Z \to ll + 2\,jets$ | */DY2JetsToLL_M-50_TuneZ2Star_8TeV-madgraph/Summer12_DR53X-PU_S10_START53_V7A-v1/AODSIM* |
| $Z \to ll + 3\,jets$ | */DY3JetsToLL_M-50_TuneZ2Star_8TeV-madgraph/Summer12_DR53X-PU_S10_START53_V7A-v1/AODSIM* |
| $Z \to ll + 4\,jets$ | */DY4JetsToLL_M-50_TuneZ2Star_8TeV-madgraph/Summer12_DR53X-PU_S10_START53_V7A-v1/AODSIM* |
| $Z \to ll$ EWK | */DYJJ01JetsToLL_M-50_MJJ-200_TuneZ2Star_8TeV-madgraph_tauola/Summer12_DR53X-PU_S10_START53_V7A-v1/* |
| $W + jets$ | */WJetsToLNu_TuneZ2Star_8TeV-madgraph-tarball/Summer12_DR53X-PU_S10_START53_V7A-v2* |
| $W + 1\,jet$ | */W1JetsToLNu_TuneZ2Star_8TeV-madgraph/Summer12_DR53X-PU_S10_START53_V7A-v1/AODSIM* |
| $W + 2\,jet$ | */W2JetsToLNu_TuneZ2Star_8TeV-madgraph/Summer12_DR53X-PU_S10_START53_V7A-v1/AODSIM* |
| $W + 3\,jet$ | */W3JetsToLNu_TuneZ2Star_8TeV-madgraph/Summer12_DR53X-PU_S10_START53_V7A-v1/AODSIM* |
| $W + 4\,jet$ | */W4JetsToLNu_TuneZ2Star_8TeV-madgraph/Summer12_DR53X-PU_S10_START53_V7A-v1/AODSIM* |
| $t\bar{t}$ | */TTJets_MassiveBinDECAY_TuneZ2star_8TeV-madgraph-tauola/Summer12_DR53X-PU_S10_START53_V7C-v1* |
| $WW(\to 2l2\nu)$ | */WWJetTo2L2Nu_8TeV-powheg-pythia6/Summer12_DR53X-PU_S10_START53_V7C-v1* |
| $W^+W^+$ | */WpWpqq_8TeV-madgraph/Summer12_DR53X-PU_S10_START53_V7A-v1* |
| $W^-W^-$ | */WmWmqq_8TeV-madgraph/Summer12_DR53X-PU_S10_START53_V7A-v1* |
| $WW$ double scattering | */WW_DoubleScattering_8TeV-pythia8/Summer12_DR53X-PU_S10_START53_V7A-v1* |
| $WW$ EWK | */WWjjTo2L2Nu_8TeV_madgraph_qed6_qcd0/Summer12_DR53X-PU_S10_START53_V19-v1/AODSIM* |
| $WZ(\to 2q2\nu)$ | */WZJetsTo2Q2Nu_TuneZ2star_8TeV-madgraph-tauloa/Summer12_DR53X-PU_S10_START53_V7A-v1* |
| $WZ(\to 2l2\nu)$ | */WZJetsTo2L2Nu_TuneZ2star_8TeV-madgraph-tauloa/Summer12_DR53X-PU_S10_START53_V7A-v1* |
| $WZ(\to 3l)$ | */WZJetsTo3L_TuneZ2star_8TeV-madgraph-tauloa/Summer12_DR53X-PU_S10_START53_V7A-v1* |
| $ZZ(\to 2q2\nu)$ | */ZZJetsTo2Q2Nu_TuneZ2star_8TeV-madgraph-tauloa/Summer12_DR53X-PU_S10_START53_V7A-v1* |
| $ZZ(\to 2l2\nu)$ | */ZZJetsTo2L2Nu_TuneZ2star_8TeV-madgraph-tauloa/Summer12_DR53X-PU_S10_START53_V7A-v1* |
| $ZZ(\to 2l2q)$ | */ZZJetsTo2L2Q_TuneZ2star_8TeV-madgraph-tauloa/Summer12_DR53X-PU_S10_START53_V7A-v1* |
| $ZZ(\to 4l)$ | */ZZJetsTo4L_TuneZ2star_8TeV-madgraph-tauloa/Summer12_DR53X-PU_S10_START53_V7A-v1* |
| $H \to WW(\to 2l)$ | */VBF_HToWWTo2LAndTau2Nu_M-125_8TeV-powheg-pythia6/Summer12_DR53X-PU_S10_START53_V7A-v1* |
| $H \to ZZ(\to 2l2\nu)$ | */VBF_HToZZTo2L2Nu_M-120_8TeV-powheg-pythia6/Summer12_DR53X-PU_S10_START53_V7A-v1* |
| $H \to ZZ(\to 2l2q)$ | */VBF_HToZZTo2L2Q_M-125_8TeV-powheg-pythia6/Summer12_DR53X-PU_S10_START53_V7A-v1* |
| $H \to ZZ(\to 4l)$ | */VBF_HToZZTo4L_M-125_8TeV-powheg-pythia6/Summer12_DR53X-PU_S10_START53_V7A-v1/AODSIM* |
| $H \to ZZ(\to 4\nu)$ | */VBF_HToZZTo4Nu_M-120_8TeV-pythia6/Summer12_DR53X-PU_S10_START53_V7A-v1/AODSIM* |
| $H \to \tau\tau$ | */VBF_HToTauTau_M-125_8TeV-powheg-pythia6/Summer12_DR53X-PU_S10_START53_V7A-v1* |
| $QCD(* < p_T < *)$ | */QCD_Pt-*to*_TuneZ2star_8TeV_pythia6/Summer12_DR53X-PU_S10_START53_V7A-v1/AODSIM* |
| $Z \to \nu\nu + jets(* < H_T < *)$ | */ZJetsToNuNu_*_HT_*_TuneZ2Star_8TeV_madgraph/Summer12_DR53X-PU_S10_START53_V7A-v1/AODSIM* |

## A.2 VBF Trigger Performance with Monte Carlo Samples

Figures A.1 and A.2 show the CALO-based **DiJet35_MJJ700_AllJets_DEta3p5_VBF_v*** trigger efficiency as a function of $m_{jj}$ for various $p_{\mathrm{T}}^{\mathrm{miss}}$ cuts. For a low $p_{\mathrm{T}}^{\mathrm{miss}}$ cut of 50 GeV, the trigger efficiency reaches $\sim 70\%$ at around $m_{jj} = 750$ GeV with a plateau efficiency of $\sim 85\%$. The inefficiency of the trigger in these plots is a reflection of the slow trigger turn-on for the L1 $p_{\mathrm{T}}^{\mathrm{miss}}$ seed. At L1, the computation of $H_{\mathrm{T}}$ does not include jets with $|\eta| > 3.0$. The effect of this L1 $H_{\mathrm{T}}$ seed definition is a degradation in trigger efficiency for the $\widetilde{\chi}_1^0\widetilde{\chi}_1^0 jj$ signal samples at values of $m_{jj} \sim 2$ TeV (when $|\Delta\eta_{jj}| > 6.0$). This loss of efficiency is not seen in simulated $\mathrm{Z}(\rightarrow \nu\bar{\nu})$ + jets events due to the more central nature of this background. It is interesting to note that the inefficiency at high $m_{jj}$ is less pronounced with higher $p_{\mathrm{T}}^{\mathrm{miss}}$ cut values since the L1 trigger is mostly satisfied through the $p_{\mathrm{T}}^{\mathrm{miss}}$ seed and therefore does not rely on L1 $H_{\mathrm{T}}$ (does not rely on whether events with $|\Delta\eta_{jj}| > 6.0$ pass L1 $H_{\mathrm{T}}$).

From Figure A.2, it is also worth noting that the trigger efficiency for signal and $\mathrm{Z}(\rightarrow \nu\bar{\nu})$ + jets background events is similar for $p_{\mathrm{T}}^{\mathrm{miss}}$ cuts larger than 50 GeV. This feature provides a nice handle for understanding the trigger efficiency for signal events by measuring it with $\mathrm{Z}(\rightarrow \nu\bar{\nu})$ + jets control samples in data. Figures A.3 and A.4 show the efficiency of the CALO-based trigger as a function of $p_{\mathrm{T}}^{\mathrm{miss}}$ for various $m_{jj}$ cuts. For $m_{jj} > 750$ GeV, the trigger efficiency reaches $\sim 70\%$ at around $p_{\mathrm{T}}^{\mathrm{miss}} = 75$ GeV with a plateau efficiency of $\sim 100\%$ at $p_{\mathrm{T}}^{\mathrm{miss}} = 200$ GeV..

Figures A.5 and A.6 show the PF-based **HLT_DiPFJet40_PFMETnoMu65_MJJ600VBF_LeadingJets_v*** trigger efficiency as a function of $m_{jj}$ for various $p_{\mathrm{T}}^{\mathrm{miss}}$ cuts. For background $\mathrm{Z}(\rightarrow \nu\bar{\nu})$ + jets events, the trigger efficiency as a function of $m_{jj}$ for $p_{\mathrm{T}}^{\mathrm{miss}} > 50$ GeV is significantly lower than the CALO-based VBF trigger efficiency. The PF-based VBF trigger is seeded by only L1 $p_{\mathrm{T}}^{\mathrm{miss}}$, whereas the CALO-based VBF trigger is seeded by both L1 $p_{\mathrm{T}}^{\mathrm{miss}}$ and L1 $H_{\mathrm{T}}$. Thus, events with low $p_{\mathrm{T}}^{\mathrm{miss}}$ can be picked up by the CALO-based trigger, but not the PF-based trigger. This can be seen from Figures A.7 and A.8,

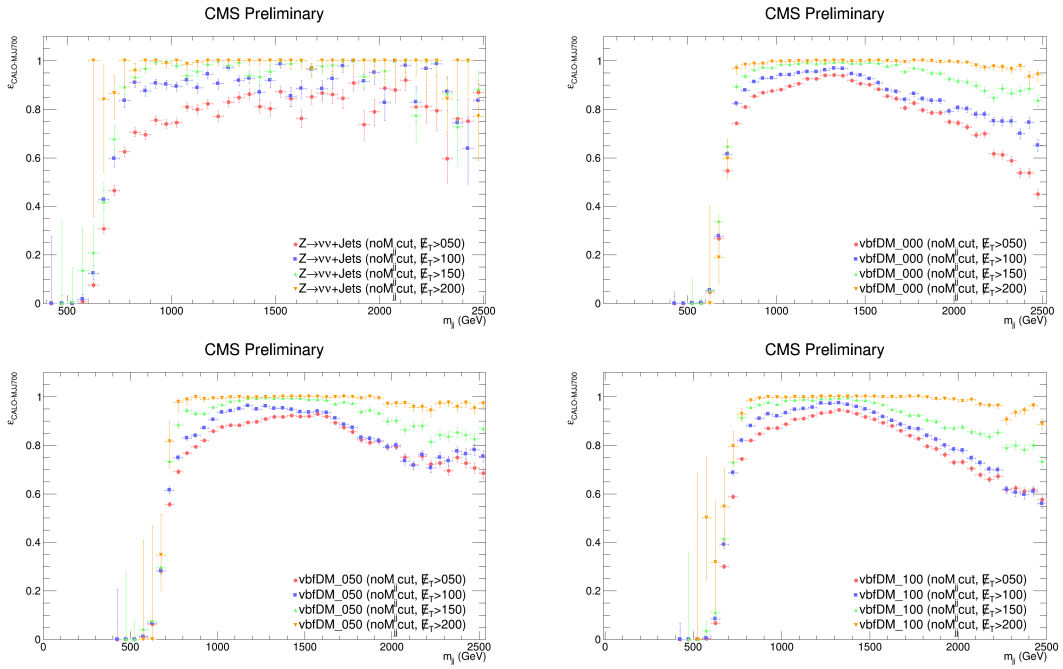


Figure A.1: $\varepsilon_{\textbf{DiJet35\_MJJ700\_AllJets\_DEta3p5\_VBF\_v*}}$ vs. $m_{jj}$ given various $p_{\mathrm{T}}^{\mathrm{miss}}$ selections for (a) $\mathrm{Z}(\rightarrow \nu\bar{\nu})$ + jets and $\widetilde{\chi}_1^0\widetilde{\chi}_1^0 jj$ with LSP mass of (b) 0 GeV, (c) 50 GeV, and (d) 100 GeV.

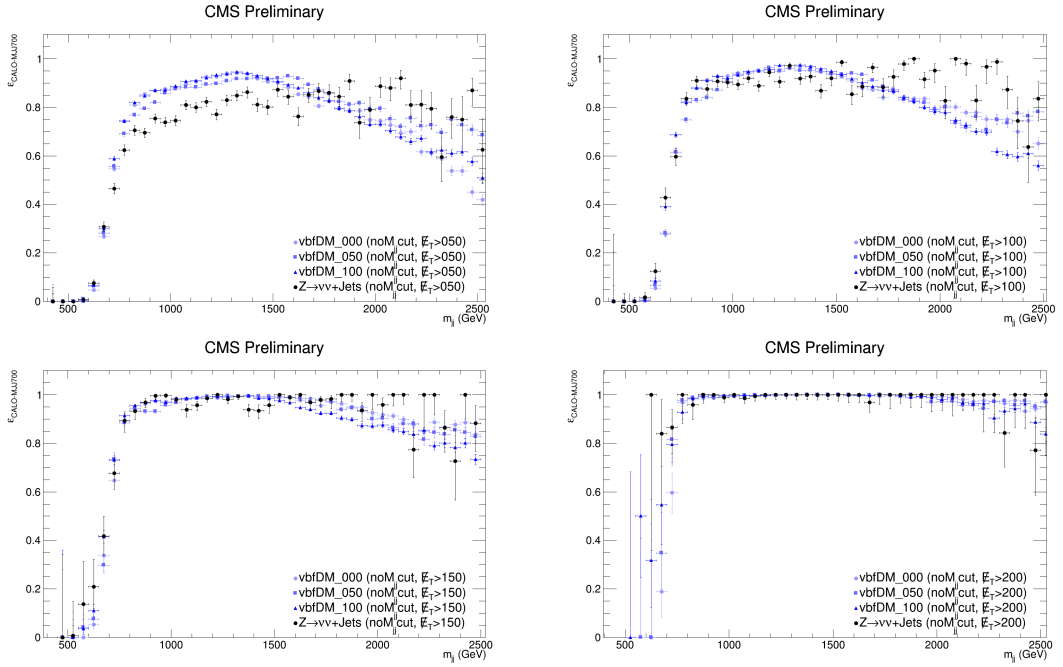


Figure A.2: $\varepsilon_{\textbf{DiJet35\_MJJ700\_AllJets\_DEta3p5\_VBF\_v*}}$ vs. $m_{jj}$ given various $p_{\mathrm{T}}^{\mathrm{miss}}$ selections for (a) $\mathrm{Z}(\rightarrow \nu\bar{\nu})$ + jets and $\widetilde{\chi}_1^0\widetilde{\chi}_1^0 jj$ with LSP mass of (b) 0 GeV, (c) 50 GeV, and (d) 100 GeV.

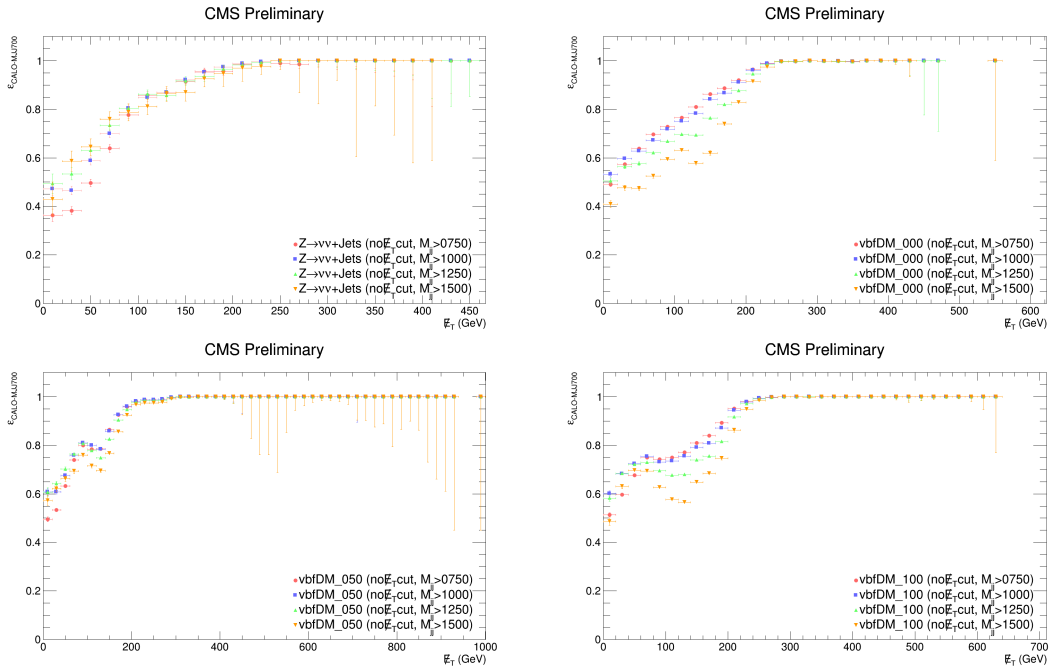


Figure A.3: $\varepsilon_{\textbf{DiJet35\_MJJ700\_AllJets\_DEta3p5\_VBF\_v*}}$ vs. $p_{\mathrm{T}}^{\mathrm{miss}}$ given various $m_{jj}$ selections for (a) $\mathrm{Z}(\rightarrow \nu\bar{\nu})$ + jets and $\widetilde{\chi}_1^0\widetilde{\chi}_1^0 jj$ with LSP mass of (b) 0 GeV, (c) 50 GeV, and (d) 100 GeV.

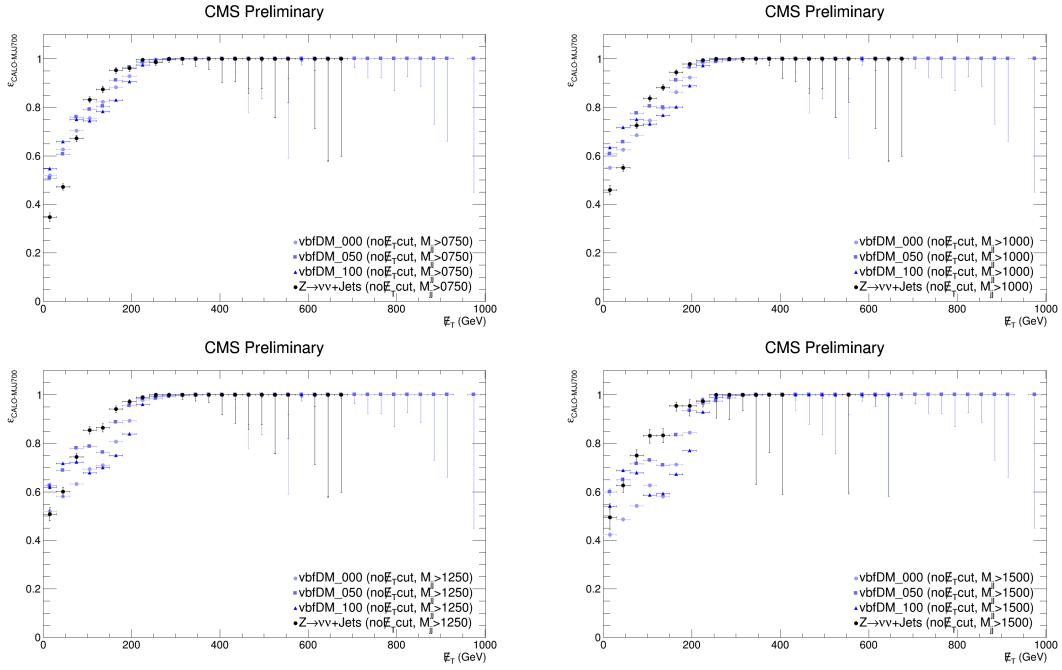


Figure A.4: $\varepsilon_{\textbf{DiJet35\_MJJ700\_AllJets\_DEta3p5\_VBF\_v*}}$ vs. $p_{\mathrm{T}}^{\mathrm{miss}}$ given various $m_{jj}$ selections for (a) $\mathrm{Z}(\rightarrow \nu\bar{\nu})$ + jets and $\widetilde{\chi}_1^0\widetilde{\chi}_1^0 jj$ with LSP mass of (b) 0 GeV, (c) 50 GeV, and (d) 100 GeV.

which show the **HLT_DiPFJet40_PFMETnoMu65_MJJ600VBF_LeadingJets_v*** trigger efficiency as a function of $p_{\mathrm{T}}^{\mathrm{miss}}$ for various $m_{jj}$ cuts. The $p_{\mathrm{T}}^{\mathrm{miss}}$ distributions show this trigger becoming efficient after 75 GeV.

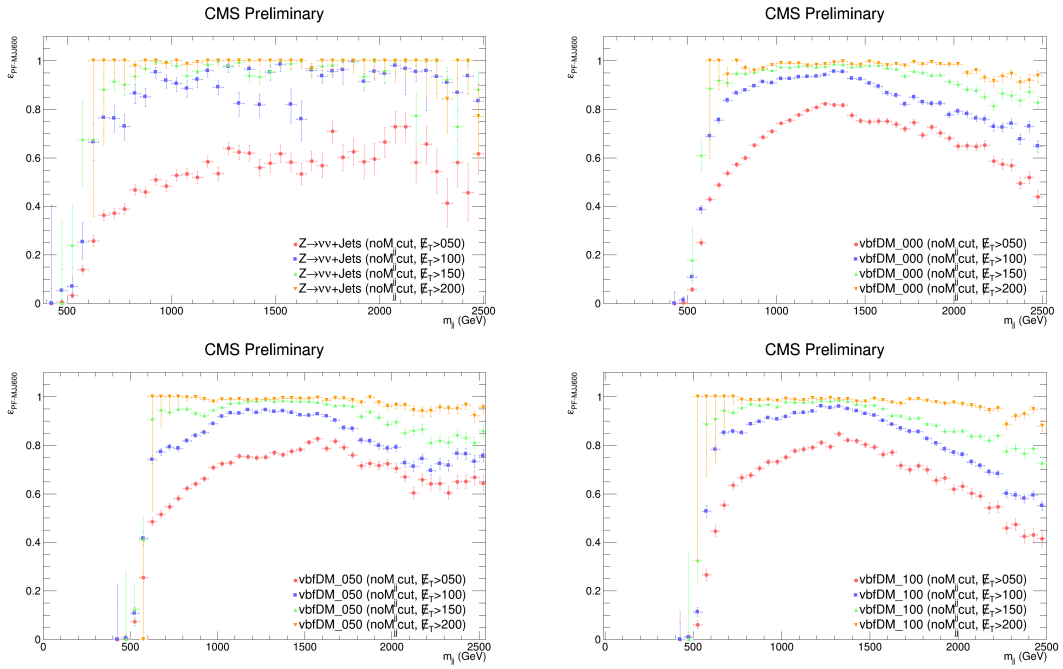


Figure A.5: $\varepsilon_{\textbf{HLT\_DiPFJet40\_PFMETnoMu65\_MJJ600VBF\_LeadingJets\_v}*}$ vs. $m_{jj}$ given various $p_{\mathrm{T}}^{\mathrm{miss}}$ selections for (a) $\mathrm{Z}(\rightarrow \nu\bar{\nu})$ + jets and $\widetilde{\chi}_1^0\widetilde{\chi}_1^0 jj$ with LSP mass of (b) 0 GeV, (c) 50 GeV, and (d) 100 GeV.

Figures A.9 and A.10 show the PF-based **HLT_DiPFJet40_PFMETnoMu65_MJJ800VBF_AllJets_v*** trigger efficiency as a function of $m_{jj}$ for various $p_{\mathrm{T}}^{\mathrm{miss}}$ cuts. This second PF-based trigger, which selects events with $m_{jj} > 800$ GeV, also reaches an efficiency plateau at approximately 750 GeV. Figures A.11 and A.12 show the **HLT_DiPFJet40_PFMETnoMu65_MJJ800VBF_AllJets_v*** trigger efficiency as a function of $p_{\mathrm{T}}^{\mathrm{miss}}$ for various $m_{jj}$ cuts. The trigger efficiency in the $p_{\mathrm{T}}^{\mathrm{miss}}$ distribution becomes efficient after 75 GeV.

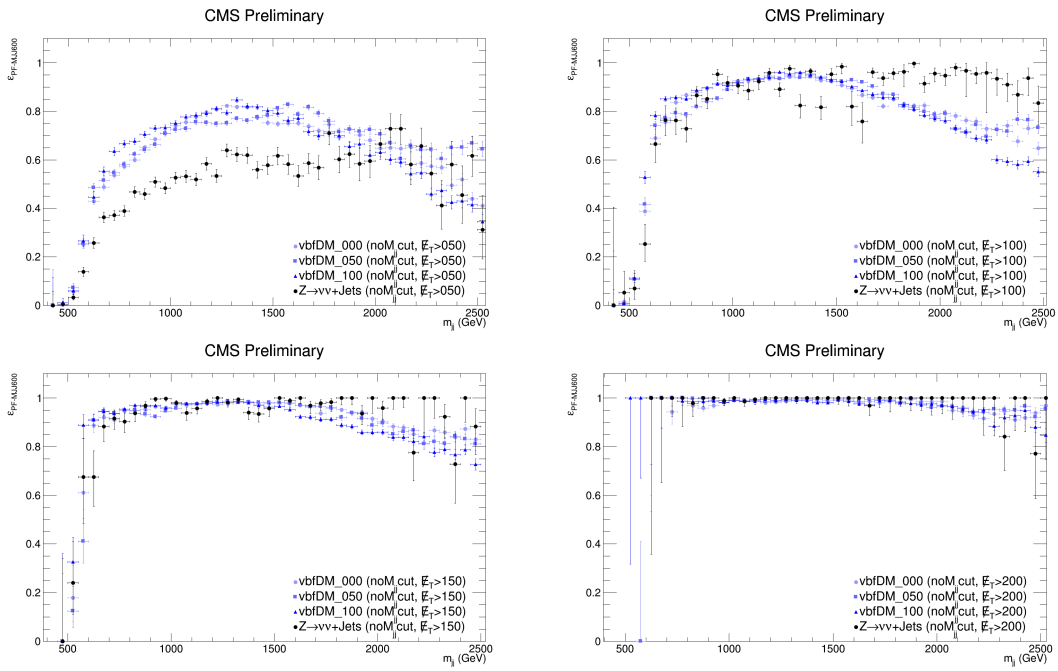


Figure A.6: $\varepsilon_{\textbf{HLT\_DiPFJet40\_PFMETnoMu65\_MJJ600VBF\_LeadingJets\_v*}}$ vs. $m_{jj}$ given various $p_{\mathrm{T}}^{\mathrm{miss}}$ selections for (a) $\mathrm{Z}(\rightarrow \nu\bar{\nu})$ + jets and $\tilde{\chi}_1^0\tilde{\chi}_1^0 jj$ with LSP mass of (b) 0 GeV, (c) 50 GeV, and (d) 100 GeV.

## A.3 Validation

### A.3.1 Statistical Features of Trigger Efficiency in Data Events

As evident in Figure 6.14(a)-(d), the trigger efficiency in data events as a function of $p_{\mathrm{T}}^{\mathrm{miss}}$ does not appear to increase monotonically. Since events with $p_{\mathrm{T}}^{\mathrm{miss}} < 250$ GeV are discarded in the final selection, this effect should not be important. However, several studies were carried out to investigate this feature in the data trigger efficiency curves. The data trigger efficiency calcualtion was reproduced with $\mathrm{W}_{\mu}$+Jets events, where the $p_{\mathrm{T}}^{\mathrm{miss}}$ in the event was recomputed after subtracting the $p_{\mathrm{T}}^{\mu}$ (thus treating the muons as neutrinos). Additionally, the data trigger efficiency calcualtion was reproduced with $\mathrm{Z}_{ee}$+Jets events, where the $p_{\mathrm{T}}^{\mathrm{miss}}$ in the event was recomputed after subtracting the $p_{\mathrm{T}}^{ee}$ (thus treating the electrons as neutrinos). Figure A.13(a) shows the trigger turn-on curves in data events as a function

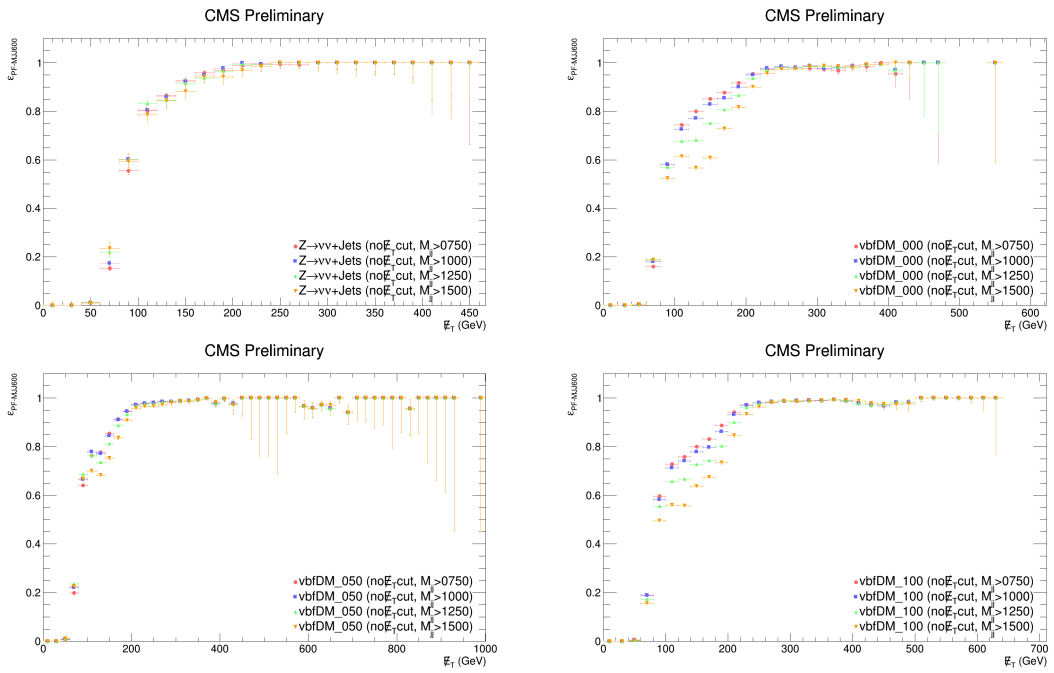


Figure A.7: $\varepsilon_{\textbf{HLT\_DiPFJet40\_PFMETnoMu65\_MJJ600VBF\_LeadingJets\_v*}}$ vs. $p_{\mathrm{T}}^{\mathrm{miss}}$ given various $m_{jj}$ selections for (a) $\mathrm{Z}(\rightarrow \nu\bar{\nu})$ + jets and $\widetilde{\chi}_1^0\widetilde{\chi}_1^0 jj$ with LSP mass of (b) 0 GeV, (c) 50 GeV, and (d) 100 GeV.

of $p_{\mathrm{T}}^{\mathrm{miss}}$ for the three methods described. The plot indicates that the feature in the trigger efficiency curve for $\mathrm{Z}_{\mu^+\mu^-\rightarrow\nu\bar{\nu}}$+Jets data events is likely due to limited statistics. Figure A.13(b) shows the trigger turn-on curve corresponding to the sum of $\mathrm{Z}_{\mu^+\mu^-\rightarrow\nu\bar{\nu}}$+Jets and $\mathrm{W}_{\mu\rightarrow\nu}$+Jets data events, again suggesting that the effect is due to limited statistics in the sample of $\mathrm{Z}_{\mu^+\mu^-\rightarrow\nu\bar{\nu}}$+Jets events.

### A.3.2 Validation of Number of b-jets distribution in Z_CR1

A study was done to check for consistency between the expected and observed number of b-jets for the Z_CR1, shown in Figure A.14(a). The general strategy was to determine the corresponding light-quark b-jet data/MC correction factor, use this factor to calculate the expected the data/MC value in each bin of the $\mathrm{N}_{\text{b-jet}}$ distribution, and finally compare the predicted and observed values of the ratio of data/MC events in said distribution. The

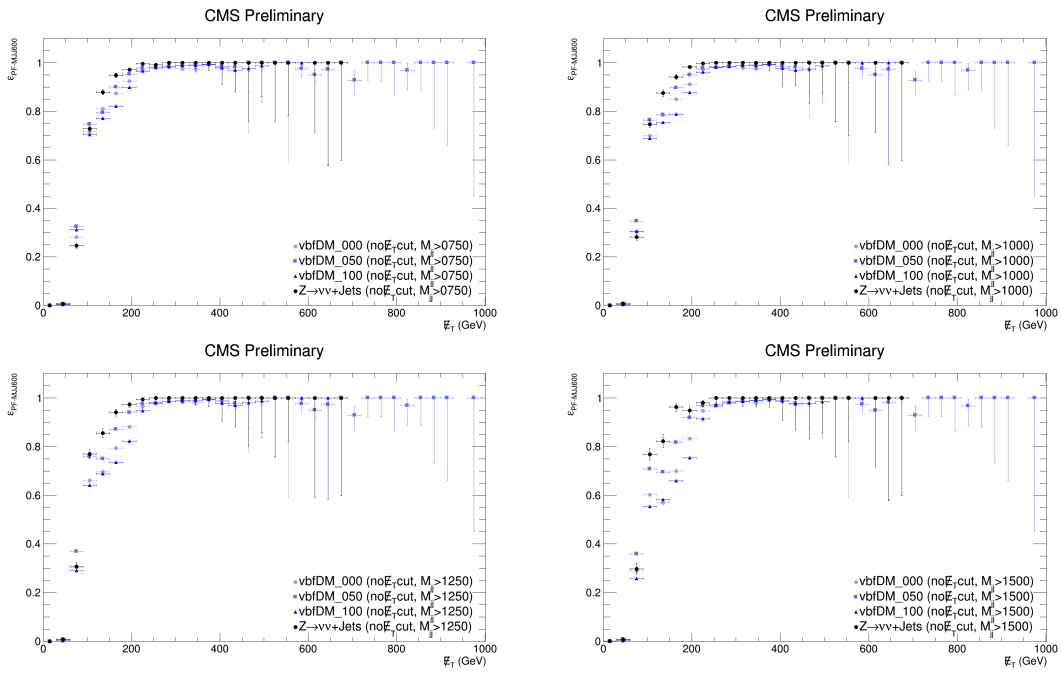


Figure A.8: $\varepsilon_{\textbf{HLT\_DiPFJet40\_PFMETnoMu65\_MJJ600VBF\_LeadingJets\_v*}}$ vs. $p_{\mathrm{T}}^{\mathrm{miss}}$ given various $m_{jj}$ selections for (a) $\mathrm{Z}(\rightarrow \nu\bar{\nu})$ + jets and $\widetilde{\chi}_1^0\widetilde{\chi}_1^0 jj$ with LSP mass of (b) 0 GeV, (c) 50 GeV, and (d) 100 GeV.

b-jet data/MC correction factor ($\mathrm{SF}_{\mathrm{CSVL}}(p_{\mathrm{T}}^{j})$) was read in from a database using methods outlined here [103]. The $p_{\mathrm{T}}$-dependent b-jet mis-identification scale factors were applied as weights to the DY+Jets MC, yielding the following predicted values for the data/WeightedMC:

- Predicted Data/WeightedMC in $\mathrm{N}_{\text{b-jet}} = 0 : 0.93 \pm 0.02$
- Predicted Data/WeightedMC in $\mathrm{N}_{\text{b-jet}} = 1 : 1.08 \pm 0.09$
- Predicted Data/WeightedMC in $\mathrm{N}_{\text{b-jet}} = 2 : 1.21 \pm 0.15$

These predicted values are consistent, within statistical uncertainties, to the observed data/MC values:

- Observed Data/MC in $\mathrm{N}_{\text{b-jet}} = 0 : 0.890 \pm 0.010$
- Observed Data/MC in $\mathrm{N}_{\text{b-jet}} = 1 : 1.086 \pm 0.019$

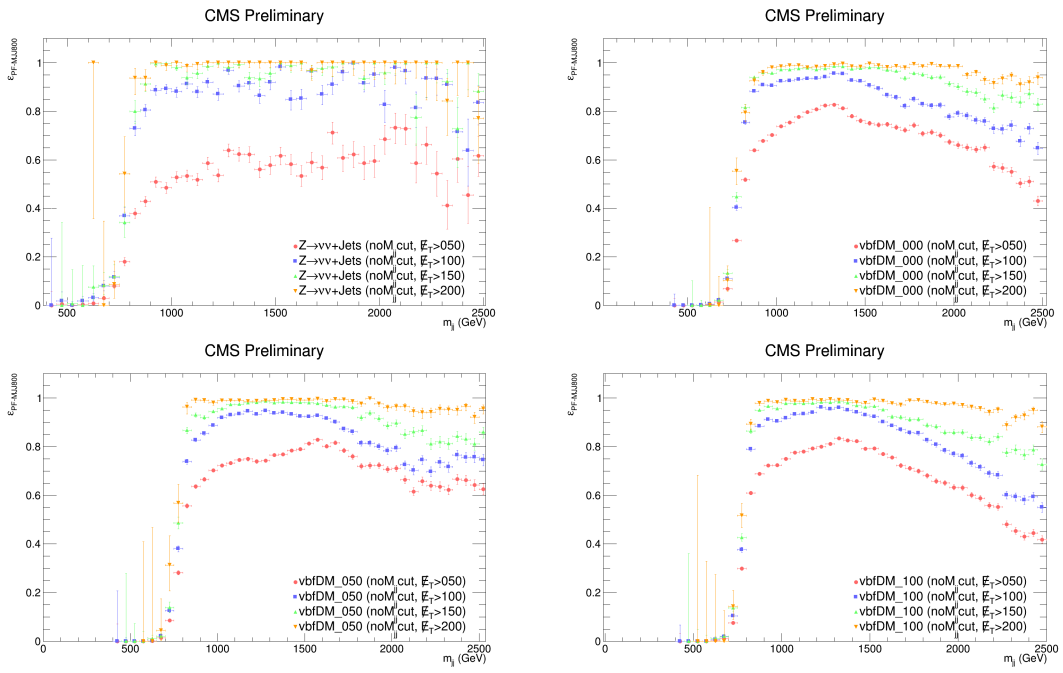


Figure A.9: $\varepsilon_{\textbf{HLT\_DiPFJet40\_PFMETnoMu65\_MJJ800VBF\_AllJets\_v*}}$ vs. $m_{jj}$ given various $p_{\mathrm{T}}^{\mathrm{miss}}$ selections for (a) $\mathrm{Z}(\rightarrow \nu\bar{\nu})$ + jets and $\tilde{\chi}_1^0\tilde{\chi}_1^0 jj$ with LSP mass of (b) 0 GeV, (c) 50 GeV, and (d) 100 GeV.

- Observed Data/MC in $\mathrm{N_{b\text{-}jet}} = 2 : 1.047 \pm 0.030$

As an extra check, an additional simple combinatorics calculation is performated for a fixed $\mathrm{SF}_{\mathrm{CSVL}}^{p_{\mathrm{T}}^{j}=50\ \mathrm{GeV}} = 1.18 \pm 0.06$:

**Given $\mathbf{N_{b\text{-}jet}} = 1$**

- Probability for MC events with 1 real jet to fake 1 b-jet
  - $\mathrm{P_{MC}}(1\mathrm{b}|1\mathrm{j}) = f = 0.10 \pm [0.10 \cdot \sqrt{(0.01)^2 + (0.05)^2}] = 0.10 \pm 0.01$
- Probability for data events with 1 real jet to fake 1 b-jet
  - $\mathrm{P_{data}}(1\mathrm{b}|1\mathrm{j}) = f \cdot \mathrm{SF_{CSVL}} = (0.10 \pm 0.01) \cdot (1.18 \pm 0.06) = 0.12 \pm 0.01$
- Probability for MC events with 2 real jets to fake 1 b-jet

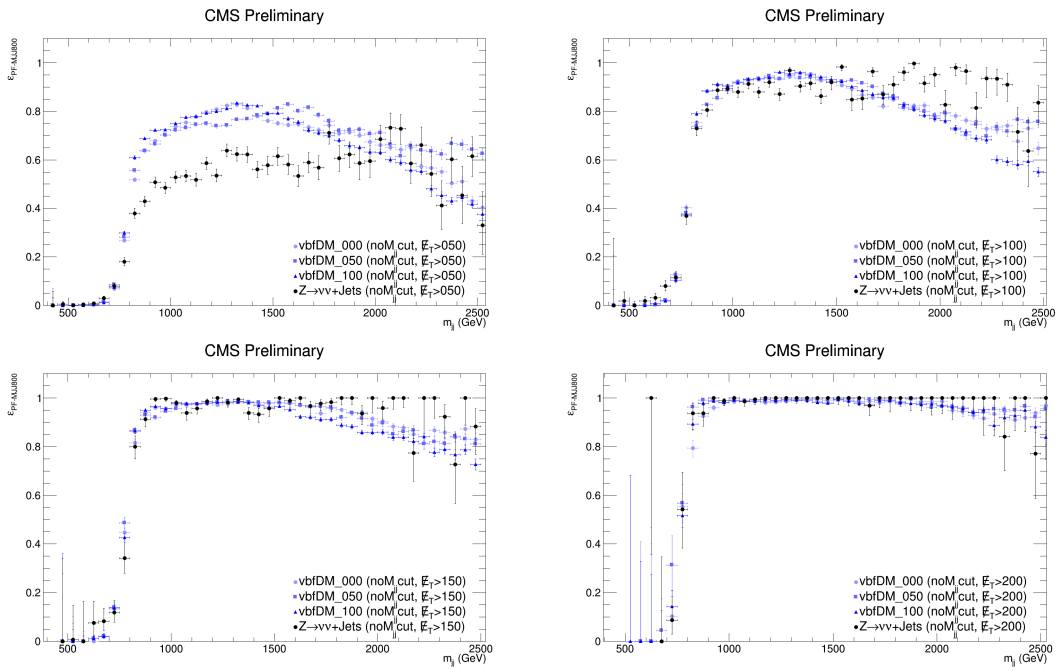


Figure A.10: $\varepsilon_{\textbf{HLT\_DiPFJet40\_PFMETnoMu65\_MJJ800VBF\_AllJets\_v*}}$ vs. $m_{jj}$ given various $p_{\mathrm{T}}^{\mathrm{miss}}$ selections for (a) $\mathrm{Z}(\rightarrow \nu\bar{\nu})$ + jets and $\tilde{\chi}_1^0\tilde{\chi}_1^0 jj$ with LSP mass of (b) 0 GeV, (c) 50 GeV, and (d) 100 GeV.

  - $\mathrm{P_{MC}(1b|2j)} = 2 \cdot f \cdot (1-f) = 0.18 \pm 0.01$

- Probability for data events with 2 real jets to fake 1 b-jet

  - $\mathrm{P_{data}(1b|2j)} = 2 \cdot f \cdot \mathrm{SF_{CSVL}} \cdot (1 - f \cdot \mathrm{SF_{CSVL}}) = 0.21 \pm 0.02$

- Expected data/MC value in $\mathrm{N_{b\text{-}jet}} = 1$ bin given 2 jets

  - $\frac{\mathrm{P_{data}(1b|2j)}}{\mathrm{P_{MC}(1b|2j)}} = 1.16 \pm 0.10$

**Given $\mathbf{N_{b\text{-}jet}} = 2$**

- Probability for MC event with 2 real jets to fake 2 b-jets

  - $\mathrm{P_{MC}(2b|2j)} = f \cdot f = 0.010 \pm 0.001$

- Probability for data event with 2 real jets to fake 2 b-jets

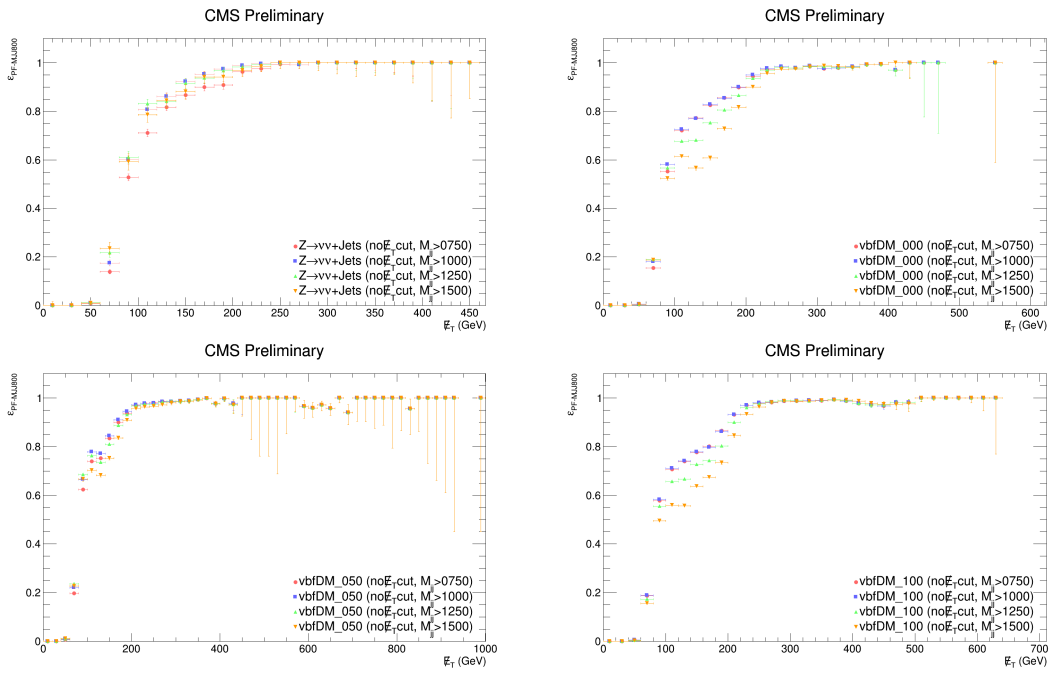


Figure A.11: $\varepsilon_{\textbf{HLT\_DiPFJet40\_PFMETnoMu65\_MJJ800VBF\_AllJets\_v*}}$ vs. $p_{\mathrm{T}}^{\mathrm{miss}}$ given various $m_{jj}$ selections for (a) $\mathrm{Z}(\rightarrow \nu\bar{\nu})$ + jets and $\tilde{\chi}_1^0\tilde{\chi}_1^0 jj$ with LSP mass of (b) 0 GeV, (c) 50 GeV, and (d) 100 GeV.

  - $\mathrm{P}_{\mathrm{data}}(2\mathrm{b}|2\mathrm{j}) = f \cdot \mathrm{SF}_{\mathrm{CSVL}} \cdot f \cdot \mathrm{SF}_{\mathrm{CSVL}} = 0.014 \pm 0.001$

- Expected data/MC value in $\mathrm{N}_{\text{b-jet}} = 2$ bin given 2 jets
  - $\frac{\mathrm{P}_{\mathrm{data}}(2\mathrm{b}|2\mathrm{j})}{\mathrm{P}_{\mathrm{MC}}(2\mathrm{b}|2\mathrm{j})} = 1.39 \pm 0.17$

**Given $\mathrm{N}_{\text{b-jet}} = 0$**

- Probability for MC event with 2 real jets to fake 0 b-jets
  - $\mathrm{P}_{\mathrm{MC}}(0\mathrm{b}|2\mathrm{j}) = 1 - \mathrm{P}_{\mathrm{MC}}(1\mathrm{b}|2\mathrm{j}) - \mathrm{P}_{\mathrm{MC}}(2\mathrm{b}|2\mathrm{j}) = 0.81 \pm 0.01$
- Probability for data event with 2 real jets to fake 0 b-jets
  - $\mathrm{P}_{\mathrm{data}}(0\mathrm{b}|2\mathrm{j}) = 1 - \mathrm{P}_{\mathrm{data}}(1\mathrm{b}|2\mathrm{j}) - \mathrm{P}_{\mathrm{data}}(2\mathrm{b}|2\mathrm{j}) = 0.78 \pm 0.02$
- Expected data/MC value in $\mathrm{N}_{\text{b-jet}} = 0$ bin given 2 jets
  - $\frac{\mathrm{P}_{\mathrm{data}}(0\mathrm{b}|2\mathrm{j})}{\mathrm{P}_{\mathrm{MC}}(0\mathrm{b}|2\mathrm{j})} = 0.96 \pm 0.02$

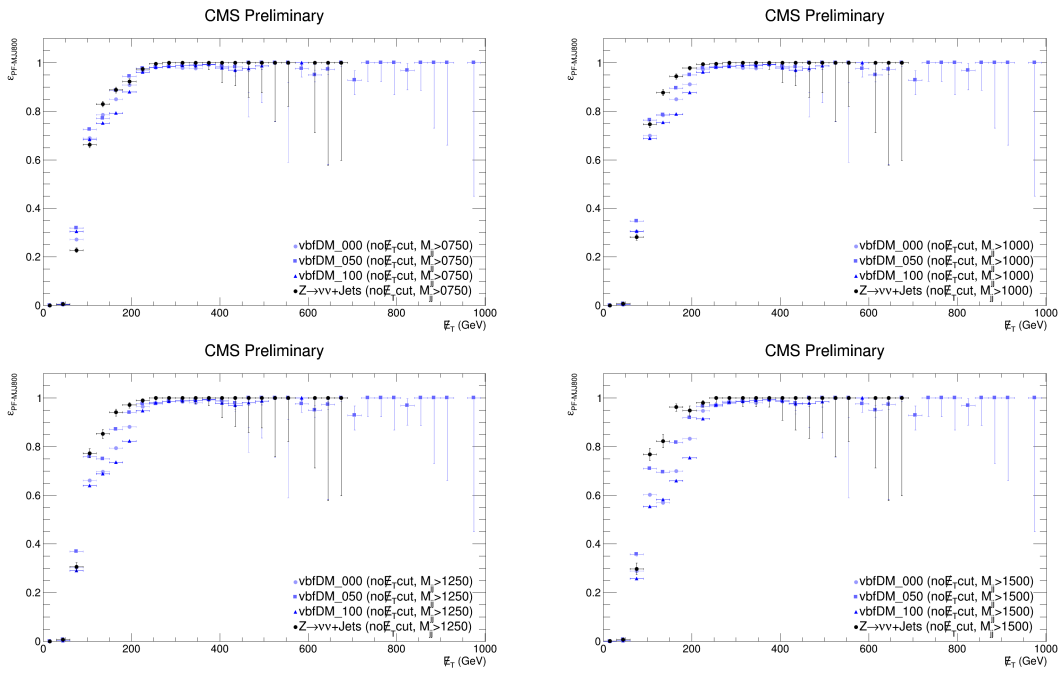


Figure A.12: $\varepsilon_{\textbf{HLT\_DiPFJet40\_PFMETnoMu65\_MJJ800VBF\_AllJets\_v*}}$ vs. $p_{\mathrm{T}}^{\mathrm{miss}}$ given various $m_{jj}$ selections for (a) $\mathrm{Z}(\rightarrow \nu\bar{\nu})$ + jets and $\widetilde{\chi}_1^0\widetilde{\chi}_1^0 jj$ with LSP mass of (b) 0 GeV, (c) 50 GeV, and (d) 100 GeV.

### A.3.3 TTBar Background Estimate

In order to obtain a $t\bar{t}$ enhanced region, we make use of the fact that $t\bar{t}$ events always contain b-jets from the decay of the top quarks. Therefore, in order to obtain a $t\bar{t}$ control sample, one can require the presence of one or more tagged b-jets. We require two jets to be tagged as b-jets when selecting the $t\bar{t}$ control region in order to reduce the V + jets contribution in this region.

Measuring the $t\bar{t}$ contribution in the signal region makes use of b-tagging to obtain a clean sample of $t\bar{t}$ events, where efficiencies can be measured and used to extrapolate to the signal region. Therefore, a natural concern or question is whether the use of b-tagging produces any bias on the measured VBF efficiency. It is important to note that cross-checks have indeed been carried out to determine any possible bias introduced by the b-tagging requirements. We find that no bias is introduced due to the requirement of at

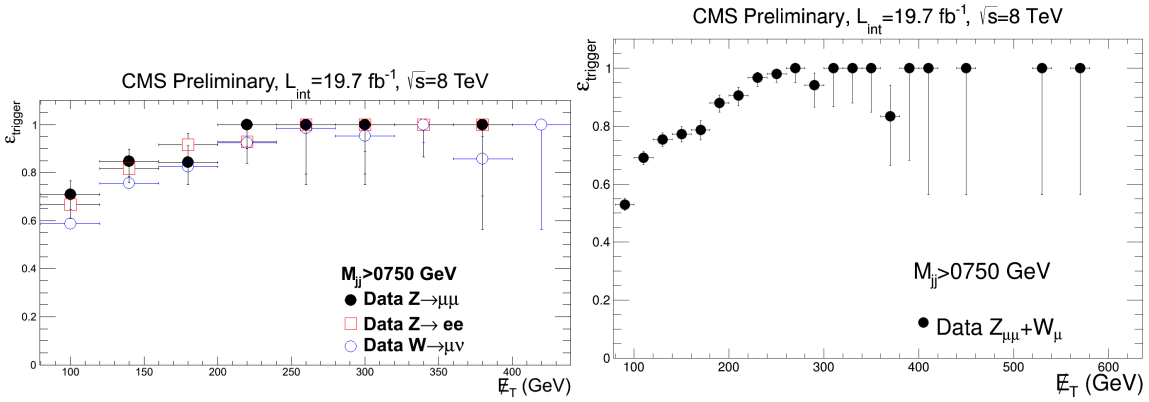


Figure A.13: Trigger efficiency in data events as a function of $p_{\mathrm{T}}^{\mathrm{miss}}$ for (a) $\mathrm{Z}_{\mu^+\mu^-\to\nu\bar{\nu}}$+Jets, $\mathrm{W}_{\mu\to\nu}$+Jets, and $\mathrm{Z}_{ee}$+Jets events and (b) the sum of $\mathrm{Z}_{\mu^+\mu^-\to\nu\nu}$+Jets and $\mathrm{W}_{\mu\to\nu}$+Jets data events.

least 1 or 2 b-tagged jets (Figures A.15 and A.16). The closure test is performed using two different $t\bar{t}$ MC samples generated using POWHEG (v1.0r1380) [104, 105] and MADGRAPH (v5.1.3) [106]. Since MADGRAPH and POWHEG model jet kinematics differently, this comparison is done to check the robustness of our method against mismodeling within our background simulation.

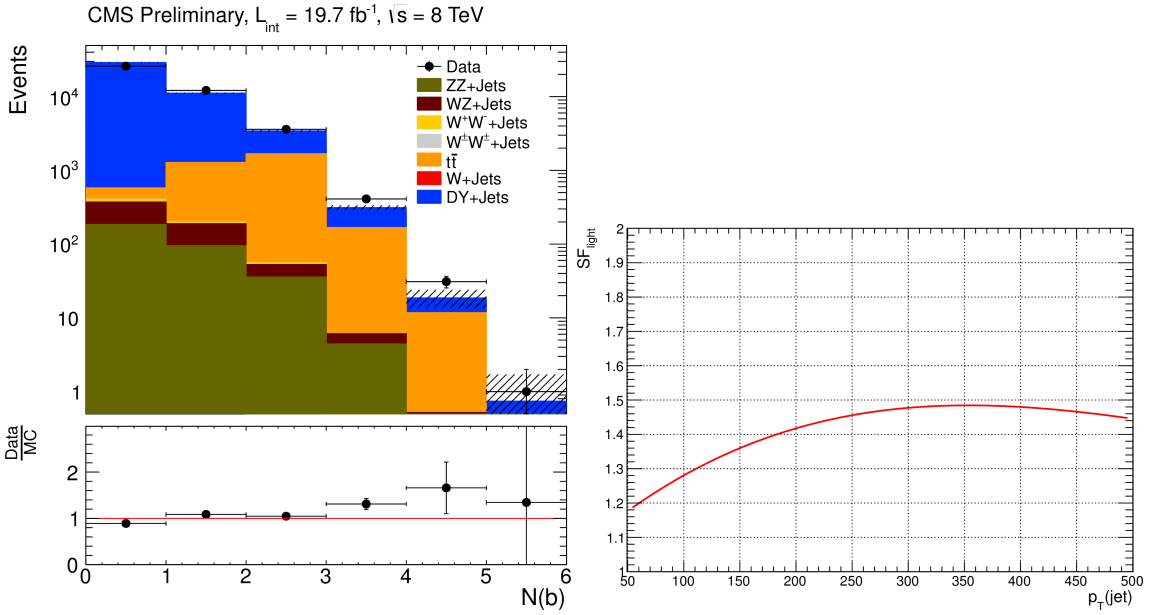


Figure A.14: (a) Distribution of number of b-jets in the Z_CR1. (b) b-jet mis-identification scale factor as a function of $p_{\mathrm{T}}$.

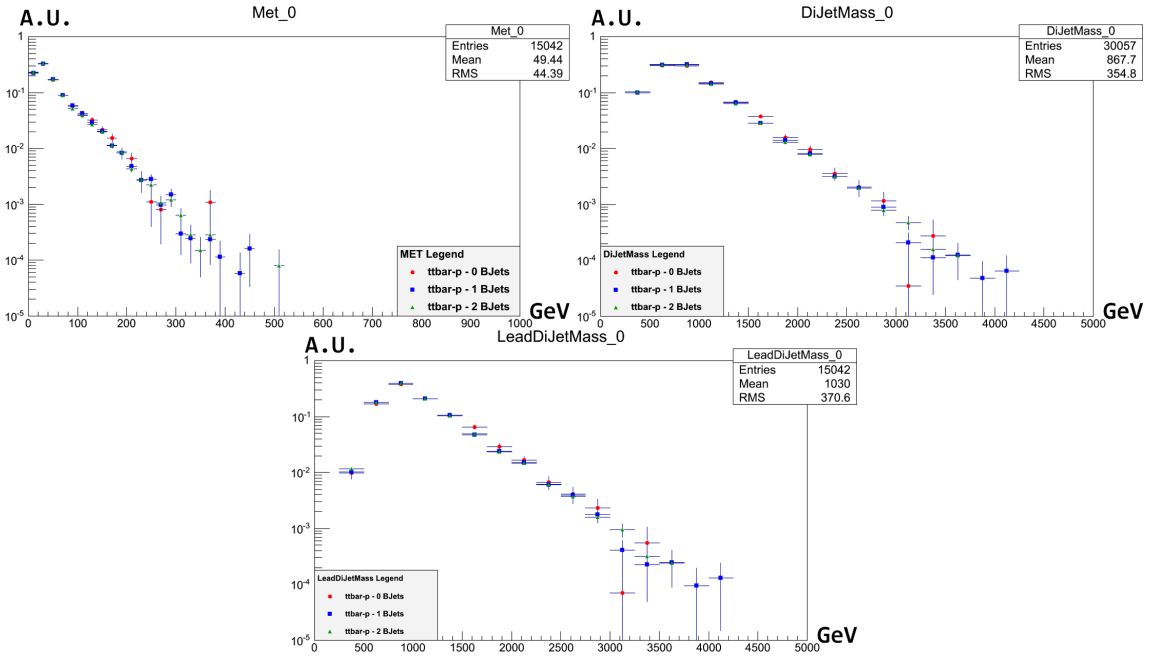


Figure A.15: (a) $p_{\mathrm{T}}^{\mathrm{miss}}$ distribution (b) $m_{jj}$ distribution, and (c) Leading $m_{jj}$ distribution given 0, 1, and 2 b-jet requirements for a Powheg-based $t\bar{t}$ MC sample.

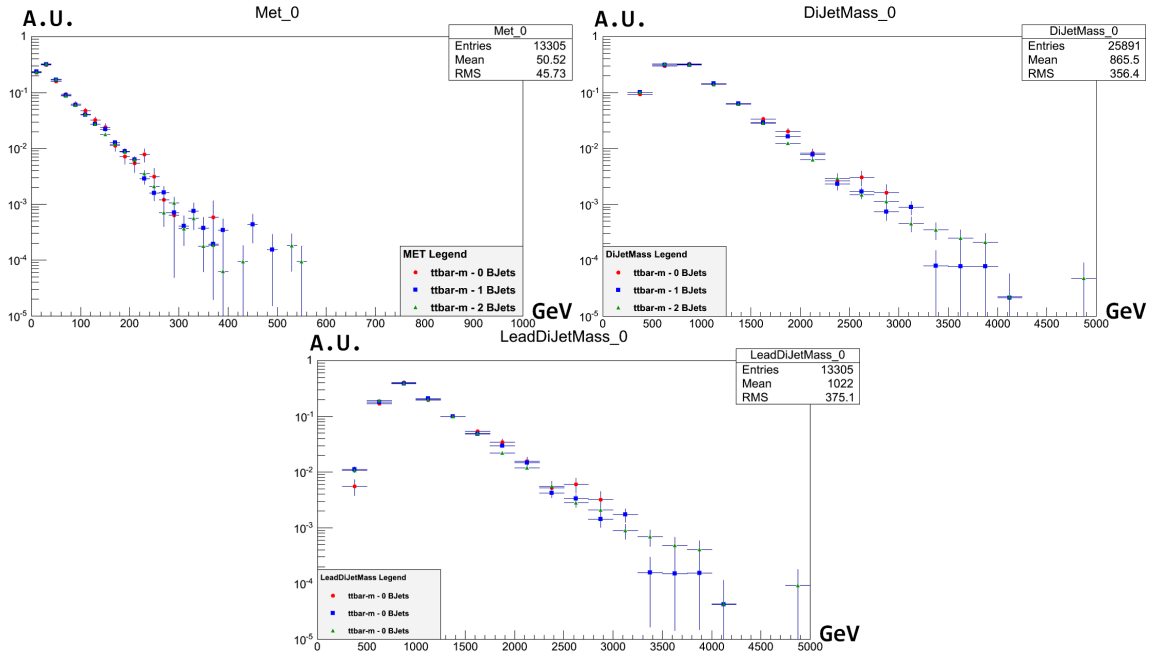


Figure A.16: (a) $p_{\mathrm{T}}^{\mathrm{miss}}$ distribution and (b) Leading $m_{jj}$ distribution given 0, 1, and 2 b-jet requirements for a MadGraph-based $t\bar{t}$ MC sample.

## A.4 Validation of Dark Matter effective field theory model

The effective field theory model for the interactions of electroweak bosons and DM particles is used to re-interpret the results obtained for $\tilde{b}$ in the compressed SUSY mass spectrum. In particular, we present the result for the scalar operator, which is equivalent to the Higgs portal model, i.e. two electroweak bosons fuse to a scalar mediator particle (like a SM Higgs boson), and then the scalar particle decays to two DM particles (see Fig. A.17). To interpret the result with a EFT model, we need to be careful about events in which too much momentum flows, as the EFT description breaks down when $Q_{tr}^2 \gg M_{med}$, where $Q_{tr}^2$ is momentum transfer and $M_{med}$ is a mediator mass. The $Q_{tr}^2$ is defined by

$$Q_{tr}^2 = (p_q^\mu + p_q^\mu - p_j^\mu - p_j^\mu)(p_{q_\mu} + p_{q_\mu} - p_{j_\mu} - p_{j_\mu}), \tag{A.1}$$

which is equivalent to the mass of DM–DM system given by

$$Q_{tr}^2 = (p_\chi^\mu + p_\chi^\mu)(p_{\chi_\mu} + p_{\chi_\mu}) = M(\chi,\chi)^2, \tag{A.2}$$

in the VBF production of DM particles: $\mathrm{pp} \to \chi\chi jj$. The center of mass energy of a DM pair, $Q_{tr} = M(\chi,\chi)$, is used to indicate the regions of validity by following the procedure outlined in the reference [107]. Figure A.18 shows $Q_{tr}$ distributions of various DM masses. Sharp turn-on at the DM pair production thresholds (= $2M(\chi)$) is observed there as expected. Please see ref. [108] for details.

### A.4.1 $E_{cm}$ truncation of DM–DM system

There are two key ingredients in the $E_{cm}$ truncation procedure. First, there is always an inertial frame of reference so that the mediator particle is at rest. In such a frame, the total energy flowing in equals to the energy going out. If too much energy pours into this interaction vertex, then signal predictions obtained using a EFT model may not be accurate.

Therefore the criterion to assess the validity of the EFT model is to compute the fraction of generated events that satisfy a cutoff energy in the rest frame of the mediator. In this study, we take a critical fraction as 80%, following reference [109]. Namely, we determine the value of a center of mass energy $E_{cm}$ so that the following condition is met:

$$R_\Lambda = 80\% = \frac{\int_0^x E_{cm} dE_{cm}}{\int_0^\infty E_{cm} dE_{cm}} = \frac{\int_0^x E_{in} dE_{in}}{\int_0^\infty E_{in} dE_{in}} = \frac{\int_0^x E_{out} dE_{out}}{\int_0^\infty E_{out} dE_{out}},$$

where $E_{in} = E_{out}$ are the incoming and outgoing energy of particles in the rest frame, and $x$ is the critical mediator mass for the condition. In this calculation, the events are required to satisfy signal selection criteria described in Sec. 7.1. The distributions of DM–DM pair mass and VBF jet $p_{\mathrm{T}}$ are plotted in Fig. A.19 for simulated events with the DM mass of 50, 200, and 600 GeV.

Second, a EFT model does not specify a mass of the mediator. Instead, one of its input parameters is a $M_*$( or $\Lambda$), which is related to the mass of the mediator by $M_* = M_{med}/\mathrm{g}_{eff}$, where $\mathrm{g}_{eff}$ is the effective coupling between electroweak bosons and DM particles. The effective coupling is one of the unknown parameters, and thus we take few benchmark points, $\mathrm{g}_{eff}$ = 1, 2, and 4, to evaluate the fraction of events satisfying the condition mentioned above. Figure A.20 shows comparison of DM–DM $p_{\mathrm{T}}$ (equivalent to $p_{\mathrm{T}}^{\mathrm{miss}}$) and VBF jet pair mass with and without $E_{cm}$ truncation for $R_\Lambda = 80\%$. The shape of distributions are consistent with and without the truncation. The resultant $R_\Lambda = 80\%$ curves are superposed with the 95% CL limits in Fig. A.21. The bulk of 95% limit band lies above $\mathrm{g}_{eff}$ = 2 in lower DM mass regions, while the band lies between $\mathrm{g}_{eff}$ = 2 and 4 in the higher mass regions, before entering to the $\Lambda < 2M_\chi$ hashed region. Truncated limits, after removing events failing to satisfy $Q_{tr} < \Lambda/\mathrm{g}_{eff}$, are plotted for $\mathrm{g}_{eff}$ = 1 and 2. The sharp turn-off is observed there as expected from Fig. A.18 when $\Lambda/\mathrm{g}_{eff}$ approaches to the DM pair production thresholds.

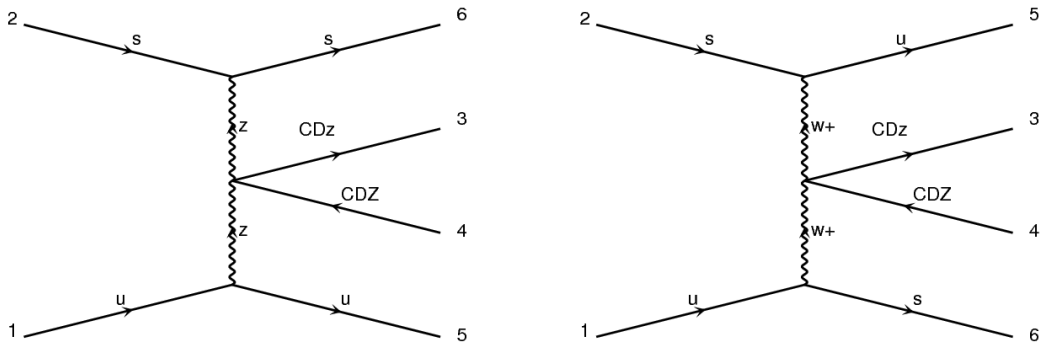


Figure A.17: Feynman diagrams of electroweak bosons and DM particles interactions. The CDz symbol denotes a DM particle.

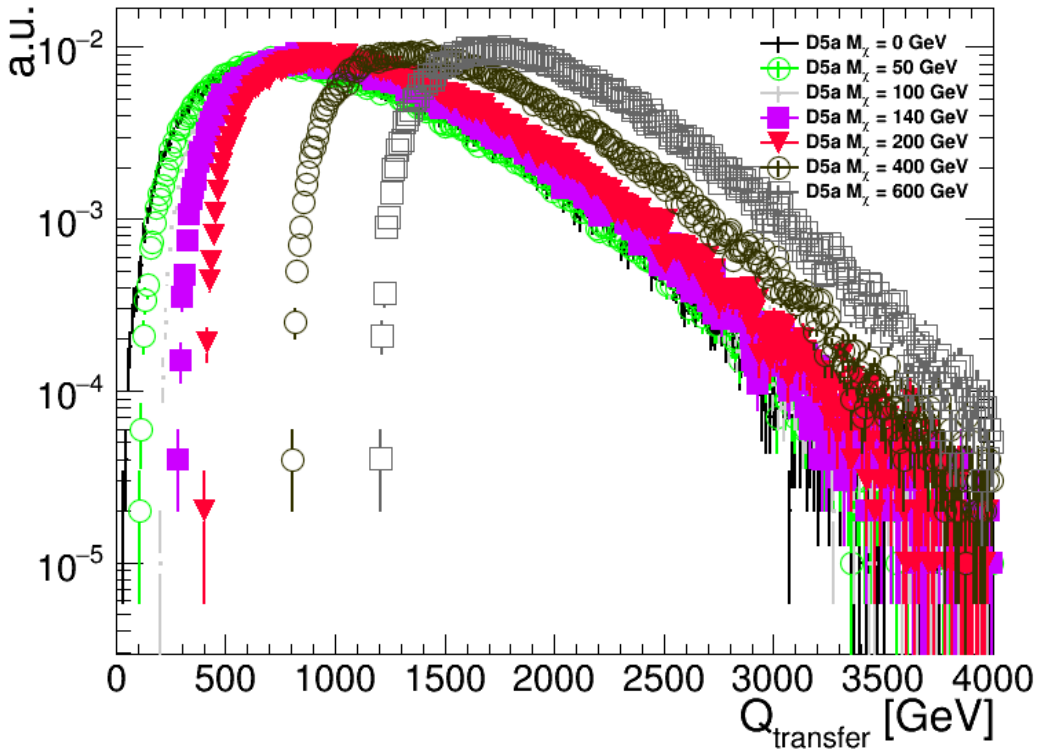


Figure A.18: Momentum transfer in $\mathrm{pp} \to \chi\chi jj$.

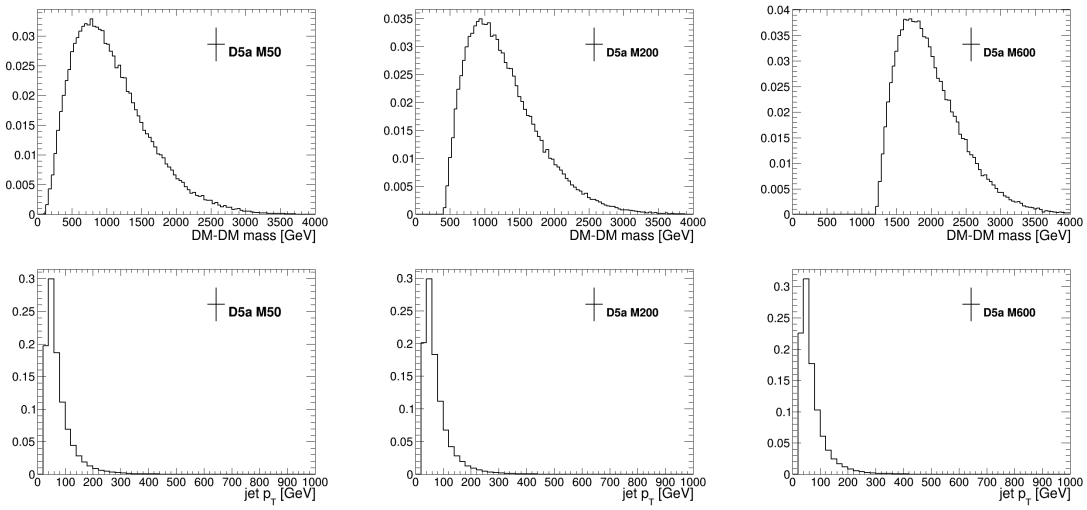


Figure A.19: Distributions of the mass of DM–DM pairs (upper row), and VBF jet $p_{\mathrm{T}}$ in the simulated samples with the DM mass of (50, 200, 600) GeV (lower row).

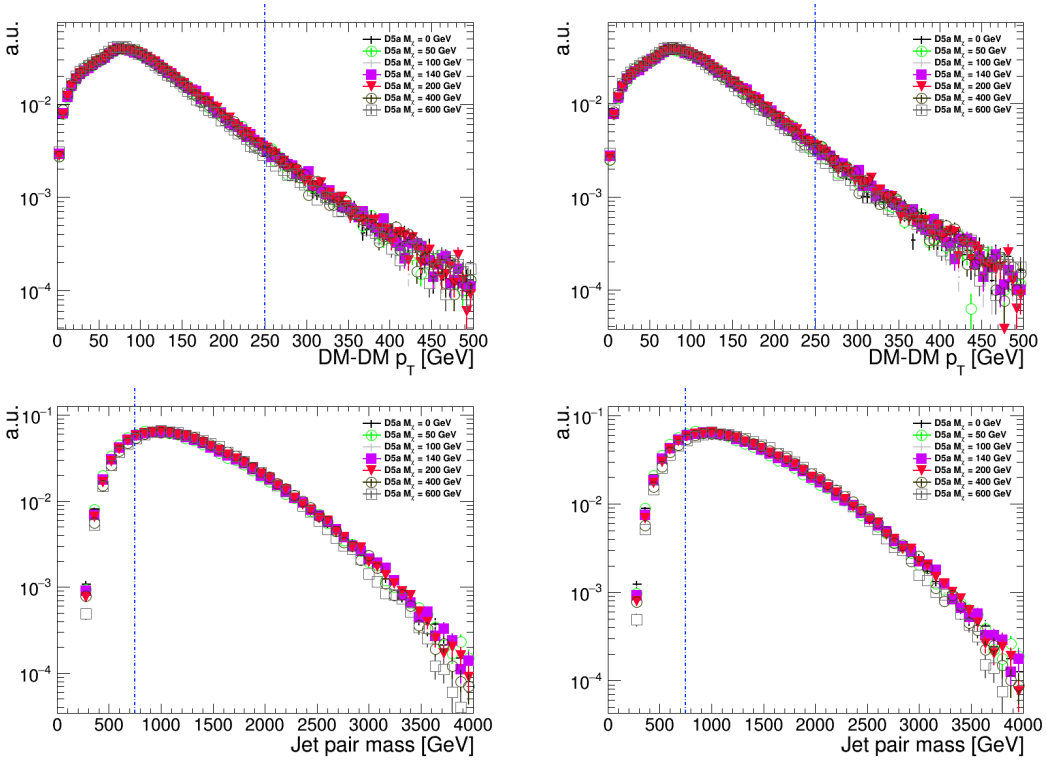


Figure A.20: Distributions of DM–DM $p_{\mathrm{T}}$ (upper row), and VBF jet pair mass (lower row), with and without removal of the highest 20% $Q_{tr}$ events. Dashed vertical lines indicate event selection values.

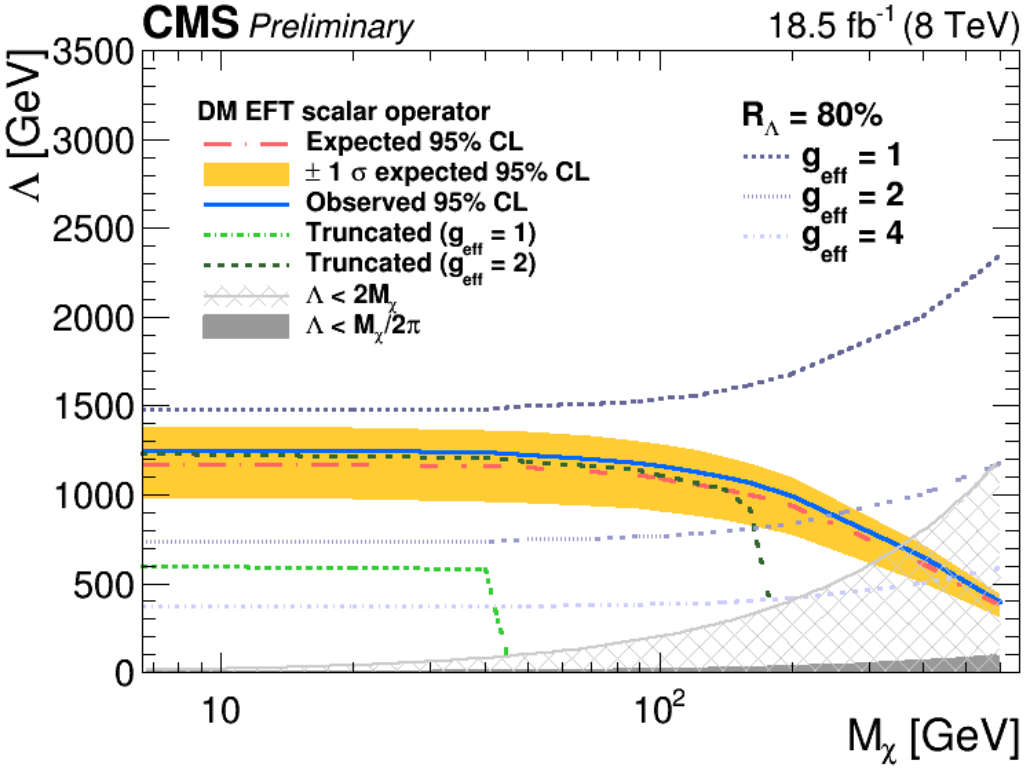


Figure A.21: Re-interpretation of the $\tilde{b}$ results. The validity of DM EFT model is indicated by the $R_\Lambda$=80% curves with benchmark $g_{eff}$ values. Limits after event removal are indicated for $g_{eff}$ = 1 and 2.

# BIBLIOGRAPHY


[1] The ATLAS collaboration. Observation and measurement of Higgs boson decays to $WW^*$ with ATLAS at the LHC. *Phys. Rev. D*, 92(1), Jul 2015.

[2] Planck collaboration. Planck 2013 results. XVI. Cosmological parameters. *Astronomy & Astrophysics*, 571:A16, Oct 2014.

[3] Glennys R. Farrar and Pierre Fayet. Phenomenology of the production, decay, and detection of new hadronic states associated with supersymmetry. *Phys. Lett. B*, 76(5):575–579, Jul 1978.

[4] Stephen P. Martin. A Supersymmetry Primer. *Adv. Ser. Direct. High Energy Phys.*, 18:1–153, Apr 2010.

[5] The CMS collaboration. Searches for electroweak production of charginos, neutralinos, and sleptons decaying to leptons and W, Z, and Higgs bosons in $pp$ collisions at 8 TeV. *Eur. Phys. J. C*, 74(9):3036, Sep 2014.

[6] The ATLAS collaboration. Search for direct production of charginos and neutralinos in events with three leptons and missing transverse momentum in $\sqrt{s} = 8$ TeV $pp$ collisions with the ATLAS detector. *JHEP*, 2014(4):169, Apr 2014.

[7] Particle Data Group. Review of Particle Physics. *Chin. Phys. C*, 38(9):090001, Aug 2014.

[8] The CMS collaboration. Search for invisible decays of Higgs bosons in the vector boson fusion and associated ZH production modes. *Eur. Phys. J. C*, 74(8):2980, Aug 2014.

[9] The ATLAS collaboration. Search for invisible decays of a Higgs boson using

vector-boson fusion in $pp$ collisions at $\sqrt{s} = 8$ TeV with the ATLAS detector. *JHEP*, 2016(1):172, Jan 2016.

[10] Bhaskar Dutta, Alfredo Gurrola, Will Johns, Teruki Kamon, Paul Sheldon, and Kuver Sinha. Vector boson fusion processes as a probe of supersymmetric electroweak sectors at the LHC. *Phys. Rev. D*, 87(3):035029, Feb 2013.

[11] Andres G. Delannoy, Bhaskar Dutta, Alfredo Gurrola, Will Johns, Teruki Kamon, Eduardo Luiggi, Andrew Melo, Paul Sheldon, Kuver Sinha, Kechen Wang, and Sean Wu. Probing Dark Matter at the LHC using Vector Boson Fusion Processes. *Phys. Rev. Lett.*, 111(6):061801, Aug 2013.

[12] The CMS collaboration. Searches for third-generation squark production in fully hadronic final states in proton-proton collisions at $\sqrt{s} = 8$ TeV. *JHEP*, 06(6):116, Jun 2015.

[13] The ATLAS collaboration. Search for new phenomena in final states with an energetic jet and large missing transverse momentum in $pp$ collisions at $\sqrt{s} = 8$ TeV with the atlas detector. *Eur. Phys. J. C*, 75(7):299, Jul 2015.

[14] The CMS collaboration. Search for dark matter, extra dimensions, and unparticles in monojet events in proton-proton collisions at $\sqrt{s} = 8$ TeV. *Eur. Phys. J. C*, 75(5):235, May 2015.

[15] R. C. Cotta, J. L. Hewett, M.-P. Le, and T. G. Rizzo. Bounds on dark matter interactions with electroweak gauge bosons. *Phys. Rev. D*, 88(11):116009, Dec 2013.

[16] Wolfgang Pauli. The Connection Between Spin and Statistics. *Phys. Rev.*, 58(8):716–722, Oct 1940.

[17] Richard P. Feynman and Steven Weinberg. *Elementary Particles and the Laws of Physics: The 1986 Dirac Memorial Lectures*. Cambridge University Press, 1999.

[18] Kerson Huang. *Introduction to Statistical Physics*. Taylor & Francis, 2001.

[19] James Clerk Maxwell. A Dynamical Theory of the Electromagnetic Field. *Royal Society of London Philosophical Transactions Series I*, 155:459–512, 1865.

[20] Marek Zralek. 50 Years of Neutrino Physics. *Acta Phys. Polon.*, B41:2563–2582, 2011.

[21] Fredrick Reines and Clyde L. Cowan. The Neutrino. *Nature*, 178(4531):446–449, Sep 1956.

[22] J.F. Donoghue, E. Golowich, and B.R. Holstein. *Dynamics of the Standard Model*. Cambridge Monographs on Particle Physics, Nuclear Physics and Cosmology. Cambridge University Press, Jul 1994.

[23] Francis Halzen and Alan D. Martin. *Quarks and Leptons: An Introductory Course in Modern Particle Physics*. Wiley, 1st edition, 1984.

[24] B.R. Martin and G. Shaw. *Particle Physics*. Manchester Physics Series. Wiley, 3rd edition, Dec 2008.

[25] V. Barger and R. Phillips. *Collider Physics*. Frontiers in physics. Addison-Wesley Pub., revised edition, Dec 1996.

[26] Gordon L. Kane. *Modern Elementary Particle Physics: The Fundamental Particles and Forces?* Advanced book classics. Addison-Wesley Pub., Apr 1993.

[27] Emmy Noether. Invariante variationsprobleme. *Nachrichten von der Gesellschaft der Wissenschaften zu Gttingen, Mathematisch-Physikalische Klasse*, 1918:235–257, 1918.

[28] Sean M. Carroll. *Spacetime and Geometry: An Introduction to General Relativity*. Addison Wesley, Sep 2003.

[29] M. Dalarsson and N. Dalarsson. *Tensor Calculus, Relativity, and Cosmology: A First Course*. Elsevier Academic Press, 1st edition, Apr 2005.

[30] Richard L. Liboff. *Introductory Quantum Mechanics*. Addison-Wesley, 4th edition, Aug 2002.

[31] Franz Mandl and Graham Shaw. *Quantum Field Theory*. Wiley, 2nd edition, May 2010.

[32] James D. Bjorken and Sidney D. Drell. *Relativistic Quantum Mechanics*. Mcgraw-Hill College, June 1965.

[33] Carl D. Anderson. The Positive Electron. *Phys. Rev.*, 43:491–494, Mar 1933.

[34] J. Schechter and J. W. F. Valle. Neutrino masses in SU(2) $\bigotimes$ U(1) theories. *Phys. Rev. D*, 22:2227–2235, Nov 1980.

[35] Utpal Sarkar. *Particle and Astroparticle Physics (Series in High Energy Physics, Cosmology and Gravitation)*. CRC Press, 2007.

[36] Michael S. Turner. Cosmological parameters. *AIP Conf. Proc.*, 478(1):113–128, 1999.

[37] A. Dekel, F. Stoehr, G. A. Mamon, T. J. Cox, G. S. Novak, and J. R. Primack. Lost and found dark matter in elliptical galaxies. *Nature*, 437(7059):707–710, Sep 2005.

[38] Douglas Clowe, Marusa Bradac, Anthony H. Gonzalez, Maxim Markevitch, Scott W. Randall, Christine Jones, and Dennis Zaritsky. A direct empirical proof of the existence of dark matter. *The Astrophysical Journal Letters*, 648(2):L109, 2006.

[39] Gerard Jungman, Marc Kamionkowski, and Kim Griest. Supersymmetric dark matter. *Physics Reports*, 267(5-6):195 – 373, 1996.

[40] David J. Griffiths. *Introduction to Electrodynamics (4th Edition)*. Addison-Wesley, 4th edition, Oct 2012.

[41] HERA collaboration. Search for contact interactions, large extra dimensions and finite quark radius in ep collisions at HERA. *Phys. Lett. B*, 591:23 – 41, 2004.

[42] V. F. Weisskopf. On the Self-Energy and the Electromagnetic Field of the Electron. *Phys. Rev.*, 56:72–85, Jul 1939.

[43] P. van Nieuwenhuizen. Supergravity. *Physics Reports*, 68(4):189 – 398, 1981.

[44] Oliver Sim Brning, Paul Collier, P Lebrun, Stephen Myers, Ranko Ostojic, John Poole, and Paul Proudlock. *LHC Design Report*. CERN, 2004.

[45] The ATLAS collaboration. *ATLAS detector and physics performance: Technical Design Report, 1*. Technical Design Report ATLAS. CERN, Geneva, 1999.

[46] The ATLAS collaboration. *ATLAS detector and physics performance: Technical Design Report, 2*. Technical Design Report ATLAS. CERN, Geneva, 1999.

[47] The CMS collaboration. *CMS Physics: Technical Design Report Volume 1: Detector Performance and Software*. Technical Design Report CMS. CERN, Geneva, 2006.

[48] The CMS collaboration. CMS Physics: Technical Design Report Volume 2: Physics Performance. *J. Phys. G*, 34(CERN-LHCC-2006-021. CMS-TDR-8-2):995–1579. 669 p, 2007.

[49] The LHCb collaboration. The LHCb Detector at the LHC. *JINST*, 3(LHCb-DP-2008-001. CERN-LHCb-DP-2008-001):S08005, 2008.

[50] P Cortese, Christian Wolfgang Fabjan, Lodovico Riccati, Karel Safark, and Hans de Groot. *ALICE physics performance: Technical Design Report*. Technical Design Report ALICE. CERN, Geneva, 2005.

[51] C.E.Hill. CERN Hadron Linacs. http://linac2.web.cern.ch/linac2/, 2008. Accessed: 2016-03-08.

[52] Karlheinz Schindl. The injector chain for the LHC. page 6, Jan 1999.

[53] CMS Collaboration. *CMS Physics: Technical Design Report Volume 1: Detector Performance and Software*. Technical Design Report CMS. CERN, Geneva, 2006.

[54] The CMS collaboration. The CMS experiment at the CERN LHC. *JINST*, 3(08):S08004, 2008.

[55] The CMS collaboration. *The CMS magnet project: Technical Design Report*. Technical Design Report CMS. CERN, Geneva, 1997.

[56] V Karimaki, M Mannelli, P Siegrist, H Breuker, A Caner, R Castaldi, K Freudenreich, G Hall, R Horisberger, M Huhtinen, and A Cattai. *The CMS tracker system project: Technical Design Report*. Technical Design Report CMS. CERN, Geneva, 1997.

[57] H.Chr. Kastli, M. Barbero, W. Erdmann, Ch. Hormann, R. Horisberger, D. Kotlinski, and B. Meier. Design and performance of the CMS pixel detector readout chip. *Nucl. Instrum. Meth. A*, 565(1):188 – 194, 2006.

[58] Ozhan Koybasi, Kirk Arndt, Gino Bolla, Daniela Bortoletto, Petra Merkel, and Ian Shipsey. Assembly and qualification procedures of CMS forward pixel detector modules. *Nucl. Instrum. Meth. A*, 638(1):55 – 62, 2011.

[59] D. Kotlinski, E. Bartz, W. Erdmann, K. Gabathuler, R. Horisberger, Ch. Hormann, H-Ch. Kastli, B. Meier, and S. Schnetzer. The control and readout systems of the CMS pixel barrel detector. *Nucl. Instrum. Meth. A*, 565(1):73 – 78, 2006.

[60] M.J. French, L.L. Jones, Q. Morrissey, A. Neviani, R. Turchetta, J. Fulcher, G. Hall, E. Noah, M. Raymond, G. Cervelli, P. Moreira, and G. Marseguerra. Design and re-

sults from the apv25, a deep sub-micron CMOS front-end chip for the CMS tracker. *Nucl. Instrum. Meth. A*, 466(2):359 – 365, 2001.

[61] The CMS collaboration. *The CMS electromagnetic calorimeter project: Technical Design Report*. Technical Design Report CMS. CERN, Geneva, 1997.

[62] The CMS collaboration. Energy calibration and resolution of the CMS electromagnetic calorimeter in pp collisions at $\sqrt{s}$= 7 TeV. *JINST*, 8(09), Sep 2013.

[63] The CMS collaboration. *The CMS hadron calorimeter project: Technical Design Report*. Technical Design Report CMS. CERN, Geneva, 1997.

[64] HCAL Endcaps: From artillery to absorbers. https://cmsinfo.web.cern.ch/cmsinfo/Detector/HCAL/History.html, 2011. Accessed: 2016-03-08.

[65] The CMS collaboration. *The CMS muon project: Technical Design Report*. Technical Design Report CMS. CERN, Geneva, 1997.

[66] M Tytgat, A Marinov, P Verwilligen, N Zaganidis, A Aleksandrov, V Genchev, P Iaydjiev, M Rodozov, M Shopova, G Sultanov, Y Assran, M Abbrescia, C Calabria, A Colaleo, G Iaselli, F Loddo, M Maggi, G Pugliese, L Benussi, S Bianco, M Caponero, S Colafranceschi, F Felli, D Piccolo, G Saviano, C Carrillo, U Berzano, M Gabusi, P Vitulo, M Kang, K S Lee, S K Park, S Shin, and A Sharma. The upgrade of the CMS RPC system during the first LHC long shutdown. *JINST*, 8(02):T02002, 2013.

[67] The CMS collaboration. *CMS TriDAS project: Technical Design Report, Volume 1: The Trigger Systems*. Technical Design Report CMS. 2000.

[68] L Agostino, G Bauer, B Beccati, U Behrens, J Berryhil, K Biery, T Bose, A Brett, J Branson, E Cano, H Cheung, M Ciganek, S Cittolin, J A Coarasa, B Dahmes, C Deldicque, E Dusinberre, S Erhan, D Gigi, F Glege, R Gomez-Reino, J Gutleber,

D Hatton, J Laurens, C Loizides, F Ma, F Meijers, E Meschi, A Meyer, R K Mommsen, R Moser, V O'Dell, A Oh, L Orsini, V Patras, C Paus, A Petrucci, M Pieri, A Racz, H Sakulin, M Sani, P Schieferdecker, C Schwick, J F S Margaleff, D Shpakov, S Simon, K Sumorok, A S Yoon, P Wittich, and M Zanetti. Commissioning of the CMS High Level Trigger. *JINST*, 4(10), 2009.

[69] Werner Herr and B Muratori. Concept of luminosity. 2006.

[70] J. D. Bjorken. Rapidity gaps and jets as a new-physics signature in very-high-energy hadron-hadron collisions. *Phys. Rev. D*, 47:101–113, Jan 1993.

[71] Tilman Plehn. *Lectures on LHC Physics (Lecture Notes in Physics, Vol. 844)*. Springer, 1st edition, Mar 2012.

[72] G. C. Cho, K. Hagiwara, J. Kanzaki, T. Plehn, D. Rainwater, and T. Stelzer. Weak boson fusion production of supersymmetric particles at the CERN LHC. *Phys. Rev. D*, 73:054002, Mar 2006.

[73] The CMS collaboration. Search for supersymmetry in the vector-boson fusion topology in proton-proton collisions at $\sqrt{s}$= 8 TeV. *JHEP*, 2015(11), Nov 2015.

[74] The CMS collaboration. Performance of the CMS missing transverse momentum reconstruction in pp data at $\sqrt{s}$= 8 TeV. *JINST*, 10(02):P02006, 2015.

[75] Arely Cortes-Gonzalez. Searches for mono-X at the LHC. Technical Report ATL-PHYS-PROC-2014-073, CERN, Geneva, Jul 2014.

[76] The CMS collaboration. Commissioning of the particle-flow event with the first LHC collisions recorded in the CMS detector. CMS Physics Analysis Summary CMS-PAS-PFT-10-001, 2010.

[77] M. Cacciari, G. P. Salam, and G. Soyez. The anti-$k_t$ jet clustering algorithm. *JHEP*, 04:63, 2008.

[78] The CMS collaboration. Particle-flow event reconstruction in CMS and performance for jets, taus, and $E_{\mathrm{T}}^{\mathrm{miss}}$. CMS Physics Analysis Summary CMS-PAS-PFT-09-001, 2009.

[79] The CMS collaboration. Measurement of electroweak production of two jets in association with a Z boson in proton-proton collisions at $\sqrt{s} = 8$ TeV. *Eur. Phys. J. C*, 75(2), 2015.

[80] The CMS collaboration. Identification of b-quark jets with the CMS experiment. *JINST*, 8(04):P04013, 2013.

[81] The CMS collaboration. BTagSFMethods. https://twiki.cern.ch/twiki/bin/viewauth/CMS/BTagSFMethods. (Accessed on 03/09/2016).

[82] Dan Green. *The Physics of Particle Detectors (Cambridge Monographs on Particle Physics, Nuclear Physics and Cosmology)*. Cambridge University Press, Jul 2005.

[83] S. Baffioni, C. Charlot, F. Ferri, D. Futyan, P. Meridiani, I. Puljak, C. Rovelli, R. Salerno, and Y. Sirois. Electron reconstruction in CMS. *Eur. Phys. J. C*, 49(4):1099–1116, 2007.

[84] The CMS collaboration. EGammaScaleFactors2012. https://twiki.cern.ch/twiki/bin/view/Main/EGammaScaleFactors2012#2012_8_TeV_Jan22_Re_recoed_data. (Accessed on 03/09/2016).

[85] The CMS collaboration. Performance of CMS muon reconstruction in $pp$ collision events at $\sqrt{s} = 7$ TeV. *JINST*, 7(10), 2012.

[86] The CMS collaboration. The performance of the CMS muon detector in proton-proton collisions at $\sqrt{s} = 7$ TeV at the LHC. *JINST*, 8(11), 2013.

[87] The CMS collaboration. MuonReferenceEffs. https://twiki.cern.ch/twiki/

bin/viewauth/CMS/MuonReferenceEffs#22Jan2013_ReReco_of_2012_data_re. (Accessed on 03/09/2016).

[88] M. Pioppi. Tau reconstruction and identification with particle-flow techniques using the CMS detector at LHC. *Nucl. Phys. B Proc. Suppl.*, 189:311 – 316, 2009. Proceedings of the Tenth International Workshop on Tau Lepton Physics.

[89] The CMS collaboration. Reconstruction and identification of $\tau$ lepton decays to hadrons and $\nu$ $\tau$ at CMS. *JINST*, 11(01):P01019–P01019, Jan 2016.

[90] The CMS collaboration. Swguidehiggsanalysiscombinedlimit. https://twiki.cern.ch/twiki/bin/viewauth/CMS/SWGuideHiggsAnalysisCombinedLimit. (Accessed on 03/09/2016).

[91] Glen Cowan, Kyle Cranmer, Eilam Gross, and Ofer Vitells. Asymptotic formulae for likelihood-based tests of new physics. *Eur. Phys. J. C*, 71(2), 2011.

[92] The CMS collaboration. Performance of muon identification in $pp$ collisions at $\sqrt{s} = 7$ TeV. Technical Report 10, 2012.

[93] The CMS collaboration. Performance of electron reconstruction and selection with the CMS detector in proton-proton collisions at $\sqrt{s} = 8$TeV. *JINST*, 10(06):P06005, 2015.

[94] Pavel M. Nadolsky, Hung-Liang Lai, Qing-Hong Cao, Joey Huston, Jon Pumplin, Daniel Stump, Wu-Ki Tung, and C.-P. Yuan. Implications of CTEQ global analysis for collider observables. *Phys. Rev. D*, 78:013004, Jul 2008.

[95] A. D. Martin, W. J. Stirling, R. S. Thorne, and G. Watt. Update of parton distributions at NNLO. *Phys. Lett. B*, 652:292, 2007.

[96] Maria Ubiali. NNPDF1.0 parton set for the LHC. *Nucl. Phys. B Proc. Suppl.*,

186:62, 2009. Proceedings of the QCD 08, 14th High-Energy Physics International Conference On Quantum ChromoDynamics.

[97] G. Nanava and Z. Was. How to use SANC to improve the PHOTOS Monte Carlo simulation of bremsstrahlung in leptonic W boson decays. *Acta Phys. Polon.*, B34:4561–4570, 2003.

[98] Gabriela Miu and Torbjörn Sjöstrand. W production in an improved parton-shower approach. *Phys. Lett. B*, 449:313, 1999.

[99] The CMS collaboration. Absolute Calibration of the Luminosity Measurement at CMS: Winter 2012 Update. 2012.

[100] R. C. Cotta, J. L. Hewett, M.-P. Le, and T. G. Rizzo. Bounds on dark matter interactions with electroweak gauge bosons. *Phys. Rev. D*, 88:116009, Dec 2013.

[101] A. L. Read. Presentation of search results: the $CL_s$ technique. *J. Phys. G*, 28(10):2693, 2002.

[102] Thomas Junk. Confidence level computation for combining searches with small statistics. *Nucl. Instrum. Meth. A*, 434:435 – 443, 1999.

[103] The CMS collaboration. Btagrecommendation53xrereco. https://twiki.cern.ch/twiki/bin/viewauth/CMS/BtagRecommendation53XReReco. (Accessed on 03/09/2016).

[104] Paolo Nason and Carlo Oleari. NLO Higgs boson production via vector-boson fusion matched with shower in POWHEG. *JHEP*, 02:037, 2010.

[105] Simone Alioli, Paolo Nason, Carlo Oleari, and Emanuele Re. A general framework for implementing NLO calculations in shower Monte Carlo programs: the POWHEG BOX. *JHEP*, 06:043, 2010.

[106] J. Alwall, R. Frederix, S. Frixione, V. Hirschi, F. Maltoni, O. Mattelaer, H. S. Shao, T. Stelzer, P. Torrielli, and M. Zaro. The automated computation of tree-level and next-to-leading order differential cross sections, and their matching to parton shower simulations. *JHEP*, 07:079, 2014.

[107] D. Abercrombie, N. Akchurin, E. Akilli, J. Alcaraz Maestre, B. Allen, B. Alvarez Gonzalez, J. Andrea, A. Arbey, G. Azuelos, et al. Dark Matter Benchmark Models for Early LHC Run-2 Searches: Report of the ATLAS/CMS Dark Matter Forum. *ArXiv e-prints*, July 2015.

[108] Giorgio Busoni, Andrea De Simone, Enrico Morgante, and Antonio Riotto. On the validity of the effective field theory for dark matter searches at the LHC. *Phys. Lett. B*, 728:412 – 421, 2014.

[109] The CMS collaboration. Search for dark matter direct production using razor variables in events with two or more jets in $pp$ collisions at 8 TeV. CMS Physics Analysis Summary CMS-PAS-EXO-14-004, 2015.